

Transmon-based quantum computers from a many-body perspective

Inaugural-Dissertation

zur

Erlangung des Doktorgrades

der Mathematisch-Naturwissenschaftlichen Fakultät

der Universität zu Köln

vorgelegt von

Christoph Berke

aus Bergisch Gladbach



Köln 2023

Berichterstatter: Prof. Dr. Simon Trebst

Prof. Dr. Achim Rosch

Tag der mündlichen Prüfung: 15.02.2023

Disclaimer: This version of the thesis “Transmon-based quantum computers from a many-body perspective” is not the published version, but an updated version in which (i) references are updated and (ii) typos are corrected. The published version is available on the publication server of the University of Cologne at <https://kups.ub.uni-koeln.de/71997/>.

As of now (2024-12-03), the following changes have been made in the version at hand:

1. Update Ref. [P2], arXiv:2304.14435, now published in Phys. Rev. Res. **6** (3), 033128 (2024).
2. Update Ref. [378], arXiv:2212.03805, now published in Phys. Rev. B **109** (14), 144201 (2024).

Die vorliegende Dissertation wurde von der Mathematisch-Naturwissenschaftlichen Fakultät der Universität zu Köln angenommen.

Cover illustration: Fock space lattice for a chain of capacitively coupled transmons with $L = 12$, $N_{\text{ex}} = 6$, cf. Fig. 4.5.

Abstract

The quest for quantum computers is in full swing. Over the past decade, the frontiers of quantum computing have broadened from exploring few-qubit devices to developing viable multi-qubit processors. One of the protagonists of the present era is the superconducting transmon qubit. By harmoniously combining applied engineering with fundamental research in computer science and physics, transmon-based quantum processors have matured to a remarkable level. Their applications include the study of topological and nonequilibrium states of matter, and it is argued that they have already ushered us into the era of quantum advantage. Nevertheless, building a quantum computer that can solve problems of practical relevance remains a massive challenge. As the field progresses with unbridled panache, the question of whether we have a comprehensive picture of the potential dangers lurking in the wings acquires increasing urgency. In particular, it needs to be thoroughly clarified whether, with viable quantum computers of $\mathcal{O}(50)$ qubits at hand, new and hitherto unconsidered obstacles associated with the *multi-qubit* nature can emerge. For example, the high accuracy of quantum gates in small-scale devices is hard to obtain in larger processors. On the hardware side, the unique requirements posed by large quantum computers have already spawned new approaches to qubit design, control, and readout.

This thesis introduces a novel, less applied perspective on multi-qubit processors. Specifically, we fuse the field of quantum engineering and many-body physics by applying concepts from the theories of localization and quantum chaos to multi-transmon arrays. From a many-body perspective, transmon architectures are synthetic systems of interacting and disordered nonlinear quantum oscillators. While a certain amount of coupling between the transmons is indispensable for performing elementary gate operations, a delicate balancing with disorder—site-to-site variations in the qubit frequencies—is required to prevent locally injected information from dispersing in extended many-body states. Transmon research has established different modalities to cope with this dilemma between inefficiency (slow gates due to small coupling or large disorder) and information loss (large couplings or too small disorder). We analyze small instances of transmon quantum computers in exact diagonalization studies, using contemporary quantum processors as blueprints. Scrutinizing the spectrum, many-body wave functions, and qubit-qubit correlations for experimentally relevant parameter regimes reveals that some of the prevalent transmon design schemes operate close to a region of uncontrollable chaotic fluctuations. Furthermore, we establish a close link between the advent of chaos in the classical limit and the emergence of quantum chaotic signatures. Our concepts complement the traditional few-qubit picture that is commonly exploited to optimize device configurations on small scales. Destabilizing mechanisms beyond this local scale can be detected from our fresh perspective. This suggests that techniques developed in the field of many-body localization should become an integral part of future transmon processor engineering.

Contents

Outline	1
1 Introduction	3
1.1 Brief history lesson	3
1.2 How to build a quantum computer	4
1.3 Macroscopic quantum systems and transmons	6
1.4 The current state: NISQ, transmons and quantum advantage	7
1.5 The art of quantum computing	9
1.6 Changing perspective: the transmon many-body problem	10
1.7 A comment on the units	11
2 Quantum chaos and many-body localization	13
2.1 Quantum chaos	13
2.1.1 Integrability and classical chaos	13
2.1.2 Quantum chaos and random matrix theory	15
2.1.3 Chaotic eigenfunctions	18
2.2 Thermalization	19
2.2.1 The eigenstate thermalization hypothesis	20
2.2.2 ETH and quantum chaos	21
2.3 Avoiding chaos by disorder: many-body localization	22
2.3.1 From single-particle localization to many-body localization	22
2.3.2 Emergent integrability and local integrals of motion	24
2.4 Signatures of many-body localization and eigenstate thermalization	26
2.5 Selected aspects of many-body localization	29
2.6 Summary	32
3 The transmon platform for quantum computing	33
3.1 The transmon	33
3.1.1 Superconductivity and the Josephson junction	34
3.1.2 The transmon Hamiltonian	35
3.1.3 Quantum circuit theory	37
3.1.4 Adding control knobs: the flux tunable transmon	40
3.2 Properties of the transmon	41
3.2.1 The transmon as a rigid quantum rotor	41
3.2.2 Charge dispersion	42
3.2.3 Anharmonicity and effective Hamiltonian	43
3.2.4 Eigenfunctions	46

3.3	Interacting transmons	48
3.3.1	Capacitive coupling	49
3.3.2	Tunable couplers	50
3.4	Entangling gates	51
3.4.1	Gates in flux-tunable transmon architectures	52
3.4.2	Gates in fixed-frequency architectures: the CR gate	52
3.5	Transmon processor design schemes	54
3.5.1	Fixed-frequency architectures	55
3.5.2	Tunable transmon architectures	59
3.5.3	Tunable transmons with tunable couplers	60
3.6	Summary	61
4	Many-body localization and quantum chaos in transmon quantum computers	63
4.1	The model	64
4.2	Noninteracting transmon arrays	64
4.2.1	Excitation bundles and excitation structures	65
4.3	Interacting transmon arrays	67
4.3.1	Configuration space hopping	68
4.3.2	Truncating the Hilbert space	69
4.4	Chaos and MBL in coupled transmon arrays	70
4.4.1	Spectrum of a coupled transmon array: spaghetti plots	70
4.4.2	Level statistics	72
4.4.3	Results for the Kullback-Leibler divergences	74
4.4.4	Wave function statistics	75
4.4.5	Varying the disorder strength.	78
4.5	Quantum chaos in prevalent transmon architectures	79
4.5.1	Results for scheme-A disorder	79
4.5.2	Results for scheme-B disorder	82
4.5.3	Data collapse	84
4.6	Further properties of the MBL-chaos transition	85
4.6.1	Many-body mobility edge	85
4.6.2	Influence of the filling fraction	88
4.6.3	Influence of the system size	89
4.6.4	Anderson localization	90
4.7	Towards two dimensions	91
4.8	Qubit correlations	92
4.8.1	Identifying qubit states	94
4.8.2	Extracting l -qubit correlations: Walsh transformation	96
4.9	Dynamics	98
4.10	Summary	101
5	Quantum chaos and frequency engineering	105
5.1	Frequency pattern	105
5.2	Overview: Bloch states, global MBL and permutation multiplets	106
5.2.1	The two limiting cases: strongly disordered and clean devices	107
5.2.2	Permutation multiplets	108
5.3	Quantum chaos in engineered frequency patterns	109
5.3.1	A simple example: the $L = 5$ chain	109

5.3.2	Unveiling quantum chaos: chaotic multiplets	112
5.3.3	Wave functions	114
5.3.4	Delocalization of computational states	114
5.4	Effect of LASIQ on IBM's recent chips	115
5.4.1	IPR before and after annealing	115
5.4.2	Chaos on the heavy-hexagon lattice	116
5.5	Summary	117
6	Classical transmon dynamics	119
6.1	Equations of motion	119
6.1.1	Mimicking qubit states	120
6.2	Lyapunov exponents and methods	120
6.3	Results	121
6.3.1	Two coupled transmons	121
6.3.2	Ten coupled transmons	123
6.3.3	Towards larger system sizes	125
6.3.4	Classical chaos in frequency-engineered transmon arrays	126
6.4	Summary	128
7	Concluding remarks	131
A	Appendix for Chapter 3	135
A.1	Examples of LASIQ tuned chips	135
B	Appendix for Chapter 4	139
B.1	Truncation of the Hilbert space	139
B.1.1	Comparison of the full, the truncated, and the effective model	142
B.2	Details on the implementation	143
B.2.1	The single transmon Hamiltonian in the charge basis	143
B.2.2	Matrix representation of the interacting Hamiltonian	144
B.2.3	Verifying the implementation	144
B.2.4	Calculation of the reduced density matrix	145
B.3	Influence of the disorder distribution	146
B.4	Quantifying chaos near the maximal density of states	147
B.5	Results for scheme-B parameters and two-dimensional geometries	148
C	Appendix for Chapter 5	151
C.1	Additional details on the $L = 5$ chain	151
C.1.1	Data collapse for the T - δE_J phase diagrams	151
C.1.2	Detailed analysis of all multiplets of the $N_{\text{ex}} = 3$ bundle	152
C.2	Two-dimensional representation of the IPR	153
C.3	Quantifying chaos with level statistics in a restructuring Hilbert space	153
C.4	Permutation multiplets for the 3×3 geometry with AB pattern	157
D	Field-driven effects in Kitaev spin liquids	159
Bibliography		163

Outline

This thesis applies concepts from the theory of *many-body localization* (MBL) to the *transmon* platform for quantum computing to scrutinize prevalent processor architectures for the emergence of *quantum chaotic* behavior. In detail, this work is organized as follows:

Chapter 1 intends to give readers without prior knowledge of quantum computing a brief outline of the subject. It positions the transmon in the zoo of possible qubit platforms and discusses its leading role in the current NISQ era. We introduce some frequently used basic vocabulary. Following this, **Chapter 2** acquaints with the concepts of many-body localization and quantum chaos. The discussion highlights which properties of the chaotic phase constitute a fundamental obstacle for quantum computing. Furthermore, a selection of diagnostic tools is introduced, based on which one can distinguish between the chaotic and the harmless regime. In **Chapter 3**, attention is focused exclusively on this thesis's main protagonist: the superconducting transmon qubit. We discuss its properties in detail and show how many transmons combined can form a quantum computer. Arrays of interconnected transmons are the main object of interest to which we apply the MBL toolbox. Contemporary processors from companies like IBM or Google serve as the blueprint for our simulations. Therefore, the second half of the chapter takes a closer look at the design philosophies to which different groups subscribe. In particular, this discussion emphasizes the close link between the choice of a specific gate implementation and the parameters of the static ‘gate-off’ Hamiltonian. The insights from this analysis guide the parameter choices for the simulations. **Chapter 4** then provides a detailed and rigorous discussion of the transmon processor from the many-body perspective. We show that a regime of dangerous chaotic fluctuations can be found in some pervasive design classes. A particular focus lies on establishing quality indicators for parameter regimes that show deviations from deep localization but are not in the immediate vicinity of hard quantum chaos. The focus in **Chapter 5** is on the critical examination of one of the most recent engineering enhancements—the implementation of frequency patterns to augment the precision in the entangling gate operations—from the many-body perspective. For **Chapter 6**, we switch perspectives and solve the classical equations of motion for a system of coupled transmons. In the classical limit, a transmon reduces to a nonlinear pendulum. Our quantitative analysis of these coupled pendulum systems reveals a striking similarity between the quantum mechanical and the classical system regarding their susceptibility to chaos. We conjecture that classical analysis can be a tool to gauge the quality of specific parameter configurations for system sizes beyond the feasibility of a quantum mechanical simulation. Finally, **Chapter 7** combines a broad summary, concluding remarks, and a brief outlook on future research directions. In particular, we highlight again why merging the theoretical field of many-body physics with the applied field of quantum chip design is fruitful and why quantum engineers should include many-body concepts in their efforts to design viable processor architectures.

Outline

These chapters are further supplemented by three appendices, providing examples of state-of-the-art transmon processors, additional results, and an extended discussion of some of the more technical aspects of this work, including details on the implementation.

Last mentioned, Appendix D provides a concise overview of results obtained in an independent branch of research (field-induced effects in Kitaev spin liquids) conducted during the course of this thesis.

Chapter 1 Introduction

No other technology is said to have a similar society-transforming potential as quantum computing. Its ability to solve specific problems dramatically faster than a classical computer is expected to lead to groundbreaking new insights in, e.g., pharmaceutical research, materials science, and a revolution in cryptography [1]. We are only beginning to glimpse the possibilities, with most applications still in the shadows (just as the invention of the transistor did not preordain the development of the smartphone). To realize a quantum computer that can solve a problem of social and practical relevance, one must be able to control *many* quantum mechanical degrees of freedom simultaneously. Unfortunately, nobody knows when (and if ever) this will happen because nobody knows whether “...controlling large-scale quantum systems (is) merely really, really hard, or (...) ridiculously hard” [2]. Optimists hope for the first to be true and that—maybe after a decade of further intensive research—a ‘large-scale’ quantum computer can be built. Pessimists believe in the latter and doubt that we will ever get there in any foreseeable future [3] (they also like to point out that the optimist’s answer ‘In ten years’ remains unchanged over the years [4]). Regardless of one’s position, there are two common grounds for agreement: (i) Quantum computing is in its infancy, and the best current quantum processors are orders of magnitude too poor to solve any relevant problems. (ii) In recent years, however, impressive experimental progress has been made, ushering in a new era characterized by $\mathcal{O}(100)$ -*qubit* devices that address the challenge of integrating an ever-increasing number of qubits into a processor while preserving phase coherence. In contrast, earlier years focused on proof-of-principle demonstrations of, e.g., high-fidelity gates [5, 6] or small instances of quantum algorithms [7, 8] on minimal processors consisting of two to a few qubits. The single most important platform in this new era is the superconducting *transmon* quantum computer.

In this thesis, we attempt to bridge the gap between two previously distinct domains: *many-body localization* and transmon processor engineering. This introductory chapter is intended to provide readers with no expertise in quantum computing with some basic vocabulary that later chapters will frequently use. Furthermore, we contextualize this work in the burgeoning field of quantum computing and point out why our approach offers new insights. This chapter was compiled based on Refs. [9–11] that are recommended to the reader for further details.

1.1 Brief history lesson

Classical computers are powerful tools that fundamentally changed society, but even the best supercomputers falter when simulating systems of only a few atoms. The (vague) idea that simulating nature cannot be efficiently done on a classical computer and that a quantum computer, playing by the same quantum mechanical rules that nature obeys, should be used instead was already envisioned more than 40 years ago by Manin [12] and later popularized by Feynman [13]. David Deutsch embraced and formalized these ideas, shaping the modern conception of

a *universal quantum computer* as a device that is capable of efficiently simulating any physical system [14]. His pioneering work also contains the first example that quantum computers have computational resources that classical devices cannot match. Expanding on this initial step, the following decade has seen essential contributions to the theory of quantum computation. Outstanding examples include Deutsch's circuit model for quantum computing [15] and further demonstrations of quantum algorithms that outperform their classical counterparts [16, 17].

Even though the primacy of specific quantum algorithms over their classical counterparts was repeatedly shown, the research domain has not received much attention, given the apparent insignificance and artificiality of the tackled problems. In 1994, Peter Shor [18, 19] liberated the field of quantum computing from its niche existence and transformed it into one of the most flourishing research areas. He demonstrated that the related problems of prime factorization and finding discrete logarithms could be solved exponentially faster¹ using a quantum algorithm than any known classical algorithm. This discovery received widespread attention outside of physics, as Shor's algorithm implemented on a large-scale quantum computer would have devastating consequences for current cryptography protocols like RSA [20], whose assumed security is predicated on the premise that the factoring time grows exponentially in the length of the input. Grover [21, 22] provided another important example of the superiority of quantum computers in 1995. He considered the problem of finding a target element in an unstructured search space, e.g., a specific entry in a database with n entries. Classically, the computational resources scale linearly in n . Grover's algorithm completes the same task using resources of the order \sqrt{n} . Even if this is only a modest quadratic speed-up, this algorithm has caught considerable attention because of its countless possible applications. Moreover, in contrast to factorization, the classical complexity class of the unstructured search is known, which implies that the superiority of Grover's algorithm is strictly proven.

Notably, a quantum computer is not superior to its classical counterpart in every task: its superiority is limited to algorithms tailored to solve specific problems efficiently. We saw examples of exponential and modest speed-up, but other tasks might not benefit at all [23]. Designing quantum algorithms that outperform their classical counterparts is tremendously challenging. It is an important quest to identify tasks feasible for a quantum computer but hard to simulate classically. Another challenge, needless to say, is to realize a quantum computer capable of implementing these algorithms. Shor's algorithm may go down in history as the end of cryptography, or just a small amusing footnote of it, if it fails to build a device that can achieve the hypothetical, hardly imaginary speed-up over classical computers. Currently, the record for the largest prime number reliably factorized with Shor's algorithm is 21 [24].

1.2 How to build a quantum computer

The theoretical advances that cumulated in Shor's and Grover's algorithms were quickly followed by an increasing interest in possible realizations of quantum computers. As a guidance, DiVincenzo [11] formulated a set of five basic requirements that every viable physical implementation of a quantum computer must obey: One needs (i) well-characterized and scalable two-level states (*qubits*) and (ii) a decoherence time that allows many two- and single-qubit gates to be performed. It must be possible to (iii) initialize and (iv) measure qubit states, and (v) a *universal*

¹Computational complexity is measured by investigating how the number of steps required to complete a task grows with the size of the input n . In Shor's algorithm, this number is polynomial in $\log n$, which is an almost exponential speed-up compared to the sub-exponential scaling of the best classical algorithms.

set of gates must be provided, allowing any unitary operation to be implemented. Some of these points require further explanation.

Qubits. The two-level system required by the first criterion is called the quantum bit or *qubit*. One denotes its two states as $|0\rangle$ and $|1\rangle$. It replaces the classical bit as the fundamental unit of information. Contrary to the classical bit (either 0 or 1), the permitted states of a qubit are all linear combination $|\psi\rangle = \alpha|0\rangle + \beta|1\rangle$ with $|\alpha|^2 + |\beta|^2 = 1, \alpha, \beta \in \mathbb{C}$. Rewriting $|\psi\rangle = \cos\theta|0\rangle + e^{i\phi}\sin\theta|1\rangle$, a qubit can be visualized as a point on the unit sphere, called Bloch sphere, defined by the angles (ϕ, θ) . A quantum computer owes its potency to the exponential increase in information with the number of qubits: An N -bit system contains N pieces of information. A system of N qubits can be in a superposition of 2^N basis states and contains the information about 2^N probability amplitudes. Unfortunately, nature hardly offers us perfect two-level systems. In any physical hardware, the *computational space* spanned by the qubit states $|0\rangle$ and $|1\rangle$ is just a projection of a more complicated Hilbert space. For a ‘well-characterized’ qubit, one has to ensure that it faithfully mimics the properties of a true two level-system by shielding the computational subspace from the complementary Hilbert space such that the noncomputational states do not compromise the operation of the quantum computer. For the transmon—the qubit variant that is at the core of this thesis—the ground state $|0\rangle$ with energy E_0 and the first excited state $|1\rangle$ with energy E_1 serve as the two qubit states. The quantity $\omega_q = (E_1 - E_0)\hbar$ is called the qubit frequency. Any physical implementation of a qubit is an erroneous object. It couples to many environmental degrees of freedom, rendering a coherent superposition unstable due to a mechanism called decoherence.

Decoherence. Nature is quantum mechanical, yet, we do not perceive quantum mechanical properties in our daily life. The process behind the emergence of classical behavior is called decoherence. It describes the loss of quantum coherence in a system due to interactions with the environment. Originally developed to enrich the discussion of the measurement problem [25], decoherence is a major threat to the realization of a quantum computer, where coherent superpositions are to be maintained undisturbed over a time long enough to perform many gate operations. Broadly simplified, the interactions with the environment transform the coherent superposition $|\psi\rangle = \alpha|0\rangle + \beta|1\rangle$ into a classical probability mixture described by the density matrix $\rho = |\alpha|^2|0\rangle\langle 0| + |\beta|^2|1\rangle\langle 1|$ in a characteristic time known as decoherence time (or qubit lifetime). Decoherence thus abrogates the superposition principle, nullifying the power of algorithms that harness this property. An adequate description of decoherence takes additional aspects into account, e.g., a decoherence time that depends on the initial configuration [11]. The coherence properties of a qubit are characterized by two different times: the relaxation time T_1 , which is the characteristic time for the qubit to relax from its $|1\rangle$ state to its $|0\rangle$ state, and the dephasing time T_2 , which, as above, quantifies the lifetime of coherent superpositions [26, 27]. Improving the decoherence time is one of the most critical hurdles on the way to a quantum computer.

Gates. In the circuit model [15], each computation is a sequence of quantum gates, i.e., elementary unitary operations that act on the elements of a Hilbert space of one or more qubits. A small set of gates sufficient to complete any calculation is said to be universal for quantum computing [28]. It has been shown that single- and two-qubit gates suffice for universality [29, 30]. To be precise, a complete set of single-qubit gates, enabling arbitrary rotations on the Bloch sphere, complemented by any entangling two-qubit gate is universal [31–33]. A prototypical entangling

gate is the CNOT gate, which acts on two qubits, the *target* (T) and the *control* qubit (C), and flips the target qubit if the control qubit is in the state $|1\rangle$. Further common examples are the CPHASE, iSWAP, or $\sqrt{i\text{SWAP}}$ gate [28]. Every physical realization of a quantum computer must be equipped with some control hardware necessary to perform arbitrary single-qubit manipulations and entangling two-qubit gates. Note the intrinsic inconsistency between the criteria (ii) and (iii)–(v): coupling of qubits to the environment is indispensable for gates and measurement, but coherence can only be maintained by the best possible isolation from the environment. Just as every real qubit is an error-prone object, gate implementations also never work to perfection. A wrong gate output is produced with a certain probability, known as the error rate. A related (yet different [34]) metric that is easily accessible experimentally and, therefore, widely used is the gate fidelity [28]. A variety of methods to obtain the gate fidelity exists, e.g., quantum process tomography [35], randomized benchmarking [36–38], or cross-entropy benchmarking [39] but finding a reliable, scalable gate validation measure is a complex and as yet unsolved problem.

Platforms. It is a massive challenge to realize a quantum computer that harmonizes good coherence properties with the necessary coupling to the environment for gates and readout. Many different computing platforms have been proposed, some have reached considerable maturity, and others, like NMR-based quantum computers [40], have been abandoned over time because they have proven incompatible with the DiVincenzo criteria. Among the most auspicious platforms are optical quantum computers with photonic qubits [41], Rydberg atoms [42, 43], silicon quantum dots [44], ultracold trapped ions [45, 46], and superconducting circuits. Regarding the five criteria, all these approaches come with their own merits and drawbacks. It is impossible to predict which (or if any) of the current major platforms can be used in the long run to build a fully viable large-scale quantum computer.

1.3 Macroscopic quantum systems and transmons

One expects quantum mechanical effects to play a pivotal role mainly at the level of electrons, atoms, or molecules, that is, in microscopic systems. Therefore, it seems natural to use microscopic degrees of freedom to store and process information, as is common in most quantum computing platforms. In contrast, superconducting qubits rely on quantum effects in circuits of macroscopic extent. They have the advantage that one can easily manufacture them with lithographic techniques developed for integrated circuits. The system parameters are not “God-given constants” [47] but are determined by macroscopic circuit elements that can be adjusted to specific needs through a suitable chosen system design. Whether macroscopic systems allow for the observation of quantum mechanical phenomena was already investigated in the early 1980s, pioneered by Leggett [48, 49]. Seminal experiments suggesting that quantum tunneling [50] and quantized energy levels [51] could indeed be observed in superconducting circuits containing Josephson junctions followed a few years later. This showed that, remarkably, it is possible to tailor systems with an atom-like energy spectrum from macroscopic building blocks [52]. A groundbreaking experiment by Nakamura *et al.* demonstrated the first coherent control and manipulation of a qubit in a superconducting circuit in 1999 [53].

The Josephson tunnel junction. Suppose one has built a circuit with discrete energy levels and aims to process information with the lowest states $|0\rangle$ and $|1\rangle$. Does this constitute a qubit in the sense of criterion (i)? The general answer is no! For a well-defined qubit subspace, it is essential that the qubit frequency ω_q is sufficiently different from transitions between higher

states. Otherwise, it cannot be addressed in a targeted manner as required for gate operations. In particular, one cannot pick qubits from the spectrum of a harmonic oscillator. The heart of any superconducting qubit is a Josephson tunnel junction (a thin insulating layer sandwiched by two superconductors) [54], which, as detailed in Chapter 3, brings the required *nonlinearity* in the form of a nonparabolic inductive potential energy and thus generates an energetic barrier separating the computational subspace from the surrounding Hilbert space [55].

The transmon. There is a plethora of qubits based on superconducting circuits, all founded on the nonlinearity of the Josephson junction. Most qubit types derive from one of three possible initial modalities, the charge, flux, and phase qubit [56, 57], named initially after the information-bearing variable. For example, the qubit states in early charge qubit designs are defined by the presence or absence of an additional Cooper pair in one of the superconductors [55]. The transmon [58], a derivative of the charge qubit, is currently the most widely used qubit variant. Circuits of transmon-type qubits (again, there is a vast zoo) offer a delicate balance between the nonlinearity and protection from random charge fluctuations in circuit components that cause rapid decoherence.

Transmon qubits fulfill the DiVincenzo criteria: The nonlinearity of the junction ensures the existence of a well-defined qubit subspace. Due to its macroscopic extent, transmons decohere faster than microscopic qubits like trapped ions. However, the superconducting, dissipationless metal components combined with careful shielding from environmental noise and operating temperatures of a few Millikelvins enables sufficiently long decoherence times. In the past two decades, the coherence time has increased by more than five orders of magnitude, from about one nanosecond in the first qubit experiment [53] to several hundred microseconds in contemporary chips [59]. The macroscopic size is well suited to engineer strong couplings to resonators, other transmons, or microwave drive lines, enabling high-fidelity readout [26] and fast gates (about 1,000 times faster than for trapped ions [10]). Finally, advanced techniques for qubit state initialization exist [60].

1.4 The current state: NISQ, transmons and quantum advantage

The holy grail of quantum computing, a fault-tolerant large-scale quantum computer, is a distant dream. Two-qubit gates often have error rates exceeding 0.1%, which restricts the number of gates that can be performed before the noise overwhelms the encoded information. Quantum error correction (QEC) [61–63] might eventually enable the realization of fault-tolerant quantum computers with error-prone components at the cost of overhead in the number of qubits. For example, an error-free quantum computer could accomplish the factorization of a 2048-bit RSA integer with 4099 qubits [64], whereas, when using current noisy hardware, this number increases to 20 million [65]. Alternatives with much lower gate errors, such as topological quantum computing [66, 67] with Majorana qubits [68], are long-term challenges to solve, as they bring their own experimental hurdles [69].

Despite the promised land not yet being in sight, a few years ago, we entered a new technological era in which the long-term problem of scalable error-correcting processors is postponed. The focus, roughly said, is on exploring how far one can get with the hardware *now* at hand if suitable problems are picked. This era is dubbed ‘NISQ’ [10], an acronym for *noisy intermediate scale quantum*. ‘Noisy’ refers to the imperfect qubit quality and ‘intermediate scale’ to the fact that arrays of $\mathcal{O}(100)$ qubits are reachable, an important landmark as this is beyond what classical computers can simulate. The guiding philosophy of this epoch is to implement ‘hardware-

informed’ quantum algorithms [70] that are resilient to noise, optimized for a specific processor, and run on noisy hardware with erroneous gates unprotected by QEC. NISQ devices will not solve problems of societal relevance. Instead, one should view this era as a precursor and testing ground of a more advanced future technology. The NISQ era is not only an advance in hardware: as quantum computing prototypes continue to improve, the algorithm side needs to catch up, and problems feasible for NISQ devices but ideally intractable for classical computers have to be designed [71–73]. Some consortia, pioneered by IBM [59, 74], are making NISQ devices publicly available to drive the development of suitable algorithms (with the ulterior motive of maturing quantum computers into a commercial technology).

Quantum advantage and other transmon milestones. Transmon-based quantum computers are a NISQ-era protagonist and were used in much pioneering work. A prominent example is Google’s 53-qubit ‘Sycamore’ processor from the headline-grabbing 2019 experiment [39], which claimed to be the first demonstration of ‘quantum advantage’. Quantum advantage [75, 76] describes a regime where a programmable quantum computer performs a task that is intractable for a state-of-the-art supercomputer on any reasonable timescale.² ‘Sycamore’ completed a computation in about 200 seconds that was argued to have taken 10,000 years on the then-best supercomputer. In many facets, this is a prototypical NISQ experiment: the task—sampling from the output distribution of a pseudorandom quantum circuit—is only of academic interest, known to be exponentially hard on classical computers [73], and was specifically designed to characterize quantum advantage in devices of around 50 noisy qubits [72, 79]. Whether Google has actually demonstrated quantum advantage, however, has been questioned. It was argued that with optimized hardware use, 2.5 days might suffice on a classical machine [80]. Very recently, using a newly developed classical algorithm, the ‘Sycamore’ task was performed in about 15 hours on 512 GPUs [81], showing that quantum advantage is a volatile, impermanent concept that also depends on the availability of classical methods. These criticisms and counterexamples—with all its *raison d’être*—do not touch the point of why Google’s experiment is considered a NISQ era milestone [82, 83]. It is a crucial proof of concept, showing that the coherent control of the states of a 2^{53} -dimensional computational space over a sufficiently long time is possible, a feat whose accomplishment has often been doubted [3, 84]. In 2021, a similar experiment with a 66-transmon processor (‘Zuchongzhi’) was conducted [85], where the cost for a classical simulation is about three orders of magnitude higher, further strengthening the claim that the age of quantum advantage has already begun [86].³

It was also demonstrated that transmon NISQ-devices are well suited for the study of topological (e.g., the toric code model [66, 89]) and nonequilibrium phases of matter (‘time crystals’ [90, 91]), and to probe ideas from quantum gravity [92]. Recently, IBM launched the first transmon processor that surpasses the 100-qubit barrier [59]. Primitives of the surface code [93] (a QEC code with moderate, experimentally feasible error tolerance) were implemented on scalable smaller devices [7, 94], culminating in the demonstration of repeated quantum error-correction cycles in a 17-qubit geometry [95]. Further showcases of the potential of the NISQ era can be found in Ref. [70].

²This definition faces criticism as it depends on the problematic benchmarking of classical computers. Demonstrations of quantum advantage tend to entail a discussion on optimal classical simulations. Besides, the term risks exacerbating the hype surrounding quantum computers [77] and gives the false impression that classical computers will become obsolete [78].

³Other platforms have also followed suit, see, e.g., Ref. [87, 88] for photonic demonstrations of quantum advantage.

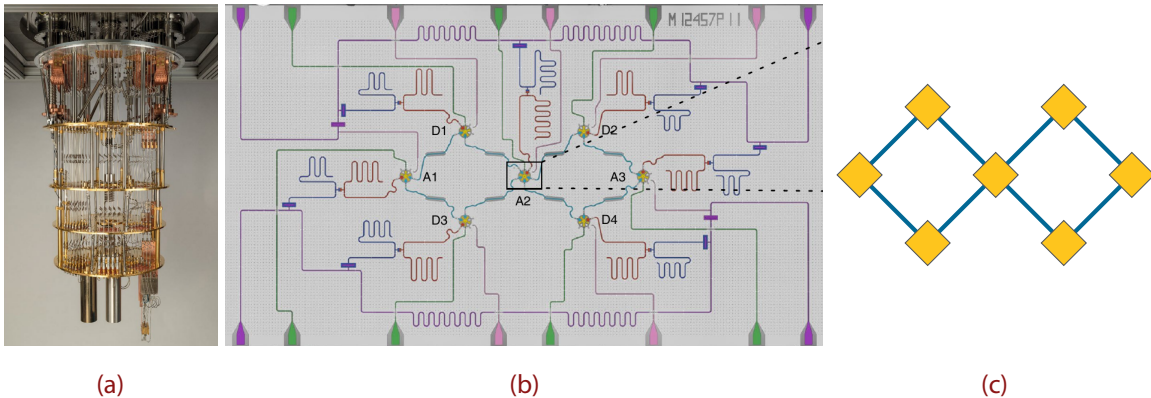


Figure 1.1 – Transmon hardware. (a) Dilution refrigerator used to house and thermalize the actual processor that is located on the bottom side and cooled down to about 10 mK. The tangle of wires that travel vertically transmit the signals for qubit manipulation and readout. Figure taken from Ref. [103] with permission. (b) Electrical circuit of a seven-transmon processor, showing the hardware required for single- and two-qubit gates and readout. The transmons are shown in yellow. Figure taken from Ref. [108] with permission. The two panels illustrate that a quantum computer requires many hardware components to intertwine. In contrast, our model, cartoonishly shown in (c), neglects all processor functionalities and the associated noise and perturbations and considers perfect qubits with nearest-neighbor coupling, indicated by the blue lines.

1.5 The art of quantum computing

In the 1990s, Rolf Landauer suggested a mandatory footnote for all papers on quantum computing: “This proposal, like all proposals for quantum computation, relies on speculative technology, does not in its current form take into account all possible sources of noise, unreliability and manufacturing error, and probably will not work.” [96]. As shown, the current situation is not quite as bleak, but operating even a small quantum computer remains a Brobdingnagian task and demands a whole bundle of technologies to operate seamlessly together, including the actual processor, readout and control electronics, and control software. Figs. 1.1(a) and (b) give an impression of the complexity of the task, see the caption for details.

When scaling up to a larger number of qubits, some problems become more pressing, and others emerge anew: Most importantly, a fault-tolerant computer requires improvements in coherence times, gate fidelities, and readout errors, which needs progress in engineering and material science [97], and demands a deeper theoretical understanding of gate Hamiltonians and new tools to validate gate fidelities [36, 72, 98]. Furthermore, scaling up is only possible if transmon fabrication and cryogenics techniques are improved [99, 100] and nonplanar packaging techniques [101, 102], i.e., arranging circuit elements in multiple layers, are refined. Another major problem is that processors require a tangle of cables, resulting in a vast bulk of wiring even for small devices when each qubit uses separate sets of control and readout electronics. Hardware-saving technologies like multiplex readout, where one line is used for several qubits, must be brought to full fruition, and the list goes on [70, 103]. Danger also threatens from unexpected directions: recently, it was shown that cosmic rays could be a veritable obstacle for a large-scale quantum computer [104].

Progress has been made in some of these challenges (for example, IBM’s ‘Eagle’ processor employs features of 3D integration and multiplex readout [105]), but a plethora of problems remains unresolved, see Refs. [106, 107] for a concise summary. It is estimated that quantum computers with more than $\sim 1,000$ qubits cannot be realized with current technology. A processor with 10^6 – 10^7 qubits cannot be built by refining existing methods but requires groundbreaking new ideas.

1.6 Changing perspective: the transmon many-body problem

The road to a fully featured quantum computer is long and paved with intricate challenges, as shown. In this thesis, we study whether the danger posed by *quantum chaotic* many-body effects that may arise in arrays of *many* transmons also deserves a spot on the list of potential problems. To do so, we consider a minimal model that can be grasped by looking at the transition from Fig. 1.1(b) to (c): we throw away all hardware for qubit control, readout, and initialization and keep only a set of perfectly isolated, noise-free qubits with infinite coherence time and add a qubit-qubit coupling. So to speak, we model an entirely dysfunctional skeleton that is extended to a quantum computer with additional hardware. We intend to ascertain whether this device is already threatened by chaos.

The outwardly isolated array of coupled transmons is approximately described by a Bose-Hubbard Hamiltonian (Chapter 3 elucidates this connection in full detail) with on-site energies $\hbar\omega_{q,i}$, nearest-neighbor hopping amplitude J_{ij} stemming from the coupling, and an attractive on-site interaction U ,

$$\hat{H} = \sum_i \hbar\omega_{q,i} \hat{b}_i^\dagger \hat{b}_i - \frac{U}{2} \sum_i \hat{b}_i^\dagger \hat{b}_i^\dagger \hat{b}_i \hat{b}_i + \sum_{\langle i,j \rangle} \hbar J_{ij} (\hat{b}_i \hat{b}_j^\dagger + \hat{b}_j \hat{b}_i^\dagger) = \hat{H}_0 + \sum_{\langle i,j \rangle} \hbar J_{ij} (\hat{b}_i \hat{b}_j^\dagger + \hat{b}_j \hat{b}_i^\dagger). \quad (1.1)$$

The first two contributions, \hat{H}_0 , describe the uncoupled array. The operator \hat{b}_i^\dagger (\hat{b}_i) creates (annihilates) a bosonic excitation in the transmon at site i . The on-site and hopping energies vary from transmon to transmon, either as a result of unavoidable fabrication imprecisions or due to artificially introduced *disorder*. Thus, from the many-body perspective, a transmon processor is a man-made, interacting, and disordered many-particle system.

Specifying the occupation numbers of each transmon completely characterizes the eigenstates of \hat{H}_0 . For example, in the eigenstate $|310\rangle$ of a three-transmon array, there are 3 (1, 0) bosonic excitations in the transmon at site 1 (2, 3). The *computational states* are those comprising only local excitation numbers ‘0’ and ‘1’. Now imagine an initial state $|\psi_0\rangle$, which is an eigenstate of \hat{H}_0 with a nonuniform particle density $\langle \hat{b}_i^\dagger \hat{b}_i \rangle = \langle \hat{n}_i \rangle$, e.g., the computational state $|1010\dots\rangle$ sketched in Fig. 1.2(a), that evolves under the *full* Hamiltonian \hat{H} (this is called a *quantum quench*). What happens to $|\psi_0(t)\rangle$ under unitary time evolution in the long term? The natural answer is *thermalization* [109, 110]. If subsystems can exchange energy, the system mimics a reservoir for all its sufficiently small subsystems and reaches an effective thermal equilibrium that is fully determined by a few global conserved quantities but displays no local features [111]. For our example, the system thermalizes towards a uniformly distributed energy density, see Fig. 1.2(b), and the information about the bitstring ‘1010...’ carried by the initial state is lost. This system cannot be operated as a quantum memory, let alone as a computer. Perhaps surprisingly, not all interacting systems act as their own reservoirs, and unitary time evolution supplies an alternative outcome: sufficiently large disorder can block the energy exchange between subsystems. The long-term state remembers local details, and the system is a suitable quantum memory (and possibly a computer), see Fig. 1.2(b). This phenomenon is called *many-body localization* (MBL) [112, 113], the properties of which we discuss in detail in the next chapter.

The purpose of this work is to investigate whether arrays of interacting transmons tend to thermalize or whether they host an MBL phase. In particular, we analyze different prevalent disorder regimes, as found in real processors by, e.g., Google and IBM, and study whether signatures of *quantum chaos* might degrade the functionality of these chips.

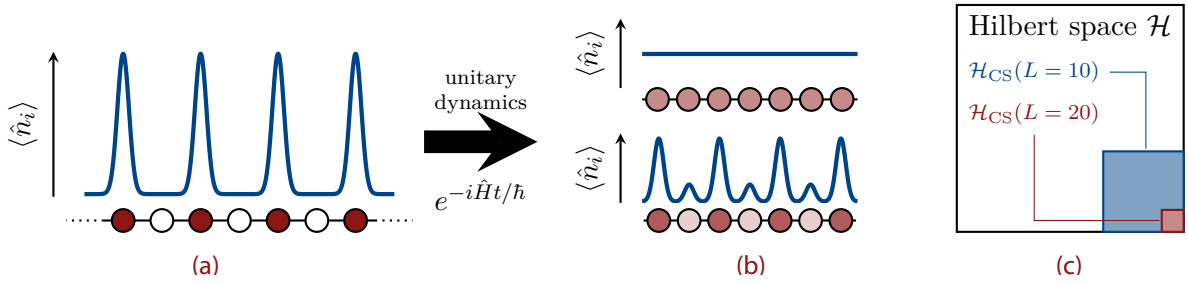


Figure 1.2 – Quantum quench probe where (a) an initial state $|1010\dots\rangle$ evolves under the full interacting Hamiltonian \hat{H} . The colored lattice sites symbolize the nonuniform energy density (red (white)): $\langle \hat{n}_i \rangle = 1(0)$. (b) Under unitary time evolution, the system can either thermalize and relax towards the state with uniform density (top) or many-body localize and remember some details of its initial configuration even after long times (bottom). (c) Comparison of the Hilbert space dimensions of an L -transmon system restricted to the states with a fixed excitation number $N_{ex} = L/2$ (symbolized by the black square) with the number of the computational states, i.e., those with local excitation numbers ‘0’ and ‘1’. (a) and (b) inspired by Ref. [114].

Another potential hazard arises from the fact that the transmon, albeit used as a qubit, is a multi-level system. In a many-transmon processor, the eigenstates of \hat{H}_0 are divided into computational states and states, where at least one transmon has an occupation greater than one. The number of these remaining ‘junk’ states far dwarfs that of computational states, as illustrated in Fig. 1.2(c). The large white square symbolizes the dimension of the total Hilbert space \mathcal{H} spanned by all states with a total excitation number $N_{ex} = L/2$, where L is the system size. For $L = 6$, this includes states of the form $|300000\rangle$, $|210000\rangle$, and $|111000\rangle$. The dimension of the computational subspace \mathcal{H}_{CS} , denoted by the colored squares for $L = 10$ and 20 , accounts only for a small fraction of this. For realistic disorder, the computational states are wholly commingled with the much larger set of junk states. To what extent do the computational states mix with junk states when the interaction is switched on? Are there states still ‘close enough’ to the perfect qubits of the noninteracting system to not compromise the quantum computer? How can one unambiguously filter out the small subset of computational states from the myriad of junk states in the interacting system?

Answering these questions requires applying concepts and methods of many-body theory to the coupled transmon Hamiltonian. The many-body approach adds a new and complementary facet to the existing theoretical work that often restricts to models of very few transmons, e.g., two transmons between which an entangling gate is to be executed and one additional ‘spectator’ transmon. As will be demonstrated, naively extending a processor configuration that is optimized for specific tasks in minimal setups to larger geometries can cause instabilities that are only resolved from the many-body perspective.

1.7 A comment on the units

The superconducting qubit literature usually provides explicit values of the frequency ν_q instead of ω_q , e.g., $\nu_q = 5$ GHz for a typical transmon qubit frequency. To specify all parameters in the same units, it is common to measure the hopping J in Eq. (1.1) in units of 2π , e.g., $J/2\pi = 5$ MHz. Accordingly, the interaction is usually given in the form $U/h = 250$ MHz. In some cases, one avoids ν_q and sticks to $\omega_q/2\pi$ instead, e.g., $\omega_q/2\pi = 5$ GHz. Depending on the context, each variant ($\nu_q, \omega_q, \omega_q/2\pi$) may be more appropriate at some point; accordingly, all appear in the further course. Furthermore, it is common to set $h = 1$ and measure all energies in Hertz, e.g., $U = 250$ MHz. We explicitly include all factors h or \hbar in the introductory chapters but later set $h = 1$ in discussing numerical results. We point this out separately.

Quantum chaos and many-body localization

In Chapter 1, we caught a brief glimpse of the system of interest, the superconducting transmon array for quantum computing. Chapter 2 equips us with an idea of what we want to screen this system for: the presence and absence of *quantum chaos*.

Edward Lorenz poetically encapsulated the essence of chaos theory in the famous title of a talk given in 1972 “Does the flap of a butterfly’s wing in Brazil set off a tornado in Texas?” [115]. Despite its exaggerated formulation, this accurately represents what we naturally associate with chaos: a high degree of uncontrollability, unpredictability, and sensitivity to minor perturbations. Indeed, one calls a classical system chaotic if it reacts to small changes in the initial conditions in such an extreme way that predicting its future behavior is impossible. It stands to reason that a quantum computer behaving ‘uncontrolled’ and ‘unpredictable’ would fail to achieve its intended purpose. However, quantum mechanics largely eludes the characterization of chaos in these familiar terms. Therefore, Sec. 2.1 is devoted to sharpening the concept of *quantum chaos*. We discuss *eigenstate thermalization*, tightly interwoven with and sometimes used synonymously for quantum chaos in Sec. 2.2. Following this, Sec. 2.3 examines how a system can escape chaos and transition to the *many-body localized* (MBL) phase. When contrasting the properties of MBL and thermalizing phase in Sec. 2.4, particular attention is paid to how they enable or prevent quantum computing. Several quantitative measures based on which one can distinguish between these two options are introduced. This provides us with the necessary armamentarium to diagnose the transmon array. Finally, Sec. 2.5 discusses selected aspects of the many-body localized phase.

There is extensive literature on all topics we touch upon in this chapter. The main sources of information from which this compendium was created were Refs. [111, 114, 116–120].

2.1 Quantum chaos

2.1.1 Integrability and classical chaos

Classical systems can show very simple dynamics, that is, the trajectories are a superposition of periodic motion and uniform translations. This is exemplified in Fig. 2.1(a). The trajectory of a particle moving in a circular billiard is easily seen to be composed of (quasi-)periodic radial and angular motions. Evidently, the motion in the Sinai billiard [121], illustrated in (b), is qualitatively different and appears completely random. One refers to this trajectory as ‘chaotic’. An important property separating the two models is *integrability*. A system is called integrable if one can solve its equations of motion (EOMs) via reduction to quadrature, i.e., by calculating one-dimensional integrals [116]. A sufficient condition for integrability is due to Arnold and Liouville

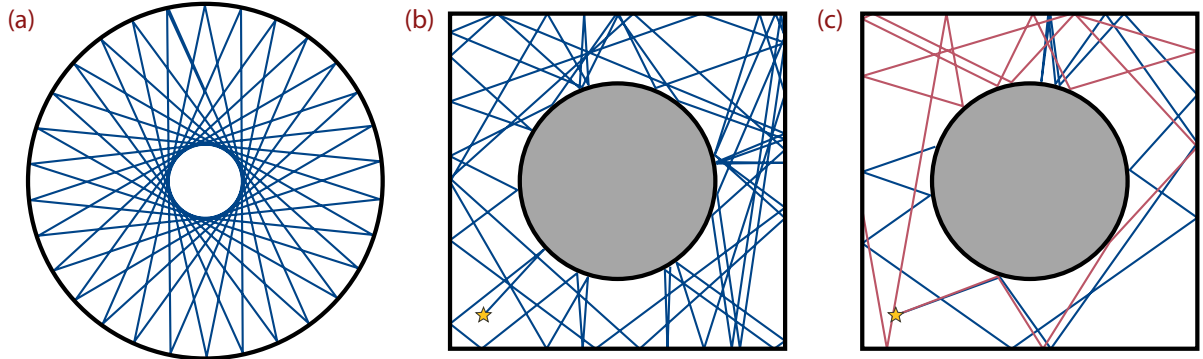


Figure 2.1 – Trajectories in integrable and chaotic billiards. (a) Particle in an integrable circular billiard. The path is a superposition of a radial and an angular periodic motion. (b) In contrast, the trajectory in a Sinai billiard is chaotic. (c) Comparison of trajectories with identical initial positions (yellow star) but slightly different momenta. After a few bounces, the trajectories diverge (in phase space), a hallmark of classical chaos.

[122], who showed that it is related to the existence of ‘sufficient’ conserved quantities: a classical system described by a Hamiltonian $H(\mathbf{q}, \mathbf{p})$ that depends on S coordinates $\mathbf{q} = (q_1, \dots, q_S)$ and momenta $\mathbf{p} = (p_1, \dots, p_S)$, is integrable if there exist S independent conserved quantities $I_i(\mathbf{q}, \mathbf{p})$ that are in involution. This guarantees the existence of a canonical transformation $(q_i, p_i) \rightarrow (\phi_i, I_i)$ such that the transformed Hamiltonian \tilde{H} depends solely on the I_i . Solving the EOMs for the *action-angle* variables ϕ_i, I_i is then trivially achieved by calculating one-dimensional integrals [116]. In Fig. 2.1, the circular billiard is integrable because energy and angular momentum are conserved, whereas, in the chaotic Sinai billiard, energy is the only integral of motion.

Fig. 2.1(c) shows a typical trait of nonintegrable dynamics, often invoked to *define* chaos, namely an extreme sensitivity to small perturbations. The blue and red trajectory start their motion with identical initial positions, marked by the yellow star, but slightly different momenta. Following their evolution for a few bounces shows that they become quickly uncorrelated in momentum (direction of motion) and position. In chaotic systems, initially nearby trajectories diverge exponentially in phase space insofar as it is consistent with energy conservation. Although the motion is strictly deterministic, any attempt to predict the trajectory becomes arbitrarily inaccurate for sufficiently late times in practice: even with perfect knowledge about the initial conditions, small numerical errors in the integration of the EOMs cause large deviations [116].

Unfortunately, defining chaos as the sensitivity of phase space trajectories to small changes in initial conditions does not translate to the quantum mechanical case. First, there is no well-defined concept of a trajectory in quantum mechanics where each state is a vector in Hilbert space instead of a point in phase space and where sharp initial conditions do not exist due to the uncertainty principle. Second, taking the overlap $|\langle \phi | \psi \rangle|$ as a natural measure for the proximity of two vectors, any two states maintain their distance in time because [123]

$$|\langle \phi(t) | \psi(t) \rangle| = |\langle \phi(0) | \hat{U}^{-1}(t) \hat{U}(t) | \psi(0) \rangle| = |\langle \phi(0) | \psi(0) \rangle|. \quad (2.1)$$

Since transferring the classical manifestations of chaos to the quantum world fails, the question naturally arises of what constitutes quantum chaos and how it can be distinguished from integrable quantum systems.¹ Of peculiar interest for our purposes is the question of whether an eventual definition of quantum chaos implies properties that conflict with quantum information

¹Eq. (2.1) also raises the question of how diverging trajectories emerge from quantum theory in the $\hbar \rightarrow 0$ limit.

processing, as expected from a naive conception of chaos. An unambiguous definition of quantum chaos does not exist. However, the study of quantized versions of classically chaotic systems reveals recurring universal signatures that have been proposed as identifiers of quantum chaos. What comes closest to a definition of quantum chaos relies on concepts from *random matrix theory*, which is the subject of the next section.

2.1.2 Quantum chaos and random matrix theory

The sequence of prime numbers derives from fixed, deterministic rules. However, much of what we know about prime numbers is statistical in nature, like the distribution of spacings between consecutive primes [118]. In a similar spirit, random matrix theory (RMT) was developed in the 1950s by Wigner [124–126] and successors to explain the spectra of complex atomic nuclei: The idea is to abandon the idea of calculating the spectra of sufficiently complex systems exactly. Instead, one concentrates on the statistical properties [127]. This is a perplexing thought: As the Hamiltonian determines the level spectrum unambiguously, how can statistics come into play? Wigner’s pivotal insight was that a complex Hamiltonian restricted to a small energy interval looks like a random matrix. Statistical properties of suitable chosen random matrix ensembles deliver information on the properties of complex systems, just as statistical concepts enrich our understanding of prime numbers. ‘Suitable’ means that the random matrices must incorporate the fundamental symmetries of the Hamiltonian. Expanding on earlier work from Wigner [124–126], Dyson proposed three universality classes [128], differentiated by their behavior under spin rotations (SR) and time reversal (TR), whose statistics are described by distinct random matrix ensembles. More precisely, he distinguished²

- (i) TR invariant systems. The Hamiltonian can be chosen to be real and symmetric, i.e., the matrix elements fulfill $H_{ij} = H_{ji} = H_{ij}^*$
- (ii) systems with broken TR, where the Hamiltonian matrices fulfill $H_{ij} = H_{ji}^*$.
- (iii) TR invariant half-integer spin systems with broken SR symmetry, whose matrix elements can be expressed in terms of quaternions (or, equivalently, Pauli matrices). H can be viewed as an $N \times N$ matrix with 2×2 entries [118].

The symmetry properties of the H_{ij} and hence the universality classes are invariant under the transformation $H \rightarrow U^{-1}HU$, where U is an (i) orthogonal, (ii) unitary, or (iii) symplectic matrix. The corresponding random matrix ensembles are called orthogonal, unitary or symplectic ensembles. Each instance of these ensembles is a random Hermitian matrix in which the entries not connected by symmetry are stochastically uncorrelated (i) real, (ii) complex, or (iii) quaternionic random numbers. The ensembles are characterized by an integer β counting the degrees of freedom in the matrix elements, i.e., (i) $\beta = 1$, (ii) $\beta = 2$, and (iii) $\beta = 4$.

The *Gaussian* random matrix ensembles are defined through the matrix probability densities

$$P_\beta(H) \propto \exp\left[-\frac{\beta}{2a^2}\text{Tr}(H^2)\right], \quad (2.2)$$

where a sets the overall energy scale and the choices $\beta = 1, 2$ and 4 define the Gaussian orthogonal (GOE), unitary (GUE) and symplectic (GSE) ensemble. The definition in Eq. (2.2) is

²This classification scheme is very comprehensive, although novel ensembles, not covered by Dyson’s ‘threefold way’, may arise when additional symmetries are introduced [129, 130].

reasonable as it fulfills two natural requirements [131]: invariance under the respective symmetry transformation, $P(H) = P(U^{-1}HU)$ and factorization of $P(H)$ in a product of the densities of the independent matrix elements. For example, for a 2×2 GOE matrix,

$$H = \begin{pmatrix} H_{11} & H_{12} \\ H_{12} & H_{22} \end{pmatrix}, \quad (2.3)$$

one obtains $P(H) = P_{11}(H_{11})P_{12}(H_{12})P_{22}(H_{22})$. A derivation of Eq. (2.2) for a 2×2 matrix from the invariance and factorization requirements is presented in Ref. [132]. A more formal introduction can be found in Ref. [118]. The exponent in Eq. (2.2) sometimes contains additional factors accounting for the dimension N or to fix the average level spacing to one.

To make it explicit, Eq. (2.2) implies that a GOE matrix takes the general form

$$H_{\text{GOE}} = \begin{pmatrix} H_{11} & \cdots & H_{1N} \\ \vdots & \ddots & \vdots \\ H_{1N} & \cdots & H_{NN} \end{pmatrix}, \quad (2.4)$$

where $H_{ij} \in \mathbb{R}$. The diagonal entries H_{ii} are independent and identically distributed (i.i.d.) Gaussian random variables with $\mu = 0$ and $\sigma^2 = a^2/\beta$, i.e., drawn from $\mathcal{N}(0, a^2/\beta)$. The off-diagonal entries are i.i.d. variables drawn from $\mathcal{N}(0, a^2/2\beta)$. The difference in σ is readily seen from Eq. (2.2) when rewriting the trace as $\text{Tr}(H^2) = \sum_{i=1}^N H_{ii}^2 + 2 \sum_{i < j} H_{ij}^2$.

Level repulsion. To analyze properties of complex systems, the most commonly used observable is the nearest-neighbor level spacing distribution $p(s)$, which measures the probability density for two adjacent levels, E_n and E_{n+1} , to have the energy spacing s . For 2×2 matrices, $p(s)$ can be obtained analytically [118]. The generic result for all ensembles reads

$$p_W(s) = a_\beta s^\beta \exp(-b_\beta s^2), \quad (2.5)$$

where the requirement of normalization and an average level spacing of one set a_β and b_β . This result is known under the name Wigner surmise [133]. It is shown in Fig. 2.2(a). The essential characteristic of Eq. (2.5) is that it describes the tendency of levels to repel each other: the probability of finding two levels close to each other vanishes as s^β for $s \rightarrow 0$. Figs. 2.2(b)–(c) illustrates the prototypical behavior of levels when varying a system parameter in systems with and without level repulsion. The exact level spacing distributions for $N \times N$ Gaussian matrices, firming under the name Wigner-Dyson distribution, do not have a closed analytic form but are well approximated by the 2×2 result [118]. For example, the correction to Eq. (2.5) for $N \rightarrow \infty$ remains below 1% for all s [134]. In particular, level repulsion is a generic feature for all matrix sizes N .

What RMT can predict: fluctuations, universality, and ergodicity. The Gaussian ensembles contain no system-specific information except for the fundamental symmetries. Therefore, it is evident that RMT can never exactly reproduce the spectrum of a given system. Why then is RMT so successful? This relies on a clear distinction between *average* values of observables and *fluctuations* around them [118]. The belief wedded to the application of RMT is that fluctuation properties are universal, whereas average quantities cannot be modeled. For example, all Gaussian ensembles have a semicircle-shaped average level density $\rho(E)$ hardly encountered in real physical systems [133]. In Eq. (2.5), the variable s is the level spacing, measured in units of the mean *local* spacing. One must therefore cleanse a measured data set from the system-specific

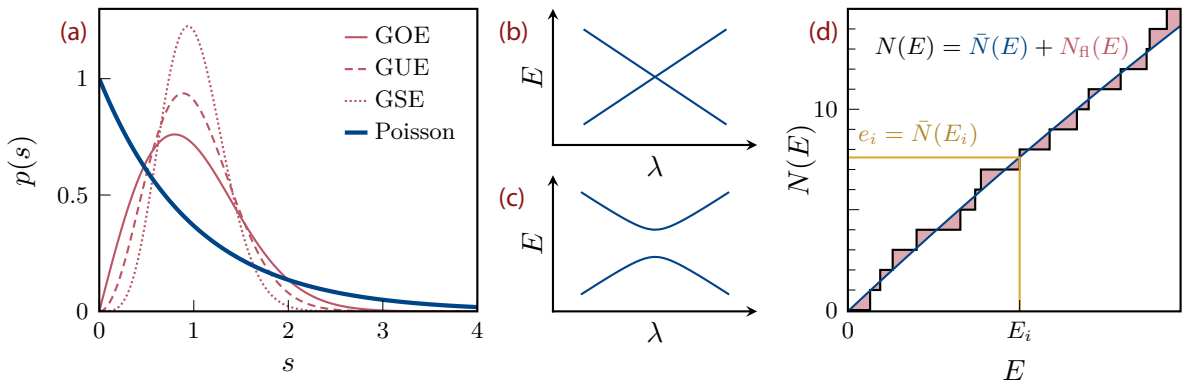


Figure 2.2 – Level repulsion and unfolding. (a) Comparison of the level spacing distribution for integrable quantum systems, i.e., uncorrelated levels with a Poisson distribution, and the Wigner-Dyson distribution expected for RMT ensembles. The central attribute of the latter is level repulsion, i.e., $p_w(s \rightarrow 0) \rightarrow 0$. (b) and (c) illustrate the behavior of energy levels under variation of a system parameter λ . In integrable systems (b), the levels intersect, whereas quantum chaotic systems (c) show avoided crossings where levels repel. (d) Level unfolding. The staircase function $N(E)$ comprises a smooth part $\bar{N}(E)$ and fluctuations $N_{\text{fl}}(E)$. Only the latter shows universal behavior, and the influence of the local average must be eliminated. The mapping from an energy E_i to its unfolded value e_i is illustrated in yellow. See the main text for details.

average values before RMT can be employed, a procedure referred to as *unfolding* and illustrated in Fig. 2.2(d). Shown is the spectral staircase $N(E) = \sum_i \Theta(E - E_i)$, which counts the number of levels E_i smaller than E . Here, $\Theta(x)$ is the Heaviside step function. $N(E)$ comprises a smooth, system-specific average part $\bar{N}(E)$ and fluctuations around that value $N_{\text{fl}}(E)$. Assuming that $N(E)$ is known, the unfolded levels are obtained as $e_i = \bar{N}(E_i)$. The new spectrum has a mean level spacing of one and can be compared to the predictions of RMT. Unfolding the spectrum is a delicate step, since only in rare cases the function $\bar{N}(E)$ is analytically known [135]. To overcome this issue, it has been proposed to study the ratio of consecutive level spacings, $r_n = (E_{n+1} - E_n)/(E_n - E_{n-1})$ [136]. As these ratios are independent of the local density, the unfolding procedure is obsolete, see Chapter 4.

When discussing random matrices, one usually refers to the Gaussian ensembles. However, the Gaussian (H^2) in Eq. (2.2) is convenient but not necessary. In fact, the probability density

$$P(H) \propto \exp(-\text{Tr}[V(H)]) \quad (2.6)$$

guarantees invariance under the respective symmetry transformations. $V(H)$ must permit the normalization of $P(H)$ but is otherwise arbitrary. This raises the question of *universality*: are the results, e.g., the Wigner surmise or Wigner's semicircle, generic for all ensembles in Eq. (2.6) or specific to the Gaussian ones? There is convincing empirical evidence for the former. For statistically independent matrix elements, one always obtains the semicircle-shaped density of states. The Wigner surmise is even more universal. For a detailed discussion, see Ref. [133] and Ref. [118] and references therein.

In RMT, observables are calculated as averages over many members of an ensemble. Applying these ensemble predictions to experiments, where observables are extracted from an individual system, requires further justification in the form of an ergodicity statement. More precisely, the ensemble average must correspond to the experimentally obtained *running* average, taken over a sufficiently large interval of the spectrum of a single sample. Although no general proof of ergodicity in the above sense exists, the equality of the two averages was extensively tested numerically and proven in specific cases [137–139].

BGS and Berry-Tabor conjecture. In the decades following Wigner’s pioneering work, RMT has been extended and successfully applied to understand the spectra of complex nuclei [140] (these were the first systems where data sets suitable for the application of RMT existed). However, when exactly a ‘complex’ system is adequately characterized by RMT had been unsettled until 1984, when Bohigas, Giannoni, and Schmit (BGS) observed that the level statistics of a single particle in a Sinai billiard-shaped infinite potential well displays Wigner-Dyson statistics at high energies. They conjectured that the level statistics of *any* quantum system with a chaotic classical counterpart are described by RMT [141]. Numerous numerical and experimental studies on systems as diverse as a hydrogen atom in a magnetic field [142], spinless fermions on a lattice [143], the aforesaid complex nuclei, or—perhaps surprisingly—the city bus transport in Cuernavaca (Mexico) [144] have demonstrated the almost universal validity of the BGS conjecture. A formal proof of the BGS conjecture is missing, but some analytical approaches, usually relying on a semiclassical approximation, exist [118, 145]. All counterexamples known to date are highly nongeneric [146]. In fact, the examples for the conjecture are so convincing that the occurrence of level repulsion and Wigner-Dyson statistics is often taken as the defining property of quantum chaos, regardless of whether the system has any classical analog at all.

On the other hand, the level spacing distribution in quantized versions of classically integrable systems³ is often found to be described by Poisson statistics,

$$p_P(s) = \exp(-s) . \quad (2.7)$$

This distribution is compared to the prediction for the Gaussian ensembles in Fig. 2.2(a). Again, s is measured in units of the local spacing. Most importantly, there is no level repulsion as $p_P(s \rightarrow 0) \neq 0$. Eq. (2.7) is also the expected result for uncorrelated random numbers. A simple example easily clarifies the connection: Consider the classically integrable system of independent oscillators with incommensurate frequencies ω_i , occupation numbers n_i , and total energy $E = \sum_i \hbar\omega_i(n_i + 1/2)$. For high energies, nearby energies can correspond to an entirely different combination of occupation numbers n_i , implying that adjacent energy levels are effectively uncorrelated. The proposition that in quantum systems with an integrable classical analog, the energies are a sequence of uncorrelated random numbers is known as the Berry-Tabor conjecture [147]. Whilst found to be true in many systems, there are also some counterexamples [148], often due to degeneracies caused by additional symmetries of the Hamiltonian. We will discuss an example of this later.

2.1.3 Chaotic eigenfunctions

The emergence of Wigner-Dyson statistics replaces the divergence of initially adjacent trajectories as the primary indicator of chaos in quantum mechanical systems. So far, quantum chaos seems to be just a somewhat eccentric name for level repulsion. It is not yet clear why such systems are unsuitable for quantum computing. The analysis of eigenvectors of random matrices sheds light on this conundrum and sets the stage for discussing *thermalization* in Sec. 2.2.

In the following, we consider the GOE. As the ensemble is invariant under orthogonal transformations, the joint probability distribution $P(\{c_i\})$ for the eigenvector components c_i , $i =$

³The exact definition of quantum integrability is under debate. A widely used attempt relies on the existence of local operators \hat{I}_i that commute with each other and with the Hamiltonian. The analogy to classical Liouville-Arnold integrability is obvious. We pick up this discussion in Sec. 2.3.

$1, \dots, N$ can only depend on the (squared) norm $\sum_i c_i^2$. Taking into account the normalization yields

$$P(c_1, \dots, c_N) \propto \delta \left(\sum_{i=1}^N c_i^2 - 1 \right), \quad (2.8)$$

which states that eigenvectors of random matrices are random unit vectors [117]. In particular, the correlations between eigenvectors stemming from the required orthogonality can be ignored because two uncorrelated, sufficiently large vectors are nearly orthogonal (more rigorously, the first $\lambda < N$ components of n eigenvectors with $n \ll N$ are uncorrelated for $N \rightarrow \infty$ [149]). To prevent confusion, we note that this statement holds for matrix *ensembles* in a fixed basis, even if it does not apply to a single ensemble instance. Imagine that we pick one random matrix and write it in its eigenbasis. Obviously, in the diagonal form, the eigenvectors are not uncorrelated. However, the basis is not particular for all other instances, and the above statement regains validity for the whole ensemble [117].

As a random unit vector, the eigenvector of a random matrix is distributed over many basis states. We refer to this as delocalization over a given basis. The following example, adapted from Ref. [117], illustrates how the concept of delocalization can unify the classical and quantum mechanical perception of chaos. The underlying idea is to study delocalization in both cases—in phase space for classical systems and in energy space for quantum systems—using suitable entropic measures. One option to reveal delocalization in phase space is to perform a quench experiment, i.e., evolve a stationary probability distribution of H_0 under some Hamiltonian $H \neq H_0$ and calculate the entropy S of the time averaged probability distribution $\bar{\rho}$. Chaos causes the system to delocalize and ergodically explore all achievable points in phase space, see Fig. 2.1(b). $S(\bar{\rho})$ will then increase to the microcanonical entropy. For the quantum analog, one considers operators $\hat{\rho}, \hat{H}_0, \hat{H}$ and studies the entropy of the time-averaged density matrix $\bar{\hat{\rho}}$. One can show that

$$\bar{\hat{\rho}} = \lim_{t \rightarrow \infty} \frac{1}{t} \int_0^t \hat{\rho}(t') dt' = \sum_i \rho_{ii} |i\rangle\langle i|, \quad (2.9)$$

where $|i\rangle$ is the eigenbasis of \hat{H} and ρ_{ii} are the diagonal elements of the initial $\hat{\rho}$ in the basis $|i\rangle$. This equation states that the spreading of the initial state (in the simplest case, an eigenstate of \hat{H}_0 , $\hat{\rho}_0 = |m_0\rangle\langle m_0|$) over the eigenbasis of \hat{H} is the quantum version of delocalization in phase space. In particular, if \hat{H} is a random matrix describing a quantum chaotic system, the density matrix in Eq. (2.9) will generically be delocalized. This puts classical and quantum mechanical chaos on the common foundation of delocalization. The analogy between quantum delocalization and classical chaos has been experimentally studied in a transmon processor [150].

2.2 Thermalization

The last 15 years have seen impressive experimental progress in synthesizing isolated quantum many-body systems, including superconducting transmon arrays. This has triggered increasing efforts to understand the possible outcomes of their intrinsic unitary dynamics. Consider again a quantum quench: a system, described by the Hamiltonian \hat{H} , is prepared in the nonequilibrium state $|\psi_0\rangle$ and undergoes unitary time evolution. $|\psi_0\rangle$ is typically a ‘simple’ state that is easily prepared in an experiment, e.g., a product state (quenches are important because the eigenstates of a generic many-body system \hat{H} can only be prepared in an exponentially long time [114]). In

the introductory example in Sec. 1.6, $|\psi_0\rangle = |1010\dots\rangle$ was an eigenstate of the noninteracting transmon array described by \hat{H}_0 . Note that such states usually have a high energy density. Experience shows that many systems thermalize: after a sufficiently long time, they reach an effective equilibrium, and local observables appear thermal, i.e., their expectation values are given by the microcanonical ensemble. All sufficiently small subsystems reach a thermal Gibbs state because the coupling to the remainder of the systems mimics a heat bath, provided that efficient energy exchange between subsystems is possible.

To put this in more quantitative terms, we consider the initial state $|\psi(0)\rangle = \sum_i c_i |i\rangle$ where $|i\rangle$ are the many-body eigenstates of \hat{H} with energy E_i . Its time evolution is ($\hbar = 1$)

$$|\psi(t)\rangle = e^{-i\hat{H}t}|\psi(0)\rangle = \sum_i c_i e^{-iE_i t} |i\rangle. \quad (2.10)$$

The time-dependent expectation value $O(t)$ of some observable \hat{O} in this state is

$$\begin{aligned} O(t) &= \langle\psi(t)|\hat{O}|\psi(t)\rangle = \sum_{i,j} c_i^* c_j e^{i(E_i - E_j)t} \langle i|\hat{O}|j\rangle \\ &= \sum_i |c_i|^2 \langle i|\hat{O}|i\rangle + \sum_{i,j \neq i} c_i^* c_j e^{i(E_i - E_j)t} \langle i|\hat{O}|j\rangle. \end{aligned} \quad (2.11)$$

Thermalization of the system (more precisely of the observable \hat{O}) means that after some relaxation time, (i) the long-time average of $O(t)$ is equal to the microcanonical prediction and (ii) that the fluctuations of $O(t)$ around this value are small at most later times [117]. As the off-diagonal contributions in Eq. (2.11) oscillate, the long-time average of $O(t)$ is

$$\langle O \rangle_\infty = \lim_{t \rightarrow \infty} \frac{1}{t} \int_0^t O(t') dt' = \sum_i |c_i|^2 \langle i|\hat{O}|i\rangle. \quad (2.12)$$

Reconciling this equation with the above definition of thermalization (and experimental observations) encounters two difficulties: First, the coefficients $|c_i|^2$ appearing in $\langle O \rangle_\infty$ contain information on the initial state. How can this be equal to the microcanonical expectation value? In particular, as information on $|\psi(0)\rangle$ is seemingly preserved, how can different initial states thermalize to the same equilibrium? Second, Eq. (2.12) is only valid for $t \rightarrow \infty$. Many-body levels are exponentially close (in system size) such that the time needed for the off-diagonals to average out can easily exceed the age of our universe [117], in contrast to what is observed in experiments. A proposal surmounting these problems and explaining how unitary time evolution leads to thermalization is the *eigenstate thermalization hypothesis*.

2.2.1 The eigenstate thermalization hypothesis

The eigenstate thermalization hypothesis (ETH) is an ansatz for the matrix elements of few-body⁴ operators between eigenstates $|i\rangle, |j\rangle$ of \hat{H} with corresponding energies E_i, E_j . It reads

$$\langle i|\hat{O}|j\rangle = \mathcal{O}_{\text{mc}}(\bar{E}) \delta_{ij} + e^{-S(\bar{E})/2} R_{ij} f_O(\Delta E, \bar{E}), \quad (2.13)$$

⁴Few-body refers to observables that differ on $n \ll N$ lattice sites, spins, etc., from the identity, where N is the system size. This is not a true restriction, as these are the experimentally accessible observables. ETH can apply up to $n \approx N/2$ [151] but not to global operators such as projection operators to the eigenstates of \hat{H} .

where $\bar{E} = (E_i + E_j)/2$ is the mean energy, $S(\bar{E})$ is the thermodynamic entropy, and R_{ij} is a random variable with zero mean and unit variance. \mathcal{O}_{mc} is the microcanonical expectation value of \hat{O} at energy \bar{E} , and $f_O(\Delta E, \bar{E})$ is a smooth, observable-dependent function of the average energy and the energy difference $\Delta E = E_j - E_i$. The interpretation of the first summand is that individual many-body eigenstates are thermal, i.e., they are described by equilibrium statistical mechanics, and their expectation values $\langle i|\hat{O}|i\rangle$ are equal to the microcanonical ones at energy $E = E_i$. This explains why different initial states from a narrow energy shell evolve to the same equilibrium. However, the first term only ensures thermalization after an infinitely long time. Hence, Srednecki [152] postulated the ansatz (2.13) and demonstrated that it is sufficient to explain thermalization in the above sense (whether it is also necessary is an open question [117]). In particular, the form of the off-diagonal elements implies that $\langle(O(t) - \langle O_\infty \rangle)^2 \rangle_\infty \propto \exp(-S(\bar{E}))$, meaning that the long-time average of the fluctuations is exponentially small in the system size. $O(t)$ remains near its equilibrium value for most of the time, i.e., not only their time average but the temporal fluctuations themselves vanish. The function $f_O(\Delta E, \bar{E})$ determines the relaxation times [111, 152]. They are not exponentially large and, in some cases, do not even necessarily increase with the system size [117]. The rather strong conjecture on the matrix elements in Eq. (2.13) has been confirmed in various numerical studies, see Refs. [153, 154] for two prominent examples. One often refers to thermalizing systems as *ergodic* (although a quantum mechanical definition of this term must overcome some subtleties [155]). We use the terms quantum chaotic, ergodic and delocalized interchangeably.

Our initial motivation was the possible outcome of unitary dynamics after a quench. However, the above discussion reveals that it is appropriate to focus on the static properties of the Hamiltonian \hat{H} under which the system evolves. All information on thermalization is encoded in its eigenstates; time evolution merely exposes this hidden information. It is further apparent why a quantum computer cannot operate in the thermalizing phase: any locally encoded initial information is scrambled during relaxation. Unitary time evolution cannot erase information, see Eq. (2.10), but hides it in an inaccessible way in nonlocal correlations such that local measurements cannot regain it. Such a system cannot serve as a quantum memory. Moreover, eigenstates living at the same energy are similar in that local measurements, e.g., of the state of a single qubit, give the same thermal result for all states. Therefore, it is impossible to identify or distinguish computational states at all. A quantum computer must find a way to avoid thermalization. Before discussing how systems can escape this fate of failure, let us further elaborate on the close connection between quantum chaos and thermalization.

2.2.2 ETH and quantum chaos

The first seed of the strong link between thermalization and chaos dates back to work by Berry in 1977 [156]. Considering semiclassical wave functions, he conjectured that the expectation value in these states takes the form of a microcanonical average if the classical counterpart of the system exhibits chaos. The importance of RMT for understanding thermalization was emphasized in a seminal paper by Deutsch in 1991 [110]. Under the assumption that the eigenstates of ergodic systems are uncorrelated random unit vectors, Deutsch extended Berry's conjecture beyond the semiclassical limit. Indeed, if \hat{H} were a true random matrix, the caveats to the validity of Eq. (2.12) discussed above would no longer apply. Using the results from Sec. 2.1.3, one easily shows that the matrix elements of any operator $\hat{O} = \sum_\alpha O_\alpha |\alpha\rangle\langle\alpha|$ in the eigenbasis of the random

matrix are [117]

$$\langle i|\hat{O}|j\rangle \approx \bar{O}\delta_{ij} + \sqrt{\frac{\bar{O^2}}{\mathcal{D}}}R_{ij}, \quad (2.14)$$

where \mathcal{D} is the Hilbert space dimension, R_{ij} is a random variable defined as in Eq. (2.13), and the bar denotes the average over the eigenstates of \hat{O} , i.e., $\bar{O} = \sum_\alpha O_\alpha/\mathcal{D}$ and similar for $\bar{O^2}$. Combining Eq. (2.12) and (2.14) yields $\langle O \rangle_\infty = \bar{O}$, which can be regarded as a microcanonical expectation value. It is a peculiarity of RMT that all eigenstates have the same *energy-independent* expectation value \bar{O} (formally, that corresponds to an effective temperature $T \rightarrow \infty$ for the subsystems). Regarding the long relaxation times, it has been argued that the values $\langle O \rangle_\infty$ are approached on timescales shorter than the inverse level spacing required in Eq. (2.11): because of the exponentially small off-diagonal matrix elements, it is sufficient to destroy phase coherence between a small fraction of the eigenstates [114, 117].

Thus, RMT explains thermalization, but one must proceed further to obtain predictions consistent with experiments where one encounters energy-dependent thermal expectation values. Srednicki extended Deutsch's work [109] to account for the additional information in the matrix elements of experimental observables, eventually leading to the celebrated formula in Eq. (2.13) replacing the RMT result (2.14) [152]. The RMT predictions reemerge from Eq. (2.13) when focusing on narrow energy windows ΔE where f is approximately constant (an energy scale known as the Thouless energy E_T [157]). From this, one can infer another similarity between classically and quantum chaotic systems: Consider a perturbation $\epsilon\hat{O}$ with $\epsilon \ll 1$ of the Hamiltonian \hat{H} . The energy window $\Delta E < E_T$ where $f \approx \text{const}$ vanishes in the thermodynamic limit. The same holds for the magnitude of off-diagonal matrix elements. However, as the many-body level spacing vanishes exponentially faster, the energy shell still contains exponentially many levels whose eigenstates strongly mix through $\epsilon\hat{O}$ [114]. The eigenstates of $\hat{H} + \epsilon\hat{O}$ will thus differ strongly from the original ones. This extreme sensitivity of thermal eigenstates to perturbations can be thought of as the quantum counterpart of the sensitivity of chaotic trajectories to small perturbations in the initial conditions. It also appears from the above discussion that ETH systems inherit the Wigner-Dyson statistics from RMT.

2.3 Avoiding chaos by disorder: many-body localization

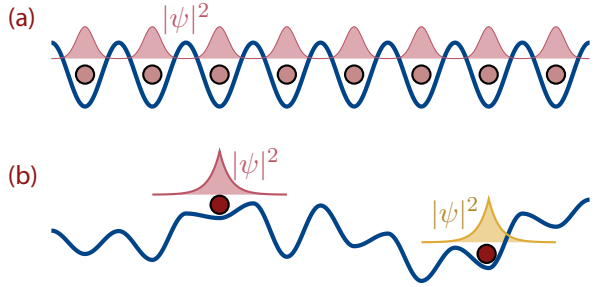
Imagine a multi-qubit transmon array initialized in the state $|10101\dots\rangle$. How can one prevent this state from relaxing towards the equilibrium where local qubit measurements on all sites give the same result? As of today, there is a single known *robust* mechanism by which isolated systems can avert thermalization [114]. This mechanism is known as many-body localization. The primary ingredient for MBL to occur is strong *disorder*. In a nutshell, this localizes excitations normally transporting energy and heat. By blocking these transport processes, the system cannot operate at a heat bath to thermalize its subsystems. It permanently stays out of equilibrium, such that the predictions of conventional statistical physics fail. Instead, new concepts are needed to describe MBL systems adequately.

2.3.1 From single-particle localization to many-body localization

A natural starting point for discussing MBL physics is the model of a single particle moving in a lattice with a random potential, first discussed by Anderson [158]. It is described by the

Figure 2.3 –

Bloch waves and Anderson localization. (a) In a clean crystal, the wave functions are Bloch waves extending over the entire lattice. (b) In a disordered potential, the particles localize around a particular lattice position \mathbf{R}_j . This mechanism is known as Anderson localization and occurs at arbitrarily low disorder in one and two dimensions. Inspired by Ref. [114].



tight-binding Hamiltonian

$$\hat{H} = -t \sum_{\langle ij \rangle} (\hat{c}_i^\dagger \hat{c}_j + \hat{c}_j^\dagger \hat{c}_i) + \sum_i U_i \hat{c}_i^\dagger \hat{c}_i, \quad (2.15)$$

where t is the hopping amplitude, \hat{c}_i^\dagger creates a particle at site i and U_i is the lattice-site dependent potential. For $U_i = U$, the system exhibits translational symmetry, and the eigenstates are Bloch waves extending over the entire lattice, as sketched in Fig. 2.3(a). For uncorrelated disorder, i.e., if the U_i are independent random numbers, the nature of the wave functions ψ changes, and they localize around a site \mathbf{R}_j , i.e., $|\psi(\mathbf{r})| \propto \exp(-|\mathbf{r} - \mathbf{R}_j|/\xi)$, see Fig. 2.3(b). Particles remain at the lattice site where they are initially located. This is easily understood in the strong disorder limit. If the magnitude of site-to-site variations in U_i exceeds the hopping strength t , transitions between neighboring sites are off-resonant. A similar argument holds for hopping between more distant positions that arise in higher-order perturbation theory [114]. In low-dimensional systems, $d = 1, 2$, however, single-particle or Anderson localization occurs at arbitrarily weak disorder. In $d \geq 3$, particles localize if the disorder strength exceeds a critical threshold.

The above picture remains valid if we consider Eq. (2.15) to be a many-body Hamiltonian, describing several *noninteracting* particles. Imagine, for example, an initial nonuniform particle density distribution akin to the one shown in Fig. 1.2. As all particles are Anderson-localized, the entire pattern remains intact, indicating the breakdown of ergodicity also in this many-body setting. Any realistic system, however, contains interactions between particles. Understanding the fate of Anderson localization at finite energy (or particle) density in the presence of interactions has been identified as a problem of utmost importance early on [158, 159].

Noninteracting particles moving in a disordered lattice provide the most accessible illustration of single-particle localization. However, when studying localization in the presence of interactions, it is convenient to consider another paragon in MBL physics that allows for an intuitive elucidation of some MBL hallmarks, namely the spin 1/2 Heisenberg chain in a random magnetic field,⁵

$$\hat{H} = J \sum_i \hat{\sigma}_i \hat{\sigma}_{i+1} - \sum_i h_i \hat{\sigma}_i^z. \quad (2.16)$$

Here, $\hat{\sigma} = (\hat{\sigma}^x, \hat{\sigma}^y, \hat{\sigma}^z)$, and the fields h_i are randomly drawn from a distribution with disorder strength h , e.g., a box distribution $[-h, h]$. To capture localization, it is reasonable to ask whether many-body eigenstates of Eq. (2.16) (with nonzero density for both up and down spins) obey

⁵Eq. (2.16) maps onto a model of interacting fermions in a disordered lattice using a Jordan-Wigner transformation [160]. The single-particle Anderson model (2.15) corresponds to a single spin flip in Eq. (2.16).

the ETH. Arguing similar to above, we start with the $h/J \rightarrow \infty$ case, where each eigenstate is a product state of $\hat{\sigma}^z$ eigenstates and completely specified by a set of single-spin quantum numbers $\{\sigma_i^z\}$. For a small $J \neq 0$, the significant level distance between neighboring sites, set by h , blocks the hybridization over different lattice sites. Early groundbreaking work that also coined the expression ‘many-body localization’ [112, 113] argued in this perturbative sense (for disordered fermionic systems) and showed that the nonthermalizing limit withstands the onset of interactions to any order in perturbation theory [113].⁶ However, the MBL phase and the violation of ETH occur even for strong interactions where perturbation theory is not valid, as has been shown in numerous numerical studies, often focusing on variations of the model in Eq. (2.16) [162–164] or fermionic models [136]. These models observe a phase transition when the disorder strength is tuned. The transition reflects in a change in the many-body eigenstate properties: for small disorder, the system thermalizes because all eigenstates satisfy the ETH, whereas once the MBL phase is entered for large disorder, the ETH is disobeyed.

2.3.2 Emergent integrability and local integrals of motion

One of the salient features of the MBL phase—often equated with MBL—is its simple but powerful description through quasi-local operators. Within this picture, many of the pivotal characteristics can be intuitively captured. We consider a system of N *local* two-state degrees of freedom, but one can argue analogously for systems with more levels. These local two-level systems are referred to as physical bits or p -bits. They can be, for example, spins $|\uparrow\rangle, |\downarrow\rangle$ or qubits $|0\rangle, |1\rangle$ on a lattice. For concreteness, we proceed with the model (2.16). Switching off the interaction J , all spins point either up or down and all eigenstates are simply product states, i.e.,

$$|\{\sigma_i^z\}\rangle = |\sigma_1^z \sigma_2^z \dots \sigma_N^z\rangle, \quad \sigma_i^z = \uparrow, \downarrow. \quad (2.17)$$

For $J = 0$, the p -bits $\hat{\sigma}_i^z$ form a complete set of independent local integrals of motion as they commute with the Hamiltonian and each other. Once the spins start interacting, the Hamiltonian is not diagonal in the $|\{\sigma_i^z\}\rangle$ basis. The crucial hallmark of MBL is that each eigenstate can still be specified by providing the individual quantum numbers $\uparrow_\tau, \downarrow_\tau$ of a two-level object. However, this new, emergent degree of freedom is not the perfectly local p -bit but a *quasi-local* integral of motion (LIOM), the so-called l -bit or localized bit, denoted as $\hat{\tau}_i^z$.

More formally, that implies that there exists a quasi-local unitary transformation \hat{U} , i.e., a transformation which intermingles only nearby spins⁷ and transforms the integrals of motion for $J = 0$, the p -bits, into the l -bits according to

$$\hat{\tau}_i^z = \hat{U} \hat{\sigma}_i^z \hat{U}^\dagger \propto \hat{\sigma}_i^z + \sum_{j,k} \sum_{\alpha,\beta=x,y,z} c_{\alpha\beta}(i,j,k) \hat{\sigma}_j^\alpha \hat{\sigma}_k^\beta + \dots, \quad (2.18)$$

where \dots denotes terms with more than two spin operators. The $\hat{\tau}_i^z$ operators commute with the Hamiltonian (by definition) and each other, i.e.,

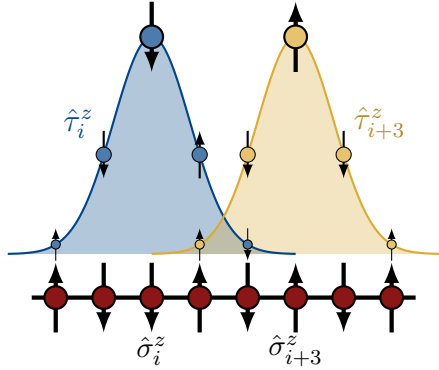
$$[\hat{\tau}_i^z, \hat{H}] = 0, \quad [\hat{\tau}_i^z, \hat{\tau}_j^z] = 0, \quad (2.19)$$

⁶Here, Anderson localization appears to be the noninteracting limit of MBL. This is not generically true; switching off the interactions in the MBL phase does not necessarily result in Anderson localization [161].

⁷ \hat{U} is called quasi-local if it takes the form $\hat{U} = \prod_i \dots \hat{U}_{i,i+1,i+2}^{(3)} \hat{U}_{i,i+1}^{(2)}$ where $\hat{U}_{i,\dots,i+k}^{(k)}$ acts on k sites and approaches the identity exponentially fast, i.e., $\|1 - \hat{U}_{i,\dots,i+k}^{(k)}\| < \exp(-k/\xi)$ with the Frobenius norm $\|\cdot\|$ [114].

Figure 2.4 –

***l*-bits and *p*-bits.** The physical bits, denoted by $\hat{\sigma}_i^z$, are truly local two-state degrees of freedom. Their individual quantum numbers $\{\sigma_i^z\}$ completely specify the eigenstates of the noninteracting system. Once the interaction is switched on, a new set of conserved quantities emerges, the *l*-bits, denoted by $\hat{\tau}_i^z$. They are local in the sense that they are concentrated at one lattice site, but neighboring *p*-bits also contribute to an *l*-bit. The eigenstates of the interacting system are still fully specified by a set of local quantum numbers $\{\tau_i^z\}$. The (exponentially small) overlap between far-apart *l*-bits induces long-range interactions.



meaning that the *l*-bits form a set of independently conserved quantities. Consequently, a set of *l*-bit eigenvalues $|\{\tau_i^z\}\rangle$, $\tau_i^z = \uparrow_\tau, \downarrow_\tau$ akin to Eq. (2.17) completely specifies each eigenstate of \hat{H} . The heart of MBL is the quasi-locality of \hat{U} , which implies that the coefficients c in Eq. (2.18) decay exponentially with the distance between site i and the sites j, k , i.e.,

$$c_{\alpha\beta}(i, j, k) \propto \exp(-\max\{|i - j|, |i - k|\}/\xi). \quad (2.20)$$

Hence, the $\hat{\tau}_i^z$ are similar to the $\hat{\sigma}_i^z$ in the regard that their support predominantly stems from the site i , but they are *dressed* with minor contributions from neighboring sites, as illustrated in Fig. 2.4. Thus, the *l*-bits are not only conserved but quasi-local. This property of the MBL phase is sometimes referred to as emergent local integrability. The length scale ξ can be interpreted as the MBL localization length, although it should be noted that separate characteristic length scales can control different properties of MBL systems. In contrast to ETH eigenstates, MBL eigenstates, being uniquely specified by a set of $\{\tau_i^z\}$, $\tau_i^z = \uparrow_\tau, \downarrow_\tau$, carry local information that is trivially preserved under unitary time evolution at arbitrarily large times, providing the first indication that it is the MBL phase one desires for a transmon array serving as a viable quantum computer.

Expressed in terms of the *l*-bits, a generic MBL Hamiltonian takes the universal form [165–167]

$$\hat{H}_{\text{MBL}} = E_0 + \sum_i h_i \hat{\tau}_i^z + \sum_{i>j} J_{ij} \hat{\tau}_i^z \hat{\tau}_j^z + \sum_{i>j>k} J_{ijk} \hat{\tau}_i^z \hat{\tau}_j^z \hat{\tau}_k^z + \dots, \quad (2.21)$$

where the dots denote interaction terms between four or more $\hat{\tau}^z$. E_0 is an energy offset that does not influence the dynamics, the second term is a local field term, and all higher terms describe interactions between the *l*-bits. Note that Eq. (2.21) contains long-range interactions arising because two far-apart *l*-bits have an (exponentially small) overlap. Crucially, as the Hamiltonian in Eq. (2.16) only couples nearby *p*-bits and those are related to the *l*-bits via a quasi-local unitary \hat{U} , these couplings decrease exponentially with the maximal distance of the involved operators,⁸

$$J_{ij} \propto J_0 \exp(-|i - j|/\kappa), \quad J_{ijk} \propto J_0 \exp(-|i - k|/\kappa), \quad \dots, \quad (2.22)$$

where J_0 is the typical interaction scale. The *l*-bit interactions distinguish the MBL phase from Anderson localization, where all J s strictly vanish. They cause distant *l*-bits to dephase slowly, which leads to the MBL-typical slow dynamics, e.g., the logarithmic spreading of entanglement,

⁸The length scales κ and ξ emerging in the Eqs. (2.20) and (2.22) satisfy $\kappa^{-1} \geq (\xi^{-1} + \ln 2)/2$ [114].

see the discussion in the next section. One should note that neither Eq. (2.18) nor the specific form in Eq. (2.21) are a peculiarity of the MBL phase. The $\hat{\tau}_i^z$ operators can also be defined in ETH systems, where they are just of no practical relevance since they are ‘too complicated’ [168] and spread over all p -bits. The essence of MBL is captured in the exponential decay in Eq. (2.20) and Eq. (2.22) and the simplicity and locality of the associated l -bits.

The description of the MBL phase by LIOMs is a highly successful concept. Their existence has been confirmed in various numerical studies and can even be proven analytically in specific one-dimensional systems [169, 170]. In the next section, when we summarize the features separating ETH and MBL, we frequently invoke Eq. (2.21) to explain MBL properties. Ref. [168, 171] provide a more in-depth discussion of MBL physics from the LIOM standpoint.

l-bit dynamics. The dynamic of an individual l -bit under Eq. (2.21) is trivial: it precesses in a magnetic field h_i^{eff} such that its z -component is conserved. Notably, the effective field and hence the precession frequency depends on the τ_j^z values of all other l -bits $j \neq i$, which is easily verified for two l -bits in the initial state $(a|\uparrow\rangle + |\downarrow\rangle) \otimes |\tau_2^z\rangle$. This has direct, detrimental effects on one of the most widespread two-qubit gates, as discussed in the next chapter.

Robustness of the integrability. There are various examples of systems violating ETH through integrability (i.e., an extensive number of conserved quantities), e.g., systems satisfying the Bethe ansatz [172] or Yang-Baxter [173] integrable systems. However, weak perturbations destroy the integrability and restore ergodicity. In contrast, the emergent local integrability of MBL systems is robust: for small perturbation of an MBL system, one can define a new ‘deformed’ [114] set of l -bits. MBL is an extended *phase of matter*, covering a finite range in the space of the Hamiltonian parameters, in contrast to the other mechanisms, which are points or lines of measure zero in this space [114]. We note that in recent years a controversy has ensued whether there can be a stable MBL phase in the thermodynamic limit [174]. We will touch on this at the end of this chapter.

2.4 Signatures of many-body localization and eigenstate thermalization

In this section, we revisit some distinguishing characteristics of the ETH and MBL phases and introduce quantitative measures used to separate between them in subsequent chapters.

Transport. The initial idea in our discussion on how to violate ETH was to introduce strong disorder to suppress transport between subsystems by making it off-resonant. Indeed, MBL systems exhibit zero DC conductivity for all conserved densities [119]. Rigorous reasoning within the l -bit picture can be found in Ref. [175]. Note that MBL differs in this aspect from disorder-free integrable systems [176]. However, the absence of transport is not the key feature distinguishing it from the delocalized phase, which, under certain circumstances, displays subdiffusive transport [177].

Entanglement entropy. The entanglement entropy S_{EE} measures the degree of entanglement between subsystems in the eigenstates of the system. If we bisect a physical system in two parts, A and B , then the entanglement entropy for the eigenstate $|i\rangle$ is defined as

$$S_{\text{EE}}(|i\rangle, A) = -\text{Tr}(\hat{\rho}_A \ln \hat{\rho}_A) , \quad (2.23)$$

where $\hat{\rho}_A = \text{Tr}_B(|i\rangle\langle i|)$ is the reduced density matrix of the subsystem A in the eigenstate $|i\rangle$. In ETH systems, all observables have thermal expectation values, reflecting that every subsystem's reduced density matrix $\hat{\rho}_A$ is thermal. Eq. (2.23) then becomes the definition of the *thermodynamic* entropy of subsystem A . As the thermodynamic entropy is extensive and scales with the volume of A , S_{EE} obeys the same *volume law* scaling with the subsystem size, $S_{\text{EE}}(A) \propto \text{vol}(A)$. Eigenstates of MBL systems have a much lower entanglement that scales with the boundary of the subsystem, $S_{\text{EE}} \propto \text{vol}(\partial A)$. This *area law* scaling is intuitively clear from the l -bit picture: All eigenstates are l -bit product states. Only the l -bits that are intersected by the bipartition contribute to the entanglement entropy, indicating that S_{EE} is proportional to the number of LIOMs in the vicinity ($\sim \xi$) of the boundary. In $d = 1$ chains of length $L \gg \xi$, for example, S_{EE} is bounded by a constant in the MBL phase and scales with L_A , the length of subsystem A in the ETH phase. This behavior was verified in a variety of models [136, 178, 179]. Entanglement properties are also displayed by other diagnostics tools like the entanglement spectrum [180] or bipartite fluctuations [181, 182] of globally conserved quantities, like the fluctuation of the particle number [183] in subsystem A . In a loose sense, the low amount of entanglement makes MBL eigenstates at finite energy density similar to the ground states of gapped systems, which obey the same area law. This paves the way for applying methods initially targeting at ground states of gapped systems to MBL systems.

Level statistics. As discussed, the spectrum of ETH systems exhibits level repulsion and is described by the Wigner-Dyson distributions of RMT. In MBL systems, the eigenvalues obey Poisson statistics, as instantly apparent in the LIOM picture with an argument analogous to the one provided in Sec. 2.1.2: Each level corresponds to a particular set $\{\tau_i^z\}$. Nearby levels typically differ in many τ_i^z , making the eigenvalues uncorrelated random numbers.

Wave function statistics. Recall that RMT eigenvectors are random unit vectors delocalized over a given basis. Two measures to quantify the degree of (de)localization are the inverse participation ratio (IPR) and the information or participation entropy, defined as

$$\text{IPR} = \sum_{\alpha} |c_i^{\alpha}|^4, \quad (2.24)$$

$$S_P = - \sum_{\alpha} |c_i^{\alpha}|^2 \ln |c_i^{\alpha}|^2 \quad (2.25)$$

for the eigenstate $|i\rangle = \sum_{\alpha} c_i^{\alpha} |\alpha\rangle$, where $c_i = \langle i|\alpha\rangle$. Both quantities convert the complete information about the wave function to a single number carrying all information on the localization properties. The illustrative meaning of the IPR is easily visualized in real space by considering a particle in a lattice, as shown in Fig. 2.5(a). Choosing the local eigenfunctions as a basis, an IPR of 1 describes a particle localized at one lattice point. As the particle spreads out over a larger region, the IPR decreases and reaches $1/\mathcal{D}$ for a completely delocalized particle. The inverse IPR can be interpreted as the localization length. For an arbitrary Hilbert space with dimension \mathcal{D} , an IPR of one indicates that the wave function has only support for a single vector $|\alpha\rangle$ of a given basis. If all basis states contribute equally, the IPR approaches $1/\mathcal{D}$. The inverse IPR measures how many basis states contribute on average to the wave function. The participation entropy S_P is maximal for uniformly distributed $|c_i^{\alpha}|^2$, i.e., maximally delocalized states, and vanishes for a localized state with $c_i^{\alpha} = \delta_{ij}$ for some j .

Both quantities are commonly exploited to measure how much an eigenstate extends over a given basis that is usually taken to be the p -bit basis, e.g., the σ_i^z -product states for the spin

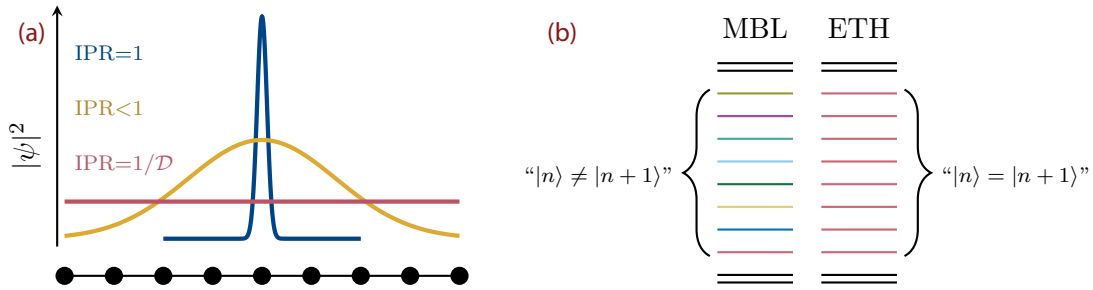


Figure 2.5 – IPR and eigenvector similarity. (a) In real space, a particle localized at a specific lattice point has an IPR of one (measured with respect to the local basis vectors). As the particle delocalizes, the IPR decreases and reaches its minimal value of $1/\mathcal{D}$ for complete delocalization. Here, \mathcal{D} is the number of lattice points. (b) In the ETH phase, eigenvectors belonging to levels taken from the same narrow energy interval are similar in that all local observables \hat{O} give the same expectation value, i.e., $\langle n|\hat{O}|n \rangle = \langle n+1|\hat{O}|n+1 \rangle$. In contrast, local measurements can distinguish between two nearby eigenvectors in the MBL phase. Panel (b) inspired by Ref. [120].

system in Eq. (2.16). They work with the caveat that their predictive power depends on the choice of the basis $|\alpha\rangle$. However, for our purposes, the IPR is helpful because we are interested in asking how far the given qubit states deviate from the perfect ones.

As discussed, eigenstates in ETH systems that belong to nearby energies are similar in the sense that in all states, the same microcanonical expectation value for observables \hat{O} is obtained, whereas they are different in the MBL phase, as pictorially shown in Fig. 2.5(b). One way to measure the similarity of two eigenfunctions $|i\rangle$, $|j\rangle$ is to compare the distributions of the coefficients c_i^α , c_j^α . A suitable measure to evaluate the distance between the two distributions is the eigenvector similarity (EVS)

$$\text{EVS} = \sum_\alpha |c_i^\alpha|^2 \ln \left(\frac{|c_i^\alpha|^2}{|c_j^\alpha|^2} \right). \quad (2.26)$$

This specific form of proximity measure for probability distributions (here c_i and c_j) firms under the name Kullback-Leibler divergence. In Chapter 4, we utilize Kullback-Leibler divergences to examine level statistics, see the discussion there for more details on their properties.

Quantum quench experiments. Following a quench, where some initial state $|\psi_0\rangle$ is prepared and evolves under the Hamiltonian \hat{H} , local observables relax towards the thermal expectation values in ETH systems. Information is transferred rapidly through the system and effectively erased. Consider, for example, the Néel state $|\uparrow\downarrow\uparrow\downarrow\dots\rangle$ and, as an observable suitable to record the alternating up-down pattern, the staggered magnetization $\hat{\sigma}_{\text{stag}}^z = \frac{1}{L} \sum_i (-1)^i \hat{\sigma}_i^z$ whose expectation value is 1 for $t = 0$ and approaches 0 for $t \rightarrow \infty$. A ballistic spreading of entanglement accompanies the information spread in ETH systems, i.e., the entanglement entropy grows as $S_{\text{EE}}(|\psi_0(t)\rangle, A) \propto t$ [184]. In contrast, MBL systems obey a characteristic, logarithmically slow spreading of entanglement $S_{\text{EE}}(|\psi_0(t)\rangle, A) \propto \tilde{\xi} \ln(J_0 t)$ [166, 167, 171, 185], where J_0 is the typical interaction scale as in Eq. (2.22) ($\tilde{\xi}$ is yet another length scale, see Ref. [114] for a careful discussion). Again, the l -bit picture provides an explanation: In Eq. (2.21), two l -bits dephase on a timescale τ determined by the inverse effective interaction strength, which in turn decreases exponentially with the l -bit distance r , i.e., $\tau \propto J_0^{-1} \exp(r/\tilde{\xi})$. At a time t , degrees of freedom with a distance $r(t) \propto \tilde{\xi} \ln(J_0 t)$ dephase. When starting in a product state, the entanglement

entropy is proportional to the volume in which degrees of freedom are dephased, resulting in the above $\log(t)$ spreading. For $t \rightarrow \infty$, the entanglement entropy is bounded by the system size because the volume containing dephased l -bits cannot exceed the actual system. A similar line of arguments can be exploited to examine the relaxation properties of observables in MBL quench experiments. One can show that dephasing leads to the relaxation of all local observables in a power-law fashion [186]. Most importantly, although MBL systems equilibrate, they approach a nonthermal state from which locally encoded initial information can be reconstructed [187]. This implies that in our example, for $t \rightarrow \infty$, there is a remanent staggered magnetization $\langle \psi_0(t) | \hat{\sigma}_\text{stag}^z | \psi_0(t) \rangle \rightarrow \sigma_\text{stag}^\infty > 0$ [188].

These attributes are such characteristic traits of MBL systems that they are often considered to be defining properties in numerical simulations (entropy spreading) and experiments (relaxation of observables). In particular, they provide a way to distinguish MBL from its noninteracting cousin, Anderson localization, where neither entanglement spreading nor equilibration occur.

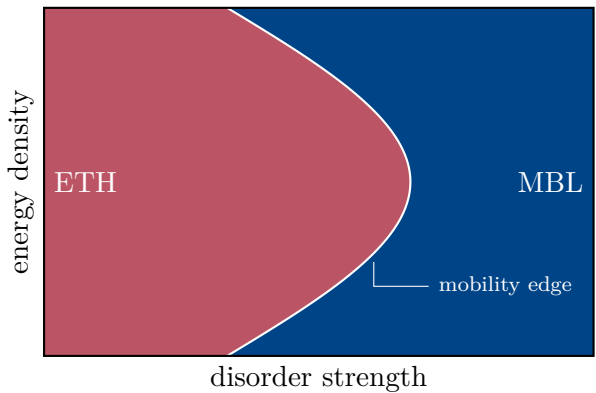
2.5 Selected aspects of many-body localization

Localization in configuration space. Early work heralding the existence of an MBL phase relied on a mapping of the interacting many-body problem to a single particle Anderson problem on a high-dimensional Fock or configuration space lattice [189]. For the model (2.16), one can interpret the simultaneous eigenstates of all $\hat{\sigma}_i^z$ as the 2^N corners of an N -dimensional hypercube. Eq. (2.16) then describes a single particle hopping on that high-dimensional cube, with disordered on-site energies stemming from the diagonal terms in Eq. (2.16) and hopping between neighboring corners due to the spin-flip terms (see Chapter 4 for a visualization for the transmon model). Various works exploit this analogy and studies the MBL problem from the perspective of localization on complex lattices, confirming an almost perfect delocalization in the ETH phase, i.e., $\text{IPR} \sim 1/\mathcal{D}$, and a clear ergodicity breaking in the MBL phase [164, 190]. Interestingly, for the MBL phase, the numerics suggest a *multifractal* scaling of the hypercube volume covered by the wave functions with the Hilbert space dimension \mathcal{D} [164]: localized wave functions extending over a finite set of states obey $\text{IPR} = \text{const}$. Eigenstates in the MBL phase, however, seem to comply with an $\text{IPR} = 1/\mathcal{D}^D$ scaling, where D is the (basis-dependent) multifractal dimension ($D = 0(1)$ for completely (de)localized states) [191]. Subsequent work has suggested the existence of an intermediate phase between MBL and ETH [192]. This phase is proposed to be nonergodic but delocalized with multifractal scaling (in the context of Anderson localization, this is dubbed a ‘bad metal’). The existence of such a phase has not yet been conclusively solved, with arguments in favor [193] and against [194]. The takeaway here is that MBL wave functions are not genuinely localized in Fock or configuration space. For a detailed discussion, see Ref. [120] and references therein.

MBL in higher dimensions. Numerical hints and—for specific spin systems—analytical proofs [169] confirm the existence of a stable MBL phase in $d = 1$. For $d > 1$, numerical studies cannot make credible statements, and heuristic arguments must be used. Consider a ‘rare fluctuation’ with an atypical large disorder amplitude (e.g., $h_{i+1} - h_i \gg 1$ in Eq. (2.16)). In a $d = 1$ system, this can block energy exchange and prevent thermalization, whereas it does not constitute an obstacle in $d \geq 2$, where the large-disorder barrier can be circumvented. More quantitatively, employing the heuristic condition that delocalization occurs when the hopping amplitude exceeds

Figure 2.6 –

Many-body mobility edge in the disordered spin-chain from Eq. (2.16), as numerically calculated in Ref. [164]. For a fixed intermediate disorder strength, localized and ergodic states coexist, with the localized states sitting at the boundary of the spectrum. In general, one finds that the critical disorder strength h_c is a function of the energy density ϵ . The figure is intended to give a qualitative impression, for details see Ref. [164].



the level spacing [195],

$$\frac{\text{hopping amplitude}}{\text{many-body level spacing}} \gtrsim 1, \quad (2.27)$$

one can show that a thermal region (called ‘ergodic grain’), generated by atypical small disorder amplitudes, destabilizes a surrounding MBL region for $d \geq 2$ but is harmless in $d = 1$ [195, 196]. There is indeed no unambiguous evidence for the existence of a $d > 1$ MBL phase. It was argued that $d \geq 2$ systems might host an ETH phase with MBL traits: thermalization happens on diverging timescales such that the systems obey MBL-typical slow dynamics (compared to the times probed experimentally) and experiments are consistent with an MBL picture [197].

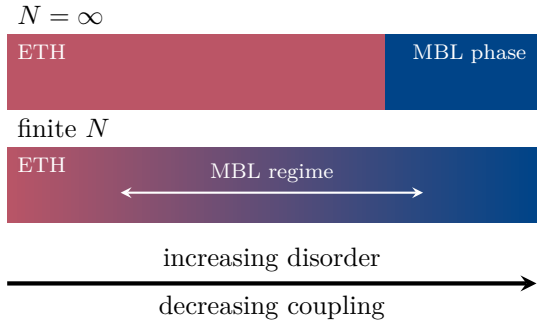
Mobility edge. Although the τ -Hamiltonian provides an intuitive explanation for many MBL traits, a few observed features cannot be described in terms of LIOMs. Most notably, reconciling the existence of a *many-body mobility edge* with the LIOM picture is an open challenge [171]. By that, one means the dependence of the critical value of the transition driving parameter, usually disorder or interaction strength, on the energy density $\epsilon = (E - E_{\min})/(E_{\max} - E_{\min})$. Such an edge, indicating the coexistence of localized and thermal eigenstates, is found in many numerical studies [164, 179]. Usually, states near the edges of a bounded spectrum or below some critical density are localized. Fig. 2.6 pictorially sketches the disorder-density phase diagram for the random-field Heisenberg model in Eq. (2.16) obtained numerically in Ref. [164].

The existence of a mobility edge is not only indecipherable in the LIOMs picture, but the phenomenon in its entirety has been called into doubt. It has been argued that ‘hot bubbles’, rare spontaneous fluctuations with high density on a low-density background, can act as a mobile bath and thermalizes the localized remainder [198]. Following this reasoning, the observed mobility edges are merely finite-size effects and vanish in the thermodynamic limit. This perspective also excludes the possibility of an MBL-ETH transition as a function of temperature. Such a transition follows from the presence of a mobility edge, as was highlighted early on [113].

Why finite-size effects matter. As already echoed, studying MBL and ETH is numerically hard. A clear transition between the two phases at a critical interaction or disorder strength only occurs in the thermodynamic limit. For numerically accessible system sizes, a smooth crossover substitutes the sharp distinction, giving rise to a finite-size MBL *regime*, where systems show MBL-like characteristics as indicated in Fig. 2.7. In this work, we do not aim to study the MBL-ETH transition via an appropriate finite-size scaling but to link the properties of the finite-size

Figure 2.7 –

ETH-MBL phase transition and crossover. The distinction between ETH and MBL phases is only sharp in the thermodynamic limit. For finite system size N , an MBL *regime* occurs, where the system exhibits MBL behavior in most respects. Recent work has brought this regime into focus. For realistic transmon arrays, the properties of the regime matter, not the actual phase transition, which only occurs for $N \rightarrow \infty$. Inspired by Ref. [204].



MBL regime to its potential application as a quantum computer. After all, a transmon quantum computer does not operate in the thermodynamic limit.

This approach seems exceptionally reasonable in light of the newly awakened, controversial discussion about the stability of the MBL phase, even in $d = 1$. A series of works [174, 199, 200] claims that the MBL phase cannot be stable in the thermodynamic limit. Even if the harsh conclusions drawn there are viewed extremely critically⁹ [201, 202], some valid points are touched on: The critical disorder strength, e.g., for the paradigmatic model (2.16), seems to lie at much higher values [203, 204] than previously thought. Furthermore, there is also agreement that finite-size effects are strong and that the extrapolation to the thermodynamic limit might give ambiguous results. While the question of the fragility of the MBL phase remains unsolved for the time being, the emergent discussion nevertheless has a few important consequences: First, it establishes the MBL *regime* in finite-size systems as an independent research object, whose characteristics may be very different from the actual MBL *phase* and that should be treated as a distinct phenomenon [204]. Second, as properties of the ETH-MBL transition probably cannot be explored with current numerical and experimental available resources [202], previous results on the transition should be critically reevaluated [205], especially in view of the dramatic shift of the critical disorder strength towards larger values. In addition, in our specific case, current transmon processors usually exploit two-dimensional geometries, and thus, given the unlikely existence of a $d = 2$ MBL phase, an MBL regime in a finite-size geometry is already the ultima ratio.

Experiments. Experimentally studying *isolated* quantum systems is an inherently contradictory endeavor, and improving isolation from the environment (apart from the necessary coupling to measuring devices) remains a crucial challenge. The synthetic systems whose realization triggered the interest in the dynamics of closed quantum systems in the first place are also the preferred platforms for probing signatures of MBL: ultracold atoms [206], trapped ions [207], and, more recently, superconducting circuits. A favored setting are quench experiments where the initial state is a density wave or Néel configuration. The conservation of information on the initial pattern indicates the presence of MBL, see Refs. [208–210] for an example for each mentioned platform. Novel many-body spectroscopy techniques also allowed for the direct probe of many-body levels and level statistics in transmon arrays [211].

Another experimental challenge is to distinguish MBL from Anderson localization. Both share

⁹The field of MBL is currently surrounded by an aura of uncertainty: The work that initially cast doubt on the stability of MBL [174] exploits a finite-size scaling in the ergodic phase. Related to this, Ref. [201] has argued that finite-size effects severely impact the utility of the metrics used in Ref. [174] in a scaling analysis. However, other studies cast doubt on more (supposedly) established findings (e.g., the saturation of the *number entropy* [199]). Yet, there is no serious evidence about a loophole in Imbrie's proof [169].

some properties, e.g., a vanishing DC conductivity of all conserved densities [119], which are therefore excluded as a reliable indicator for the presence of an MBL phase. What to look for are signatures of dephasing resulting from the weak coupling between far-apart l -bits that is absent in Anderson localization. One distinguishing feature is the logarithmic growth of entanglement entropy in MBL systems. This was recently observed in systems of ultracold atoms [212] and superconducting circuits [210]. Other dynamical properties that can be measured to distinguish between Anderson localization and MBL have been proposed [213, 214], but the experimental implementation is still lacking.

2.6 Summary

This chapter introduced two phases whose properties are in diametrical opposition to each other: the ETH phase, a quantum computer’s nemesis, and the MBL phase, where every quantum computer must be. The ETH phase cannot serve as a quantum memory since initial states thermalize, not because of the coupling to an external bath, but by their unitary dynamics: the system can act as its own bath. In addition, it is impossible to identify a unique set of distinct computational states because nearby ETH eigenstates are ‘similar’, i.e., they have the same expectation values for local observables. This contrasts with the MBL phase, which possesses many properties necessary for storing and processing quantum information. MBL is a very active and expanding research field. Few aspects are fully understood, and, as previously mentioned, controversial debates question even the existence of MBL as a stable phase [174, 200]. This chapter presented a little excerpt of the field, with topics chosen according to (subjectively perceived) importance and relevance to the results shown later. Other essential and open topics have been completely neglected. Most notably, we did not touch upon the attempts to understand the nature of the phase transition from ETH to MBL, which possesses some unique features distinguishing it from conventional phase transitions. For example, it manifests itself only in dynamical quantities as entanglement propagation but not necessarily thermodynamic signatures [215]. Other exciting areas are, e.g., the interplay of symmetries and localization [216, 217], the possibility of MBL in translational invariant (i.e., disorder-free) systems [217] or many-body localization in Floquet systems [218, 219]. From the methodological side, exact diagonalization studies of small systems provided many insights into MBL. Besides, one should mention the application of density matrix renormalization group (DMRG) methods to extract MBL eigenstates, reflecting the similarity between these and ground states of gapped systems [180] as well as RG approaches to obtain explicit (approximate) expressions for the LIOMs [220]. Recently, the concept of *out-of-time-order correlators* (OTOCs) [221] has become an increasingly widespread and vital tool for studying the logarithmically slow spread of information in MBL systems [220, 222]. All these topics are covered in the reviews commonly cited in this chapter [111, 114, 120, 171] and references therein.

The transmon platform for quantum computing

In the previous chapter, we discussed how the phenomenon of many-body localization enables specific interacting systems to eschew the fate of thermalization and the concomitant erasure of the memory of an initial state. This chapter presents in more detail the territory we will explore with the diagnostic tools of MBL theory: the superconducting transmon qubit platform for quantum computing. The transmon (*transmission-line shunted plasma oscillation* qubit [58]) is the most extensively studied type of superconducting qubit [223]. In Sec. 3.1, we discuss two complementary approaches to derive the Hamiltonian of a single transmon. The fundamental properties, which have led to the transmon becoming the most widely used superconducting qubit, are reviewed in Sec. 3.2. To build a functioning quantum processor, transmons have to be equipped with the capability of communicating with each other. How this can be accomplished is the subject of Sec. 3.3. Looking at the transmon array through the eyes of an MBL physicist, two parameters are of particular importance: the disorder and the interaction strength. In our model, these quantities cannot be chosen arbitrarily; instead, they are deeply rooted in the concrete choice of the transmon hardware, which in turn is determined by the way two-qubit gates are performed. Therefore, in Sec. 3.4, we advance beyond our actual model of a ‘nonfunctional’ quantum computer and discuss variants of entangling gates. This lays the foundation for introducing the central transmon computer design schemes in Sec. 3.5. The experimental studies and example processors showcased serve as blueprints for our simulations, the results of which are discussed in subsequent chapters.

The enormous popularity of the transmon is also reflected in the number of reviews dedicated to it. Special mention should be made to Refs. [26, 47, 58, 223, 224], which have guided the synopsis presented here and are excellent resources for further study.

3.1 The transmon

In this section, we motivate the Hamiltonian of a single transmon and show how the phenomenon of superconductivity opens up the possibility of building ‘artificial atoms’, i.e., macroscopic systems composed of innumerable microscopic building blocks, yet with an energy spectrum that is no more complex than that of a hydrogen atom. This section closely follows Refs. [47, 224]. For a more in-depth discussion of the physics of Josephson junctions, see, for example, Ref. [225].

3.1.1 Superconductivity and the Josephson junction

One can think of the electrodes of an ordinary tunnel junction as an infinite potential well with level spacings that, even for mesoscopic systems, are small enough to consider the density of states as a continuum, as shown in Fig. 3.1(a). In a conventional BCS superconductor, the situation is thoroughly different: Due to an effective, attractive interaction arising from virtual phonon exchange, electrons of opposite spin form so-called Cooper pairs. The ground state, which has all electrons paired up, is separated from the excited states by the energy 2Δ needed to break a Cooper pair (typically a few Kelvin). In experiments with superconducting qubits, frequencies and temperatures are small compared to the gap, $\hbar\omega, k_B T \ll 2\Delta$. Hence, the principal effect of superconductivity is that, by inducing the gap in the density of states, it drastically reduces the Hilbert space dimension of the relevant states to the single state $|N\rangle$, characterized by the number of Cooper pairs N , as depicted in Fig. 3.1(b). A *Josephson tunnel junction*—the primitive building block of all superconducting qubits—consists of two superconducting electrodes separated by a thin insulating layer, see Fig. 3.1(c). The junction can be modeled as a pure *Josephson tunnel element* in parallel with a capacitor. The latter describes the plate capacitor formed by the two electrodes, see the discussion in Sec. 3.1.3. In the ground state, all electrons in both superconductors are paired up. Cooper pairs can tunnel through the thin insulating barrier such that only the total number of pairs N is conserved. To fully characterize a state, the number of Cooper pairs in the left and right electrodes must be specified. Starting from a reference state with N_L (N_R) Cooper pairs in the left (right) electrode, each possible state is labeled with an integer m that counts the number of pairs transferred through the junction:

$$|m\rangle = |N_L - m, N_R + m\rangle. \quad (3.1)$$

These states are eigenstates of the Cooper pair number operator (also called charge operator)

$$\hat{n} = \sum_m m|m\rangle\langle m|. \quad (3.2)$$

Neglecting the Coulomb energy for the moment, all states $|m\rangle$ are degenerate in energy. Coherent tunneling of Cooper pairs through the barrier couples the degenerate $|m\rangle$ states, as shown in Fig. 3.1(c). The tunneling processes are described by the phenomenological Hamiltonian

$$\hat{H}_t = -\frac{E_J}{2} \sum_m (|m\rangle\langle m+1| + |m+1\rangle\langle m|). \quad (3.3)$$

The *Josephson (coupling) energy* E_J is a macroscopic parameter measuring the ability of the Cooper pairs to pass the tunnel barrier. It is given by the Ambegaokar-Baratoff relation [226]

$$E_J = \frac{\hbar}{8e^2} G_N \Delta, \quad (3.4)$$

where G_N is the normal-state conductance and Δ the superconducting gap. Eq. (3.3) is equivalent to the Hamiltonian of a one-dimensional tight-binding model with hopping amplitude E_J between nearest-neighbor ‘lattice sites’ m . By this analogy, one immediately gets

$$\hat{H}_t|\varphi\rangle = -E_J \cos \varphi |\varphi\rangle, \quad (3.5)$$

where we introduced the ‘wave vector’ φ characterizing the plane-wave-like eigenfunctions of the Hamiltonian (3.3):

$$|\varphi\rangle = \sum_{m=-\infty}^{+\infty} e^{+im\varphi} |m\rangle. \quad (3.6)$$

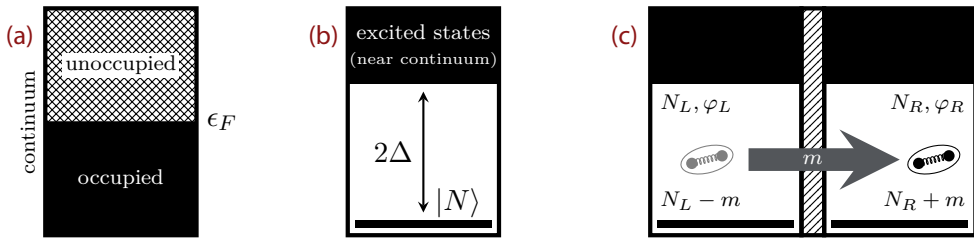


Figure 3.1 – Normal-metal and superconducting electrodes. (a) In an ordinary mesoscopic electrode, the electronic density of states forms a continuum. States up to the Fermi energy ϵ_F are occupied (solid background). (b) Superconductivity greatly simplifies the spectrum: the energy gap 2Δ separates a single ground state, characterized by the number of Cooper pairs N , from the (near) continuum of excited states. (c) A Josephson junction consists of two superconducting electrodes separated by a thin insulating layer. Each electrode is characterized by a Cooper pair number N_L, N_R and a superconducting phase φ_L, φ_R . For an isolated junction, the total number of Cooper pairs $N = N_L + N_R$ is constant, but tunneling processes change N_L and N_R . Inspired by Ref. [224].

The wave vector φ is nothing else than the phase difference of the two superconductors across the junction, $\varphi = \varphi_R - \varphi_L$ [225]. As the number of tunneled Cooper pairs m in Eq. (3.6) is an integer, the states $|\varphi\rangle$ and $|\varphi + 2\pi\rangle$ are identical. The operator $\hat{\varphi}$ associated with the superconducting phase φ is conjugated to the number operator \hat{n} [225]. Symbolically, one can write

$$[\hat{\varphi}, \hat{n}] = i, \quad (3.7)$$

keeping in mind that only operators that preserve the periodic boundary condition, like $\cos \hat{\varphi}$ or \hat{n} (but not $\hat{\varphi}$) are well-defined.

3.1.2 The transmon Hamiltonian

When a current flows through the junction and charge accumulates in one of the electrodes, the Coulomb energy that was neglected so far becomes crucial. The *charging energy* E_C necessary to transfer one electron through the junction is defined as

$$E_C = \frac{e^2}{2C_\Sigma}, \quad (3.8)$$

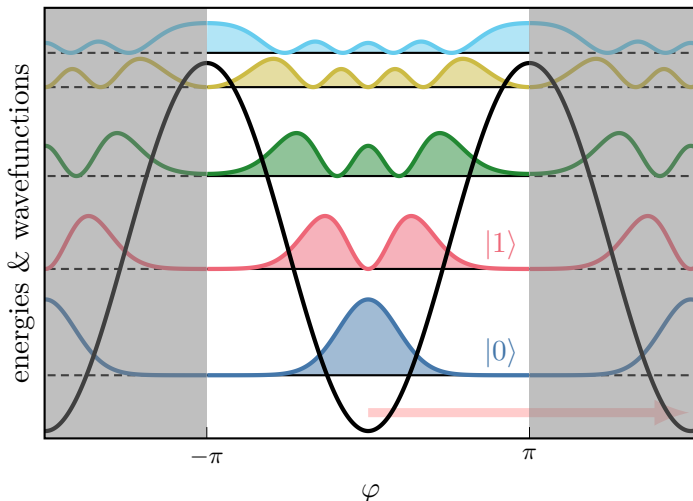
where C_Σ is the total capacitance between the two electrodes. It contains one contribution from the intrinsic capacitance of the junction C_J , but depending on the design of the complete circuit, more capacitances might add to it. Adding the Coulomb energy to the pure tunneling element in (3.5) yields the total transmon Hamiltonian

$$\hat{H}_T = 4E_C(\hat{n} - n_g)^2 - E_J \cos \hat{\varphi}. \quad (3.9)$$

The factor 4 appears because E_C measures the energy per electron, and the Coulomb energy to transfer a Cooper pair is four times larger. The parameter n_g is called *gate charge* or *offset charge*. It is a continuous variable that describes either the influence of an external gate voltage, a microscopic junction asymmetry, or unwanted degrees of freedom in the environment of the transmon [223, 224]. Charge noise, i.e., uncontrollable fluctuations in n_g , significantly reduces the lifetime of a transmon qubit. As detailed in the subsequent sections, the transmon owes its success to the fact that it can be made insensitive to charge noise by a suitable choice of the parameters E_C and E_J [58]. To be more specific, it is the ratio E_J/E_C that controls the

Figure 3.2 –

Energies and wave functions of the transmon Hamiltonian. Illustrated are the wave functions $|\psi_i(\varphi)|^2$ for $E_J/E_C = 20$ and $n_g = 0$. The two lowest states are identified as the qubit states $|0\rangle$ and $|1\rangle$. The figure advocates a reading of the transmon as a particle moving in a cosine potential. The red arrow indicates ‘tunneling processes’ between adjacent potential wells. This is fully elucidated in Sec. 3.2.1.



properties of \hat{H}_T . Modern circuit designs work in the transmon regime where $E_J/E_C \gtrsim 20$ [223]. Characteristic values for E_C/h range from 100 MHz to 400 MHz. The Josephson energy typically takes values $E_J/h \gtrsim 5$ GHz.

Fig. 3.2 gives a first impression of the properties of the Hamiltonian \hat{H}_T . Shown are the wave functions in the φ representation $|\psi_i(\varphi)|^2 = |\langle\varphi|\psi_i\rangle|^2$ and the corresponding energies for $E_J/E_C = 20$ and $n_g = 0$. The chosen representation suggests a natural interpretation of the transmon as a particle characterized by real space (not momentum!) coordinate φ moving in a cosine potential, a train of thought we pick up again later. As stated above, the spectrum is of captivating simplicity, even though the transmon is so large that it is visible to the naked eye. The ground state and the first excited state serve as the qubit states. Prototypical values of the qubit frequency $\nu_q = \omega_q/2\pi = (E_1 - E_0)/h$ lie between 4 GHz and 6 GHz, which is convenient for precise manipulation with standard microwave techniques. Only a few states are bound, i.e., have an energy smaller than the ‘cosine potential’ height.

From the Cooper pair box to the transmon and beyond. The Hamiltonian in Eq. (3.9) describes the transmons from the celebrated first qubit experiment in 1999 [53], just like the qubits used in state-of-the-art processors with lifetimes that are better by a factor of up to 10^5 [59]. In the past two decades, experimental progress has been tremendous. Nowadays, a whole family of qubits is captured by Eq. (3.9). The pioneering experiment by Nakamura *et al.* [53] used a *charge qubit* or *Cooper-pair box* (CPB) consisting of a small superconducting island connected to a large reservoir via a Josephson junction. It operates in a regime where the charging energy dominates, $E_J/E_C < 1$, and the eigenstates of \hat{H}_T are nearly eigenstates of the charge operator \hat{n} (hence the name charge qubit). The qubit states are $|m\rangle$ and $|m+1\rangle$, corresponding to the absence or presence of an additional Cooper pair on the island. Qubits with $E_J/E_C < 1$ are very sensitive to charge noise, limiting the lifetime to a few nanoseconds. Derivatives of the CPB use different circuit designs to mitigate this problem by working at different parameter points E_J/E_C or n_g .

A first attempt to soothe the charge noise sensitivity was the ‘quantronium’ [227, 228], a variant of the CPB that aims to work near specific values of n_g , where the system is immune to first-order fluctuations in n_g , which significantly increases the lifetime. Groundbreaking progress came with the introduction of the actual transmon qubit in 2007 [58]: adding an extra, large shunting capacitance C_S to the CPB increases the total capacitance entering the definition of

E_C , $C_\Sigma = C_J + C_S$, and pushes the ratio E_J/E_C to the transmon regime $E_J \gg E_C$ where the qubit is fully protected from charge fluctuations. Typical values range from $E_J/E_C = 20$ to 80. Ref. [58] also introduced the flux-tunable transmon variant, which allows for modulations of the qubit frequency during experiments and is used in some of the most sophisticated processors. We discuss this development at the end of this section. Many facets of the transmon were refined for further enhancements of the coherence time (without leaving the defining E_J/E_C regime). Examples include modifications of the geometry [229] and material [230] of the shunt capacitance or the environment in which the transmon is embedded for readout.

Occasionally, the individual enhancements are accompanied by a renaming of the qubit. Important transmon variants are the ‘xmon’ [231–233], whose cross-shaped shunt capacitance facilitates the coupling of qubits in 2D arrays, the ‘3D transmon’ [234–237], where the transmon is coupled to 3D resonators instead of planar cavities [238, 239] to minimize dielectric losses [97], and the ‘gatemon’, where the two superconducting electrodes are bridged by a semiconducting nanowire instead of the small insulating barrier which simplifies the frequency tunability [240–243]. For more details on the different derivatives of the CPB, we refer the reader to Refs. [70, 244].

While these improvements aim to ameliorate the properties of individual qubits, we are interested in arrays of *perfect* transmons with infinitely long lifetimes. Our analysis applies to all variants for which Eq. (3.9) holds, regardless of the hardware realization, except that specific hardware choices influence the variation of E_J in multi-transmon arrays, see Sec. 3.5.

3.1.3 Quantum circuit theory

The microscopic discussion of the transmon Hamiltonian in the previous section explains how the cosine-shaped potential emerges as a consequence of the tunneling of discrete Cooper pairs. It proves useful to discuss a complementary concept based on the systematic quantization of electrical circuits. This approach highlights the role of the Josephson junction as a nonlinear circuit element that provides the anharmonicity needed for an unambiguous identification of a computational subspace. The toolbox described here enables the translation of arbitrary circuits into a Hamiltonian. It can, for example, be used for a cleaner derivation of the Coulomb energy contribution in Eq. (3.9) or to derive the Hamiltonian for capacitively coupled transmons, see Sec. 3.3.1. This section follows Refs. [26, 47]. Refs. [245, 246] offer more detailed introductions to circuit quantization.

The starting point is the observation that circuit components can be treated as lumped elements when their spatial dimensions are small compared to the relevant wavelength [47]. For a typical transmon qubit frequency $\omega_q/2\pi \approx 5$ GHz, the wavelength is much larger than the size of the circuit. The extended system is then described in excellent approximation by a circuit with discrete entities like inductors, capacitors, or Josephson junctions. This abstraction is shown in Fig. 3.3(a) for the transmon: the Josephson junction can be modeled as a Josephson tunnel element, symbolized by the cross, in parallel with a capacitor. The whole junction is usually represented by a crossed square.

The general problem of systematically finding the Hamiltonian that describes an arbitrary circuit topology was first tackled by Yurke and Denker [247] and expanded in Refs. [47, 248]. In a nutshell, the main steps are to first consider the circuit as a network whose branches consist of two-terminal electrical elements. Each branch is characterized by a voltage and a current. Second, one uses the constraints that the circuit topology imposes on the branch variables (‘Kirchhoff’s law’) to identify the independent degrees of freedom of a circuit. These are called the *node fluxes*, denoted as ϕ_i , and they are defined as the time integral of the voltage measured along the path connecting the node to a chosen ground. The equations of motion for

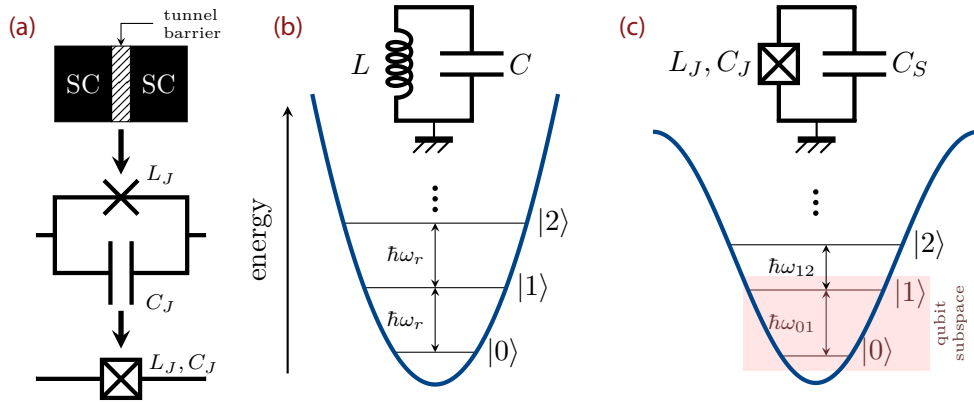


Figure 3.3 – Lumped element circuits and potentials for the LC oscillator and the transmon. (a) A Josephson junction can be considered as a pure tunneling element L_J in parallel with the intrinsic capacitance C_J . The whole junction is often schematically depicted as a crossed square. (b) A quantum LC resonator consisting of only linear circuit elements, a capacitance C in parallel with an inductor L , has an equidistant spectrum with level spacing $\hbar\omega_r = \hbar/\sqrt{LC}$. (c) Replacing the linear inductor with a Josephson junction that serves as a nonlinear inductor L_J , yields an anharmonic potential with nonequidistant levels and enables the identification of a computational subspace.

the ϕ_i , obtained by equating incoming and outgoing currents at each node, are precisely the Euler-Lagrange equations associated with a Lagrangian \mathcal{L} that is obtained by subtracting the energies of the inductive elements E_{ind} ('potential energy' \mathcal{U}) from the capacitive elements E_{cap} ('kinetic energy' \mathcal{T}).¹ A Legendre transformation that replaces the time derivatives $\dot{\phi}_i$ by the conjugate momenta of the node fluxes, the node charges $q_i = \partial\mathcal{L}/\partial\dot{\phi}_i$, yields the Hamiltonian. Promoting the classical variables q_i, ϕ_i with the standard Poisson bracket $\{\phi_i, q_j\} = 1$ to quantum operators satisfying $[\hat{\phi}_i, \hat{q}_j] = i\hbar$ completes the derivation.

It is illuminating to compare the transmon to the LC resonator, whose simple lumped element circuit is depicted in Fig. 3.3(b). This circuit topology has a single independent node flux ϕ that happens to be the physical flux through the inductance, $\phi \equiv \Phi$. The momentum conjugate to Φ is the charge on the capacitor. To find the Hamilton function $H(Q, \Phi)$, we, therefore, do not need the complete toolbox described above but can simply add the energies stored in the capacitor and the inductor. Those derive from the current and the voltage according to [223]

$$E(t) = \int_{-\infty}^t V(t')I(t')dt', \quad (3.10)$$

which, using $I = \dot{Q}$ and Faraday's induction law $V = \dot{\Phi}$, yields

$$E_{\text{cap}}(Q) = \int_0^Q V(q)dq = \frac{Q^2}{2C}, \quad (3.11)$$

$$E_{\text{ind}}(\Phi) = \int_0^\Phi I(\phi')d\phi' = \frac{\Phi^2}{2L} \quad (3.12)$$

¹The assignment $E_{\text{cap}} \leftrightarrow \mathcal{T}$, $E_{\text{ind}} \leftrightarrow \mathcal{U}$ is merely an effect of taking the ϕ_i as independent variables. Choosing charge variables instead, i.e., the time integrals of the currents, interchanges these associations.

for the energy E_{cap} and E_{ind} stored in the two circuit elements. For the last equality, the linearity of the circuit elements, $\Phi = LI$ and $Q = CV$, was used [26]. For the total energy, one now arrives at

$$H_{LC} = \frac{Q^2}{2C} + \frac{\Phi^2}{2L} = \frac{Q^2}{2C} + \frac{1}{2}C\omega_r^2\Phi^2, \quad (3.13)$$

with the resonator frequency $\omega_r = 1/\sqrt{LC}$. The final form highlights the equivalence to a harmonic oscillator with mass C and position Φ . Due to the harmonic potential $\propto \Phi^2$, quantization Q , $\Phi \rightarrow \hat{Q}$, $\hat{\Phi}$ with $[\hat{\Phi}, \hat{Q}] = i\hbar$ yields the familiar oscillator spectrum shown in Fig. 3.3(b), whose equidistance constitutes a fundamental obstacle for computing. To alleviate this, the linear inductance is replaced by a nonlinear Josephson tunnel junction. The two Josephson relations are [54]

$$I = I_c \sin \varphi, \quad (3.14)$$

$$\frac{d\varphi}{dt} = \frac{2\pi}{\Phi_0} V, \quad (3.15)$$

where $\Phi_0 = h/2e$ is the flux quantum and I_c the critical current. Eq. (3.15) can be rewritten as

$$\varphi(t) = \frac{2\pi}{\Phi_0} \int dt' V(t') (\text{mod } 2\pi) = 2\pi \frac{\Phi}{\Phi_0} (\text{mod } 2\pi), \quad (3.16)$$

where Φ is the same physical flux as in the discussion of the LC oscillator. In a Josephson junction, current I and flux Φ are linked via Eqs. (3.14) and (3.16). In a linear inductor, this connection is used to define the geometric inductance, $L = \Phi/I$. Generalizing this relation, one defines the Josephson inductance as

$$L_J(\Phi) = \left(\frac{\partial I}{\partial \Phi} \right)^{-1} = \frac{\Phi_0}{2\pi I_c \cos \frac{2\pi\Phi}{\Phi_0}}. \quad (3.17)$$

Now the inductive ‘pure tunneling’ part of the energy of the junction becomes

$$E_{\text{ind}} = I_c \int d\Phi \sin \left(2\pi \frac{\Phi}{\Phi_0} \right) = -E_J \cos \left(2\pi \frac{\Phi}{\Phi_0} \right) = -E_J \cos \varphi. \quad (3.18)$$

For the capacitive energy, we make use of Eq. (3.11) with $Q = 2en$ and combine the parallel intrinsic junction capacitance C_J and the shunt capacitance C_S to an effective capacitor $C_\Sigma = C_J + C_S$. Using Eq. (3.8), the total circuit Hamiltonian after quantization reads

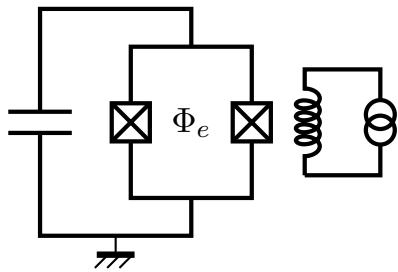
$$\hat{H} = 4E_C \hat{n}^2 - E_J \cos \hat{\varphi}, \quad (3.19)$$

which, apart from the missing offset charge n_g , reproduces Eq. (3.9). A detailed network analysis of a transmon biased by an external voltage source also properly covering the offset charge can be found in Refs. [223, 224].

Comparing resonator and transmon makes it evident how the Josephson junction acts as a nonlinear inductor with inductance L_J that adds anharmonicity to the spectrum, yielding nonequidistant energy levels. Only now, with a potential energy reshaped from quadratic to sinusoidal, can one isolate two qubit states with a unique energy separation $\hbar\omega_q = \hbar\omega_{01}$ from the encircling, larger Hilbert space, as sketched in Fig. 3.3(c).

Figure 3.4 –

Flux-tunable transmon. Shown is the circuit of the flux-tunable transmon variant. Replacing the single Josephson junction with a SQUID yields a qubit whose frequency is tunable through the external flux Φ_e threading the loop. The flux control requires additional hardware, symbolized by the inductance. The downside of this design form is the susceptibility to additional flux noise.



3.1.4 Adding control knobs: the flux tunable transmon

One of the benefits of the transmon is its simplicity: it consists of a single Josephson junction and a capacitor. This rudimentary transmon variant, see Fig. 3.3(b), is referred to as fixed-frequency transmon because E_C and E_J , and therefore the frequency ω_q , are set at fabrication. Transmons of this design form have shown superior coherence time [234, 235]. Nevertheless, it can be beneficial to include additional control knobs at the cost of adding noise sources—a balancing act that is a recurring motif in designing transmon quantum computers. Fig. 3.4 illustrates a widely used modification of the transmon circuit. The single Josephson junction is replaced by two parallel junctions that form a superconducting quantum interference device (SQUID) [58]. The transmon Hamiltonian is then modified to

$$\hat{H}_{\text{T,ft}} = 4E_C\hat{n}^2 - E_{J,1}\cos\hat{\varphi}_1 - E_{J,2}\cos\hat{\varphi}_2, \quad (3.20)$$

with the Josephson energy $E_{J,i}$ of junction i and the phase difference $\hat{\varphi}_i$ across the junction. Due to flux quantization, $\hat{\varphi}_1$ and $\hat{\varphi}_2$ are not independent and related via

$$\hat{\varphi}_1 - \hat{\varphi}_2 = 2\pi\frac{\Phi_e}{\Phi_0}(\text{ mod } 2\pi), \quad (3.21)$$

where Φ_e is the external flux threading the SQUID [225]. This allows us to rewrite Eq. (3.20) as [58, 223]

$$\hat{H}_{\text{T,ft}} = 4E_C\hat{n}^2 - E_J(\Phi_e)\cos(\hat{\varphi} - \varphi_0), \quad (3.22)$$

where $\hat{\varphi} = (\hat{\varphi}_1 + \hat{\varphi}_2)/2$ is the average phase difference and the phase $\varphi_0 = d\tan(\pi\Phi_e/\Phi_0)$ can be ignored for a time-independent flux [58]. In Eq. (3.22), in the otherwise unaltered Hamiltonian, the *effective* Josephson energy E_J is now controllable by the external flux Φ_e , which is why this circuit variant has been dubbed flux-tunable transmon. Concretely, $E_J(\Phi_e)$ is given by

$$E_J(\Phi_e) = E_{J\Sigma} \cos\left(\frac{\pi\Phi_e}{\Phi_0}\right) \sqrt{1 + d^2 \tan^2\left(\frac{\pi\Phi_e}{\Phi_0}\right)}, \quad (3.23)$$

with $E_{J\Sigma} = E_{J,1} + E_{J,2}$. The parameter $d = (E_{J,1} - E_{J,2})/E_{J\Sigma}$ measures the junction asymmetry. For identical junctions, $E_{J,1} = E_{J,2} \equiv E_J$, the Josephson energy $E_{J\Sigma}$ can be tuned from 0 to $2E_J$. The tunability comes at the expense of an additional dephasing channel due to flux noise, i.e., random fluctuations in Φ_e . According to Eq. (3.23), the tunable range of E_J can be decreased by choosing a larger junction asymmetry $|d|$, making the transmon less sensitive to flux noise [249]. By tuning E_J , the frequency $\omega_q/2\pi$ can be altered by 1 GHz in about 10 ns [250, 251], which enables the implementation of fast and high-fidelity entangling gates [6], see Sec. 3.4.1.

3.2 Properties of the transmon

In this section, we discuss in more detail some essential characteristics of the transmon, focusing on how it strikes the perfect balance between insensitivity to charge noise and sufficient anharmonicity for faithful qubit manipulation.

3.2.1 The transmon as a rigid quantum rotor

So far, it was advantageous to consider φ as the wave vector and n as the position on a one-dimensional lattice. However, as φ is limited to the range $[-\pi, \pi]$, interpreting it as an angular coordinate seems natural. From Eq. (3.6) and Eq. (3.2), it is straightforward to see that

$$\hat{n}|\varphi\rangle = -i\frac{\partial}{\partial\varphi}|\varphi\rangle. \quad (3.24)$$

This advocates an interpretation of $\hbar\hat{n}$ as the angular momentum \hat{L}_z conjugate to $\hat{\varphi}$. Due to the compactness of φ , \hat{n} naturally has integer eigenvalues as desired for an operator counting Cooper pairs. Assuming $n_g = 0$ for the moment, the transmon Hamiltonian \hat{H}_T then describes a rigid quantum rotor in a gravitational field [58, 224]

$$\hat{H}_{\text{rot}} = \frac{\hat{L}_z^2}{2ml^2} - mgl \cos \hat{\varphi}, \quad (3.25)$$

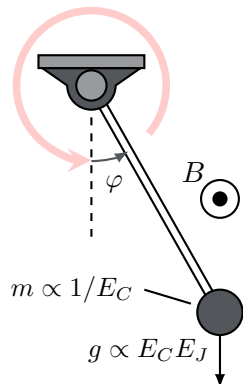
where l is the length of the pendulum stiff, the charging energy $E_C = \hbar^2/8ml^2$ determines the inverse moment of inertia (or mass if we set $l = 1$ as is common practice), and the gravitational acceleration g is related to the Josephson energy via $E_J = mgl$, see Fig. 3.5. Note how E_J , formerly describing the ability of Cooper pairs to tunnel through the junction, i.e., kinetic energy, determines now the depth of the potential. To extend the transmon-rotor analogy to the $n_g \neq 0$ case, one assigns a charge q to the pendulum mass and assumes a homogeneous magnetic field of strength B in z direction. The magnetic field enters the Hamiltonian by replacing the canonical momentum with the mechanical momentum $p_z \rightarrow [\mathbf{p} - q\mathbf{A}(\mathbf{r})]_z$. Choosing the symmetric gauge $\mathbf{A} = \mathbf{B} \times \mathbf{r}/2$, the z component of the angular momentum operator changes as $\hat{L}_z \rightarrow \hat{L}_z - qBl^2/2$ [58]. Identifying $n_g = -qBl^2/2\hbar$ finalizes the exact correspondence of the transmon with a charged quantum rotor in a constant magnetic field.

By this analogy, one can now learn about the influence of the offset charge n_g on the spectrum: only when the rotor circles completely around, as indicated by the bright red arrow in Fig. 3.5, it acquires an Aharonov-Bohm phase shift and the system can be cognizant of the magnetic field and hence the offset charge. The energies are modified through the interferences between this path and the trajectory where the rotor does not wrap around. For large masses (small E_C) and strong gravitational acceleration (large $E_J E_C$), i.e., for $E_J/E_C \gg 1$, winding the phase from 0 to 2π is only possible if the rotor tunnels through a very high energy barrier. The contributions of these tunneling processes should become exponentially small, and we expect the energies of the transmon to become insensitive to the value of the offset charge. We discuss this line of thought quantitatively in the next section.

The illustration of the rotor eigenfunctions in Fig. 3.2 suggested yet another analogy: after interpreting φ first as a momentum, then as an angular variable, we can take it to be the coordinate of a particle moving in an extended cosine potential. Full 2π rotor rotations correspond to tunneling events between adjacent wells, see the bright red arrows in Fig. 3.2. In this perspective, the wave vector k emerges as an additional continuous quantum number. However, this does

Figure 3.5 –

The transmon as a rigid quantum rotor. The transmon is equivalent to a charged rotor in a magnetic field where E_C determines the inverse mass, the gravitational acceleration is $g = 8E_C E_J / \hbar^2$ (setting the stiff length $l = 1$), and the offset charge is proportional to the product of the charge q and the field strength B .



not imply that the Hilbert space is artificially inflated. For the analogy to apply, the first step is to eliminate n_g from the Hamiltonian by a unitary transformation with $\hat{U} = \exp(-in_g\hat{\varphi})$. The boundary conditions of the wave functions are thereby modified, and one can show that the allowed values of the wave vector are constrained to $k = n_g$. For a detailed discussion, see Ref. [224]. The approach of considering n_g as a wave vector is encountered again in the discussion of the exact eigenfunctions in Sec. 3.2.4.

By preemption, we also mention here that when considering n and φ as classical variables, a strong gravitational field favors small oscillation amplitudes φ and the classical rotor is almost a harmonic oscillator. Pushing a discussion of the subtleties of this approximation to Sec. 3.2.3, we just note that after expanding the cosine potential to second order, the frequency of the resulting harmonic oscillator is given by $\omega_p = \sqrt{8E_J E_C}/\hbar$ and is known under the name Josephson plasma frequency. In the subsequent sections, we investigate the properties of the transmon for different E_J/E_C ratios. In the figures accompanying the discussion, we always keep ω_p , setting the overall energy scale, constant while tuning E_J/E_C .

3.2.2 Charge dispersion

As a macroscopic solid-state device, the transmon qubit is prone to charge noise that arises from unavoidable charge fluctuations in the circuit or its environment and causes random undulations in the offset charge n_g that modify the energies of the Hamiltonian \hat{H}_T . As shown in Fig. 3.6(a)–(c), the amplitude of the noise-induced energy fluctuations depends on the ratio of Josephson and charging energy.² For small E_J/E_C , slight variations in n_g strongly impact the transition frequencies, as shown in (a), which ultimately leads to dephasing [26, 58, 252]. In setups where $E_C \gtrsim E_J$, a first step to reduce the influence of charge noise is to carefully bias the system to the ‘sweet spot’ at $|n_g| = 1/2$ where the slope of the dispersion is zero [227]. Nevertheless, fluctuations will drive the system away from the sweet spot, enforcing a constant recalibration of the gate voltage and making this an unsatisfactory solution [253]. Fortunately, the susceptibility to charge fluctuations becomes exponentially small as E_J/E_C increases, as shown for (b) $E_J/E_C = 10$ and (c) $E_J/E_C = 50$. The latter, a typical transmon value, yields noise-protected flat levels. The transmon then acts as a charge-insensitive qubit design [58].

For a more quantitative analysis, one defines the charge dispersion ϵ_m as the ‘peak-to-peak’ difference between the energy eigenvalues, i.e.,

$$\epsilon_m = E_m(n_g = \frac{1}{2}) - E_m(n_g = 0) . \quad (3.26)$$

²The periodicity of the E_i in n_g is expected from the ‘extended cosine potential’ analogy: n_g is a wave vector living in the Brillouin zone with $-1/2 < n_g < 1/2$. See also the discussion in Sec. 3.2.4.

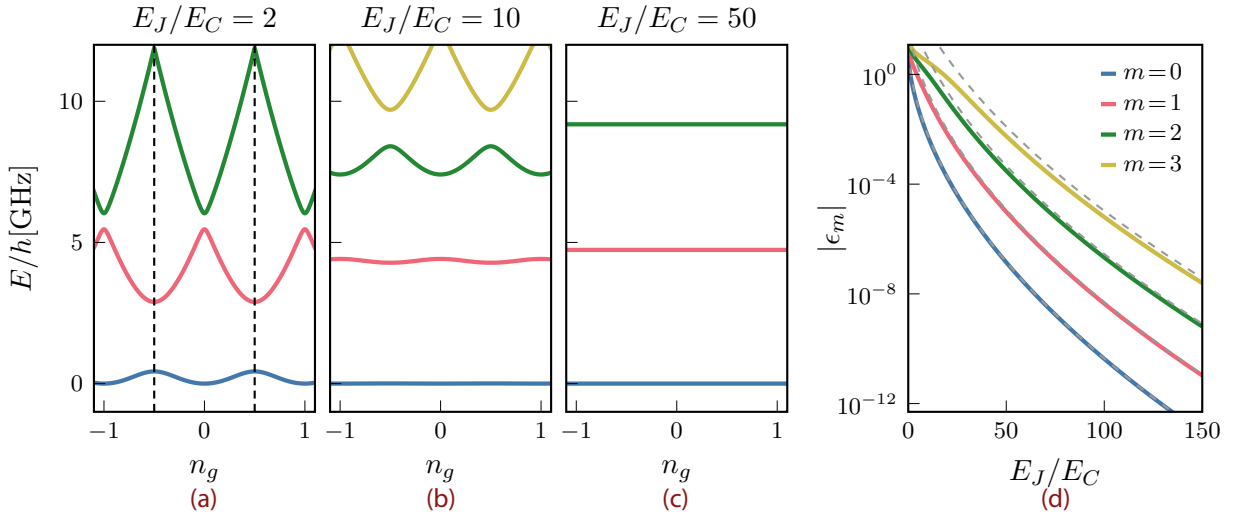


Figure 3.6 – Charge dispersion of the transmon energies. The panels (a)–(c) show the lowest levels as a function of the gate charge n_g for (a) $E_J/E_C = 2$, (b) $E_J/E_C = 10$, and (c) $E_J/E_C = 50$. Levels are shifted such that $E_0(n_g = 0) = 0$. The dispersion flattens exponentially fast when E_J/E_C increases, leading to levels that are fully protected against fluctuations in n_g . The vertical dashed lines in (a) indicate the sweet spot ($|n_g| = 1/2$) at which CPB designs with $E_J < E_C$ operate. (d) Comparison of numerical results and asymptotic expressions for the charge dispersion. The dashed curves represent the asymptotic expansion, see Eq. (3.27). We set $\omega_p/2\pi = 5$ GHz in all calculations and adopt E_J and E_C accordingly. Inspired by Ref. [58].

Numerical results for the lowest four levels are shown in Fig. 3.6(d), indicating an exponentially fast decay for large E_J/E_C . A semiclassical (WKB) expression for the charge dispersion can be obtained by writing the transmon energies in terms of the Mathieu characteristic values, see Sec. 3.2.4, and using asymptotic ($E_J/E_C \rightarrow \infty$) expressions for the latter [254]. This yields [255]

$$\epsilon_m \approx (-1)^m E_C \frac{2^{4m+5}}{m!} \sqrt{\frac{2}{\pi}} \left(\frac{E_J}{2E_C} \right)^{\frac{m}{2} + \frac{3}{4}} e^{-\sqrt{8\frac{E_J}{E_C}}}, \quad (3.27)$$

in line with the numerical results, as shown by the dashed gray lines.

Protecting the qubit from charge noise by working in the transmon regime $E_J/E_C \gtrsim 20$ drastically improves the dephasing time T_2 . One can show [58, 252] that it decreases from about one microsecond in a Cooper pair box to one second in the transmon regime, removing charge noise as a potential threat for quantum computing applications. For a more in-depth discussion, see Refs. [224, 252].

3.2.3 Anharmonicity and effective Hamiltonian

Quantum computing relies on the specific addressability of the transition frequency between two well-defined qubit states. The equidistant spectrum of a *linear* harmonic oscillator with degenerate frequencies between successive levels renders quantum computing impossible because gate operations would inevitably activate cascades of higher excitations to noncomputational states. To quantify the difference between the nonlinear transmon pendulum and the quantum harmonic oscillator, one considers the (absolute) anharmonicity, defined as

$$\alpha = \Delta E_{12} - \Delta E_{01}, \quad (3.28)$$

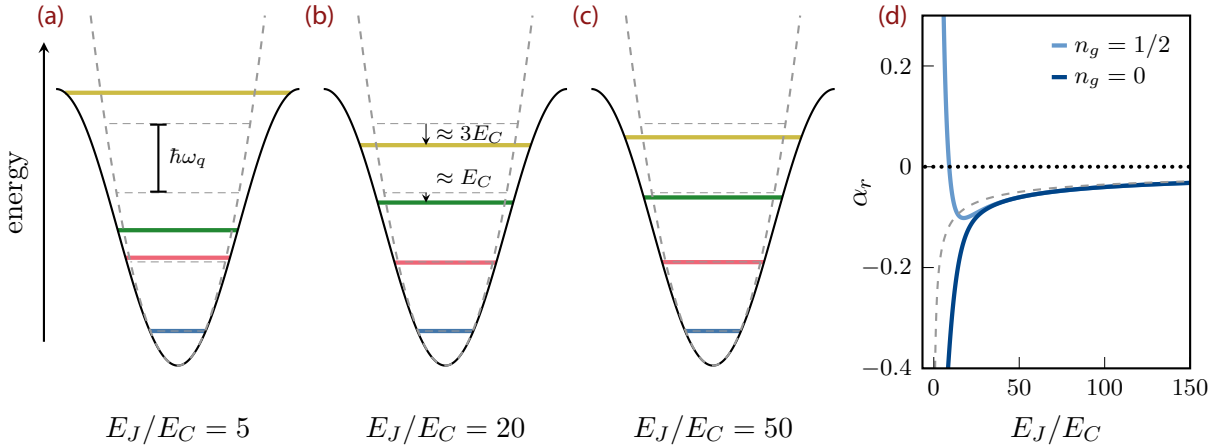


Figure 3.7 – Anharmonicity of the transmon. The panels (a)–(c) show the comparison of the levels in a transmon cosine potential (solid) and a harmonic oscillator potential (dashed) with the same qubit frequency ω_q as defined in Eq. (3.34). In (b) and (c), where the effective model in Eq. (3.33) provides an accurate description, the transmon spectrum approaches the harmonic oscillator levels, but the anharmonicity lowers transitions between higher levels according to Eq. (3.35). The relative anharmonicity α_r as a function of the ratio E_J/E_C is shown in (d). The dashed gray line corresponds to the asymptotic behavior in Eq. (3.37). Parameters are chosen as in Fig. 3.6(d). To fully bridge between the small E_J/E_C charge qubits that usually operate at $n_g = 1/2$ and the large E_J/E_C transmons, data for α_r at the sweet spot are also shown.

where $\Delta E_{ij} = E_j - E_i$. The anharmonicity thus measures the difference between the qubit transition energy ΔE_{01} and the adjacent level spacing between the qubit state $|1\rangle$ and the noncomputational state $|2\rangle$. To obtain the relative anharmonicity, one scales α by ΔE_{01} :

$$\alpha_r = \frac{\alpha}{\Delta E_{01}} = \frac{\Delta E_{12} - \Delta E_{01}}{\Delta E_{01}}. \quad (3.29)$$

That balancing anharmonicity and charge dispersion is a delicate affair can already be anticipated on the basis of Fig. 3.6(c), where the charge-noise insensitive flat levels are nearly equidistant. Reducing the charge dispersion appears to come at the cost of a lower anharmonicity. Figs. 3.7(a)–(c) compare the harmonic oscillator levels with the transmon spectrum for different values of E_J/E_C . As the ratio increases, the transmon spectrum approaches indeed the equidistant harmonic oscillator levels, which is also manifested in the asymptotic behavior of the relative anharmonicity α_r shown in Fig. 3.7(d).

To gain a better intuition of the large E_J/E_C case, we derive an effective low-energy model that will also prove helpful in discussing the many-body problem. The offset charge n_g is set to zero, as one can safely neglect its influence in the transmon regime. From the rotor analogy, the zero point fluctuations (ZPF) of $\hat{\varphi}$ are expected to be small (at least in the low-energy states) for large masses $1/E_C$ and a strong gravitational acceleration $8E_C E_J$. Terminating an expansion of the cosine potential after the first nonlinear ($\hat{\varphi}^4$) contribution is therefore expected to give an accurate description of the low-lying states and specifically of the computational subspace if

$E_J/E_C \gg 1$. The truncated Hamiltonian then reads³

$$\hat{H}_T \approx 4E_C\hat{n}^2 + \frac{1}{2}E_J\hat{\varphi}^2 - \frac{1}{4!}E_J\hat{\varphi}^4. \quad (3.30)$$

To proceed, one introduces creation and annihilation operators \hat{b}, \hat{b}^\dagger that diagonalize the first two contributions in Eq. (3.30):

$$\hat{\varphi} = \left(\frac{2E_C}{E_J}\right)^{\frac{1}{4}} (\hat{b}^\dagger + \hat{b}) = \varphi_{\text{ZPF}} (\hat{b}^\dagger + \hat{b}), \quad (3.31)$$

$$\hat{n} = \frac{i}{2} \left(\frac{E_J}{2E_C}\right)^{\frac{1}{4}} (\hat{b}^\dagger - \hat{b}) = i n_{\text{ZPF}} (\hat{b}^\dagger - \hat{b}). \quad (3.32)$$

The ZPF φ_{ZPF} are indeed small for $E_J/E_C \gg 1$, which is (self-)consistent within our assumption. Making use of \hat{b}, \hat{b}^\dagger in Eq. (3.30), dropping constant terms and keeping only terms with an equal number of creation and annihilation operators (rotating-wave approximation) yields

$$\hat{H}_T \approx \hbar\omega_q \hat{b}^\dagger \hat{b} - \frac{E_C}{2} \hat{b}^\dagger \hat{b}^\dagger \hat{b} \hat{b}, \quad (3.33)$$

with

$$\hbar\omega_q = \sqrt{8E_C E_J} - E_C. \quad (3.34)$$

Terminating the Taylor series in Eq. (3.30) after the leading quadratic term would have resulted in a harmonic oscillator with $\hat{H} = \hbar\omega_p \hat{b}^\dagger \hat{b}$, where $\omega_p = \sqrt{8E_C E_J}/\hbar$ is the already introduced Josephson plasma frequency. The next higher quartic term has two effects: For one, it lowers the plasma frequency by E_C/\hbar , such that ω_q is the qubit frequency for transitions within the computational subspace. Moreover, the attractive interaction—the second term in Eq. (3.33)—is also a remnant of the leading order nonlinearity. It shifts the frequency of each additional excitation by $-E_C$, disrupting the otherwise equidistant spectrum. Energy differences between neighboring levels decrease as the quantum numbers progressively increase,

$$\Delta E_{n,n+1} = E_{n+1} - E_n \approx \hbar\omega_q - nE_C. \quad (3.35)$$

In Fig. 3.7(b), this causes the second (third) excited transmon level to be lower by E_C ($3E_C$) than the second (third) harmonic oscillator level. From Eqs. (3.34) and (3.35), the asymptotic expressions for absolute and relative anharmonicity are directly inferred as

$$\alpha \approx -E_C, \quad (3.36)$$

$$\alpha_r \approx - \left(\frac{8E_J}{E_C}\right)^{-\frac{1}{2}}. \quad (3.37)$$

The asymptotic form of the relative anharmonicity α_r is shown in Fig. 3.7(d) (gray dashed line). In the limit $E_J/E_C \gg 1$, it agrees with the results obtained from diagonalizing the full

³Expanding the cosine potential is a subtle task: we promote φ from a compact variable to one that is defined on the whole real axis, notwithstanding the fact that this changes the boundary condition from PBC to $\psi(\varphi \rightarrow \pm\infty) \rightarrow 0$. As we want to capture the physics of low-lying states with significant support only around $\varphi = 0$, this does not compromise our considerations: for such states, the different boundary conditions are effectively equivalent. However, it should be kept in mind that the resulting Hamiltonian has no general validity (note, e.g., that the spectrum is unbounded from below).

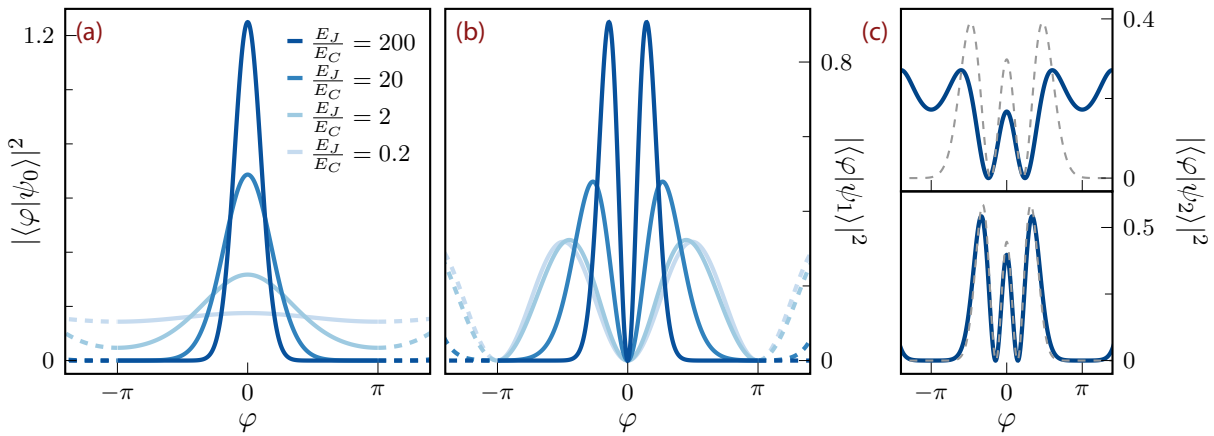


Figure 3.8 – Eigenfunctions of the transmon Hamiltonian in the φ basis. (a) Ground state wave function $|\psi_0(\varphi)|^2$ for varying E_J/E_C . (b) Wave function of the first excited state $|\psi_1(\varphi)|^2$ for the same E_J/E_C ratios. (c) Comparison of the wave function $|\psi_2(\varphi)|^2$ (solid blue) to the corresponding harmonic oscillator eigenfunctions (dashed gray) for $E_J/E_C = 10$ (upper panel) and $E_J/E_C = 50$ (lower panel).

Hamiltonian in Eq. (3.9). The (negative) anharmonicity E_C typically ranges from $E_C/h \approx 100$ MHz – 400 MHz.

The pivotal hallmark of the transmon is that it allows a fine balance between protection from charge noise and anharmonicity. Whereas the sensitivity to charge noise, Eq. (3.27), decreases *exponentially* fast in $\sqrt{E_J/E_C}$, the anharmonicity vanishes only slowly, following a *power law* $\propto 1/\sqrt{E_J/E_C}$. The qubits can be made immune to charge noise without sacrificing so much of the anharmonicity that standard experimental microwave pulse techniques for coherent control are limited in their applicability [58, 256]. It is precisely this property that has made the transmon the most widely used superconducting qubit.

3.2.4 Eigenfunctions

Eigenfunctions in phase representation. In the phase basis, the Schrödinger equation for the energies E_m and wave functions $\psi_m(\varphi)$ reads

$$\left[4E_C \left(-i \frac{d}{d\varphi} - n_g \right)^2 - E_J \cos \varphi \right] \psi_m(\varphi) = E_m \psi_m(\varphi). \quad (3.38)$$

Introducing the function $g_m(x) = \exp(-2in_g x) \psi_m(2x)$, Eq. (3.38) can be recast in the form

$$g_m''(x) + (a - 2q \cos(2x)) g_m(x) = 0, \quad (3.39)$$

where $q = -\frac{E_J}{2E_C}$ and $a = \frac{E_m}{E_C}$. This is the standard form of Mathieu's equation [257] which first appeared in the context of studies of the vibration of elliptical membranes [258]. The solutions to Eq. (3.39) are formally known as Mathieu functions, see, e.g., Ref. [259] for a detailed discussion. Even though Eq. (3.39) is independent of n_g , the offset charge affects its solution via the boundary conditions. For a given constant ν , Floquet's theorem predicts that a solution of Eq. (3.39) obeying the pseudoperiodic property

$$g(x + \pi) = e^{i\pi\nu} g(x) \quad (3.40)$$

exists [257, 260]. The parameter ν is called the characteristic exponent. Using $\psi_m(\varphi) = \psi_m(\varphi + 2\pi)$, one obtains $\nu = -2(n_g - k)$, where $k \in \mathbb{Z}$. Solutions fulfilling Eq. (3.40) are called Floquet solutions and denoted as $\text{me}_\nu(x, q)$ [257, 261]. A simple closed-form expression of $\text{me}_\nu(x, q)$ does not exist. When expanded in a Fourier series, a three-term recursion relation for the Fourier coefficients can be derived [257, 260]. For given q and n_g , Eq. (3.39) determines an infinite set of eigenvalues a_k , the Mathieu characteristic values. Each k determines one of the eigenenergies E_m . What remains to clarify is the correct assignment between the integers m and k . One naturally wishes the energies E_m to increase as m increases, i.e., the integer k —not necessarily $k = 0$ —belonging to the smallest $\lambda_{\nu(n_g, k)}(q)$ is assigned to the ground state energy $m = 0$. Therefore, $k = k(m, n_g)$ is a function of m and n_g . The explicit (and somewhat complicated) form of $k(m, n_g)$ is derived in Refs. [58, 262]. Going back to the Schrödinger equation (3.38), one can show that the appropriately sorted energies and wave functions are now given as

$$E_m(n_g) = E_C a_{2(n_g+k(m,n_g))} \left(q = -\frac{E_J}{2E_C} \right), \quad (3.41)$$

$$\psi_m(\varphi) = \frac{\exp(in_g\varphi)}{\sqrt{2}} \text{me}_{-2(n_g-k(m,n_g))} \left(q = -\frac{E_J}{2E_C}, \frac{\varphi}{2} \right). \quad (3.42)$$

In Fig. 3.8(a) and Fig. 3.8(b), we show the probability density for the wave functions of the ground and first excited state and find the conclusion drawn from the rotor analogy confirmed: For large E_J/E_C , i.e., a large mass or gravitational acceleration, the phase φ localizes strongly, and the width of the wave functions decreases. In particular, already for $E_J/E_C = 20$, that is, at the lower bound of the transmon range, the wave functions do not have significant support at $\varphi = \pm\pi$, and only small fluctuations around $\varphi = 0$ appear. Consequently, the harmonic oscillator approximation gains accuracy as E_J/E_C increases. We show this in Fig. 3.8(c), where the transmon eigenfunction $|\psi_2(\varphi)|^2$ (solid, blue) is compared to the eigenfunction of the harmonic oscillator with the same mass $m = \hbar^2/8E_C$ and frequency $\omega_p = \sqrt{8E_J E_C}$ for $E_J/E_C = 10$ (upper panel) and for $E_J/E_C = 50$. The implementation of the Mathieu functions $\text{me}_\nu(\varphi)$ in Ref. [263] was used to compile Fig. 3.8.

Note how this discussion sheds more light on the previously discussed ‘extended cosine potential’ analogy and the periodicity of the transmon energies in n_g . For one, when comparing Eq. (3.40) with the Block theorem, ν naturally appears as a wave vector living in the Brillouin zone $-\pi/a \leq \nu < \pi/a$ where $a = \pi$. Consequently, one can interpret n_g as a wave vector restricted to $[-1/2, 1/2]$. Besides, the above treatment shows explicitly how n_g , although eliminated from the ‘Hamiltonian’ in Eq. (3.39), picks out discrete energies of the continuous spectrum characterized by ν by constraining the allowed values of the wave vector via the boundary conditions (3.40).

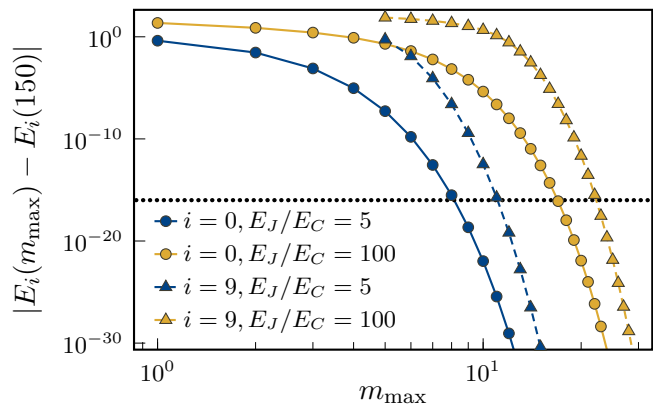
Eigenfunctions in charge representation. Although the eigenstates and energies are (formally) known in terms of Mathieu functions and characteristic values, the eigenbasis $|m\rangle$ of the Cooper pair number operator \hat{n} is more convenient for numerical purposes. The Coulomb energy contribution is then diagonal, and the $\cos\hat{\varphi}$ contribution of the pure tunneling element is tridiagonal with the simple matrix elements

$$\langle m | \cos\hat{\varphi} | n \rangle = \frac{1}{2} \delta_{m\pm 1, n}. \quad (3.43)$$

The—in principle infinite-dimensional—basis $|m\rangle$ must be cut off at a certain $|m| = m_{\max}$, resulting in a $2m_{\max} + 1$ -dimensional Hilbert space. The number of basis states should be chosen

Figure 3.9 –

Convergence of energy eigenvalues as a function of the Hilbert space dimension $2m_{\max} + 1$ for the ground state energy E_0 and the energy of the ninth excited state E_9 for two different ratios E_J/E_C . In order to obtain a desired precision, more basis states must be included for the higher levels and larger E_J/E_C , as expected from Eq. (3.44).



such that all basis vectors $|m\rangle$ that contribute significantly to a transmon eigenstate $|\psi_i\rangle$ are included in the truncated Hilbert space, meaning that $m_{\max} \gg \Delta\hat{n}$, where $\Delta\hat{n}$ is the fluctuation of the charge operator in the respective state $|\psi_i\rangle$. Using the harmonic oscillator limit of the transmon, one obtains

$$m_{\max} \gg \sqrt{1 + 2N} n_{\text{ZPF}} = \frac{\sqrt{1 + 2N}}{2} \sqrt{\frac{E_J}{2E_C}} \quad (3.44)$$

as a rough estimate for the m_{\max} needed to capture the lowest N states with high accuracy. Fig. 3.9 shows the convergence of the energies towards the exact values (here taken to be the eigenvalues for $m_{\max} = 150$; using the Mathieu characteristic values instead leaves the figure unaltered) as the dimension of the truncated Hilbert space increases. In agreement with Eq. (3.44), to obtain a desired precision, more basis states must be included for larger E_J/E_C ratios (blue vs. yellow) and higher lying energies (triangles vs. circles). However, only a moderate $m_{\max} \sim \mathcal{O}(10)$ is needed to obtain the standard double floating-point precision marked by the dotted line, even for the ninth excited energy E_9 and $E_J/E_C = 100$. Throughout the remainder of this thesis, we use $m_{\max} = 50$. For the results in Fig. 3.9, the software library MPFR [264] was used for arbitrary precision arithmetic.

In Fig. 3.10, the charge representations of the eigenfunctions $\langle n|\psi_i\rangle$ of the ground state ($i = 0$) and the second excited state ($i = 2$) are shown for various E_J/E_C . For increasing E_J/E_C , the spreading of the eigenfunctions indicates the increase in the charge fluctuations $\Delta\hat{n}$. For comparison, the solid line denotes the momentum space eigenfunctions $\psi_i(p)$ of a harmonic oscillator with $m = \hbar^2/8E_C$ and $\omega = \sqrt{8E_C E_J}/\hbar$. As expected from the analysis in Sec. 3.2.3, the eigenfunctions converge to discretized versions of the harmonic oscillator.

3.3 Interacting transmons

As discussed in Sec. 1.2, an array of transmons cannot act as a universal quantum computer unless it is equipped with additional hardware to perform arbitrary single-qubit gates and one entangling two-qubit gate.

The predominant approach to implement single-qubit gates is to couple the transmon to a microwave source from which pulses can be applied [245, 265]. Arbitrary Bloch sphere rotations can then be performed by controlling phase and amplitude of the microwave drive. State-of-the-art single-qubit gates employ special pulse-shaping techniques [266] to routinely obtain gate errors below 10^{-3} [5, 6, 267], making single-qubit gates no obstacle to implementing error-correcting codes.

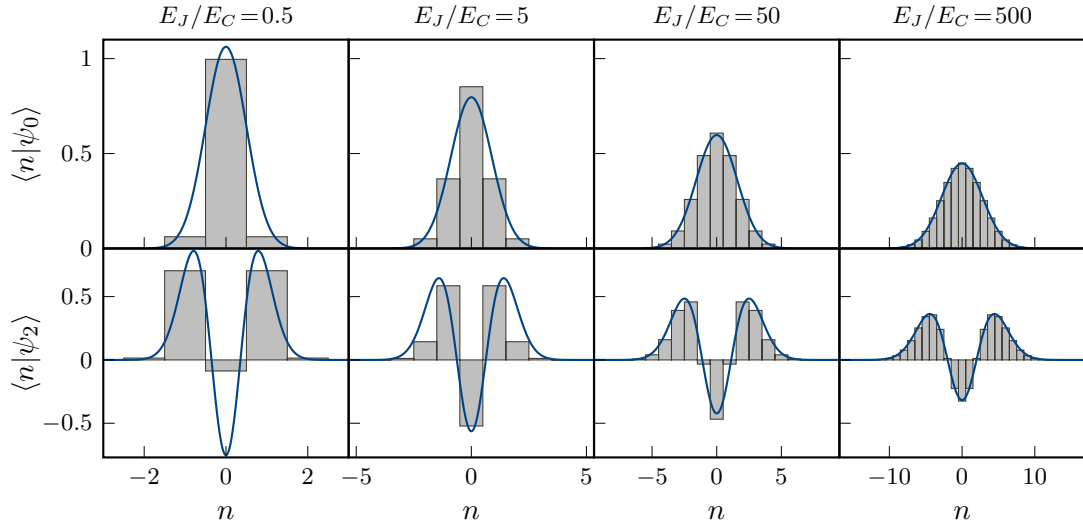


Figure 3.10 – Eigenfunctions in charge representation for different values of E_J/E_C and $n_g = 0$. For increasing E_J/E_C , the width of the eigenfunctions increases, and they converge towards the momentum space eigenfunctions of the harmonic oscillator (blue) with $m = \hbar^2/8E_C$ and $\omega = \sqrt{8E_C E_J}/\hbar$.

Two-qubit gates, on the other side, are far more challenging, with error rates that are usually an order of magnitude higher. The error-proneness of two-qubit gates is the key bottleneck on the road to large-scale quantum computing. Implementing fast and high-fidelity gates is a flourishing area of research. Two mechanisms can cause errors: decoherence and nonideal interactions. The latter, also arising in other platforms [268], describes the phenomenon that a physical gate implementation, like a capacitor connecting two transmon circuits or a microwave drive, generates not only the ideal gate Hamiltonian but also unwanted parasitic interactions. These two error-generating mechanisms are opposed to each other: additional control hardware can suppress unwanted interactions, but the increased architectural complexity often reduces the decoherence time.

A prerequisite for entangling gates between two transmon qubits is some form of physical coupling between the circuits hosting them. Many gates rely on a *capacitive* interaction of the form

$$\hat{H}_{12} = T\hat{n}_1\hat{n}_2 \approx \hbar J\hat{b}_1^\dagger\hat{b}_2 + \text{h.c.} \quad (3.45)$$

between two transmons. In this section, we discuss methods to engineer such a coupling. The primary objects of interest in this work are transmon arrays with an interaction of the form (3.45) between neighboring qubits. In general, Eq. (3.45) alone cannot describe two-qubit gates but is to be understood as a static ‘background’ Hamiltonian that is valid during ‘gate-off’ times and by which gate execution through different mechanisms becomes possible. This is further elucidated in Sec. 3.4.

3.3.1 Capacitive coupling

Depending on whether the physical form of the required interaction is an electric or a magnetic field, one distinguishes between capacitive and inductive coupling. The latter mechanism, where the qubits are coupled via a mutual inductance, is typically used for flux qubits. A simple and widely applied scheme to implement a capacitive coupling between two transmon qubits is to connect the respective circuits via a capacitor with small capacitance C_g , as illustrated

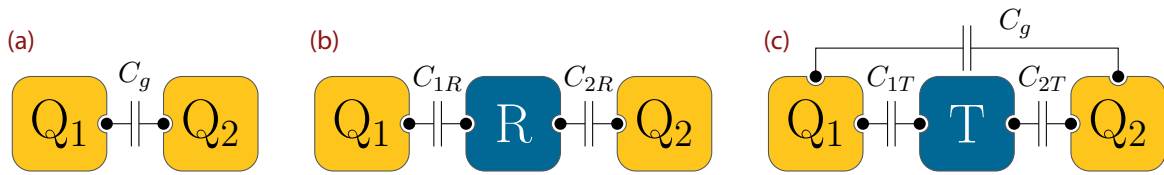


Figure 3.11 – Coupling schemes for transmon qubits. (a) Direct capacitive coupling of two transmon qubit circuits (yellow, Q) by connecting them with a capacitor with capacitance C_g . (b) Indirect capacitive coupling, where both transmons are connected to the same linear resonator (blue, R) via two capacitors C_{1R}, C_{2R} . (c) Tunable coupling scheme as proposed in Ref. [272], where the two transmon qubits are coupled directly and indirectly, with a flux-tunable transmon (blue, T) serving as a coupler. Tuning the frequency of the coupler transmon allows one to tune the effective qubit-qubit interaction strength.

in Fig. 3.11(a). This adds the charging energy of the capacitor to the Lagrangian of the two uncoupled transmons. Following the recipe outlined in Sec. 3.1.3, circuit quantization yields an interaction term of the form

$$\hat{H}_{12} = 4e^2 \frac{C_g}{C_1 C_2} \hat{n}_1 \hat{n}_2 \equiv T \hat{n}_1 \hat{n}_2, \quad (3.46)$$

valid in the limit $C_g \ll C_1, C_2$, where C_i is the capacitance of transmon i [26, 269]. The coupling energy depends on the coupling capacitance C_g and on the matrix elements of the charge operators [26, 231]. Using Eq. (3.32) and invoking the rotating-wave approximation, one obtains

$$\hat{H}_{12} \approx \frac{T}{4\sqrt{2}} \sqrt[4]{\frac{E_{J,1} E_{J,2}}{E_{C,1} E_{C,2}}} \left(\hat{b}_1 \hat{b}_2^\dagger + \hat{b}_2 \hat{b}_1^\dagger \right) \equiv \hbar J \left(\hat{b}_1 \hat{b}_2^\dagger + \hat{b}_2 \hat{b}_1^\dagger \right) \quad (3.47)$$

for the effective low-energy coupling Hamiltonian.

An alternative approach to this direct coupling is to mediate the qubit-qubit interaction through a resonator that is capacitively coupled to both transmons, as depicted in Fig. 3.11(b). Superconducting resonators can be made much larger than any transmon, and the resonator-mediated coupling can implement an effective interaction between physically well-separated (~ 1 cm) qubits [238, 270, 271]. In the dispersive regime, where both qubits are strongly detuned from the resonator, the combined transmon-resonator system reduces—after a series of transformations, approximations, and assuming that the resonator is initialized in its vacuum state—to the form of Eq. (3.47) [223].

3.3.2 Tunable couplers

Whether the coupling is direct or mediated, the above scheme yields an ‘always-on’ interaction T or J between two transmons. In order to improve two-qubit gate fidelity, it is desirable to make the coupling itself controllable, such that it can be switched on only during gate operations between the involved qubits. This can be accomplished with tunable couplers, i.e., additional hardware that mediates the qubit-qubit interaction and is controllable via some external parameter. Different blueprints of tunable couplers have been demonstrated, see Refs. [273, 274] for two early examples. However, all the attempts face the generic and complex challenge of increasing hardware complexity without downgrading the device quality by introducing additional decay channels or crosstalk [275].

A notable example is the ‘gmon’ device [276] (two modified ‘xmons’, one coupler), which suppresses parasitic couplings to the extent that decoherence is the limiting factor for the gate

fidelity, but at the sacrifice of a reduced coherence time compared to the bare ‘xmon’. Promising experimental results [39] have been obtained with an approach proposed by Yan *et al.* [272]. The pivotal idea is to countervail a direct qubit-qubit interaction by a virtual interaction that is mediated by a coupler and whose strength can be tuned by the coupler’s frequency. This scheme is broadly applicable and not restricted to superconducting qubits. It is often implemented for three mutually coupled tunable transmons, where two serve as qubits and one as the coupler. This layout is sketched in Fig. 3.11(c). To grasp the central idea, instead of considering the full model, it is sufficient to restrict to the generic two-level Hamiltonian

$$\frac{\hat{H}}{\hbar} = \sum_{j=1,2} \frac{\omega_j}{2} \hat{\sigma}_j^z + \frac{\omega_c}{2} \hat{\sigma}_c + \sum_{j=1,2} J_j (\hat{\sigma}_j^+ \hat{\sigma}_c^- + \hat{\sigma}_j^- \hat{\sigma}_c^+) + J_{12} (\hat{\sigma}_1^+ \hat{\sigma}_2^- + \hat{\sigma}_2^- \hat{\sigma}_1^+) , \quad (3.48)$$

describing two qubits, $\hat{\sigma}_j^z, j = 1, 2$, and a coupler $\hat{\sigma}_c^z$ with small direct qubit-qubit coupling J_{12} and qubit-coupler couplings J_1, J_2 . The qubits are negatively detuned from the coupler, i.e., $\Delta_j = \omega_j - \omega_c < 0$. For $J_j \ll |\Delta_j|$, the coupler can be decoupled from the qubit-qubit system to the desired order in J_j/Δ_j using a Schrieffer-Wolf transformation [252, 277]. To second order, one obtains

$$\frac{\hat{H}}{\hbar} = \sum_{j=1,2} \frac{\tilde{\omega}_j}{2} \hat{\sigma}_j^z + \left(\frac{J_1 J_2}{\Delta} + J_{12} \right) (\hat{\sigma}_1^+ \hat{\sigma}_2^- + \hat{\sigma}_2^- \hat{\sigma}_1^+) , \quad (3.49)$$

where $1/\Delta = (1/\Delta_1 + 1/\Delta_2)/2 < 0$ and $\tilde{\omega}_j = \omega + J_j^2/\Delta_j$ are the renormalized qubit frequencies. In the effective qubit-qubit coupling $J_{\text{eff}}(\omega_c) = J_1 J_2 / \Delta + J_{12}$, the first indirect contribution is negative and depends on the coupler frequency (directly through Δ but possibly also implicitly through J_1 and J_2). J_{eff} can be tuned negative (positive) by increasing (decreasing) the coupler frequency ω_c , and, as long as the tuning range of the coupler is large enough, the existence of a critical ω_c^{off} with $J_{\text{eff}}(\omega_c^{\text{off}}) = 0$ is guaranteed. A thorough analysis of the multilevel system, where the qubits and the coupler are tunable transmons, can be found in the original publication [272]. The result is again a capacitive interaction of the form (3.47). As for the two-level model, the coupling $J(\omega_c)$ can be tuned to zero by adjusting the coupler’s frequency.

Fast high-fidelity gates have also been demonstrated in variations of the above coupling schemes, e.g., with fixed-frequency qubits [278] or by implementing a tunable $\hat{\sigma}_1^z \hat{\sigma}_2^z$ interaction [279]. Recently, Ref. [280] introduced a coupling mechanism where ramping up a control parameter suppresses the residual coupling strength exponentially fast, which removes the sensitive dependence on a fine-tuned control parameter.

3.4 Entangling gates

For two qubits and in the low-energy limit, our central object of interest—a transmon quantum computer in the absence of gates but with capacitively coupled qubits—is described by the Hamiltonian

$$\hat{H}_{2T} = \sum_{i=1}^2 \left(\hbar \omega_{q,i} \hat{b}_i^\dagger \hat{b}_i - \frac{E_C}{2} \hat{b}_i^\dagger \hat{b}_i^\dagger \hat{b}_i \hat{b}_i \right) + \hbar J (\hat{b}_1^\dagger \hat{b}_2 + \hat{b}_1 \hat{b}_2^\dagger) , \quad (3.50)$$

see Eq. (3.33) and Eq. (3.47), where $E_{C,1} = E_{C,2} \equiv E_C$ was assumed. A two-qubit gate enters this Hamiltonian as (i) a periodic modulation of one of the system parameters (*parametric gates*), see, e.g., Ref. [281], (ii) an additional microwave drive term (*all-microwave gates*), or (iii) as a

modulation in E_J and hence ω_q in flux-tunable transmons. Even though we do not aim to study the dynamics of two-qubit gates, we review different methods to extend Eq. (3.50) to a gate Hamiltonian because this discussion and the subsequent in-depth coverage of different transmon array design schemes naturally introduce distinct ranges of system parameters, to each of which we devote separate numerical simulations. We focus on the predominantly used approaches (ii) and (iii).

3.4.1 Gates in flux-tunable transmon architectures

A conceptually simple realization of a two-qubit gate with flux-tunable transmons is to switch on an interaction for a desired time t by tuning them in resonance, $\omega_1 = \omega_2 \equiv \omega$, as shown in Fig. 3.12(a). In a frame⁴ rotating with ω , the two-level version \hat{H}_{2Q} of Eq. (3.50) takes the form

$$\hat{H}_{2Q} = \hbar J (\hat{\sigma}_1^+ \hat{\sigma}_2^- + \hat{\sigma}_1^- \hat{\sigma}_2^+) . \quad (3.51)$$

Time evolution under this Hamiltonian for a time $\pi/2J$ ($\pi/4J$) generates the *iSWAP* ($\sqrt{i\text{SWAP}}$) [282] gate, both of which can be used to generate entanglement. To switch off the interaction, the qubits are detuned from each other [283]. One can show that the residual, unwanted interaction is of the form $J^2/\Delta_{12}\hat{\sigma}_1^z\hat{\sigma}_2^z$, where $\Delta_{12} = \omega_1 - \omega_2$ is the detuning [223], see Fig. 3.12(b). Fast gates with strongly suppressed interactions in the ‘gate off’ state are obtained for large ratios of ‘gate on’ J and ‘gate off’ J^2/Δ_{12} . For fixed (i.e., non-tunable) J , this on-off ratio is Δ_{12}/J and can be made large for large detunings. Flux-tunable transmons can also exploit degeneracies between higher energy levels, e.g., between the states $|11\rangle$ and $|02\rangle$, to implement a CPHASE gate [284]. Regardless of which resonance one uses, the gates work irrespective of the concrete origin of the coupling in Eq. (3.50), whether it is direct or mediated by a resonator or a tunable coupler.

3.4.2 Gates in fixed-frequency architectures: the CR gate

A disadvantage of the gate scheme reviewed above is that it necessarily requires flux-tunable transmons and possibly also tunable couplers. As discussed, this might introduce new noise channels, ultimately reducing the decoherence time. A complementary approach is to dispense with additional parameter control and instead implement two-qubit gates in fixed-frequency architectures using only the hardware required for single-qubit gates. An example is the cross-resonance (CR) gate, originally proposed in 2006 [285] and independently rediscovered four years later [286], that exploits an interaction generated by driving one ‘control’ qubit (C) at the frequency of a second ‘target’ qubit (T), see Fig. 3.12(c). The qubits are detuned with $\Delta_{CT} = \omega_C - \omega_T$ and capacitively coupled, either direct or resonator-mediated. Due to the coupling, the actual qubits are nonlocal objects, spreading over both transmons. A genuinely local microwave drive hence induces a qubit-qubit interaction that can be exploited to create entanglement.

More concretely, we start with the two-level version of Eq. (3.50),

$$\hat{H}_{2Q} = \frac{\hbar\omega_C}{2}\hat{\sigma}_C^z + \frac{\hbar\omega_T}{2}\hat{\sigma}_T^z + \hbar J (\hat{\sigma}_C^+ \hat{\sigma}_T^- + \hat{\sigma}_C^- \hat{\sigma}_T^+) . \quad (3.52)$$

⁴The transformation into the rotating frame has the form $\hat{H} \rightarrow \hat{U}^\dagger \hat{H} \hat{U} - i\hbar \hat{U}^\dagger \frac{\partial \hat{U}}{\partial t}$, where $\hat{U}(t) = \exp(-i\frac{\hbar\omega}{2}t[\hat{\sigma}_1^z + \hat{\sigma}_2^z])$ and $\hat{H} = \frac{\hbar\omega}{2}(\hat{\sigma}_1^z + \hat{\sigma}_2^z) + \hbar J (\hat{\sigma}_1^+ \hat{\sigma}_2^- + \hat{\sigma}_1^- \hat{\sigma}_2^+)$.

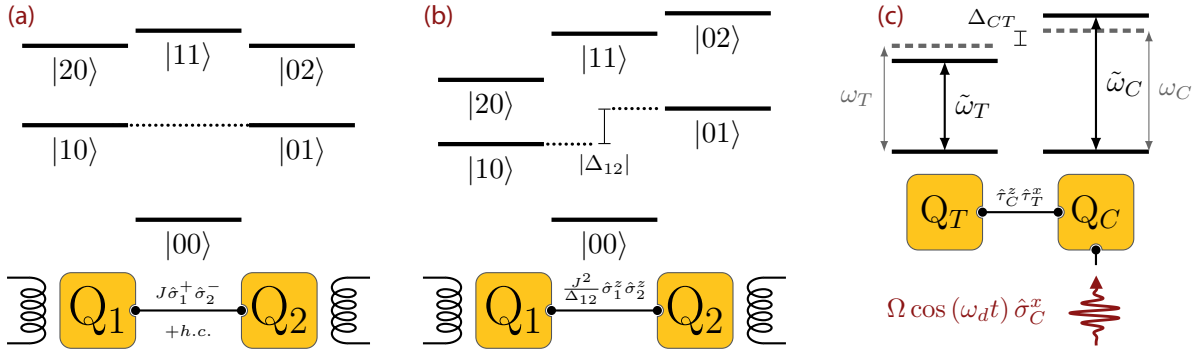


Figure 3.12 – Two-qubit gate implementations for transmons. (a) and (b): In tunable-frequency architectures (symbolized by the inductors), two-qubit gates can be implemented by employing degeneracies in the spectrum, e.g., by tuning the two qubits into resonance, as shown in (a), which activates a qubit-qubit interaction of the form $\hat{\sigma}_1^+ \hat{\sigma}_2^- + \text{h.c.}$. To switch off the gate, the qubits are parked at distinct frequencies with distance Δ_{12} , as shown in (b). The remaining parasitic interaction is of the form $\hat{\sigma}_1^z \hat{\sigma}_2^z$. (c) A capacitive coupling between two detuned qubits renormalizes the frequencies $\omega_T, \omega_C \rightarrow \tilde{\omega}_T, \tilde{\omega}_C$, but the system can still be considered as describing noninteracting but also nonlocal qubits. A microwave drive on the control qubit $\hat{\sigma}_C$ induces an interaction $\hat{\tau}_C^z \hat{\tau}_T^x$ between the dressed qubits.

The diagonalized Hamiltonian can be rewritten as [287, 288]

$$\hat{H}_{2Q} = \frac{\hbar \tilde{\omega}_C}{2} \hat{\tau}_C^z + \frac{\hbar \tilde{\omega}_T}{2} \hat{\tau}_T^z, \quad (3.53)$$

where $\hat{\tau}_C^z$ and $\hat{\tau}_T^z$ are again Pauli matrices describing two-level systems. The Hamiltonian does not contain an interaction term of the form $\hat{\tau}_C^z \hat{\tau}_T^z$, which implies that Eq. (3.53) still describes a set of noninteracting qubits with renormalized frequencies given by $\tilde{\omega}_{C/T} = \omega_C \pm J^2/\Delta_{CT}$ to second order in J/Δ_{CT} . Due to the coupling, the new underlying degrees of freedom $\hat{\tau}_T, \hat{\tau}_C$ are not perfectly localized on a specific transmon but dressed with small contributions from the neighboring qubit. In MBL terminology, the $\hat{\sigma}^z(\hat{\tau}^z)$ are the p -bits (l -bits). Now, a local microwave drive $\hat{H}_{\text{drive}} = \hbar \Omega(t) \cos(\omega_d t) \hat{\sigma}_C^x$ [223, 252] on the control qubit C expressed in the eigenbasis of the coupled system reads

$$\hat{H}_{\text{drive}} \approx \hbar \Omega(t) \cos(\omega_d t) \left(\hat{\tau}_C^x + \frac{J}{\Delta_{CT}} \hat{\tau}_C^z \hat{\tau}_T^x \right). \quad (3.54)$$

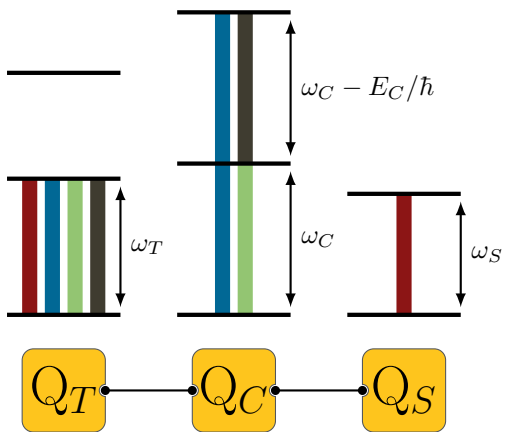
For a suitably chosen drive frequency, $\omega_d \approx \tilde{\omega}_T$, driving the control (p -)qubit generates an interaction of the form $\hat{\tau}_C^z \hat{\tau}_T^x$ (ZX) between nonlocal l -qubits⁵. Time evolution under $\hat{\tau}_C^z \hat{\tau}_T^x$ for a time $t = \frac{\pi \Omega J}{4 \Delta_{CT}}$ produces a unitary transformation that is locally equivalent [286, 289] to a CNOT gate, i.e., only single-qubit gates are required to complete the CNOT gate.

The simplified view above neglected the higher transmon levels. A better starting point is Eq. (3.50), extended by a drive term. Deriving an effective Hamiltonian for the qubit subspace of this multilevel system is a reasonably sophisticated task and was done only recently, e.g., using time-dependent Schrieffer-Wolf perturbation theory [290], generalizations thereof [291], or semi-analytical approaches [292], partly supported by experiments with tunable transmons allowing a systematic investigation of the influence of Δ_{CT} [293]. Regardless of the method, one finds that due to the influence of the higher levels, (i) the strength of the ZX interaction is renormalized

⁵From here on we adapt the notation to our purposes and refer to l -qubits instead of l -bits.

Figure 3.13 –

Examples of frequency collisions in a minimal setup consisting of one control qubit Q_C , one target qubit Q_T , and one spectator qubit Q_S . Unintended degeneracies between energies drawn in the same color must be avoided because they significantly reduce the gate fidelity. More concretely, for $\omega_C \approx \omega_T$ (green), Q_C and Q_T hybridize, for $\omega_T = \omega_C - E_C/\hbar$ (gray) or $2\omega_T \approx 2\omega_C - E_C/\hbar$ (blue), Q_C is excited into the noncomputational state $|2\rangle$, and for $\omega_T \approx \omega_S$ (red) the CR pulse falsely addresses the spectator qubit. Therefore, the CR gate imposes several restrictions on the frequencies of NN qubits and NNN qubits that share a control qubit.



and (ii) parasitic terms, e.g., a $\hat{\tau}_C^z \hat{\tau}_T^z$ interaction⁶, emerge. Concretely, the amplitude of the ZX interaction acquires a factor $E_C/\hbar \Delta_{CT}$ [291], which implies that a detuning large compared to E_C slows down the gate. Further constraints on Δ_{CT} arise upon closer examination of the parasitic terms. They become large if degeneracies between transition frequencies of nearest-neighbor (NN) and next-nearest-neighbor (NNN) qubits occur. One refers to these degeneracies as frequency collisions. Based on the effective model in Ref. [291], the seven most serious collisions have been identified in Ref. [294]. Some examples and their qualitative explanation are provided in Fig. 3.13. The difficulty of populating a transmon lattice without violating these restrictions is known as the frequency crowding problem, and it is a severe hindrance to deploying high-fidelity gates on larger transmon arrays, especially in two dimensions. Steps toward a solution to this issue are discussed in Sec. 3.5.1.

3.5 Transmon processor design schemes

One can assign most medium-scale transmon-based quantum computers to one of three categories: (i) fixed-frequency transmons with fixed ‘always-on’ coupling T and microwave-driven two-qubit gates, (ii) flux-tunable transmons with likewise fixed ‘always-on’ T , but an effective qubit-qubit interaction that is tunable via the qubit frequencies and (iii) flux-tunable transmons where T is tunable through a coupler. As alluded to in the previous discussion and shown schematically in Fig. 3.14, one has to choose a modus vivendi between tunability of system parameters and sensitivity to fluctuations in control parameters, which are an inescapable by-product of more complex circuit architectures. The three design schemes correspond to different choices in weighing these factors. In this section, we highlight some milestones that have been achieved with the different strategies and discuss the special system parameters inherent to the distinct approaches, particularly the site-to-site variations of the frequencies in larger transmon arrays. This discussion guides the choices for the various disorder and coupling parameters in our simulations.

In this section, we adhere to the established convention of considering ν_q instead of ω_q when discussing parameters of real transmon devices. Furthermore, we omit the index q , as we already did in the discussion of the two-level systems in the previous section.

⁶Note that we discussed this interaction in the context of the MBL τ -Hamiltonian in Chapter 2. It is detrimental to the gate fidelity, as it makes the qubit precession frequency dependent on the state of the other qubit, such that one cannot choose a drive frequency ω_d without knowing the state of the control qubit.

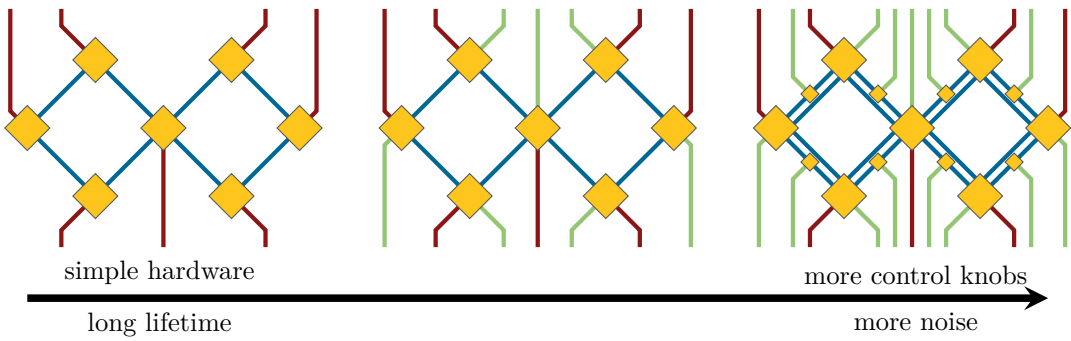


Figure 3.14 – Trade-off between tunability and sensitivity to noise in three major transmon design schemes. The cartoons show a surface-7 quantum computer [295] consisting of seven transmons (yellow) that are capacitively coupled (blue). The control lines to apply microwave pulses for single-qubit gates are shown in red. In addition, we show the hardware that is required for two-qubit gates. In the simplest case (fixed-frequency transmons with the CR gate), no additional hardware is needed. For flux-tunable transmons, additional flux lines (green) allow for the control of E_J and hence the frequency. Adding tunable couplers further complicates the hardware setup and makes the system more prone to noise but allows the coupling strength T to be adjusted during an experiment.

3.5.1 Fixed-frequency architectures

Fixed-frequency transmons offer several advantages: they are easy to build, exhibit long coherence times of a few hundred microseconds, and the CR gate minimizes the amount of control wiring, which is especially beneficial when scaling up to larger transmon arrays. Most prominently, IBM follows this approach in the processors that are publicly available via cloud access [59]. Since the first five-qubit processor was launched in 2016, several chip generations have been in operation. IBM’s timeline on the road to a large-scale quantum computer promises annual launches of ever-larger quantum processors (flanked by improvements in many other areas, e.g., cooling systems) [296]. As of today, various chip types are in operation, e.g., devices of the ‘Falcon’ (released in 2019, 27 qubits), ‘Hummingbird’ (2020, 65 qubits), and ‘Eagle’ families (2021, 127 qubits). The first member of the ‘Osprey’ line (433 qubits) was presented in late fall 2022. For 2025, the 4,158-qubit ‘Kookaburra’ processor, capable of error suppression and mitigation, is expected according to IBM’s roadmap [297].

Since its first demonstration [288], the CR gate has improved significantly, driven by a better theoretical understanding of the gate [290–292] that motivated experimental modifications like the introduction of additional drive pulses to counteract parasitic terms appearing in the Hamiltonian [5, 36, 298]. Fidelities of 99.1% are nowadays possible, with gate times pushed down to 160 ns [5]. Small-scale fixed-frequency devices of only a few qubits have been used in a couple of proof-of-principle experiments, for example, to demonstrate a quantum error detection code in a four-qubit square lattice [8] or parity measurements on a five-qubit lattice [299]. Recently, a discrete time crystal was realized in a 57-qubit chain on two ‘Hummingbird’ processors [91].

Natural disorder and frequency collisions. Despite IBM’s ambitious goals and the promising results already achieved, medium-scale fixed-frequency processors suffer from some serious teething problems. Typical CR gate times of approximately 300 ns are longer than what can be achieved with tunable circuit elements: to minimize adverse effects beyond the ones obtained in the effective Hamiltonian [291], neither the drive amplitude Ω nor the interaction strengths T or J can be made large (recall that $t_{\text{Gate}} \propto \Omega J$). Suggestions on how specially shaped control pulses could provide a significant speed-up exist [300] but have never been tested experimentally. The

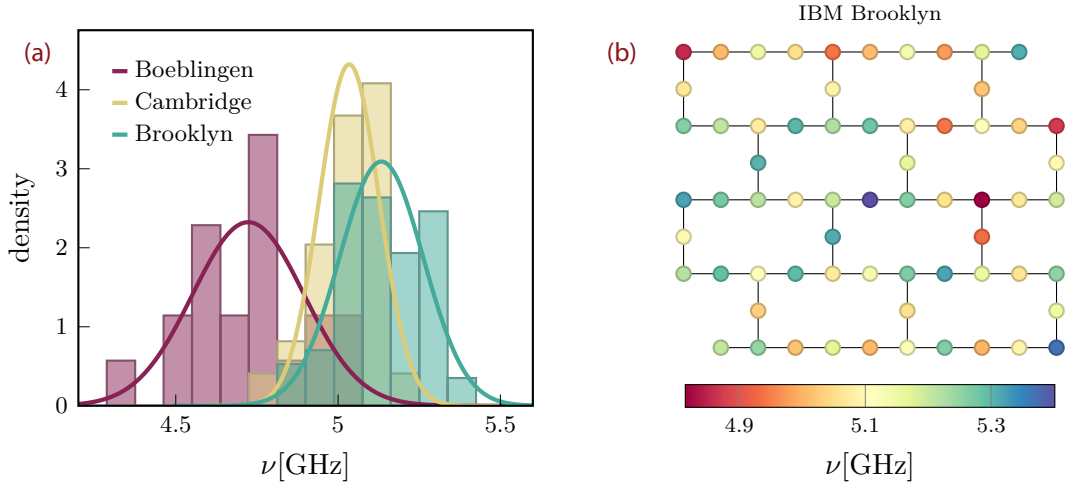


Figure 3.15 – Frequency distributions of IBM devices. (a) Frequency histograms for two IBM chips that are subject to natural disorder and one LASIQ-tuned chip ('Brooklyn'), see main text for details. In all cases, the distributions are compatible with Gaussian disorder of similar strength (~ 100 MHz). (b) Distribution of frequencies in the 'Brooklyn' processor, belonging to the 65-qubit 'Hummingbird' family. There are no clearly recognizable spatial correlations between frequencies of adjacent lattice points.

fastest CR gate implementation used an effective qubit-qubit coupling of $J/2\pi \approx 3.8$ MHz [5].

Also high on the list of major issues is that it becomes increasingly challenging to avoid frequency collisions in larger transmon arrays, i.e., to meet the stringent restrictions imposed by the CR gate on nearest-neighbor and next-nearest-neighbor frequencies. It is impossible to accurately and reproducibly fabricate transmons with a desired Josephson energy E_J , and random fluctuations in E_J are on the order of 5% to 10% [59, 301, 302] (the charging energy E_C on the other side is easily fixed at a desired value). This results in a *natural* frequency spread of the same order of magnitude as the desired detuning. As an example, we show the frequency distributions of two 'older' IBM processors, 'Boeblingen' (20 qubits) and 'Cambridge' (28 qubits) [303] in Fig. 3.15(a). The recent 'Brooklyn' chip is discussed below. Both distributions are consistent with simple Gaussian disorder. We refer to the width $\sigma \equiv \delta\nu$ of the Gaussians as disorder strength. Here, we find values of 70 MHz to 150 MHz, corresponding to typical relative frequency spreads $\delta\nu/\nu$ of 1.5% to 3% (currently, the best achievable precision at fabrication is 1% [304]). Arrays of transmons whose frequencies are subject to this natural disorder are almost certainly not collision-free⁷. Consider, e.g., the 17-qubit geometry shown in Fig. 3.16(d). When populated with frequencies drawn from a normal distribution with conventional disorder strength $\sigma_\nu \approx 130$ MHz, the 'zero-collision yield', i.e., the probability for a collision-free lattice, is considerably lower than 0.1% [294]. On average, more than a third of the two-qubit gates would fail, making the frequency crowding problem a serious impediment to the progress toward a large-scale quantum computer. Less surprisingly, IBM's early 20-qubit processors were judged to be orders of magnitude too weak to tackle critical problems from condensed matter physics [305].

Avoiding frequency collisions. The strategy to solve the frequency crowding problem consists of two steps: arranging the qubits on the best-suited lattice and implementing frequency patterns.

Since the number of constraints increases with the connectivity of the qubits, it is reasonable

⁷By 'collision-free', we mean that all nearest- and next-nearest-neighbor frequency detunings are outside the boundaries estimated for the seven most likely types of frequency collisions in Ref. [294].

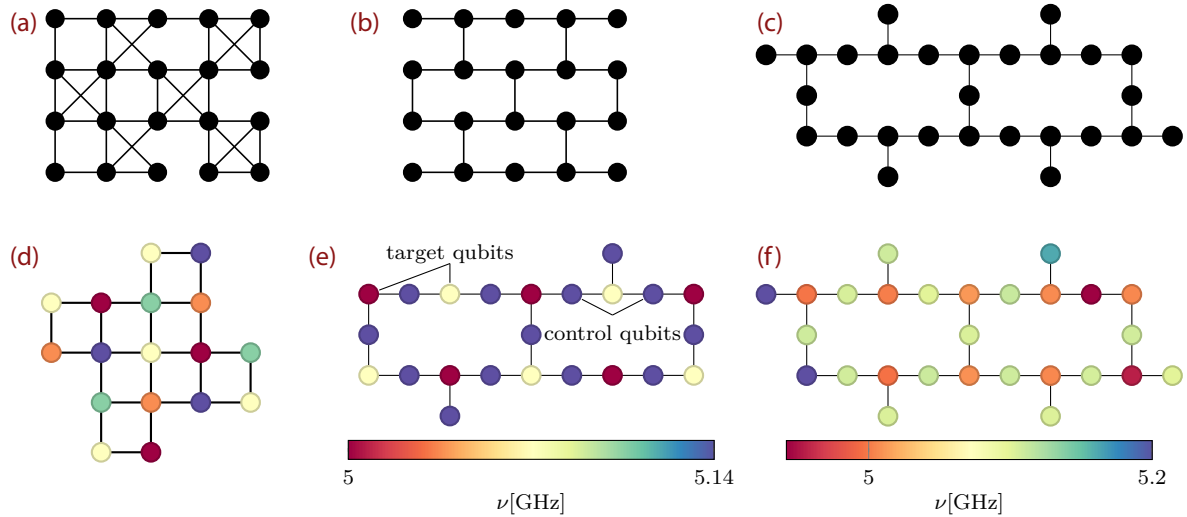


Figure 3.16 – Solving the frequency crowding problem. (a)–(c): Examples of transmon array geometries in IBM processors [307]. Over the years, IBM has moved from (a) a square lattice variant ('Penguin v2' processor, 2018) via (b) the hexagonal lattice ('Penguin v4', 2018) to (c) the more beneficial heavy-hexagon geometry (since 2020). (d) The surface-17 geometry with a 5-frequency pattern avoids all collisions for perfect frequency precision. With current LASIQ precision, the zero-collision yield is 6%. (e) 23-qubit excerpt of the heavy-hexagon lattice with a collision-free three-frequency pattern. With current precision, the zero-collision yield is 70% [294]. (e) Experimental realization of an approximate ABAB pattern that avoids all NN frequency collisions [308].

to place the qubits on lattice geometries with a small average number of neighbors. As shown in Fig. 3.16(a)–(c), IBM's chip layout has moved in this very direction over several processor iterations by switching from (a) a square lattice variant via (b) the hexagonal lattice to (c) the heavy-hexagon lattice [294, 306], which is adopted for all currently available and announced cloud processors [297]. This lattice consists of qubits sitting at the vertices of a regular hexagon lattice, with an additional qubit on each edge. However, changing the lattice topology alone does not bring fundamental improvement: for the minimal 23-qubit layout shown in Fig. 3.16(e), the zero-collision yield is only 0.1% when populated with frequencies with typical as-fabricated precision. The geometry only reveals its superiority when combined with a regular frequency pattern. Three distinct frequencies, distributed as shown in Fig. 3.16(e), suffice to eliminate all collisions for heavy-hexagon. The qubits on the edges, serving as the control qubits, are all assigned the same frequency ν_C . The target qubits on the A and B hexagon sublattices have the frequencies ν_A and ν_B , respectively. Until recently, such a pattern was not feasible because of the natural disorder. However, a newly introduced laser-annealing technique (LASIQ) [294] allows one to modify the Josephson energies E_J post-fabrication, opening up the door to cloning qubits with previously unattainable precision. LASIQ can decrease the fluctuations $\delta\nu$ around desired target frequencies by an order of magnitude compared to the as-fabricated spread [294]. A pattern as in Fig. 3.16(e), with frequencies drawn from normal distributions centered around the mean values ν_A , ν_B , ν_C and where the current LASIQ precision determines the width of each Gaussians, yields a collision-free chip with a probability of 70%. On the other side, the square lattice in Fig. 3.16(d) (needing five distinct frequencies) has a zero-collision yield of only 6%. The heavy-hexagon lattice can effectively evade collisions and, together with the pattern engineering approach, might form the basis of future collision-free processors.

However, as of today, no pattern-engineered device has occurred in the IBM cloud. Instead,

LASIQ is used to diminish the number of NN frequency collisions (types 1–3 according to Ref. [294]). Starting from an as-fabricated ν distribution, the frequencies are modified (under constraints dictated by experimental details) to obtain an NN-collision-free chip, but not to create regular frequency patterns. The resulting ‘disorder engineered’ distributions do not seem to show any spatial correlations, as depicted in Fig. 3.15(b) for the LASIQ-tuned ‘Brooklyn’ device. Although each frequency was specifically tuned to a certain value with high accuracy, the overall spread is consistent with a single Gaussian distribution, see Fig. 3.15(a). An exception is the tuned *AB* ‘Falcon’ chip reported in Ref. [308] and shown in Fig. 3.16(f), which realizes an approximate *ABAB* pattern on parts of the lattice.

The (anti-)correlations that nevertheless exist between NN qubits in LASIQ-tuned chips can be resolved by looking at the distribution of $\Delta_{CT} = \nu_C - \nu_T$, where ν_C (ν_T) is the control (NN target) frequency. Fig. 3.17 summarizes the qualitative difference in Δ_{CT} for (i) arrays of untuned qubits, (ii) ‘disorder engineered’ chips (nine ‘Falcon’ and two ‘Hummingbird’ devices from the IBM cloud [59]), (iii) the pattern-engineered *AB* ‘Falcon’, and (iv) the (not yet realized) optimal three frequency pattern (*ACBC*) on a ‘Falcon’ chip. For (i) and (iii), data are taken from Ref. [308]. The grayed areas mark the Δ_{CT} ranges to be avoided [294]. Panel (a) compares the Δ_{CT} distribution for all four cases. Only (iii) and (iv) exhibit clear peaks, mirroring the regular frequency pattern structure. There is no dominating Δ_{CT} contribution for arrays of untuned transmons, but just as little for the IBM cloud devices. In (c), we show an enlarged view of the Δ_{CT} distribution for (i) and (ii). In the untuned arrays, all collisions appear. On the IBM cloud processors, the number of collisions is significantly reduced. As a specific example, (f) displays data for the 65-qubit ‘Manhattan’ chip with clear LASIQ indications. The right column shows the ν distributions centered around the respective mean values. For (iii) and (iv), the regular pattern reappears in clear peaks, as demonstrated in (b). On the other side, despite the differences in Δ_{CT} , (i) and (ii) are both consistent with Gaussian disorder. Furthermore, the disorder strength is very similar in the cloud devices and the untuned transmons, see also Fig. 3.15(a).

To summarize, the bottom line of this analysis is that the frequency distributions for both untuned chips with natural disorder and current LASIQ-tuned cloud processors are compatible with regular Gaussian disorder with $\delta\nu \approx 100$ MHz for typical frequencies of around 5 GHz.

We conclude this section with two remarks: First, one should note that reducing the connectivity does not come for free [106]. In fact, the quantum volume metric, a holistic cross-platform measure for the performance of a quantum computer [309, 310], explicitly favors higher connectivities, e.g., a square lattice over the heavy-hexagon layout. Yet, when combined with LASIQ, the benefit of an order of magnitude higher zero-collision yield outweighs the price one pays. For example, the record value for quantum volume (for superconducting qubits) has been pushed up several times with heavy-hexagon chips [311]. Second, the LASIQ precision currently achievable is not sufficient as the qubit number increases. The zero-collision yield for an ‘Eagle’ processor is only 8% and building a collision-free chip with over 1,000 qubits, which IBM aims to do in 2023, is beyond reach without significant improvements in LASIQ precision [294]. For this reason, new alternative transmon design schemes, precisely tailored to the requirements of the CR gate, are also tested, e.g., weakly tunable transmons with a tuning range small enough to prevent losses in coherence time but large enough to avoid frequency collisions [312]. Alternatively, a newly developed gate [313, 314] for fixed-frequency architectures with similar frequency collision bounds but an additional degree of freedom on the drive frequency allows for an improved zero-collision yield [315].

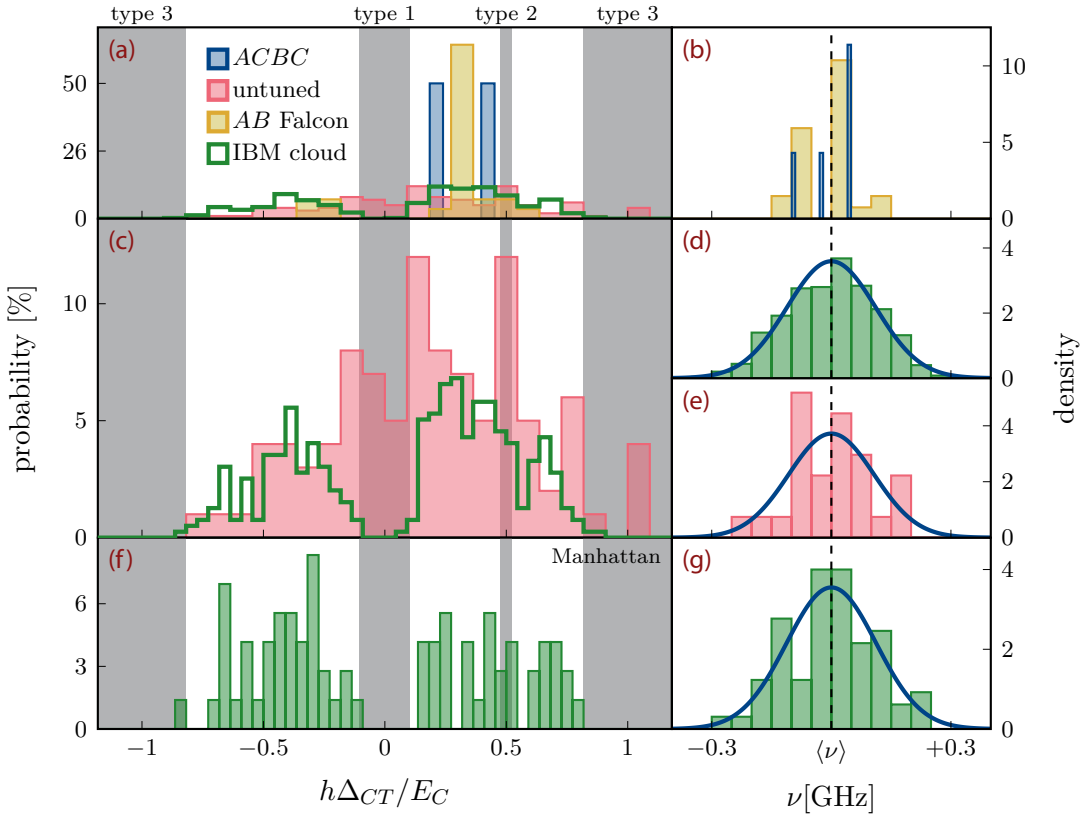


Figure 3.17 – LASIQ engineering. The left column shows the distribution of NN frequency differences. The right column shows the distribution of frequencies. Grayed areas mark the ranges where NN frequency collisions occur ($h\Delta_{CT}/E_C = 0, 1/2, \pm 1$). Their width is based on the estimates in Ref. [294]. In (a), the Δ_{CT} distribution of pattern-tuned processors, the *AB ‘Falcon’* from Ref. [308] (yellow), and the optimal *ACBC* pattern (blue) are compared to IBM cloud devices (green, average over nine ‘Falcons’ and two ‘Hummingbirds’) and an untuned chip (red). Only the pattern-tuned configurations feature clear peaks. The enlarged view in (c) shows that the cloud devices have significantly fewer collisions than the untuned transmons due to LASIQ adjustments. However, in both cases, the overall frequency spread is consistent with Gaussian disorder, as shown in (d) (IBM cloud) and (e) (untuned). This has to be contrasted with the sharp peaks found for the pattern-tuned chips in (b). (f) and (g) present results for one specific IBM processor, the 65-qubit ‘Manhattan’ chip. Each individual frequency is achieved with high precision via LASIQ to avoid NN collisions, see (f), but the overall ‘disorder-engineered’ distribution in (g) is well described by a single Gaussian. This holds true for all individual cloud devices, including the newest ‘Eagle’ processor, see Appendix A.1. The bin width is 50 MHz for the right column, 1/22 for the cloud devices in (c) and (f) and 1/11 otherwise.

3.5.2 Tunable transmon architectures

The two conflicting demands of strong coupling for fast gates and low residual coupling during ‘off’ times are challenging to achieve in a fixed-frequency architecture. Tunable transmons offer more flexibility. As discussed in Sec. 3.4.1, minimizing parasitic interactions during ‘off’ times requires either a small ‘off’ coupling J or a large detuning Δ_{12} . Without tunable couplers, only the latter is possible. This approach has been widely employed, e.g., in experiments conducted at MIT [316], TU Delft [94], ETH Zürich [95], or Google [6]. Notable examples include the implementation of fast two-qubit gates (40 ns) with a fidelity of 99.4% [6], undershooting the error threshold for the surface code, state stabilization [7, 317], the realization of quantum error detection in a surface-7 geometry [94, 108] and the demonstration of quantum error correction using a surface-17 geometry [95]. Recently, two-qubit gate fidelities of 99.7% and better [316,

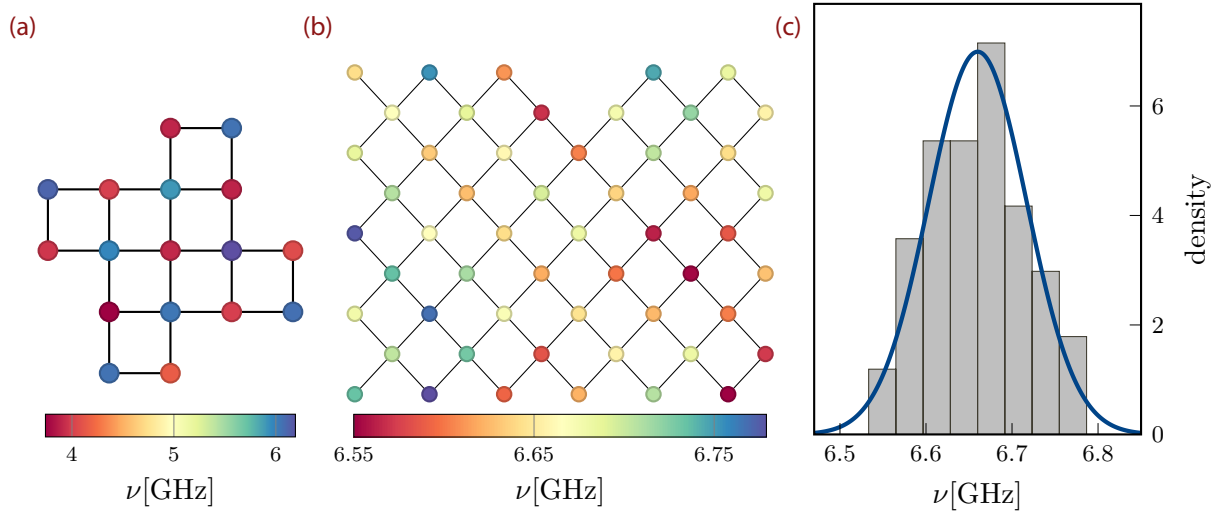


Figure 3.18 – Frequency distributions in arrays of flux-tunable transmons. (a) Surface-17 device from Ref. [95], with an *ABAB* pattern and large detuning ~ 2 GHz between NN qubits. (b) Layout of the 53-qubit transmon array ‘Sycamore’. As the coloring of the qubits indicates, the frequency variation is uncorrelated in space. (c) Frequency distribution for ‘Sycamore’, consistent with Gaussian disorder with $\delta\nu \sim 60$ MHz.

318, 319] have been reported, which almost closes the gap to the fidelity of single-qubit gates.

Many of these experiments have in common that they enable fast gates (~ 50 ns) through comparatively large T values, often exceeding 10 MHz, e.g., 30 MHz in Ref. [6], which is cushioned in ‘off’ times by a massive detuning $\Delta_{12} > 1$ GHz. Some experiments arrange the qubits in regular patterns, see Fig. 3.18(a) for an example. While the gates are much faster than the CR gate, typical qubit lifetimes of around 10 μ s to 40 μ s are somewhat shorter than in fixed-frequency designs.

3.5.3 Tunable transmons with tunable couplers

Using a fixed always-on coupling T requires tuning the qubit frequencies over an extensive range to turn the gate on and off, which makes the system susceptible to flux noise. The complementary approach is to use tunable couplers to switch off the gate by turning off J or T (in a perturbative sense). This allows one to park the qubits at much smaller frequency detunings, albeit adding additional circuitry. One example is Google’s previously mentioned ‘gmon’ device that enables an on-off ratio of 1,000 with a coupling strength of $J/2\pi = 100$ MHz in the ‘on’ state and a gate duration of only 5 ns [276]. For the ‘Sycamore’ processor from the illustrious quantum advantage[39] and a series of follow-up experiments [89, 90, 92], Google has switched paradigms and implemented the more easily scalable coupling scheme discussed in Sec. 3.3.2. In the ‘off state’, resonant swapping experiments can be used to determine the residual coupling strength, which is estimated to lie below 50 kHz [320]. The ‘on’ coupling for two-qubit gates is -20 MHz, resulting in gate times of around 12 ns. As shown in Fig. 3.18(b), frequencies are usually tuned over less than 100 MHz to be brought into resonance. In particular, similar to the LASIQ-tuned IBM chips, there are no obvious spatial correlations between the qubit frequencies, and the overall distribution is again well reconciled with Gaussian disorder, see Fig. 3.18(c), albeit with a disorder strength that is smaller than the natural (and LASIQ) disorder. Note that although the frequencies are effectively disordered, each individual frequency is the result of a multi-stage optimization procedure that washes out any prevailing regular pattern, see Ref. [39] for details.

Table 3.1 – Experimental parameters for different transmon variants. Row 1 shows data for a fixed-frequency architecture (IBM’s 127-qubit ‘Washington’ device), row 2 for a tunable-frequency architecture (Surface-17 from Ref. [95]), and row 3 for additional tunable couplers (Google’s ‘Sycamore’ [39]). Note, in particular, the last two columns: with increasing hardware complexity, the gates become faster, but the lifetime decreases. For tunable architectures, the specified data belong to the qubit’s idle points. In row 2, two entries in a cell describe the two values of the AB frequency pattern.

Variant	Coupling	ν [GHz]	E_C/h [MHz]	$\delta\nu$ [GHz]	E_J/E_C	t_{gate} [ns]	T_1 [μs]
ν fixed	always on	5.06	306	0.11	38	529	102
ν tunable	always on	3.95/6.07	177	~2	68/155	~100	33
ν tunable	tunable	6.66	208	0.057	136	12	16

3.6 Summary

This chapter introduced the transmon platform for quantum computing. The transmon plays a dominant role among the numerous variants of superconducting qubits because it strikes a perfect balance between charge-noise sensitivity, which decreases as $\exp(-\sqrt{8E_J/E_C})$, and anharmonicity, which decreases slowly as $1/\sqrt{E_J/E_C}$. The transmon operates in a regime where $E_J/E_C > 20$.

In multi-transmon arrays with a capacitive coupling between transmons, entangling gates can be implemented with microwave drives or by exploiting degeneracies in the spectrum. These distinct techniques require hardware of different complexity and define different regimes of disorder and coupling strength. For the transmon, disorder means site-to-site variations of the qubit frequencies caused by fluctuations of the Josephson energy E_J . In particular, we have noted that regardless of where one is on the path from ‘more control, more noise’ to ‘little control, little noise’, see Fig. 3.14, disorder always occurs, either due to fluctuations in the production process or as artificially engineered disorder, introduced to comply with certain conditions, e.g., to avoid frequency collisions. The disorder is often well described by a single Gaussian distribution. Regular frequency patterns, described by multiple, narrower Gaussian distributions centered around different mean values, might appear in future devices. It is important to note that the motivation for artificial disorder and frequency patterns stems from the analysis of small, usually two- or three-qubit systems but is not a corollary of many-body considerations. In Table 3.1, we summarize important experimental characteristics of selected processors, including one representative for each of the design schemes presented.

In conclusion, independent of the specific hardware choices, the transmon array is an interacting, disordered many-body system, and as such, it is predisposed to be examined for the signatures of MBL and quantum chaos presented in Chapter 2. The next chapter and those that follow discuss in detail the results of such an analysis.

In this work, we will simulate both disorder types: the one that is well described by a single normal distribution as well as frequency patterns, i.e., smaller frequency spreads around several mean values akin to the layout in Fig. 3.16(e).

Many-body localization and quantum chaos in transmon quantum computers

In this chapter, we fuse the intuitively disparate fields of many-body localization and quantum processor engineering by utilizing the diagnostic tools discussed in Chapter 2 to study arrays of capacitively coupled transmons.

The first section introduces the Hamiltonian and its low-energy limit and provides an overview of the simulation parameters. Sec. 4.2 familiarizes with the basic properties of the noninteracting Hamiltonian and, in particular, with the substructures emerging in its spectrum in different disorder regimes. After a brief overview of the properties of the coupling Hamiltonian in Sec. 4.3, we show in Sec. 4.4 that the system hosts a chaotic phase for little disorder or strong couplings, which is a no-go area for quantum computing. Sec. 4.5 is devoted to the analysis of parameter regimes of prevalent transmon processors built according to the different design paradigms introduced in Chapter 3. In Sec. 4.6, we slightly depart from the applied transmon engineering perspective and focus on some of the typical MBL properties, for example, the occurrence of a mobility edge. We then move all the closer to the current state of processor design in Sec. 4.7, where we study small yet realistic two-dimensional transmon arrangements, and in Sec. 4.8, where we extract qubit correlations with the method of the Walsh-Hadamard transformation. Comparing the correlation strengths with what transmon engineering research considers tolerable answers the question of whether quantum computing is feasible in the extended gray area between the extremes of hard quantum chaos and deep localization that we found in Sec. 4.5. In Chapter 1, possible deteriorations of a quantum computer were introduced using the example of information loss in quench experiments. Later on, we argued that knowledge about the static properties, i.e., the wave functions of the interacting Hamiltonian, is sufficient to judge the capability of the transmon array to act as a quantum memory. In Sec. 4.9, we complete the cycle and study quench experiments to show that information is scrambled on relevant timescales that are much shorter than the typical qubit lifetimes.

The simulations underlying the results presented in this and subsequent chapters have been performed on the JUWELS supercomputer at the Forschungszentrum Jülich and the CHEOPS supercomputer at RRZK Cologne. This chapter is partly based on the publication [P1] by the author of this thesis. The author of this thesis obtained all results presented in the following chapters, except for the data underlying the Figs. 4.25 and 4.26, and the identification of the l -qubits in Fig. 4.24, for each of which Evangelos Varvelis is to be credited. This chapter is further supplemented by Appendix B where some of the more technical aspects, including details of the implementation, are scrutinized.

4.1 The model

To obtain the Hamiltonian of an array of capacitively coupled transmons, we combine Eq. (3.9) and Eq. (3.46), yielding

$$\hat{H} = 4E_C \sum_i \hat{n}_i^2 - \sum_i E_{J,i} \cos \varphi_i + T \sum_{\langle i,j \rangle} \hat{n}_i \hat{n}_j. \quad (4.1)$$

The first two contributions describe the individual transmons, and the last term is the capacitive coupling between all pairs of nearest neighbors $\langle i,j \rangle$ or more distant transmons with long-range, resonator-mediated coupling. As discussed in Chapter 3, the charging energy E_C is easily fixed at a desired energy and does not vary from transmon to transmon. Here, we use the typical value $E_C/h = 250$ MHz. The Josephson energies $E_{J,i}$, on the other side, fluctuate as a result of natural or artificial disorder. In this chapter, they are drawn from a normal distribution whose standard deviation σ represents the disorder strength δE_J . We expect our results to hold for other standard forms of disorder as well (see the discussion in Appendix B.3). Common values of E_J/h in current chips lie between 10 GHz and 25 GHz, see also Table 3.1, but even larger values are possible. The coupling strength is the smallest energy scale, typically satisfying $T/h < 50$ MHz. The specific magnitude depends on the hardware choice, as discussed in Sec. 3.5. An overview of the parameter ranges used in the simulations is provided in Fig. 4.1(b).

Even though the full model (4.1) is implemented for all subsequent simulations, its low-energy limit proves helpful for gaining some intuition. Applying a sequence of approximations, akin to the discussion in Sec. 3.2.3, results in

$$\hat{H}_{\text{eff}} = \sum_i h\nu_{q,i} \hat{b}_i^\dagger \hat{b}_i - \frac{E_C}{2} \sum_i \hat{b}_i^\dagger \hat{b}_i^\dagger \hat{b}_i \hat{b}_i + \sum_{\langle i,j \rangle} \hbar J_{ij} (\hat{b}_i^\dagger \hat{b}_j + \hat{b}_i \hat{b}_j^\dagger). \quad (4.2)$$

Eq. (4.2) is the attractive, disordered Bose-Hubbard model, where the qubit frequencies $\nu_{q,i}$ play the role of the on-site energies, the charging energy E_C translates to an attractive interaction, and the capacitive coupling is interpreted as a nearest-neighbor hopping. The qubit frequencies $h\nu_{q,i} = \sqrt{8E_C E_{J,i}} - E_C$ and the hopping amplitudes $\hbar J_{ij} = \frac{T}{4\sqrt{2E_C}} \sqrt[4]{E_{J,i} E_{J,j}}$, see Eq. (3.47), vary due to the fluctuations in the Josephson energies. Unless otherwise noticed, all results shown in this chapter are obtained for a coupled transmon chain of length $L = 10$, as sketched in Fig. 4.1(a). From here on, we adapt to the default convention of transmon engineering and set $h = 1$, meaning that all energies are provided in Hertz, e.g., $E_C = 250$ MHz instead of $E_C/h = 250$ MHz. The symbol L always denotes the number of transmon sites.

4.2 Noninteracting transmon arrays

To begin with, we set $T = 0$ MHz and familiarize ourselves with the general structure of the spectrum of the Hamiltonian in Eq. (4.1). All eigenstates are then product states of single transmon wave functions. They are completely determined by the local excitation numbers. As an example, the state $|0413\rangle$ is the eigenstate of a noninteracting four-transmon array where the first (second, third, fourth) transmon is in the ground (fourth, first, third excited) state. We refer to the sum of the individual excitation numbers as the total excitation number N_{ex} (here $N_{\text{ex}} = 8$). Usually, we denote the space spanned by all product states of the local transmon eigenbases as configuration space to emphasize that we work with the full model in Eq. (4.1). Occasionally, when we exploit the intuition provided by the effective model \hat{H}_{eff} , we interpret the excitation levels of the individual transmons as bosonic occupation numbers and use the terms Fock state and configuration or transmon product state interchangeably.

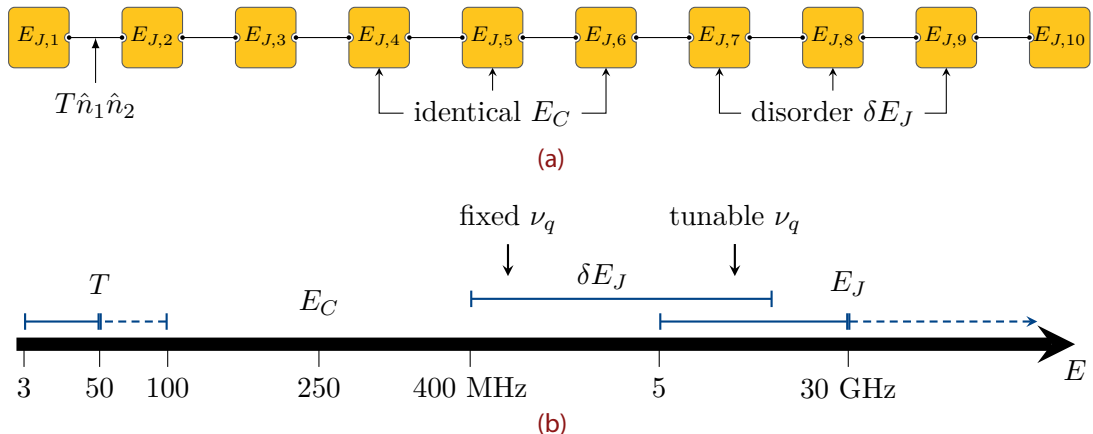


Figure 4.1 – Chain geometry and parameter ranges. (a) Chain of $L = 10$ capacitively coupled transmons for which most of the conclusions presented in this chapter have been reached. (b) Overview of the parameters exploited in the simulations. All energies are measured in Hertz ($\hbar = 1$). The dashed lines represent parameter ranges that have been investigated but lie outside the experimental core region.

4.2.1 Excitation bundles and excitation structures

Essential concepts for transmon arrays subject to not-too-strong disorder are *excitation bundles* and *excitation structures*. Consider three transmons with $N_{\text{ex}} = 2$ excitations. These excitations can be distributed on one or two transmons, corresponding to the sets of eigenstates $\{|200\rangle, |020\rangle, |002\rangle\}$ and $\{|011\rangle, |101\rangle, |110\rangle\}$. We call these distinctive distributions of excitations to the transmon array the *excitation structures*. To keep the notation simple, we denote them as $\{11\}$ and $\{2\}$. Generalizing to larger arrays and higher N_{ex} is straightforward.

From Eq. (4.2), one intuitively expects the spectrum to cluster into *excitation bundles* for small disorder. These are manifolds composed of states with the same total excitation numbers N_{ex} that are energetically separated from the rest of the Hilbert space: Adding an excitation costs an energy $h\nu_q$ minus a potential correction due to the anharmonicity that scales as E_C . On the other side, shifting excitations between transmons (e.g., $|11\rangle \rightarrow |20\rangle$) only leads to contributions of $\mathcal{O}(E_C)$. As $E_C \ll h\nu_q$ in the transmon regime, states with the same N_{ex} should be close in energy compared to the spacing between states with different N_{ex} . For an array of L transmons, the excitation bundle characterized by N_{ex} contains

$$N_{\text{states}} = \frac{(L - 1 + N_{\text{ex}})!}{(L - 1)! N_{\text{ex}}!} \quad (4.3)$$

states—the combinatorial problem is to distribute N_{ex} indistinguishable balls (the bosonic excitations) to L distinguishable bins (the transmons).

In Fig. 4.2(a) (left), we show the spectrum of the disorder-free ($\delta E_J = 0$) transmon chain with $L = 10$. As expected, it reveals a hierarchy according to the color-coded total excitation number N_{ex} . The lowest energy belongs to the unique state $|0\dots0\rangle$ where all transmons occupy the ground state. The next highest level corresponds to states with $N_{\text{ex}} = 1$, for which there is a single excitation structure $\{1\}$ containing the states $|100\dots0\rangle, |0100\dots0\rangle$, and so on. As $\delta E_J = 0$, all these states are degenerate in energy. They are very close to the energy expected from Eq. (4.2), indicated by the thin horizontal line in Fig. 4.2. The next higher energy bundle belongs to $N_{\text{ex}} = 2$. It is composed of states with the excitation structure $\{11\}$ (45 states) and $\{2\}$ (10 states). States from these distinct manifolds are not degenerate: due to the negative anharmonicity, it is energetically favorable to have two excitations on the same transmon and the

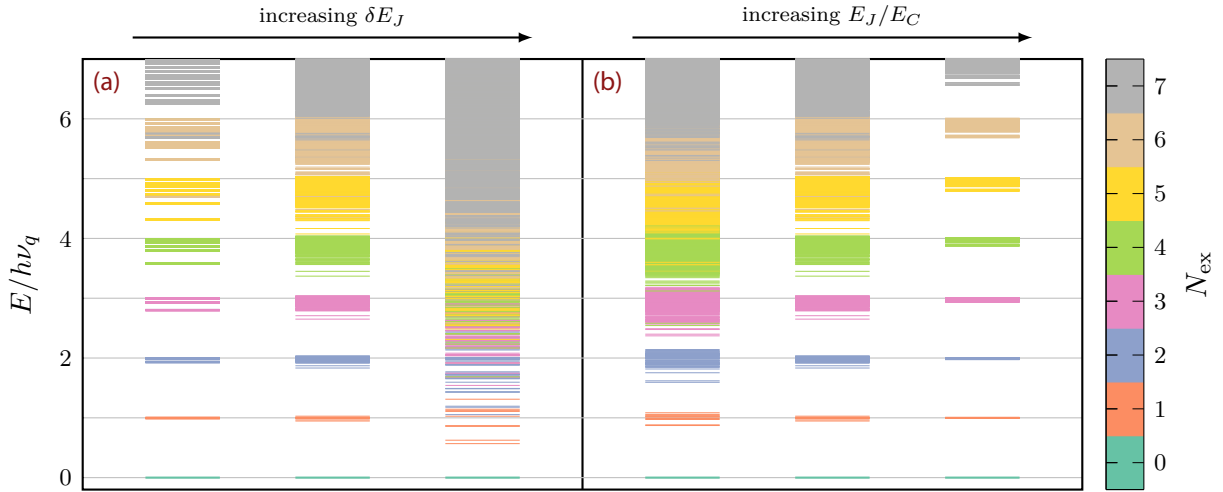


Figure 4.2 – Spectrum of the uncoupled transmon array for (a) varying disorder and fixed $E_J/E_C = 50$ and (b) varying E_J/E_C and fixed $\delta E_J = 625$ MHz. In (a), one observes a clustering of the levels to bundles of a fixed total excitation number for $\delta E_J = 0$ MHz (left) and natural disorder $\delta E_J = 625$ MHz (middle). The finer clusters emerging in the disorder free case correspond to specific excitation structures, see the discussion in the main text. For large disorder $\delta E_J = 5$ GHz (right), the notion of excitation bundles no longer applies, and states of different N_{ex} intermingle. In (b), ramping up the ratio E_J/E_C from 20 (left) via 50 (middle) to 400 (right) sharpens the bundle structure because as the system approaches the harmonic oscillator limit, the influence of the anharmonicity vanishes.

states $\{2\}$ are therefore lower by approximately E_C . This pattern continues for the further levels, where more distinct energy values in the excitation bundles indicate the increasing number of nondegenerate excitation structures. Since the anharmonicity contribution grows (quadratically) with the occupation number of a transmon, the width of the excitation bundles increases with N_{ex} . States with $N_{\text{ex}} = 6$ and $N_{\text{ex}} = 7$ mix into lower bundles, which indicates the breakdown of the Bose-Hubbard approximation (in fact, for the parameter choice made here, the transmon state $|7\rangle$ is not even a bound state). The upper edge of each bundle corresponds to the excitation structure with $N_{\text{ex}} = 1$'s. It therefore coincides almost exactly with the prediction from Eq. (4.2) marked by the horizontal lines.

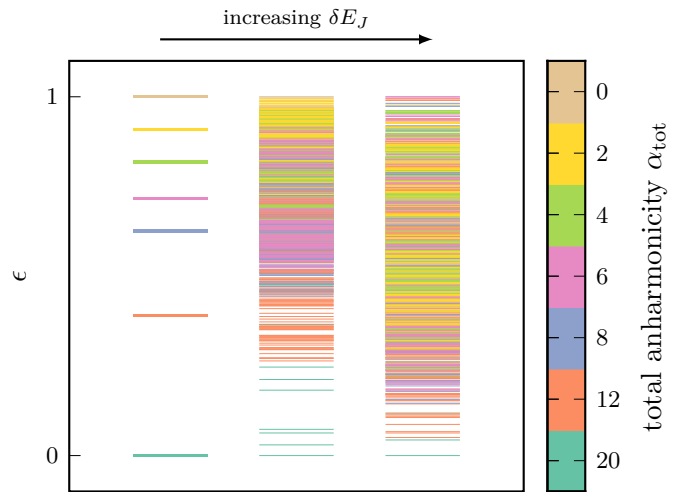
Switching on a moderate disorder, as shown in (a) (middle) for a typical natural spread $\delta E_J = 625$ MHz, lifts the degeneracies between states with the same excitation structure and broadens the width of the bundles but preserves the notion of an excitation manifold as energetically close lying states with the same N_{ex} . This changes when the disorder is increased by an order of magnitude, resulting in the regime exploited in frequency-tunable architectures without tunable couplers. Except for the two lowest bundles, the hierarchy in N_{ex} is lost.

Fig. 4.2(b) demonstrates the effect of a varying E_J/E_C whilst keeping the disorder strength fixed. For the spectrum in the middle, we choose $E_J/E_C = 50$ and natural disorder $\delta E_J = 625$ MHz, as in (a). The left panel shows the spectrum for $E_J/E_C = 20$. The transitions between different bundles are blurred because the relative anharmonicity grows upon decreasing E_J/E_C . Hence, the energy shift arising for multiple excitations on the same transmon approaches (in the example for $N_{\text{ex}} \geq 4$) the order of magnitude of the bundle-bundle distance set by ν_q . For large E_J/E_C (right), the bundle structures sharpens as the relative anharmonicity decreases and the system becomes increasingly well described by noninteracting harmonic oscillators.

Next, we move one level lower and zoom in the excitation bundle $N_{\text{ex}} = 5$ for $L = 10$ (shown

Figure 4.3 –

Excitation bundle with $N_{\text{ex}} = 5$ and $L = 10$ for $E_J/E_C = 50$ and $\delta E_J = 0$ MHz (left), natural disorder $\delta E_J = 625$ MHz (middle), and typical disorder for flux-tunable architectures $\delta E_J = 5$ GHz (right). Each degenerate level shown left corresponds to one excitation structure, ranging from $\{5\}$ with $\alpha_{\text{tot}} = 20$ to $\{11111\}$ with $\alpha_{\text{tot}} = 0$. These substructures vanish quickly as disorder is introduced, and the states start to mix. In particular, in real processors, the computational states are fully intermingled with noncomputational states. To facilitate comparison, normalized energies ϵ restricted to the interval $[0, 1]$ are shown.



in yellow in Fig. 4.2). The disorder free case is shown left in Fig. 4.3. Each of the distinct lines corresponds to one excitation structure. These differ in their anharmonicity contribution. In more quantitative terms, we calculate $\sum_i n_i (n_i - 1)$ where n_i are the local transmon excitation numbers and the sum is over all transmons of the array. In the Bose-Hubbard approximation, this corresponds to the expectation value of the anharmonicity term $\hat{b}^\dagger \hat{b}^\dagger \hat{b} \hat{b}$, and we therefore refer to it as total anharmonicity α_{tot} . The seven distinct levels correspond to the excitation structures $\{5\}$, $\{41\}$, $\{32\}$, $\{311\}$, $\{221\}$, $\{2111\}$, $\{11111\}$ with $\alpha_{\text{tot}} = 20, 12, 8, 6, 4, 2, 0$ containing 10, 90, 90, 360, 360, 840, and 252 states. Note that the number of computational states with local excitation numbers ‘0’ and ‘1’ in $\{11111\}$ (252) is much smaller than the total number of states contained in the entire excitation bundle (2,002). Once a small natural disorder is added, as shown in the middle, the hierarchy according to the total anharmonicity is lost, and states with different excitation structures mix. In particular, this means that already for small disorder, the few computational states intermingle with noncomputational states, which has severe consequences for the identification of qubit states once a finite coupling strength is added, see Sec. 4.8. Further increasing the disorder to the flux-tunable regime where the disorder strength strongly exceeds the anharmonicity augments this tendency. This is shown on the right in Fig. 4.3.

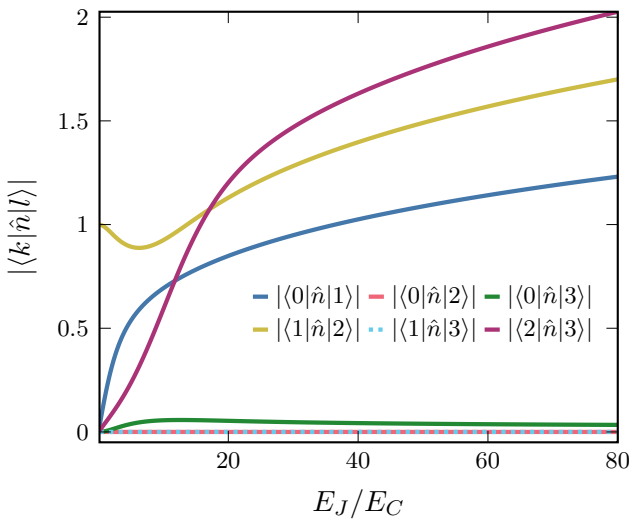
To summarize, there are different levels on which the total Hilbert space restructures. The highest layer is the formation of excitation bundles defined by a fixed N_{ex} . On the next lower ordering level is the clustering in excitation structures corresponding to different values of the total anharmonicity. For typical natural ‘IBM-like’ disorder, the excitation bundles remain intact, but the excitation structures are no longer preserved. For larger disorder, neither of these ordering frames survives. For very small disorder, the excitation structures will turn out to be essential (a specific case of this is discussed in Chapter 5). Equipped with these insights into the properties of the noninteracting problem, we now switch on the capacitive coupling and first discuss to what extent different states mix through this interaction.

4.3 Interacting transmon arrays

A natural choice of basis for the implementation of the Hamiltonian is the one formed by the configuration states, i.e., the product states of the individual transmon eigenfunctions. Each basis state is characterized by a set of L excitation numbers. The computational (p -qubit) states

Figure 4.4 –

Matrix elements of the charge operator between different single transmon eigenstates as a function of the ratio E_J/E_C . In the transmon regime, the most relevant coupling is between directly adjacent eigenstates, i.e., $\langle k+1|\hat{n}|k\rangle$. These elements asymptotically increase as $\sqrt{k+1}$ for fixed E_J/E_C . The matrix elements of the charge operator vanish if states differ by an even number in their excitations, e.g., $\langle 2|\hat{n}|0\rangle = 0$, see the discussion in the main text.



with local excitation numbers ‘0’ and ‘1’ form a subset of this basis, making it the preferred pick to apply the basis-dependent delocalization measures from Chapter 2 for the characterization of potential threads for quantum computing applications. The coupling matrix element between two product states $|k_1 \dots k_L\rangle$ and $|l_1 \dots l_L\rangle$, where $\{k_i\}, \{l_i\}$ are two sets of L single transmon excitation numbers, then depends on the matrix elements of the charge operator \hat{n} in the single transmon eigenbasis. Consider, e.g, the capacitive coupling contribution $\hat{n}_i \hat{n}_{i+1}$ with matrix elements given by

$$\begin{aligned} \langle k_1 \dots k_i k_{i+1} \dots k_L | \hat{n}_i \hat{n}_{i+1} | l_1 \dots l_i l_{i+1} \dots l_L \rangle \\ = \delta_{k_1, l_1} \dots \delta_{k_{i-1}, l_{i-1}} \langle k_i | \hat{n}_i | l_i \rangle \langle k_{i+1} | \hat{n}_{i+1} | l_{i+1} \rangle \delta_{k_{i+2}, l_{i+2}} \dots \delta_{k_L, l_L}. \end{aligned} \quad (4.4)$$

For a few values of k and l , the matrix elements of the charge operator $\langle k|\hat{n}|l\rangle$ are shown in Fig. 4.4. This exemplifies some important properties: Most relevant are matrix elements of the form $\langle k|\hat{n}|k+1\rangle$. Entries of the form $\langle k|\hat{n}|k+m\rangle$, with $|m| > 1$ and m odd, are much smaller (e.g., $\langle 0|\hat{n}|3\rangle$) and $\langle k|\hat{n}|k+m\rangle = 0$ when m is even (e.g., $\langle 0|\hat{n}|2\rangle$). The last property is easily understood from the parity of the Mathieu functions: in the φ representation, these matrix elements vanish as integrals of antisymmetric functions over the interval $[-\pi, \pi]$. For the multi-transmon array, this implies that the parity of N_{ex} is conserved. States from bundles with N_{ex} values that differ by an odd number cannot couple because the corresponding matrix elements in Eq. (4.4) involve one contribution $\langle l|\hat{n}|l+m\rangle$ with m even. In particular, neighboring bundles do not mix. One arrives at the same conclusions when arguing with the asymptotic expression of the charge operator in Eq. (3.32) (akin to the derivation of Eq. (3.47)) instead of the symmetries of the Mathieu functions. Additionally, from the asymptotic form, one immediately reads that for fixed E_J/E_C , the matrix elements $\langle k|\hat{n}|k+1\rangle$ increase as $\sqrt{k+1}$, which explains the hierarchy in the nonvanishing elements in Fig. 4.4. For further details, see the discussion in Ref. [58].

4.3.1 Configuration space hopping

It is instructive to consider Eq. (4.1) as a hopping problem on a high-dimensional configuration space lattice, as discussed in Sec. 2.5. With each additional transmon, the lattice dimension increases by one. Each lattice site (l_1, \dots, l_L) encodes one transmon array configurations $|l_1 \dots l_L\rangle$.

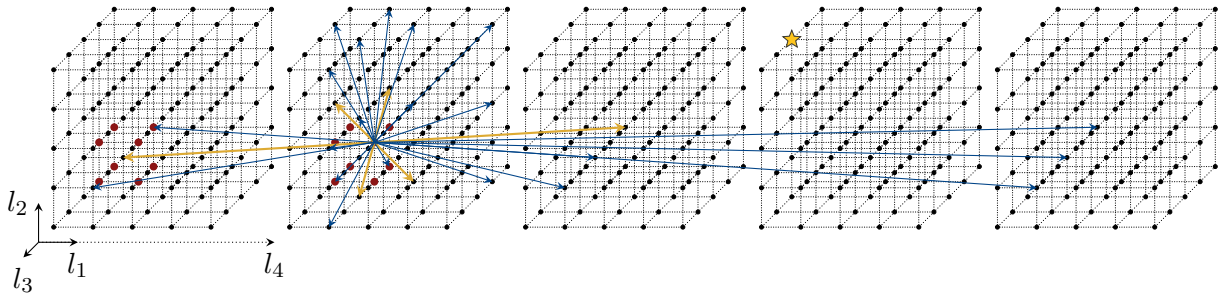


Figure 4.5 – Configuration space of the $L=4$ chain. Each individual transmon is approximated by a five-level system. Along each of the dimensions shown in the coordinate system at the bottom left, one of the local occupation numbers l_i changes, e.g., hopping right from one cube to the next while maintaining the position within the cube means that l_4 increases by one. The lattice point marked by the yellow star correspond encodes the state $|0423\rangle$. The arrows illustrate the connectivity of the state $|1111\rangle$. Blue arrows indicate that the capacitive coupling links $|1111\rangle$ to states with a different N_{ex} , whereas for the yellow arrows, N_{ex} is preserved. These hopping processes are later identified as the most relevant ones because their ‘many-body on-site’ energy is similar. As a concrete example, the coupled states from the first cube are $|1140\rangle$, $|1100\rangle$ (both with different N_{ex} , the latter is a computational state), and $|1120\rangle$ (same N_{ex}).

For illustration, consider a chain of four transmons, where the Hilbert space of each transmon is truncated after the fourth excited level $|4\rangle$. The corresponding lattice with $4^5 = 625$ lattice points is shown in Fig. 4.5. Red lattice points represent computational states. Each vertex translates into a basis state $|l_1 l_2 l_3 l_4\rangle$ according to the following recipe: the position within the individual cubes determines the quantum numbers l_1, l_2, l_3 as indicated and the number of the cube l_4 . As an example, consider the lattice point $(0,4,2)$ in the fourth cube marked by the yellow star. It represents the state $|0423\rangle$. Each individual lattice point is connected to many neighbors via the hopping matrix elements stemming from the capacitive coupling. In Fig. 4.5, this is exemplified for the state $|1111\rangle$, whose connectivity is visualized with arrows. The coupling term $T(\hat{n}_1 \hat{n}_2 + \hat{n}_2 \hat{n}_3 + \hat{n}_3 \hat{n}_4)$ links it to a total of 27 lattice points (see Appendix B.1 for more details) that divide in 19 vertices representing states with different total excitation number (blue arrows, e.g., the state $|1100\rangle$) and six from the same excitation bundle with $N_{\text{ex}} = 4$ (yellow arrows, e.g., $|1201\rangle$).

There are a few important insights that Fig. 4.5 conveys: First, it reiterates that the number of computational states is vanishingly small. Second, it shows that a lattice point couples to many of its neighbors but only to a tiny fraction of the total Hilbert space because only neighboring transmons are directly coupled and because of the ‘selection rules’ from the charge operator elements discussed above. Therefore, the Hamilton matrix is sparse and can benefit from appropriate numerical diagonalization routines. Lastly, most connected states belong to excitation bundles that differ by at least two excitations. This means that most states are far apart in energy relative to the coupling strength (remember that the bundle-bundle distance is primarily determined by $\nu_q \approx 5$ GHz, but $T < 50$ MHz). It is, therefore, reasonable to assume that the few hopping processes shown in yellow are the most crucial ones and to take this into account for an efficient truncation of the Hilbert space, as discussed in the next section.

4.3.2 Truncating the Hilbert space

The coupled-transmon array described by Eq. (4.1) possesses an infinite-dimensional Hilbert space. Making it numerically feasible requires some form of truncation. Naively, one could restrict the local Hilbert spaces of the individual transmons to a few levels, as was done for

the visualization in Fig. 4.5. However, it is much more purposeful not to constrain the Hilbert spaces of the single transmons but directly the multi-transmon basis. Otherwise, most states entering the construction of the Hamilton matrix are irrelevant to the actual target energy window. Consider, for example, the five-level approximation for each transmon in the $L = 4$ system discussed above. The Hilbert space then contains states like $|4444\rangle, |4443\rangle$, etc., with $N_{\text{ex}} \gg 4$. These are very far away from the energy of computational states, with the maximum $N_{\text{ex}} = 4$ and ‘typical’ $N_{\text{ex}} = 2$ for two ‘1’s and two ‘0’s. It is, therefore, reasonable to restrict to basis states whose energies lie in a suitably chosen window around the target energy. In fact, our numerical analysis strongly suggests that accurate results are already obtained when constructing the Hamiltonian only in the sector of a fixed excitation number. This is quite expected for small disorder due to the hierarchy in energy by N_{ex} , but we find that this truncation procedure works even for disorder sizes in which excitation bundles are no longer clearly delimited from each other. This is similar to the effective model \hat{H}_{eff} , which is block diagonal and conserves the bosonic occupation number and not only the excitation parity. However, our model goes beyond Eq. (4.2) because it does not involve any approximations apart from the truncation: it fully captures the cosine nonlinearity and still comprises more intra-bundle couplings, e.g., between the states $|\dots30\dots\rangle$ and $|\dots03\dots\rangle$ (even though these are expected to be small, see Fig. 4.4). For a more detailed discussion of the truncation and related issues, see Appendix B.1.

Eigenstate thermalization and many-body localization are phenomena of highly excited states. We are, therefore, interested in the properties of states with a finite energy density. In the following, unless otherwise noted, we diagonalize the Hamiltonian provided in Eq. (4.1) for the $L = 10$ chain geometry, restricted to the subspace spanned by the excitation bundle with $N_{\text{ex}} = L/2 = 5$. This manifold contains 2,002 states. States within this bundle that have only local excitation numbers ‘0’ and ‘1’ are typical representatives in the computational subspace, in the sense that more computational states are included in this manifold than in any other tangle ($\binom{10}{5}$ of 2^{10} computational states). First, in the Secs. 4.4–4.7, we treat computational and noncomputational states on an equal footing and examine the bundle as a whole. A particularly sensitive measure of chaos tailored to scrutinize the computational states is later applied in Sec. 4.8.

4.4 Chaos and MBL in coupled transmon arrays

The purpose of this section is twofold: In a series of proof-of-principle calculations, we show that the coupled transmon array indeed hosts both regimes, one of localized states and uncorrelated energy levels for large disorder or small couplings and one with chaotic states for small enough disorder or large couplings. Furthermore, we explain how the diagnostics introduced in Chapter 2 can be applied to quantitatively monitor the crossover between MBL and chaotic regime.

4.4.1 Spectrum of a coupled transmon array: spaghetti plots

As a starter prior to the quantitative analysis, it is instructive to inspect the spectrum of the Hamiltonian in Eq. (4.1) for a single randomly selected disorder realization as a function of the coupling strength. This is done in Fig. 4.6 for two values of the ratio E_J/E_C and on varying energy scales. Focusing first on the upper row showing data for $E_J/E_C = 50$ and $\delta E_J = 625$ MHz, i.e., a ratio from the middle of the transmon region with a typical natural Josephson energy spread, one observes that the clustering of levels into energetically separated sectors of fixed N_{ex} persists throughout the whole T range (only bundles with $N_{\text{ex}} < 5$ are clearly identifiable; for the sectors with five and six excitations, the overlap to neighboring bundles is marginal such that it

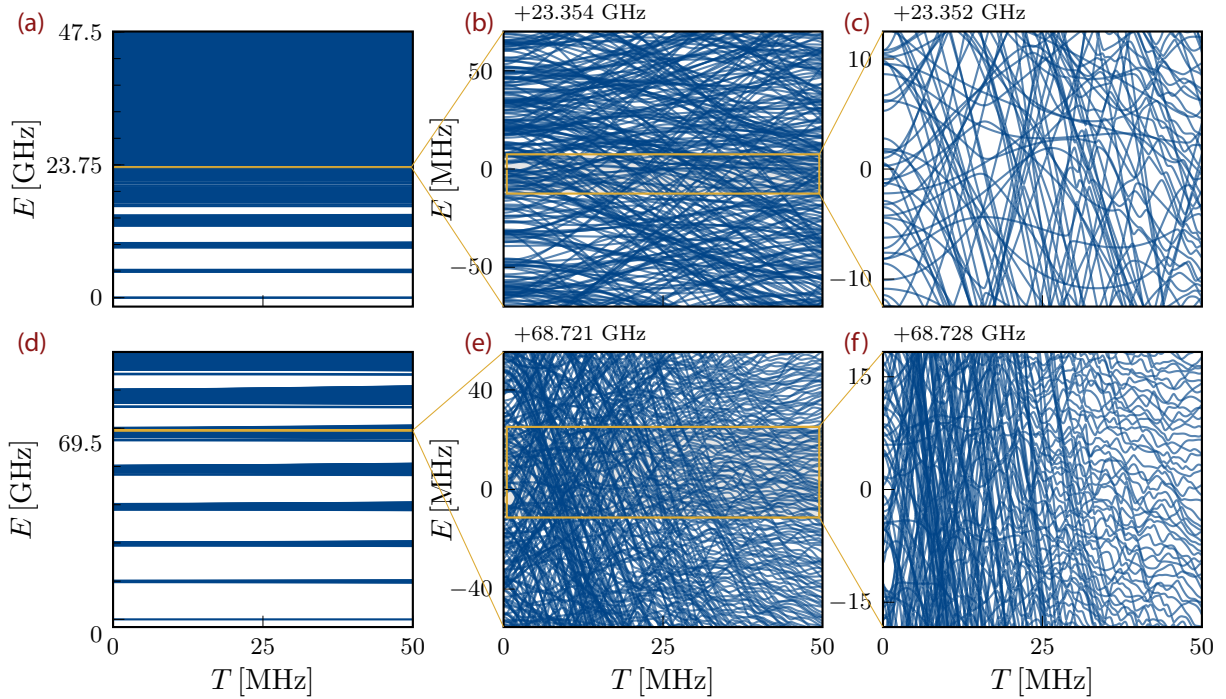


Figure 4.6 – Energy spectrum of an array of ten coupled transmons arranged in a chain geometry as a function of the coupling strength T . Illustrated is the spectrum for a realistic $E_J = 12.5$ GHz with typical natural variations of $\delta E_J = 625$ MHz (upper row) and for $E_J = 100$ GHz and $\delta E_J \approx 1.77$ GHz (lower row) on varying energy scales. Panels (a) and (d) indicate that for the whole T range under consideration, levels cluster into sectors corresponding to a total number of excitation with sharper bundles for the larger E_J/E_C ratio in the bottom row. Zooming into the $N_{\text{ex}} = 5$ bundle in (b) and (e) reveals a dense tangle of levels. A qualitative change in the level structure can already be detected in panel (e). Levels cross for small T but tend to repel as T increases. The level repulsion becomes particularly visible upon further decreasing the energy scale in the third column. The effect is more pronounced for the larger E_J/E_C ratio in (f), but even for the realistic value in (c), numerous avoided level crossings—unambiguous indicators for quantum chaotic behavior—can be made out in the right, large- T half.

is still reasonable to use the concept of an excitation bundle). Decreasing the energy scale for an enlarged view on the levels belonging to the $N_{\text{ex}} = 5$ manifold in (b) and (c) reveals a qualitative change in the behavior of the levels: whereas for small T , all levels seem to pass straight through one another, they start to wiggle around for increasing T . The spectrum exhibits a mixture of crossings and avoided crossings for values of the coupling above 20 MHz, as can be seen in the magnified panel (c).

For the larger E_J/E_C ratio used in the bottom row, $E_J/E_C = 400$ and $\delta E_J = 1.77$ GHz to be specific, the level repulsion is more prominent. At a coupling of about 25 MHz, the straight lines crossing each other disappear and are replaced by strongly wobbling lines that show a clear tendency to avoid mutual crossings. No more crossings are observed near the upper T edge in panel (f). For plausible reasons, parts of the MBL community refer to the two qualitatively different behaviors of the levels with the rather informal phrases of ‘uncooked’ and ‘cooked spaghetti’ phases.

The conclusion we draw from Fig. 4.6 is that the spectrum of an array of coupled transmons displays the most commonly exploited indication of quantum chaotic behavior—level repulsion—and that the degree of chaoticity seems to augment for larger E_J/E_C ratios. In the next section,

we consolidate this qualitative observation into quantitative measures. To start with, we fix $E_J = 44$ GHz and $\delta E_J = 1.1$ GHz to study the MBL–chaos transition as a function of the coupling strength. This specific value of the Josephson energy lies outside the experimental core region; however, it guarantees that clear waterproof signs of both regimes can be seen in all diagnostics that are considered in this section. We turn to the phase diagrams in the T - E_J planes, capturing all experimentally relevant parameter ranges, in the subsequent section.

4.4.2 Level statistics

As discussed in Sec. 2.1.2, the statistics of the energy spacings is a standard and powerful tool to probe the MBL–chaos transition: many-body spectra are expected to show Wigner-Dyson statistics in the quantum chaotic phase and Poisson statistics in the localization regime [321]. By looking at the distribution of the ratio of successive level spacings [136],

$$r_n = \frac{E_{n+1} - E_n}{E_n - E_{n-1}}, \quad (4.5)$$

we can omit the convoluted task of cleaning the spectrum from the local average level density. The expected Wigner-Dyson and Poisson distributions of r_n for chaotic and integrable systems, derived in Ref. [322], are given by

$$P_{\text{Poisson}}(r) = \frac{1}{(1+r)^2}, \quad (4.6)$$

$$P_{\text{Wigner}}(r) = \frac{1}{Z_\beta} \frac{(r+r^2)^\beta}{(1+r+r^2)^{1+3\beta/2}} + \delta P_{\text{fit}}. \quad (4.7)$$

In Eq. (4.7), the first contribution is the exact result for 3×3 matrices for the Gaussian ensembles characterized by β , see Sec. 2.1.2. Z_β is the normalization constant and δP_{fit} is a numerically obtained correction for large matrices. It reads

$$\delta P_{\text{fit}}(r) = \frac{C}{(1+r)^2} \left[\left(r + \frac{1}{r}\right)^{-\beta} - c_\beta \left(r + \frac{1}{r}\right)^{-(\beta+1)} \right], \quad (4.8)$$

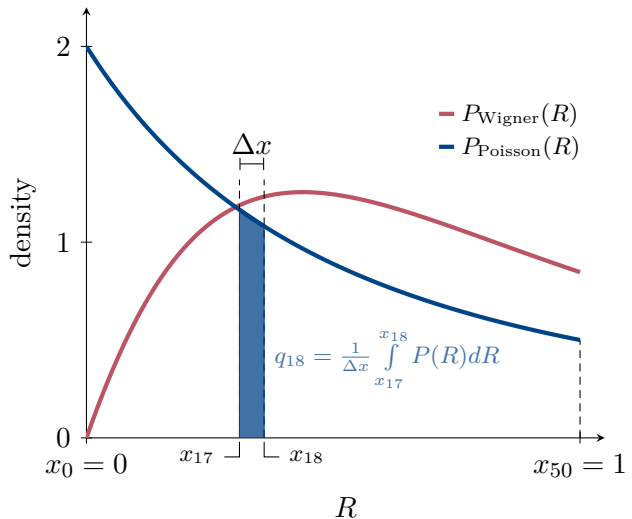
where C is the single fitting parameter and c_β follows from the condition that $\int_0^\infty \delta P(r) dr = 0$. The transmon array possesses time-reversal symmetry. Hence, we need to compare the numerical results to the GOE predictions ($\beta = 1$). One then finds $Z_\beta = \frac{8}{27}$, $c_\beta = 2\frac{\pi-2}{4-\pi}$, and $C = 0.233378$ [322].

Kullback-Leibler divergence. Since its introduction, the level ratios r_n have been used countless times to track chaoticity in seminal contributions to MBL theory [136, 162, 178, 323, 324]. The comparison between numerical data and the two distributions is often monitored by using the average ratio $\langle r \rangle$ as a measure of chaos or via qualitative observations, e.g., naked eye comparison of histograms or by focusing only on the $r \rightarrow 0$ limits. Recently, it was argued that more sophisticated quantitative measures should be used to prevent premature conclusions [325]. Therefore, we compute *Kullback-Leibler (KL) divergences* [326] as a more reliable tool for quantifying the distance of the numerically obtained level spacing distributions to the predictions in the respective regimes. For two discrete probability distributions Q and P defined over the probability space \mathcal{X} , the KL divergence is defined as

$$D_{\text{KL}}(P||Q) = \sum_{x \in \mathcal{X}} P(x) \log \left(\frac{P(x)}{Q(x)} \right). \quad (4.9)$$

Figure 4.7 –

Poisson and Wigner-Dyson (GOE) distribution for the quantity $R_n = \min(r_n, 1/r_n)$, where r_n is the ratio of adjacent level spacings as defined in Eq. (4.5). The predicted small- R behavior of the Wigner-Dyson distributions, $P_{\text{Wigner}}(R \rightarrow 0) \rightarrow 0$, reflects the inset of level repulsion in the chaotic phase. To compare these continuous functions to numerically obtained histograms, they are discretized by splitting the R interval into 50 bins with edges x_0 to x_{50} and integrating over the resulting bins, as exemplified for the Poisson distribution and q_{18} .



In our use case, Eq. (4.9) condenses the full, numerically obtained spectral information (P) over the entire r_n range into a single number that reflects the similarity of the data to one of the expected distributions (Q). $D_{\text{KL}}(P||Q)$ has several properties that make its interpretation as a measure of disparity¹ between P and Q plausible, see, e.g., Refs. [327, 328]. Most importantly, $D_{\text{KL}}(P||Q) \geq 0$, where equality holds if and only if $P = Q$.

To evaluate Eq. (4.9), we proceed as in Ref. [325] and calculate

$$R_n = \min \left(r_n, \frac{1}{r_n} \right), \quad (4.10)$$

which comes with the advantage that it limits our considerations to the range $[0, 1]$. The probability distributions $P(R)$ are obtained from the distributions $P(r)$ in Eqs. (4.6) and (4.7) as $P(R) = 2P(r)\Theta(1-r)$ [322]. They are illustrated in Fig. 4.7. The vanishing of $P_{\text{Wigner}}(R)$ for $R \rightarrow 0$ once again reflects the inset of level repulsion in chaotic systems. Next, the R interval $[0, 1]$ is split into 50 bins of equal width with the 51 edges $x_k, k = 0, \dots, 50$. The distribution $P(k) \equiv p_k$ in Eq. (4.9) is extracted from the statistics of the numerical simulations, i.e., p_k corresponds to the relative frequency with which level ratios R_n are found in the interval $[x_{k-1}, x_k]$. This is equal to the height of the corresponding bin of the normalized histogram. $Q(k) \equiv q_k$ follows one of the two principal statistics. To replace the continuous Poisson and Wigner-Dyson functions by discrete values q_k , one computes the integral over the intervals $[x_{k-1}, x_k]$, as exemplified in Fig. 4.7. Concretely, the KL divergences with respect to the (discretized) Poisson ($Q = P_{\text{Poisson}}$) and Wigner-Dyson ($Q = P_{\text{Wigner}}$) distributions are obtained as $D(P||Q) = \sum_{k=1}^{50} p_k \log(p_k/q_k)$. The KL divergence is *not* symmetric under permutation of P and Q . For presentation purposes, it is convenient to normalize the divergences such that $D(P_{\text{Wigner}}||P_{\text{Poisson}}) = 1$ and vice versa. As a result, if the numerics P suggest good agreement with what is expected in the localization regime, we obtain $D(P||P_{\text{Poisson}}) \approx 0$ and $D(P||P_{\text{Wigner}}) \approx 1$.

Disorder averages. As the considered model contains random disorder, faithful statements about typical properties for a particular set of system parameters can only be made in the form of disorder averages over many fictitious processor realizations. This is achieved by repeatedly drawing sets of Josephson energies from the same Gaussian distribution with fixed average

¹The word ‘distance’ is not avoided here coincidentally, but because the KL divergence is not symmetric and does not fulfill the triangle inequality.

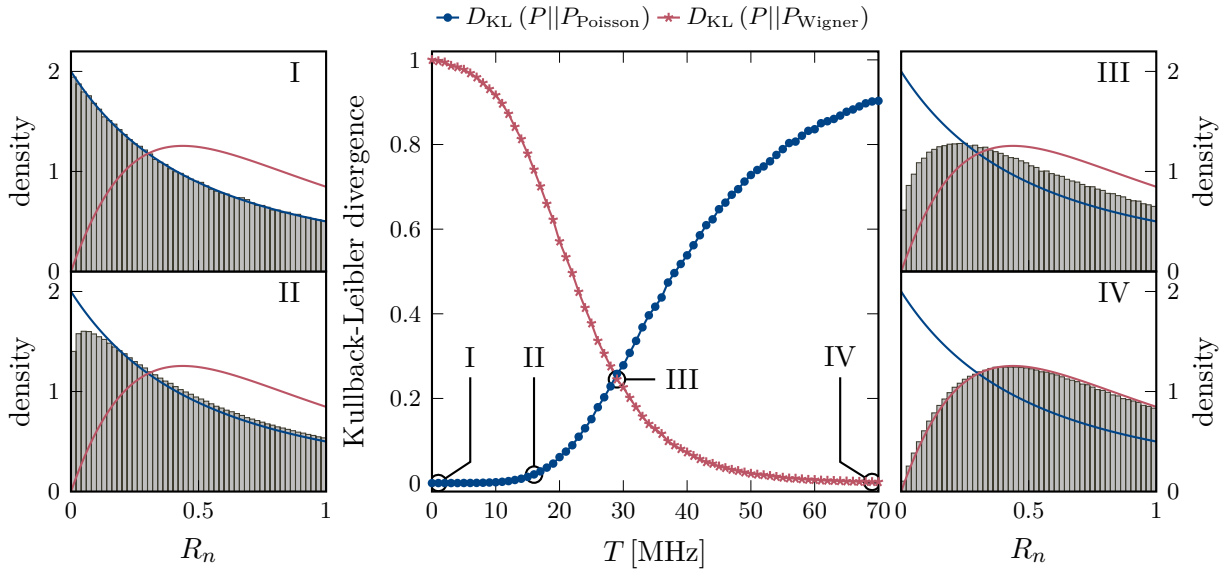


Figure 4.8 – Spectral statistics for a chain of ten coupled transmons. Shown are the KL divergences for the distribution of the R_n ratios as a function of the coupling strength T , calculated with respect to the Poisson (blue) and Wigner-Dyson (red) distributions. The average Josephson energy is fixed to $E_J = 44$ GHz, and the disorder is $\delta E_J = 1.17$ GHz. The statistics evidence a transition from an MBL regime with Poisson statistics ($D(P||P_{\text{Poisson}}) = 0$) at small T to a quantum chaotic region with Wigner-Dyson statistics at large T . This is also corroborated by the similitude between the histograms shown for selected values of the coupling strength and the predicted distributions. Each histogram is a disorder average over at least 5,000 independent disorder realizations. All 2,002 energies of the $N_{\text{ex}} = 5$ excitation bundle are considered in the calculation of the R_n values.

E_J and disorder strength δE_J . For each disorder realization, diagonalization of the Hamiltonian yields an R_n histogram. The KL divergences are then obtained by comparing the *averaged* histograms or R_n distributions to the analytic predictions.²

4.4.3 Results for the Kullback-Leibler divergences

The main panel of Fig. 4.8 shows the KL divergences $D(P||P_{\text{Poisson}})$ and $D(P||P_{\text{Wigner}})$ as a function of the coupling strength T . The result clearly manifests that the coupled transmon array hosts a many-body localized and a quantum chaotic regime. For small couplings, the KL divergence of the numerical data vanishes when calculated with respect to the Poisson distribution, indicating the presence of a localized phase where the energies are uncorrelated random numbers. As T increases, $D(P||P_{\text{Poisson}})$ quickly grows while $D(P||P_{\text{Wigner}})$ approaches zero, marking an increasingly better agreement with what is expected in the ergodic phase. For selected values of T , the disorder-averaged histograms, i.e., the p_k values entering the evaluation of the KL divergences, are also displayed. As expected, there is a striking match with Poisson for very small (I) and Wigner-Dyson statistics for large couplings (IV). For values in between ($T \approx 20$ – 50 MHz), one observes a region of ‘hybrid’ statistics, where the histograms interpolate between the clean cases of MBL and quantum chaos (II and III), and neither of the two KL divergences is close to

²The complementary approach of calculating one instance of the KL divergence for each fictitious processor and then averaging all KL divergences is not meaningful. Every single KL divergence would significantly differ from zero due to poor statistics alone. Averaging cannot cure that one never finds good agreement with one of the two principal statistics.

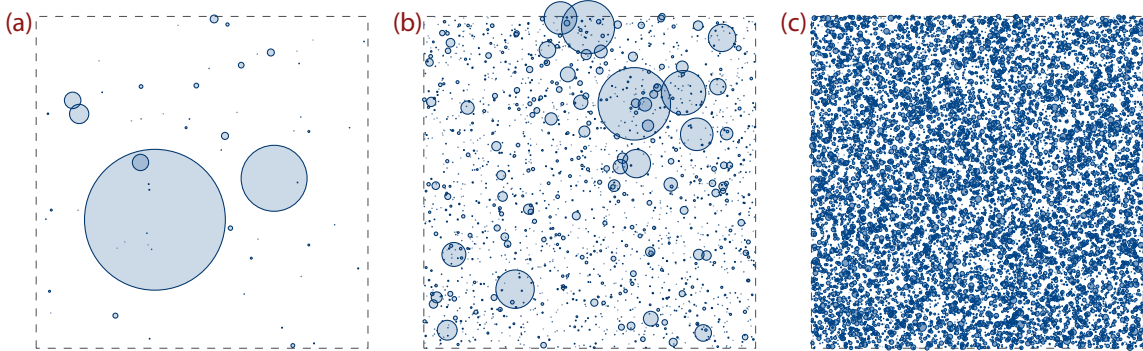


Figure 4.9 – Delocalization of a wave function in configuration space. The center of each circle represents a basis vector. The radius is proportional to the amplitude of this basis vector in the wave function. (a) For $T = 5$ MHz, $E_J = 12.5$ GHz, the wave function is nearly perfectly localized, with a single basis vector symbolized by the large circle strongly contributing to it. Upon increasing T and E_J , the wave function tends to delocalize, indicated by a higher number of significantly contributing states for (b) $T = 15$ MHz and $E_J = 50$ GHz. Furthermore, the states with a minimal weight in the wave function become more numerous. In (c), parameters ($T = 50$ MHz, $E_J = 100$ GHz) are such that the wave function is nearly ergodic: many basis states contribute with a similar magnitude to $|\psi\rangle$, see the main text for more details.

zero. Upon close inspection, one notices that for large couplings, the system is not fully chaotic. This is most clearly seen in $D(P||P_{\text{Poisson}})$, which remains well below one, the expected value for hard quantum chaos. In histogram IV, the bin height for small (large) T slightly exceeds (falls below) the Wigner-Dyson distribution. The origin for this behavior are states at the edges of the five-excitation sector that remain localized even for strong couplings but are nevertheless included in the histograms. For details, see the discussion of the mobility edge in Sec. 4.6.1.

4.4.4 Wave function statistics

The level statistics provided us with unambiguous evidence for the existence of a quantum chaotic region. Next on the agenda is the characterization of the delocalization and entanglement properties of the eigenfunctions. A qualitative insight into how the nature of typical wave functions varies for different system parameters is provided in Fig. 4.9. Here, we consider a transmon chain with $L = 12$ and $N_{\text{ex}} = 6$, possessing a 12,376-dimensional Hilbert space that is represented by the dashed gray square. An equal number of random coordinates within the squares symbolizes the different basis vectors. We randomly pick a single eigenfunction $|\psi\rangle$ from the middle of the spectrum. The sizes of the circles drawn around the coordinates designating the basis states $|k\rangle$ are proportional to the weights $|\langle k|\psi\rangle|^2$. In (a), for parameters where the system is in the MBL phase, one can distinguish between one dominating state, one state with small, but clearly visible contribution (a nearest neighbor in configuration space) and a few other states that contribute very weakly to $|\psi\rangle$. This changes for larger T and larger E_J/E_C , as shown in (b) for parameters where the level statistics suggest that the system is neither fully integrable nor chaotic: several states ($\mathcal{O}(10)$) contribute significantly to the eigenstate. The number of states with minimal but nonzero weight increases as well. Upon further increasing T and E_J/E_C , there is no dominant contribution and the wave function fully delocalizes, covering nearly all available basis states with equal weight, as illustrated in (c) for parameters where the system is nearly ergodic.

What has been observed here qualitatively is precisely what the inverse participation ratio (IPR) and the participation entropy can record quantitatively. Along with some other measures

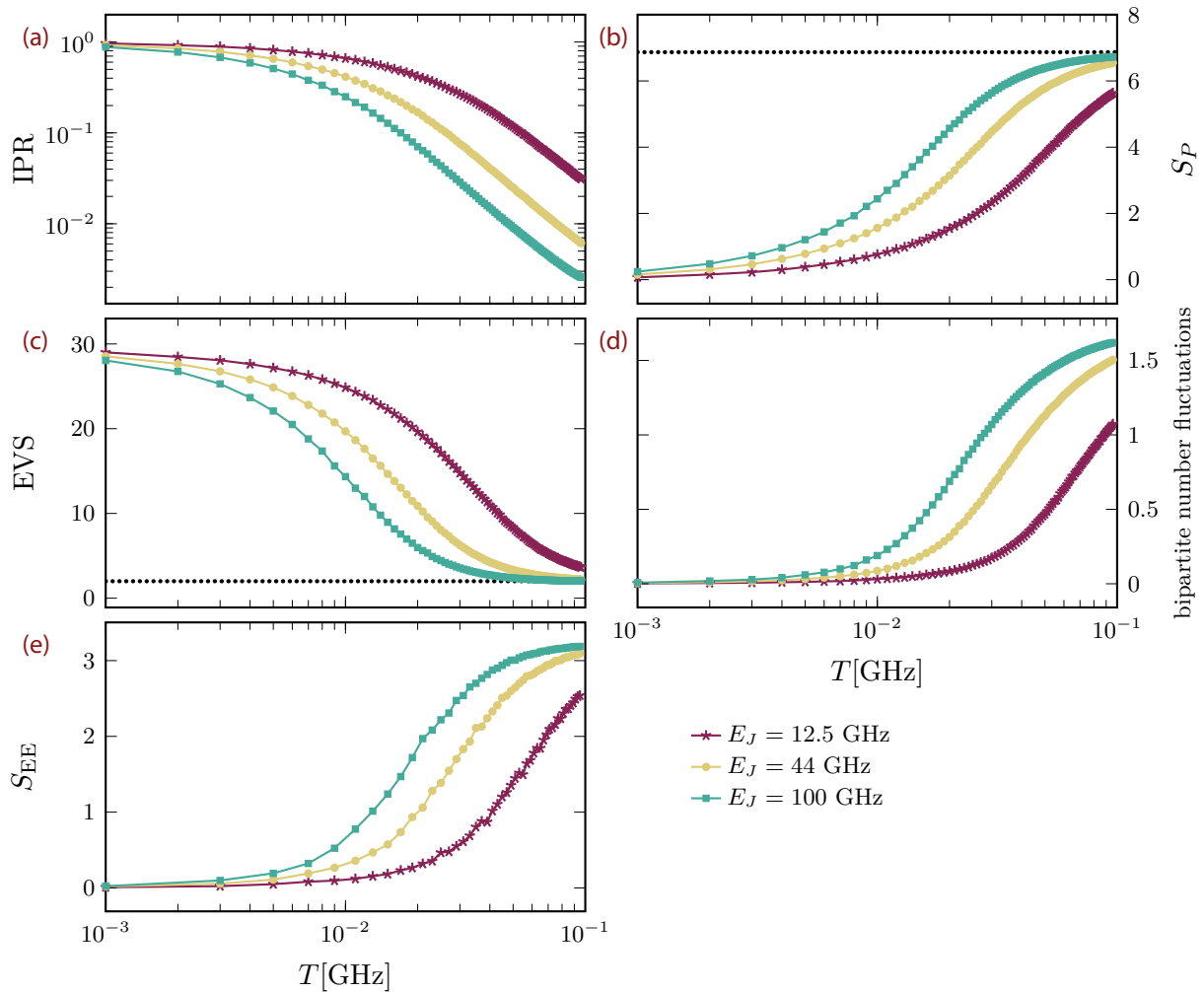


Figure 4.10 – Localization and entanglement properties of the wave functions of an $L = 10$ transmon chain. Shown are (a) IPR, (b) participation entropy, (c) eigenvector similarity, (d) bipartite number fluctuations, and (e) entanglement entropy. If existing, the asymptotic value expected in the ergodic phase are indicated by dotted horizontal lines. All measures indicate a transition from an MBL to a chaotic regime, see the main text for a detailed discussion. All results are averaged over approximately 1,800 disorder realizations, except for (e), where about 170 realizations were used. The disorder strength for $E_J = 12.5$ (44, 100) GHz is $\delta E_J = 0.625$ (1.17, 1.77) GHz. Similar to what has been observed in Fig. 4.6, the system is more susceptible to delocalization for larger E_J .

to charter the properties of wave functions, these two quantities are shown in Fig. 4.10 as a function of T ranging from 1 MHz to 100 MHz and for three different values of E_J and δE_J . As before, we depict only disorder-averaged quantities. For the wave function statistics, two averages are performed: All results are averaged over many disorder realizations. For each disorder realization, each quantity is calculated for and averaged over all 2,002 eigenstates (or 2,001 eigenstate pairs for the EVS).

Before discussing the metrics in Fig. 4.10 in detail, it is worth noting that all appear to reflect a shift in the system's properties as T is increased and that these quantitative changes are more pronounced for larger E_J/E_C , consistent with the observation from Fig. 4.6.

Specifically, Fig. 4.10 illustrates

- (a) the IPR, calculated according to Eq. (2.24), where $|\alpha\rangle$ is the configuration space basis. For small T , all wave functions strongly resemble the eigenstates of the noninteracting system, which is mirrored in an IPR close to one. As T is increased, the eigenstates quickly delocalize and for $T = 100$ MHz (and $E_J = 100$ GHz) the IPR approaches the order of magnitude of $1/\dim\mathcal{H}$, the expected value for ergodic wave functions.
- (b) the participation entropy S_P as defined in Eq. (2.25), where again the eigenstate $|i\rangle$ is expanded over the configuration space basis. It strictly vanishes for $T = 0$ MHz, increases as T is increased and saturates for large couplings. The expected value for the GOE ensemble is $S_P = \ln(0.48 \cdot \dim\mathcal{H}) + \mathcal{O}(1/\dim\mathcal{H})$ [117]. Here, $\dim\mathcal{H} = 2,002$ and hence, $S_P \approx 6.868$ is expected in the chaotic regime. This value is indicated by the dotted horizontal line in (b). The numerically obtained values converge towards this prediction for large T .
- (c) the correlations between nearby eigenstates, measured by the eigenvector similarity EVS, Eq. (2.26), calculated here for pairs of energetically adjacent eigenstates. The GOE prediction is $\text{EVS} = 2$ [164], which is approached for large T (dotted horizontal line).
- (d) the bipartite number fluctuations. In the five-excitation bundle, the total number of excitation in each basis state is (obviously) five and the same holds for all interacting eigenstates, provided that the Hamiltonian is constructed in this restricted subspace (otherwise, contributions from e.g., the sector $N_{\text{ex}} = 7$ cause petite deviations, but as discussed, this effect is nearly imperceptible). However, different eigenstates have a different number of excitations in a given half of the system, e.g., the first $L/2$ transmons. This number is determined by the operator [183]

$$\hat{N}_{L/2} = \sum_{i=1}^{L/2} \hat{n}_i, \quad (4.11)$$

where the sum is over the transmon sites i and the operator \hat{n} has the property $\hat{n}|l\rangle = l|l\rangle$, i.e., it extracts the excitation number l of the single transmon eigenstate $|l\rangle$ with energy E_l . What is shown in (c) are the fluctuations³ of $\hat{N}_{L/2}$ in a many-body eigenstate $|i\rangle$, $\langle i|\hat{N}_{L/2}^2|i\rangle - \langle i|\hat{N}_{L/2}|i\rangle^2$. As discussed in Sec. 2.4, subsystem fluctuations of globally conserved quantities are believed to capture the entanglement properties of the eigenstates $|i\rangle$ [182].

- (e) the entanglement entropy S_{EE} , whose precise definition is given in Eq. (2.23), and that is calculated for the subsystem comprising the first half of the transmon chain. This figure does not provide accurate information about the existence of an MBL or chaotic regime, as this requires simulations for various L to detect a change in the scaling behavior from area to volume law. However, it monitors qualitatively the growth of entanglement with increasing T and is consistent with similar results obtained for the Bose-Hubbard model [183].

In summary, the evidence for the existence of a quantum chaotic regime that we found in the delocalization and entanglement properties is overwhelming. Given that to a certain degree the information contained in the above wave function measures is redundant and yields the same

³We call this the bipartite number fluctuations because the operators \hat{n}_i in Eq. (4.11) correspond to the boson number operator $\hat{b}_i^\dagger \hat{b}_i$ in the analogous definition of $\hat{N}_{L/2}$ for the Bose-Hubbard model.

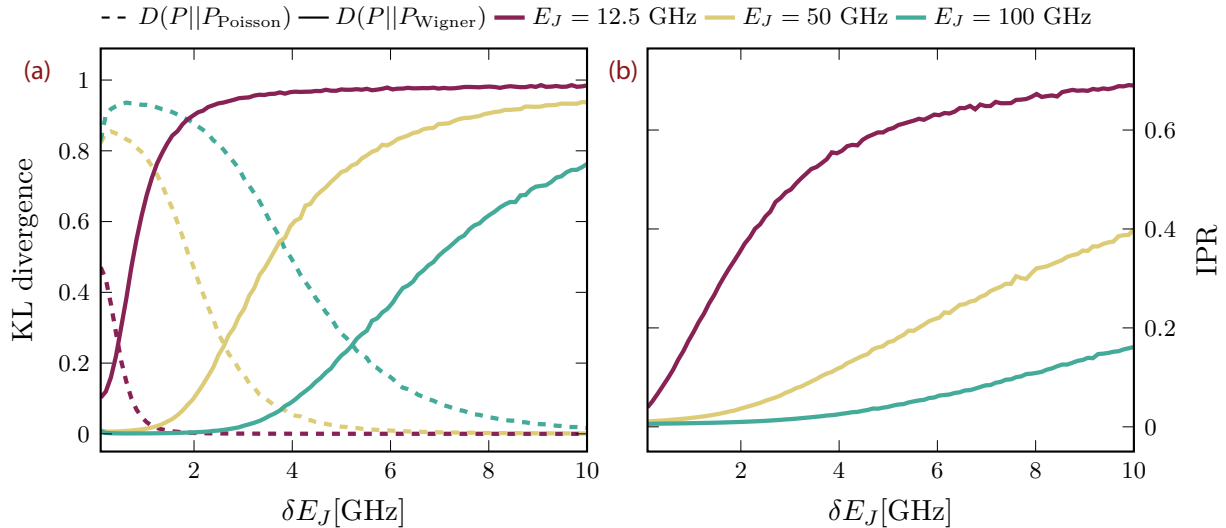


Figure 4.11 – Transition from chaos to MBL upon increasing the disorder strength. (a) The KL divergences with respect to the Poisson (dashed) and Wigner-Dyson (solid) distributions indicate a transition from the ergodic phase for low disorder to the MBL regime for strong disorder. (b) The IPR reflects the tendency of the wave function to localize as the disorder increases. All results are obtained for $T = 50$ MHz. The KL divergences are averaged over around 4,500 disorder realizations, and the IPR over 3,000. Again, localization is favored for smaller values of the Josephson energy.

conclusions, in what follows we exploit only the IPR to characterize the delocalization of the wave functions.

A final observation from Fig. 4.10 that will continue to guide us is that one has to distinguish between the watertight signs of quantum chaos and initial deviations from MBL if one is interested in quantum computing applications. For example, the IPR falls below 0.5 for $T \lesssim 10$ MHz. Compared to the ergodic value $\mathcal{O}(10^{-3})$, the wave function is fairly localized. The KL divergences also indicate a pronounced proximity to the Poisson statistics. However, this in no way guarantees that a ‘computational state’ that consists of only 50% of the original qubit is of any use. We return to this observation in Sec. 4.5.1.

4.4.5 Varying the disorder strength.

Besides the coupling T , one expects the disorder strength to be an alternative tuning parameter that can be adjusted to interpolate between the localized and the delocalized regime. This is illustrated in Fig. 4.11, where (a) KL divergences and (b) IPRs are shown as a function of the disorder δE_J . As expected, ramping up the disorder strength while keeping all other parameters fixed takes one further away from the ergodic regime. Again, the system is more prone to chaos for larger E_J/E_C . Note that for $\delta E_J \rightarrow 0$, additional features not covered by Poisson, Wigner-Dyson or hybrid statistics emerge in the level spacing distributions. For example, the spectrum resolves itself in the excitation structures discussed in Fig. 4.3 if the disorder-induced variations in the frequencies ν_q are much smaller than E_C . This and other features of very weakly disordered systems are discussed in the context of engineered disorder patterns in Chapter 5. In Fig. 4.11(a), the first indication that the case of very small disorder has additional complexity is the nonmonotonicity of the KL divergences for $E_J = 100$ GHz.

4.5 Quantum chaos in prevalent transmon architectures

Having established that arrays of coupled transmons harbor both a localized and a chaotic regime, we now turn to a detailed discussion of the experimentally relevant ranges of the coupling strength and the Josephson energies and investigate for which parameter values the first deviations from localization become apparent. We do this for two different disorder regimes corresponding to different design philosophies within the meaning of Sec. 3.5. Concretely, we consider

- scheme-A disorder, defined as $\delta\nu = \frac{E_C}{2}$.⁴ This choice is guided by what is desirable in fixed-frequency architectures with all-microwave gates, like the CR gate. The above choice of $\delta\nu$ then guarantees sufficiently fast entangling gate operations. For typical values of $E_J = 12.5$ GHz and $E_C = 250$ MHz, this yields an E_J variation of $\delta E_J = 625$ MHz, in excellent agreement with the natural, as-produced disorder strength and with what is found in chips with LASIQ-adjusted (yet not pattern-engineered) disorder. Prototypical examples are the various generations of IBM cloud devices, where both natural and designed disorder can be found. The parameters exploited in the preceding Sec. 4.4 belong to this disorder class (except for the parameters underlying Fig. 4.11).
- scheme-B disorder with $\delta\nu = 6E_C$. The disorder here is about an order of magnitude larger, such that the site-to-site variations in the frequencies exceed 1 GHz, as typically found in chips with tunable frequencies but without tunable couplers. Examples include the architectures used in Delft [295], ETH Zürich [95, 108], and ‘Sycamore’’s predecessor, Google’s ‘Bristlecone’ generation [329].

We do not investigate the case of tunable frequencies with tunable couplers (as these have $T \approx 0$), but our above analysis allows us to identify the important dimensionless scaling variable, and thus some conjectural statements concerning the vulnerability of this design class can be made as well.

Keeping $\delta\nu$ constant while tuning E_J requires an additional scaling of the disorder in the Josephson energy with the mean value E_J as $\delta E_J \propto \sqrt{E_J}$. Specifically, the above disorder choices yield

$$\delta E_J = \sqrt{\frac{E_C E_J}{8}} \text{ (scheme A)} \quad \text{and} \quad \delta E_J = \sqrt{18 E_C E_J} \text{ (scheme B).} \quad (4.12)$$

For $E_J = 12.5$ GHz and $E_C = 250$ MHz, the distributions from which we draw the Josephson energies are exemplified in Fig. 4.12. The distributions are cut off sharply at the lower edge to ensure that $E_J > 5$ GHz, which is the lower bound of the E_J/E_C transmon regime for the chosen E_C value.

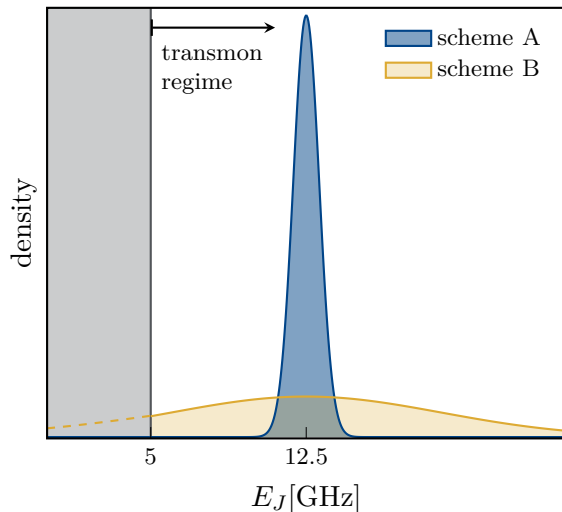
4.5.1 Results for scheme-A disorder

For scheme-A disorder, the Kullback-Leibler divergences with respect to the Poisson and Wigner-Dyson distributions for varying values of the transmon coupling T and the mean Josephson energy E_J are shown in Fig. 4.13(a) and (b). One can clearly distinguish between an MBL regime at small couplings and small E_J/E_C ratios, where $D_{KL}(P||P_{\text{Poisson}})$ vanishes, and an ergodic regime for large T and a large E_J/E_C ratio. In the latter, the level statistics follow the Wigner-Dyson distribution, as indicated by the small value of $D_{KL}(P||P_{\text{Wigner}})$ (deep orange). Both regimes are separated by a region of hybrid statistics where neither $D_{KL}(P||P_{\text{Poisson}})$ nor

⁴For the remainder of this thesis, we write ν instead of ν_q .

Figure 4.12 –

Disorder distributions. Examples for the scheme-A (blue) and scheme-B (yellow) disorder distributions for a mean Josephson energy $E_J = 12.5$ GHz. To ensure a transmon-like ratio $E_J/E_C > 20$, the Gaussians are truncated at $E_J = 5$ GHz, which can significantly reduce the effective disorder strength for scheme-B parameters and small average Josephson energies.



$D_{KL}(P||P_{\text{Wigner}})$ is small. Most experiments are performed for E_J/E_C values below the dotted horizontal line. However, the full E_J range is, in principle, experimentally accessible. The solid black line in Fig. 4.13(a) marks the points at which the KL divergence with respect to the Poisson distribution (normalized to 1 in the ergodic phase) takes the value 1/2. Roughly speaking, this is the line of equal distance to the two limiting cases of MBL and chaos. It should be kept in mind that the choice $D_{KL}(P||P_{\text{Poisson}}) = 1/2$ is somewhat arbitrary: using $D_{KL}(P||P_{\text{Wigner}}) = 1/2$ or the crossing point of the KL divergences works equally well. The main purpose of highlighting this contour line is to provide a simple way to compare different setups. Looking at the displacement of this line under changes in the system (e.g., additional couplings or variations of the system size) allows one to judge a potential higher or lower proneness to chaos under the modified circumstances. To credibly demonstrate the existence of a localized and an ergodic regime, one needs the information about both KL divergences shown in Fig. 4.13. In general, $D_{KL}(P||P_{\text{Poisson}}) = 1$ does not imply that $D_{KL}(P||P_{\text{Wigner}}) = 0$. Thus, the two panels do not contain redundant information. For the simulations presented in this chapter, the situation is similar to Fig. 4.13: the computed R_n histograms interpolate between Poisson and Wigner-Dyson statistics and are always similar to the exemplary ones shown in Fig. 4.8. Therefore, $D_{KL}(P||P_{\text{Poisson}}) \approx 1$ can be considered as a sufficient condition for the existence of a chaotic regime. Further on, the results for $D_{KL}(P||P_{\text{Wigner}})$ are therefore omitted. We note, however, that when examining very weakly disordered transmon arrays in Chapter 5, one encounters the situation where $D_{KL}(P||P_{\text{Poisson}}) \approx 1$ but the system's level statistics do not follow the Wigner-Dyson distribution.

For small values of $T \lesssim 20$ MHz, deviations from Poisson statistics are scarcely discernible in Fig. 4.13, especially for the E_J values below the horizontal line that constitute the experimental core region. One might be tempted to conclude that this parameter range is well-suited for quantum computing applications. That this would be premature is evident from a glance at Fig. 4.14, where the inverse participation ratio is shown for the same T and E_J ranges. The IPR is close to one only for a small margin of small coupling strengths $T \lesssim 3\text{--}5$ MHz. In panel (a), the contour lines represent exponentially decaying IPR values. The rapid decline of the IPR evinces very conspicuously that the wave functions quickly delocalize in configuration space, falling below 1/4 in the parameter range that, according to the level statistics analysis, appeared to be free of manifestations of chaos. Near the region of hybrid statistics, where both KL divergences are in the proximity of 1/2, the IPR drops already below 10%. We can gather that the many-body

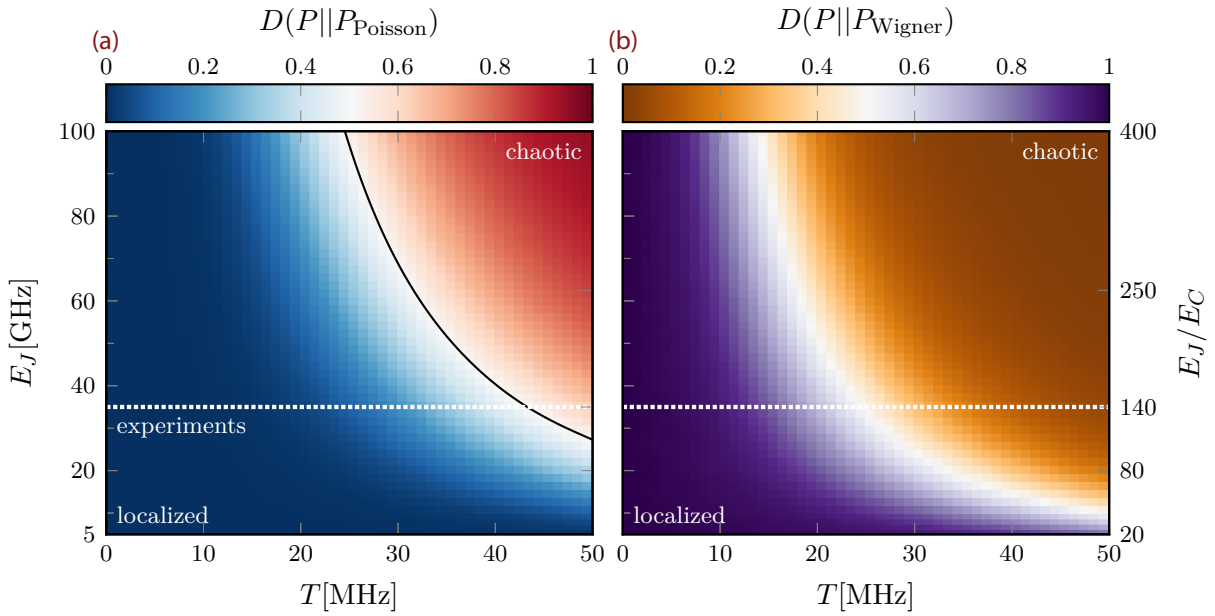


Figure 4.13 – Scheme-A level statistics. (a) KL divergence calculated with respect to the Poisson distribution. For small T and E_J/E_C , $D(P||P_{\text{Poisson}}) \approx 0$ indicates perfect agreement with what is expected for integrable systems, hence signaling the existence of an MBL regime. The solid black curve is the contour line where $D(P||P_{\text{Poisson}}) = 1/2$. (b) KL divergence calculated with respect to the Wigner-Dyson distribution. Heralded by the vanishing of $D(P||P_{\text{Wigner}})$, a quantum chaotic regime appears for larger T and E_J/E_C . Between the two limiting cases of ‘deep blue’ MBL and ‘dark orange’ chaos, an extended gray area spreads out, where the R_n ratios show hybrid statistics akin to the histogram III in Fig. 4.8. Most state-of-the-art transmon architectures operator with E_J values below the dotted white line. All results are averaged over at least 2,000 disorder realizations. The disorder strength extends from $\delta E_J \approx 0.4$ GHz for $E_J = 5$ GHz to $\delta E_J \approx 1.7$ GHz for $E_J = 100$ GHz, see Eq. (4.12).

level statistics are less responsive to early markers of delocalization than the wave functions. In particular, it is now far from evident that for the core E_J/E_C region and moderate couplings, the applicability as a quantum computer should not be affected by the strong dressing effect of the wave functions.

Fig. 4.13(b) presents the same data set with a log-scale color coding of the IPR. This highlights that the wave functions are not *completely* delocalized in the chaotic corner of the displayed parameter regime. The minimal IPR of about 0.004 found for $T = 50$ MHz and $E_J = 100$ GHz is still larger than $1/\dim\mathcal{H}$ (here $1/2,002$), the expected value for perfect delocalization. The IPR continues to decrease upon further increasing T and E_J/E_C . Due to the presence of localized states at the edges of the spectrum, a saturation of the IPR is difficult to achieve. This holds even in the limit $T, E_J \rightarrow \infty$, since this corresponds to the regime of Anderson localization, see Sec. 4.6.4.

What constitutes a small IPR? The ‘smallness’ of a specific value of the IPR can be assessed from two different perspectives, which come to different conclusions. One can take the pure many-body perspective and compare the IPR to the inverse Hilbert space dimension or keep the intended use of the system as a quantum computer in mind. In the first ‘MBL vs. fully delocalized’ approach, one might argue with some justification that the wave function statistics behave similarly to the level ratios. Only when the IPR has dropped by two orders of magnitude—indicating that

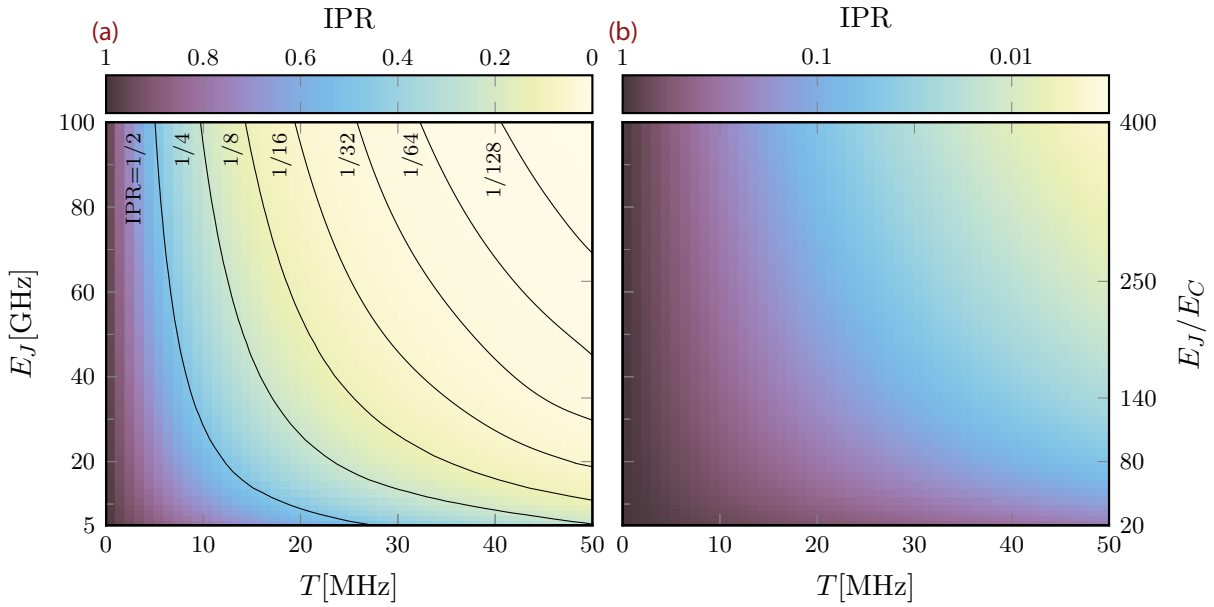


Figure 4.14 – Scheme-A wave function statistics. Both panels show the color-coded inverse participation ratio (IPR) for the same parameters and disorder realizations as in Fig. 4.13. In (a), the solid lines indicate contour lines of constant IPR. Already in the experimental particularly relevant smaller E_J/E_C region and for moderate coupling strength, the IPR drops heavily, foreshadowing that wave functions delocalize strongly for parameters where the KL divergences were nearly asymptomatic. Panel (b) shows the same data with a logarithmic color scale for the IPR for easier visualization of the behavior at large T and E_J : wave functions are not yet fully delocalized in the upper right corner, but the IPR is still in the process of decreasing.

many-body wave functions spread over a relevant fraction of the configuration space—do we find good agreement between the numerical results and the Wigner-Dyson statistics. On the other side, it is highly questionable whether a wave function with an IPR of, say, 0.2—although fairly localized in the MBL sense—can serve as a reliable computational state. It is this ‘viable vs. poor’ quantum computer perspective that we take when we judge the IPR to be more sensitive than the KL divergences.

With this in mind, our results draw the following picture of the parameter space: There is a small region with Poisson statistics and an IPR close to one and a chaotic region with Wigner-Dyson statistics and an $\text{IPR} < 0.01$. In between, there is an extended ‘twilight zone’ with Poisson and hybrid statistics characterized by significantly dressed yet not fully delocalized or even fairly localized wave functions. This region penetrates deeply into the experimentally relevant parameter regimes. Although we expect the strongly dressed wave functions with an IPR smaller than 0.5 to be compromised for quantum computing, it requires another approach that is to be discussed in Sec. 4.8 to quantify how much the computational states are endangered by these early symptoms of delocalization. As will be demonstrated, an IPR well above 0.5 is still small in the quantum-computing sense.

4.5.2 Results for scheme-B disorder

To complement the analysis for the ‘IBM-like’ design scheme A, we study the case of disorder that is larger by about an order of magnitude, exemplified in recent flux-tunable chips from TU Delft [94] and ETH Zürich [95]. The results for these simulations with scheme-B disorder,

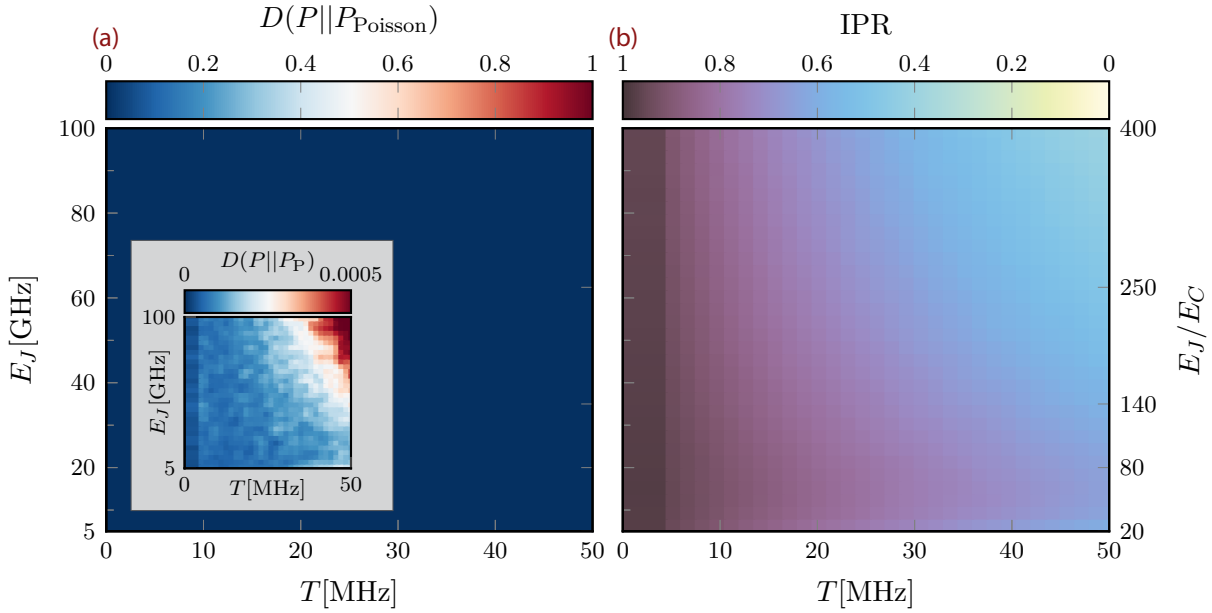


Figure 4.15 – Level and wave function statistics for scheme-B parameters. (a) The KL divergence with respect to the Poisson distribution exhibits no significant departures from MBL statistics. The small inset presents the same data set on an adapted scaling of the color coding to show that minor deflections start to set in for large T and E_J . (b) The IPR data show that wave functions hybridize to a much lesser extent than for scheme A, such that significant aberrations from the p -qubit states occur mainly outside the experimental core region. All results are averaged over at least 2,000 disorder realizations. The disorder strength extends from $\delta E_J \approx 4.7$ GHz for $E_J = 5$ GHz to $\delta E_J \approx 21$ GHz for $E_J = 100$ GHz whilst E_J is kept above 5 GHz, see Eq. (4.12) and Fig. 4.12.

as defined in Eq. (4.12), are shown in Fig. 4.15. As expected, increasing the disorder strength retracts the appearance of signatures of quantum chaos to much larger T and E_J/E_C values. The KL divergence with respect to the Poisson distribution, illustrated in Fig. 4.15(a), shows no significant deviation from what is expected in the localized phase throughout the entire considered parameter range. The small inset shows the KL divergence on a color scale that is customized to show the very marginal deviations that become visible in the upper right corner. The IPR in Fig. 4.15(b) drops below 1/2 only for parameters that lie well outside the region of particular relevance for experiments, indicating that the wave function spreading, despite still being significant, is much weaker than for scheme-A disorder. Upon very close inspection of panel (b), one observes a slight *increase* of the IPR for the lowest E_J/E_C values, in contrast to what is observed otherwise. This is a side effect of restricting the E_J distribution to values larger than 5 GHz. What, in the case of large average Josephson energies, only sorts out rare, particularly small realizations of E_J translates to a significant restriction of the disorder distribution for small mean E_J . Therefore, at the lower horizontal edge, the smaller effective disorder strengthens the tendency towards chaos, i.e., the dressing effect of the wave functions becomes stronger.

The general conclusion we draw from the level statistics and the IPR is that transmon-based quantum computers built according to scheme B and with typical E_J/E_C ratios, are considerably distant from the chaotic regime. However, as shall be discussed later, even in this seemingly advantageous scenario, many-body effects can impair the robustness of the computational states, the actual transition to the chaotic region being still very far away.

4.5.3 Data collapse

The realm of quantum chaos is entered not only for increasing the coupling T but also the Josephson energy E_J . The shape of the contour lines in Figs. 4.13 and 4.14 suggests a dependency of the form $E_J \propto 1/T^\alpha$ for curves connecting ‘equally chaotic’ parameter points. This can be confirmed by combining the effective model in Eq. (4.2) with the configuration space hopping picture visualized in Fig. 4.5. Thinking of the wave functions as states living on a high-dimensional lattice with dimension L and coordinates determined by the individual occupation numbers $i = (i_1, i_2, \dots, i_L)$, wave functions hybridize over a pair of lattice sites i and j if the hopping amplitude $t_{i,j}$ exceeds the level spacing, i.e., $|t_{i,j}| \gtrsim |\delta E_{i,j}|$, see the discussion after Eq. (2.27). Here, $\delta E_{i,j} = E_i - E_j$ is the difference in the many-body on-site energies on the two lattice sites i and j in the limit $t_{i,j} \rightarrow 0$. According to Eq. (4.2), $\delta E_{i,j}$ has two contributions, one from the disorder in the qubit frequencies and one from the anharmonicity. For illustration, consider the lattice sites $i = (\dots, i_n, i_{n+1}, \dots)$ and $j = (\dots, i_n - 1, i_{n+1} + 1, \dots)$, i.e., two nearest neighbors in configuration space that are connected via a single excitation hopping from transmon n to $n + 1$. Neglecting a potential change in the total anharmonicity, this modifies the energy due to the disorder in the transmon frequencies as $\nu_{n+1} - \nu_n$. This contribution to $\delta E_{i,j}$ is proportional to the disorder strength $\delta\nu$ and, therefore, kept constant in the T - E_J plots where δE_J scales as $\sqrt{E_J}$ to guarantee that the frequency disorder $\delta\nu$ is fixed to $E_C/2$.⁵ For the anharmonicity contribution, compare the hopping processes $(1, 0, \dots) \rightarrow (0, 1, \dots)$ and $(1, 1, \dots) \rightarrow (0, 2, \dots)$. The total anharmonicity does not change in the first process but is modified for the second. In general, $\delta E_{i,j}$ has a contribution kE_C , where k is an integer that depends on the local excitation numbers affected by the hopping process. Again, this contribution is constant in the T - E_J plots for any pair of states. Therefore, the many-body level spacing between any two high-dimensional lattice sites is independent of E_J . On the other side, the hopping amplitude $t_{i,j}$ is given by $\hbar J_{n,n+1}$, where, according to Eq. (3.47), $J \propto T\sqrt{E_J}$. In summary, one finds

$$\left| \frac{t_{i,j}}{\delta E_{i,j}} \right| \propto T\sqrt{E_J}, \quad (4.13)$$

which—for our peculiar disorder choice—should be the relevant scaling variable for the chaos-MBL transition concerning the parameters E_J and T . As anticipated from the numerical results, increasing E_J or T both reduces the distance to the territory of delocalization.

To verify the reasoning behind Eq. (4.13), we show that the individual horizontal traces of the KL divergences and the IPR underlying the phase diagrams in Fig. 4.13 and Fig. 4.14 can be collapsed onto each other when plotted as a function of the rescaled coupling parameter, $T \rightarrow TE_J^\mu$, where the exponent μ is the single free parameter. Fig. 4.16(a) and (c) show the data for the KL divergence and the IPR as a function of the coupling T , where each distinct color corresponds to one value of E_J . When the T axis for each individual line is rescaled according to its E_J value, one obtains a data collapse for $\mu \approx 0.54$, in good agreement with what is expected from Eq. (4.13). This is shown in the panels (b) and (d) of Fig. 4.16. Such a data collapse is typically considered strong evidence for the existence of a phase transition [330, 331].

Having confirmed that $|t_{i,j}/\delta E_{i,j}|$ is an important scaling variable, the connection between the scheme-A and scheme-B phase diagrams is revealed in a new light: Fig. 4.15 appears to be just

⁵As a technical remark, we note that it is the expectation value of the absolute distance between two independent draws from the ν distribution that determines $\delta E_{i,j}$. For normal distributed E_J s, the distribution of ν is not perfectly Gaussian but has a tail at smaller ν , arising from the dependence $\nu \propto \sqrt{E_J}$. We checked numerically that this ν distribution not only has the expected standard deviation of $E_C/2$, but also yields an E_J independent $\langle |\nu_i - \nu_j| \rangle$, if δE_J and E_J are related via Eq. (4.12).

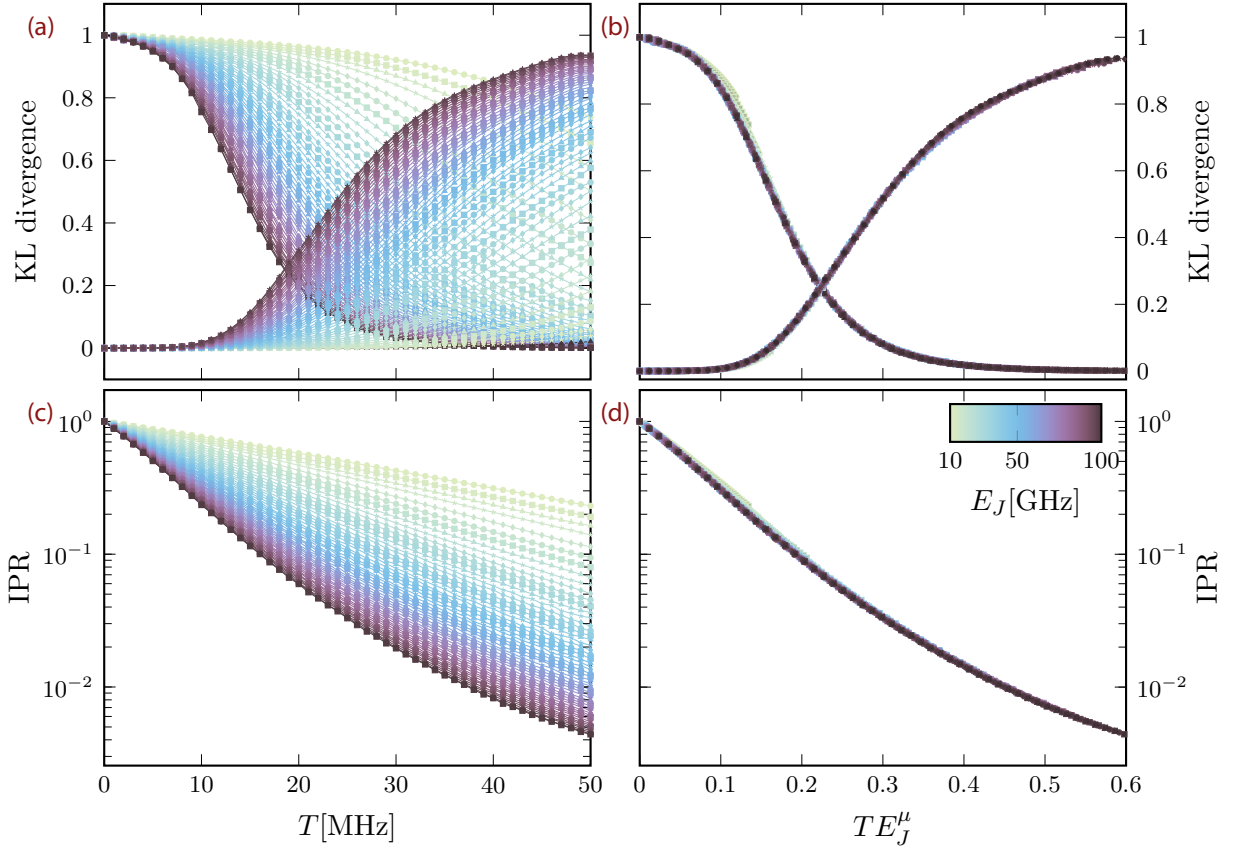


Figure 4.16 – Data collapse for KL divergence and IPR. The individual horizontal lines, forming the two-dimensional representations in the T - E_J plane from Fig. 4.13 and Fig. 4.14, are shown in the left column. They are collapsed onto each other by rescaling the coupling parameter with respect to the Josephson energy as $T \rightarrow TE_J^\mu$ with an exponent $\mu \approx 0.54$, as is shown left.

the small $|t_{i,j}/\delta E_{i,j}|$ part of the phase diagrams presented in Sec. 4.5.1. The data collapse works equally well for the IPR data of design scheme B with a similar exponent μ .

4.6 Further properties of the MBL-chaos transition

4.6.1 Many-body mobility edge

In all results presented so far, the level ratio and wave function statistics take all states of the excitation bundle with $N_{\text{ex}} = L/2$ into account. In systems where the total number of excitations (or the total magnetization in spin systems) is at least approximately conserved, many-body localization literature often follows a different path. It considers only a few states from the mid-energy range of the spectrum of an excitation bundle [183] or studies the transition between MBL and quantum chaotic regimes as a function of the normalized energy [164]

$$\epsilon = \frac{E - E_{\min}}{E_{\max} - E_{\min}}. \quad (4.14)$$

The energies E_{\min} and E_{\max} are the extremal eigenenergies. To complement our previous results, we also pursue this direction and compute Kullback-Leibler divergences as a function of the coupling T and the normalized energy (or energy density) ϵ .

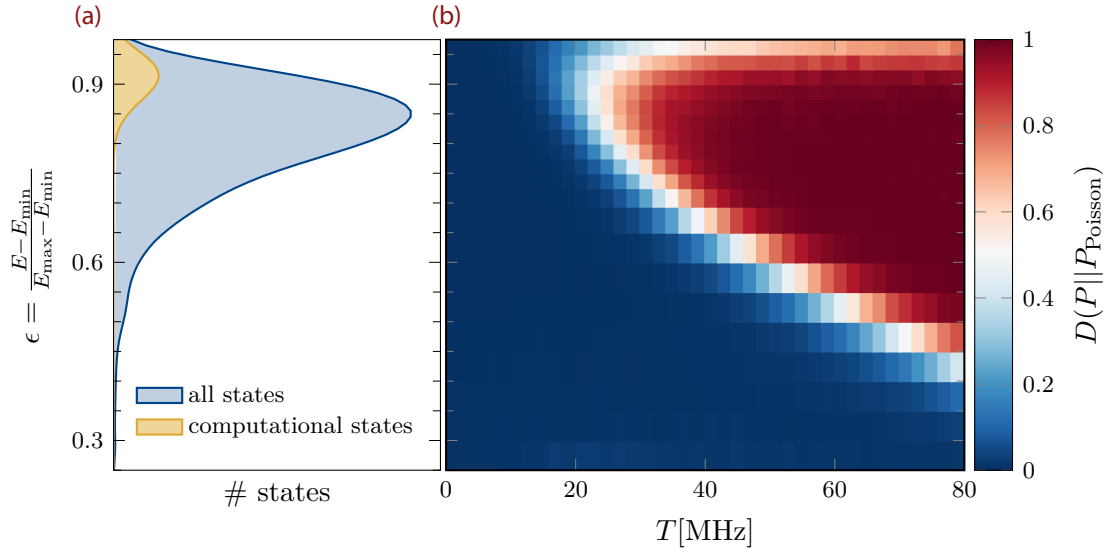


Figure 4.17 – Many-body mobility edge. (a) Number of states (blue) and number of computational states (yellow) as a function of the normalized energy ϵ for $N_{\text{ex}} = 6$, $L = 12$, $T = 0$ and averaged over 10,000 disorder realizations. The ϵ -resolved KL divergence, shown in (b) for $E_J = 44$ GHz and scheme-A disorder, demonstrates the emergence of a mobility edge, i.e., a dependence of the transition between chaos and MBL regime on the normalized energy with states close to the maximal DOS being particularly vulnerable. Results in (b) are averaged over at least 800 disorder realizations. More details are provided in the main text.

Fig. 4.17(a) shows the number of states (on the x axis) at a specific energy density ϵ for scheme-A disorder and $T = 0$. The distribution is averaged over 10,000 disorder realizations. In contrast to, e.g., the Heisenberg spin chain [181], the states are not symmetrically distributed around $\epsilon = 0.5$. The anharmonicity shifts the (few) states with a large total anharmonicity α_{tot} (see the definition in Sec. 4.2.1) downwards in energy, resulting in a long tail for small ϵ . For comparison, the number of computational states (for which $\alpha_{\text{tot}} = 0$) is also shown. As expected, they tend to sit in the upper part of the spectrum but, for the chosen disorder strength, intertwine with many more noncomputational states, similar to the situation visualized in the middle panel of Fig. 4.3.

The ϵ -resolved Kullback-Leibler divergence with respect to the Poisson distribution is shown in Fig. 4.17(b). The many-body mobility edge, i.e., the dependence of the transition between MBL and quantum chaotic regime on the energy density ϵ , is clearly apparent: For $\epsilon \lesssim 0.4$, all states remain localized even if the interaction strength increases to 80 MHz. As ϵ and along with it the density of states increases, so does the susceptibility to chaos. Near the maximal density of states, i.e., around $\epsilon \approx 0.85$, the level statistics closely follow Wigner-Dyson statistics already for $T \lesssim 30$ MHz. Finally, levels at the very top edge of the spectrum, where the number of states tails off, show fewer signatures of chaos, as can be read from the decrease in the KL divergence for the highest ϵ values shown. For all $T \gtrsim 25$ MHz, localized and chaotic states coexist. The main statement that Fig. 4.17 conveys is that the earlier stability estimate was conservative. All states were taken into account, but the relevant computational states are primarily located at energy densities that are especially prone to chaotic fluctuations.

The data underlying Fig. 4.17 are obtained for a chain of twelve transmons and the excitation bundle $N_{\text{ex}} = 6$, containing a total of 12,376 states. The discussion equally holds for the standard example of $L = 10$. For each disorder realization, the spectrum is divided into ϵ intervals of

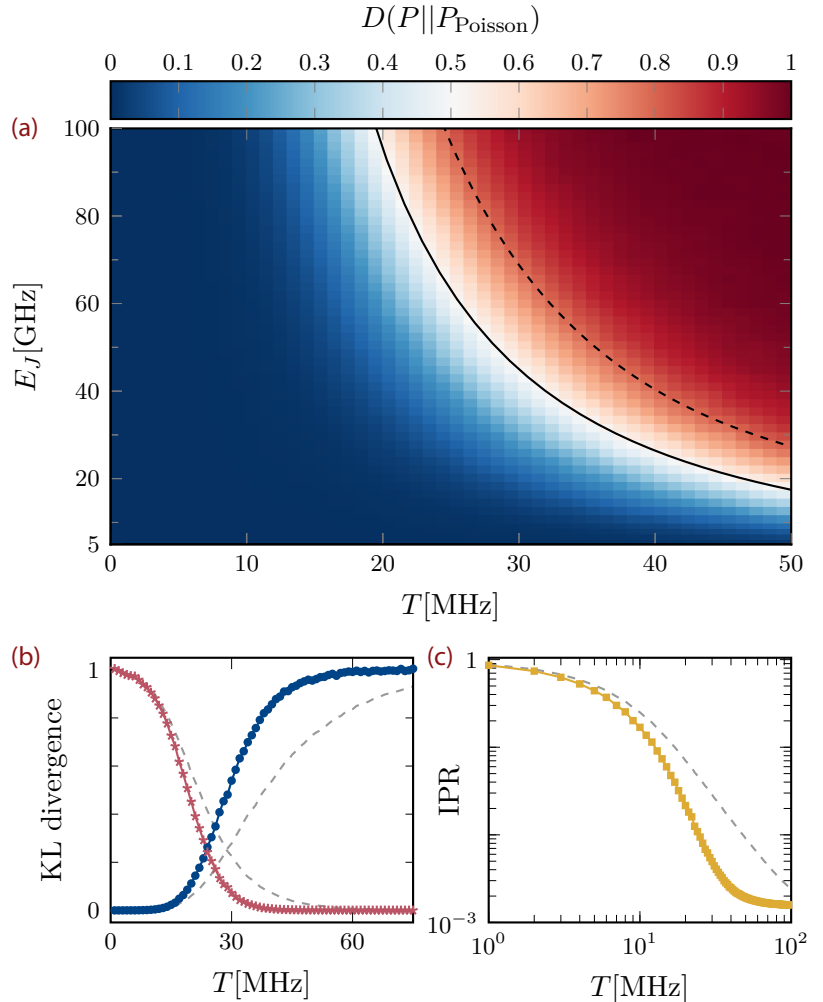


Figure 4.18 –
KL divergence and IPR for levels and states near the maximal density of states. Panel (a) is compiled for the same parameters and disorder realizations underlying Fig. 4.13(a) but only states within an interval of length $\Delta\epsilon = 0.05$ around the maximal DOS are considered. The solid (dashed) line indicates where the KL divergence has increased to 0.5 when only energies from the interval (all states) are considered for the level ratio histograms. In (b) and (c), the data underlying Figs. 4.8 and 4.10(a) are reevaluated and restricted to the levels and states near the maximal DOS. For comparison, the thin gray lines indicate the results from the earlier figures. A recurring motif in all three panels is a steepening of the curves, indicating a cleaner transition between MBL and quantum chaos. In (c), the Josephson energy is $E_J = 100$ GHz.

length 0.05 for $\epsilon < 0.7$ or 0.025 for $\epsilon > 0.7$. The R_n histograms are then calculated for all energies within the intervals. The number of levels contained in an interval varies between different disorder realizations. For each ϵ interval, the remaining steps of the evaluation of the KL divergences follow as described in Sec. 4.4.2.

The fragments of localization at the high and low ϵ edges of the spectrum explain the slow saturation of some of the exploited delocalization metrics towards the values one expects in the ergodic phase. For example, the large- T histogram in Fig. 4.8 deviates slightly from the perfect Wigner-Dyson distribution, which can be seen most clearly in the KL divergence with respect to the Poisson distribution, which is still well below one and grows only slowly upon further increase of T . Furthermore, in Fig. 4.10(a), the IPR has not yet settled toward its minimum value and continues to decrease as T increases. When focusing on a small density interval ($\Delta\epsilon = 0.05$) around the maximal density of states, these attributes disappear, as shown in Fig. 4.18. Panel (a) displays the KL divergence for the same disorder realizations as in Fig. 4.13. The levels entering the R_n histograms are now restricted to the interval specified above. The contour line where $D(P||P_{\text{Poisson}}) = 0.5$ drifts towards smaller T and E_J , and the data in the chaotic regime now show a better agreement ('deeper red') with the Wigner-Dyson distribution. This is corroborated by the data presented in the panels (b) and (c), which are based on the renewed

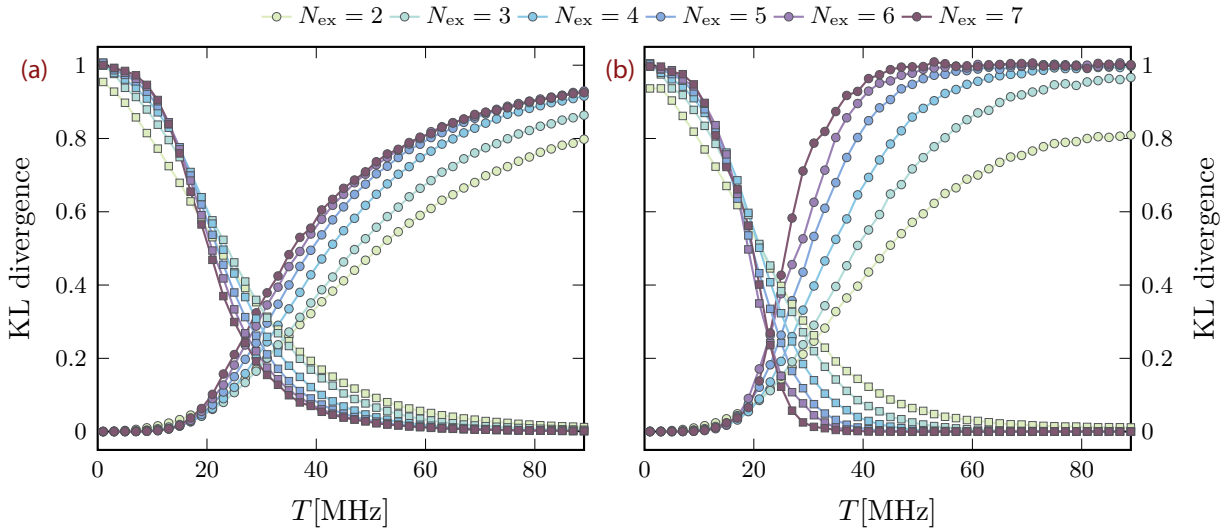


Figure 4.19 – KL divergence for various filling fractions. Shown are the KL divergences with respect to the Wigner-Dyson (square markers) and Poisson (circle markers) distribution. In (a), the KL divergence is averaged over the full bundles, whereas in (b), only the levels in an interval of width $\Delta\epsilon = 0.05(0.1)$ for $N_{\text{ex}} = 5, 6, 7(2, 3, 4)$ around the maximal DOS are considered. Both calculations show the same tendency of steeper increasing (decreasing) KL divergences for higher total excitation numbers, evidence of increasing susceptibility to chaos. The number of disorder realizations varies from $6 \cdot 10^5$ for $N_{\text{ex}} = 2$ to 500 for $N_{\text{ex}} = 7$ such that at least $2.5 \cdot 10^6 R_n$ values enter the averaged histograms in (a). The simulations use $E_J = 44$ GHz and scheme-A disorder.

evaluation of the disorder realizations underlying the representations of the KL divergences in Fig. 4.8 and the IPR in Fig. 4.10(a). When restricted to states near the maximal DOS, the KL divergence exhibits a steeper crossover from the Poisson to the Wigner-Dyson distribution. The level statistics indicate a fully chaotic behavior. This implies that the considerable extent of the zone of hybrid statistics is, to some degree, due to the fact that all states, including the integrable edges of the spectrum, entered the R_n histograms. It is considerably diminished in the above restriction scheme. The saturating of the IPR for $T \geq 40$ MHz in Fig. 4.18(c) indicates that the wave functions are now delocalized over all available states. A similar sharpening is observed for all wave function metrics considered in Fig. 4.10, as is detailed in Appendix B.4, together with a brief discussion of the data collapse near the maximal DOS.

4.6.2 Influence of the filling fraction

So far, our analysis spotlighted only properties of the ‘half-filled’ $N_{\text{ex}} = L/2$ excitation bundles. That was motivated by the observation that states with $L/2$ ‘1’s are the most numerous among the computational states. However, all computational states from $|000\dots\rangle$ to $|111\dots\rangle$ are important for computing. Therefore, we monitor the KL divergences for $L = 10$ and various filling fractions N_{ex}/L with N_{ex} ranging from 2 to 7 in Fig. 4.19. These bundles contain 55, 220, 715, 2,002, 5,005, and 11,440 states. In panel (a), the R_n histograms underlying the KL divergences contain all level ratios of a respective bundle, whereas they are restricted to levels around the maximal DOS in (b). The figure suggests a stronger predisposition to chaos in higher excited states. With increasing filling fraction, a steepening of the KL divergences signals departures from the realm of deep localization at an ever faster rate. For large coupling strength, higher-lying bundles quickly approach the regime of hard chaos that is free of remnants of

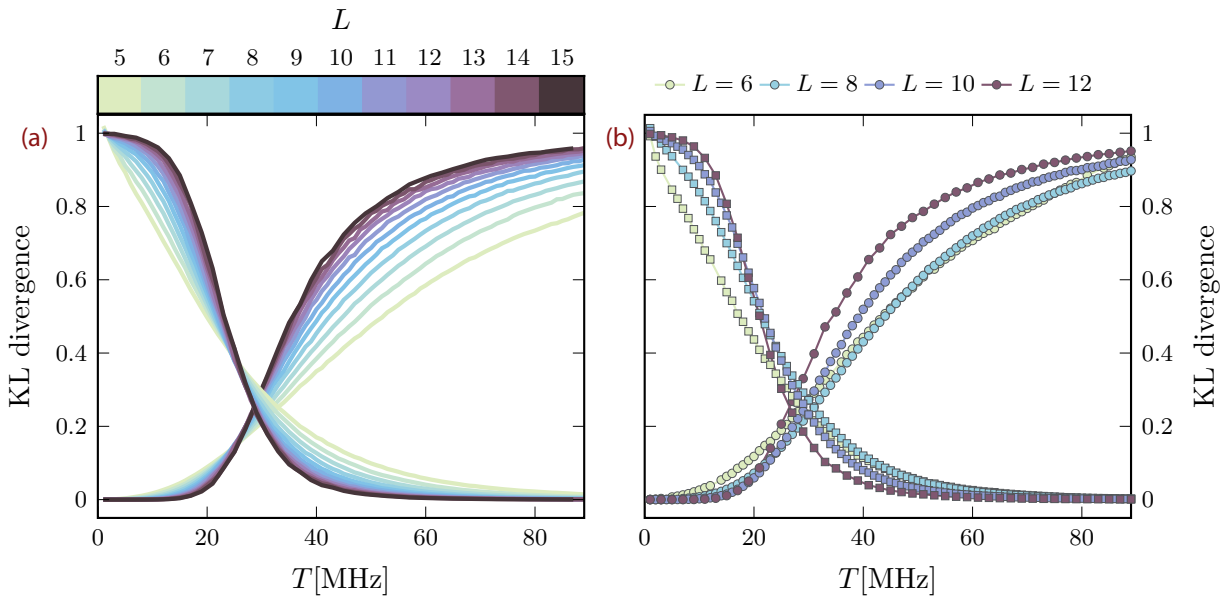


Figure 4.20 – Influence of the chain length L . (a) KL divergences for fixed $N_{\text{ex}} = 5$. The KL divergences appear to intersect at the same T values for all L , but there is a slight and barely discernible shift towards larger couplings. The number of disorder realizations varies from 60,000 ($L = 5$) to 1,200 ($L = 15$), such that roughly $8 \cdot 10^6 R_n$ values enter each averaged histogram. (b) KL divergences for fixed $N_{\text{ex}}/L = 1/2$. The crossing point between the curves for L and $L+2$ moves towards lower T for larger L . The number of disorder realizations is adjusted such that about $10^7 R_n$ values enter the histograms, except for $L=6$ ($2.5 \cdot 10^6 R_n$ values). In both panels, only full bundles are considered. The number of states per bundle is (a) 126 ($L = 5$), 252 (6), 462 (7), 792 (8), 1,287 (9), 2,002 (10), 3,003 (11), 4,368 (12), 6,188 (13), 8,568 (14), 11,628 (15), and (b) 56 (6), 330 (8), 2,002 (10), 12,376 (12). The main feature displayed in both figures is the steepening of the transition with increasing system size.

localization, as displayed by the quick saturation of $D(P||P_{\text{Poisson}})$ at 1. The KL divergences of the manifolds with fewer excitations converge much slower or, e.g., for $N_{\text{ex}} = 2$, never fully match the Wigner-Dyson prediction. This effect is more noticeable in panel (b). These findings reiterate the supposition that our previous estimation of the danger posed by quantum chaos is a conservative one. To maintain the usage of the transmon array as a quantum computer, all computational states must be sustained, including the one with $N_{\text{ex}} = L$.

4.6.3 Influence of the system size

For completeness, Fig. 4.20 provides an overview of the change of the system properties when the number of transmons is modified. For a fixed $N_{\text{ex}} = 5$ and varying chain length, the KL divergences are shown in Fig. 4.20(a). The most striking feature is the continuous steepening of the curves as the chain length L increases. Longer chains exhibit a sharper crossover with a less extended intermediate region of hybrid statistics. The KL divergences all appear to intersect at nearly the same value of the coupling (there is a slight shift towards larger T values for $L = 14$ and $L = 15$ that is not discernible in the figure). This behavior is not necessarily expected because this setup does not keep the filling fraction constant. Instead, it changes from 1 for $L = 5$ to $1/3$ for $L = 15$ and would vanish in the thermodynamic limit.

Panel (b) shows the KL divergences for varying L at the same filling fraction $N_{\text{ex}}/L = 1/2$. Ideally, the crossing points of the KL divergences for the chains of length L and length $L+2$ would

coincide for all $L = 6, 8, 10$. Instead, one observes a shift towards smaller T as L increases, where the distance between successive crossings decreases rapidly. One could expect a convergence to a finite T value, but valid statements cannot be made with the few points at one's disposal.

One should note that the system sizes under consideration are smaller than what is usually exploited for a finite-size scaling analysis [164]. Furthermore, this drift is not a pathology in MBL theory. A comparable behavior (a shift towards larger disorder strengths for a fixed coupling) has been observed in other systems, including in the level statistics of a similar Bose-Hubbard-like model [183]. Other measures also display this shift [162, 179, 332]. It is generally seen as an indication of the severity of finite-size effects at the MBL transition [201]. The latest developments in MBL theory [204, 205] teach us that even in systems where a finite-size scaling analysis seems to give unambiguous results at small system sizes, the actual transition takes place much deeper in the MBL regime than previously anticipated [333, 334]. In fact, the current discussion about the stability of the MBL phase started with an analogous observation [174]. Skeptics and MBL advocates agree that an accurate analysis of the MBL transition must inevitably incorporate numerical results beyond exact diagonalization and insights from perturbative expansions [201]. Therefore, we do not speculate on the finite-size scaling further and content ourselves with noting that the smeared step between the values expected for the extremes of deep MBL and hard quantum chaos steepens with increasing system size.

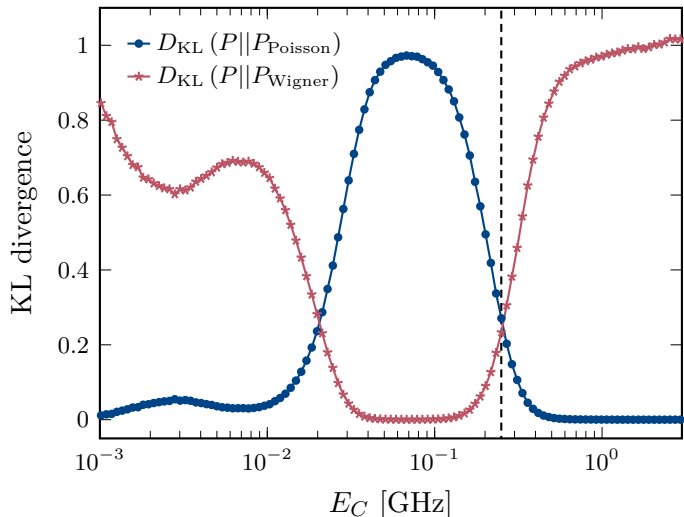
4.6.4 Anderson localization

For the moment, we depart from the experimentally relevant parameter ranges and consider the system's behavior as the charging energy E_C is varied while holding all other quantities constant. This is not possible in reality, where E_C is determined by the capacitance of the transmon's metal body and fixed at fabrication. Fig. 4.21 depicts the Kullback-Leibler divergences for scheme-A parameters for $E_J = 44$ GHz, $T = 30$ MHz, and E_C varying over several orders of magnitude. The dashed vertical line marks the charging energy of 250 MHz used in the previously discussed simulations. The parameter configuration at this point is identical to the one near the crossing point of the KL divergences in Fig. 4.8. Around this E_C value, the behavior of the KL divergences is easily deciphered: From the effective model in Eq. (4.2), the hopping amplitude for the bosonic excitations depends on E_C as $1/\sqrt{E_C}$. Hence, decreasing E_C enlarges the matrix elements $t_{i,j}$ that couple the many-body wave functions, similar to the discussion in Sec. 4.5.3. Accordingly, the system becomes more chaotic, as heralded by the drop in $D(P||P_{\text{Wigner}})$ and the increase in $D(P||P_{\text{Poisson}})$. By the same reasoning, the system penetrates deeper into the localized regime upon increasing the charging energy.

What is more striking in Fig. 4.21 is the reoccurrence of integrability for very small (and experimentally unrealistic) charging energies $E_C \lesssim 20$ MHz, reflected in a further swap of the two KL divergences. This behavior can also be inferred from the effective Hamiltonian \hat{H}_{eff} . The on-site interactions between bosons arise not from the transmon-transmon coupling but from the anharmonicity. Along these lines, the asymptotic case $E_C \rightarrow 0$ is the noninteracting Anderson insulator limit and is thus expected to be integrable. In Eq. (4.2), $E_C \rightarrow 0$ also implies $J \rightarrow \infty$ and $\nu_i \rightarrow 0$. To prevent this from inducing additional effects that are not to be attributed to the noninteracting limit, we performed further simulations where T and E_J are scaled such that ν , δ_ν , and J remain constant as E_C changes. Compared to Fig. 4.21, this does not cause any qualitative changes, indicating that the limiting case of Anderson localization is correctly portrayed as $E_C \rightarrow 0$. It should be emphasized again that this behavior is interesting from an academic perspective but irrelevant for real superconducting circuits where, for example, $E_C > T$ always holds.

Figure 4.21 –

Reentrance of Poisson statistics for small anharmonicities. When reducing the anharmonicity E_C to values way below what is acceptable for quantum computing applications, the system becomes integrable again. This is to be expected (at least in dimensions < 3) because $E_C \rightarrow 0$ corresponds to the noninteracting Anderson localization limit in the effective Hamiltonian \hat{H}_{eff} . Results are averaged over at least 4,500 disorder realizations. The simulations use $T = 30$ MHz and $E_J = 44$ GHz.



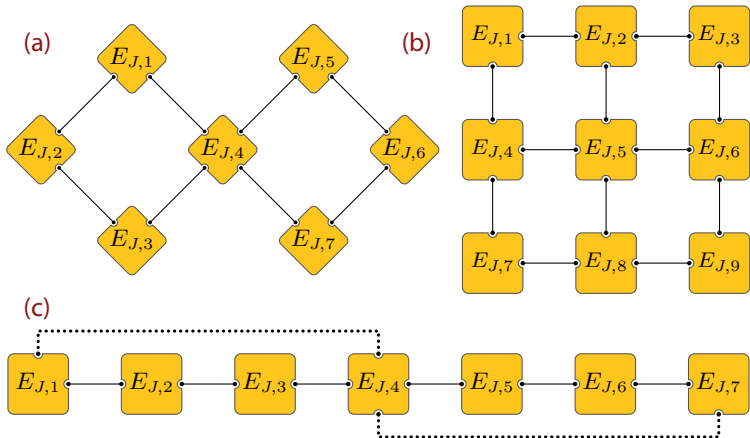
4.7 Towards two dimensions

So far, all conclusions have been reached for transmons arranged in a one-dimensional chain geometry, which is beneficial from an MBL perspective, as discussed in Chapter 2: exceptionally large disorder amplitudes can block transport between subsystems and thereby prevent thermalization. From the quantum computing perspective, however, this is deleterious because enacting controlled interactions between distant qubits involves a series of intermediate operations between nearby qubits, each of which is error-prone such that implementing circuits is substantially harder. Therefore, most real transmon quantum computers operate with a two-dimensional qubit arrangement. The most common geometries for processors are different cutouts of the square lattice in use, e.g., in chips by Google [39, 329], Delft [295], and ETH Zürich [95].

As minimal examples for two-dimensional architectures, we here discuss simulations of the surface-7 layout and a 3×3 array sketched in Fig. 4.22(a) and (b). Both geometries are employed in state-of-the-art experiments [108, 335]. The surface-7 geometry consists of a pair of square plaquettes. It emanates from the seven-transmon chain by adding two additional couplings between the transmon in the middle with the transmons at both ends, as visualized in Fig. 4.22(c). To extract the effect of the additional, higher-dimensional couplings, the simulations of the two-dimensional geometries are compared to the results for the chain geometries with the same number of qubits, i.e., $L = 7$ and $L = 9$. In the following, we discuss results obtained for scheme-A parameters. A summary of the scheme-B results is postponed to Appendix B.5.

Our findings for the spectral statistics ($D(P||P_{\text{Poisson}})$) and wave function statistics (IPR) for the surface-7 geometry are shown in Fig. 4.23(a) and (b). The dashed lines in the two panels summarize the results for the seven-transmon chain (c7). They indicate where (a) the KL divergence with respect to the Poisson distribution and (b) the IPR take the value 0.5. Adding two couplings to arrive at the surface-7 (s7) geometry dramatically changes the scenery: the comfort zone for quantum computing is considerably curtailed, and the contour lines are shifted significantly towards lower T and E_J values. This tendency is even more manifest in the findings for the geometries comprising nine transmons, shown in Fig. 4.23(c) and (d). For example, the distribution of the level ratios now shows good agreement with the Wigner-Dyson distribution in a large portion of the parameter range studied, whereas, for all one-dimensional geometries, such a good agreement was only found with a sufficient safety distance from the experimental core region.

Figure 4.22 – Two-dimensional transmon geometries. (a) Surface-7 geometry comprising a pair of square plaquettes and exploited, e.g., in Refs. [108, 295]. (b) 3×3 geometry used, e.g., in Ref. [335]. (c) Compared to an $L = 7$ chain, surface-7 has only two additional interactions created by connecting the ends of the chain to its center.



As the color coding in panel (c) further shows, the KL divergence not only increases faster but also quickly saturates at a value much closer to 1 than what has been observed before. This suggests that the effect of states at the edge of the spectrum that remain localized even at large T , as discussed, e.g., in Fig. 4.18, is considerably weaker in the 3×3 geometry. For the surface-7 geometry on the other side, after an initial sharp increase, the KL divergence climbs only slowly upon further increasing T or E_J , an effect we attribute to the smallness of the system.

In summary, the essential result here is that the vestiges of many-body localization are much less notable in two-dimensional geometries. Given that the existence of an MBL phase in two dimensions even tends to be denied, one should expect that these remnants of localization disappear quickly as the system size increases, and that chaos penetrates deeper into the experimental core region.

For all simulations, the level and wave function statistics are obtained for and averaged over all states of the $N_{\text{ex}} = 5$ bundle containing 1287 (3×3 and $L = 9$ chain) or 462 (surface=7, $L = 7$ chain) states. All results are averaged over at least 1,500 (seven transmons) and 2,500 (nine transmons) independent disorder realizations.

4.8 Qubit correlations

The preceding discussion taught us that transmon arrays of moderate size do not harbor solely a deeply chaotic and a fully localized region. Instead, it established the existence of an extended ‘twilight zone’ between the chaotic sea and the MBL regime. Therein, precursors of quantum chaos announce in the more sensitive wave function statistics, indicating a significant dressing of wave functions, whereas the level statistics give the illusion of complete safety or show merely weak indicators of hybrid statistics. A massive part of the experimentally relevant parameter range is covered by this intermediate regime. Here, we try to answer whether these parameter ranges are suitable for quantum computing or not. The approach guiding us here also cures the previous consideration of the weakness that it tends to underestimate the aftermath of delocalization by focusing on a single bundle and all states contained therein.

The dressing of wave functions is an effect the transmon community is well aware of and even knows how to turn to its advantage. An example is the implementation of the CR gate that exploits the nonlocality of qubits to produce entanglement with local microwave drives. A certain amount of dressing is thus not only inevitable but a necessary ingredient. On the other side, it is natural to assume that a small IPR renders computing impossible because qubit states

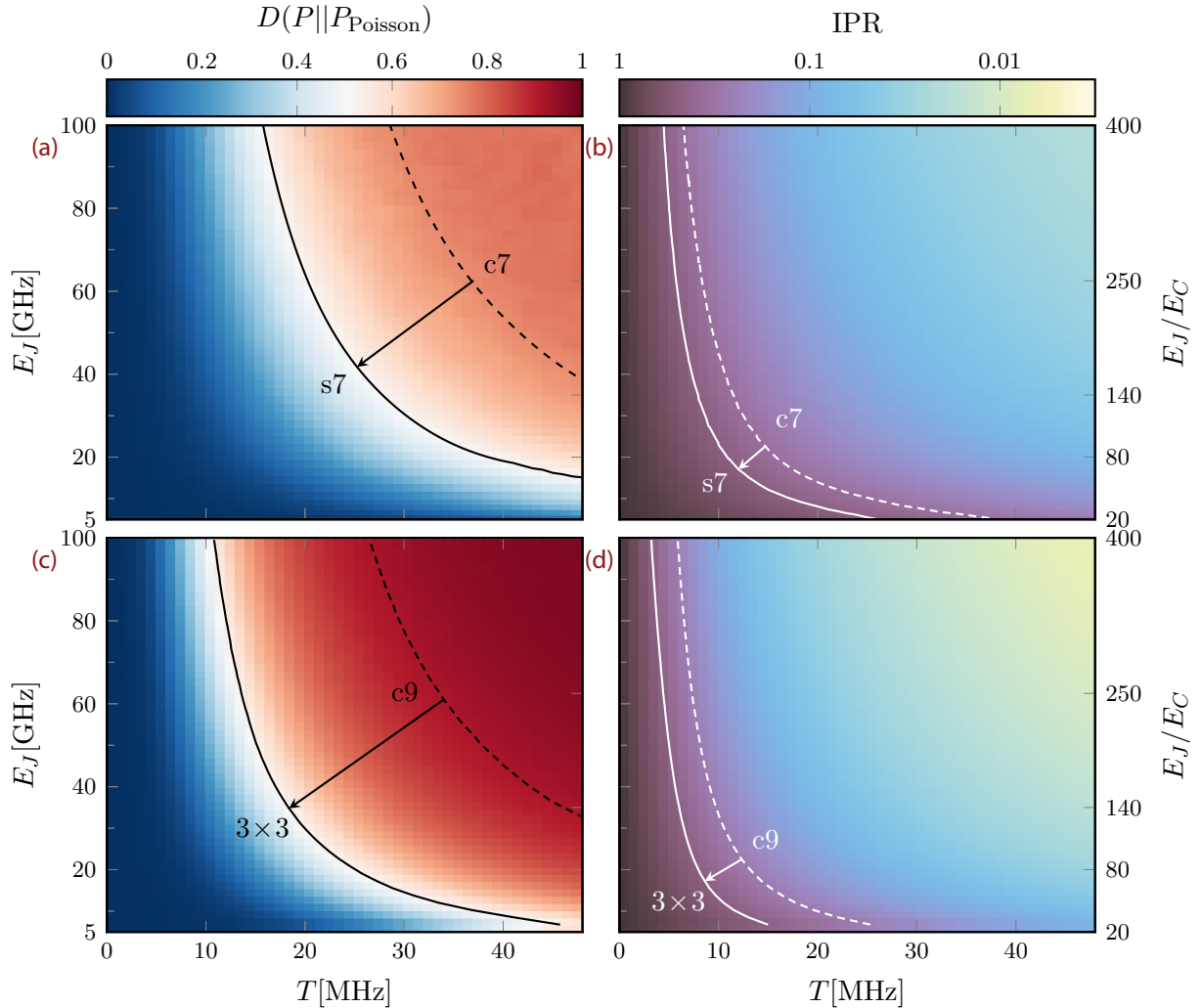


Figure 4.23 – Level and wave function statistics for two-dimensional geometries and scheme-A disorder. The upper row shows data for the surface-7 and the lower row for the 3×3 geometry. The KL divergence $D(P||P_{\text{Poisson}})$ is shown left, and the right column presents the IPR. The solid lines depict where the KL divergence (IPR) has decreased (increased) to 0.5. The equivalent contour lines obtained for the chain geometries with an equal number of transmons are drawn dashed. Compared to the chain geometries, chaos conquers a much larger part of the parameter space once coupling in a second dimension is added.

cannot be unambiguously identified. The question is whether this vague idea can be cast in a genuine measure. Can we somehow quantify how much the dressed l -qubits at our disposal can differ from the p -qubits before the obstacles become insurmountable? If yes, is an IPR of 10% sufficient, or are values closer to 90% required? Tackling these inquiries is crucial for assessing the danger posed by quantum chaos in current experiments settled in the twilight zone.

Fortunately, experimental transmon research can at least partly answer this question. What these efforts are concerned with, however, is not the IPR or a related delocalization metric but the strength of the correlations between the dressed l -qubits. The starting point is the general

form of a diagonal multi-qubit Hamiltonian,

$$\hat{H}_{\text{MBL}} = E_0 + \sum_i h_i \hat{\tau}_i^z + \sum_{i>j} J_{ij} \hat{\tau}_i^z \hat{\tau}_j^z + \sum_{i>j>k} J_{ijk} \hat{\tau}_i^z \hat{\tau}_j^z \hat{\tau}_k^z + \dots \quad (4.15a)$$

$$= \sum_{\mathbf{b}} c_{\mathbf{b}} \hat{Z}_1^{b_1} \hat{Z}_2^{b_2} \dots \hat{Z}_L^{b_L}. \quad (4.15b)$$

The second line introduces the quantum-information terminology for the familiar τ -Hamiltonian of MBL theory [165, 166], which is restated in Eq. (4.15a). The operators $\hat{\tau}_i^z$ are replaced by the Pauli-Z operators \hat{Z}_i . The b_i in Eq. (4.15b) are to be understood as exponents, not indices, i.e., $\hat{Z}_i^0 = \mathbb{1}$ and $\hat{Z}_i^1 = \hat{\tau}_i^z$. The sum is over the 2^L bitstrings $\mathbf{b} = b_1 b_2 \dots b_L$ of length L where each b_i is either ‘0’ or ‘1’. As a concrete example, consider the bitstrings $\mathbf{b} = 0010$ and $\mathbf{b} = 1011$ in a chain of four transmons. The corresponding contributions are $c_{0010} \hat{Z}_1^0 \hat{Z}_2^0 \hat{Z}_3^1 \hat{Z}_4^0 \equiv h_3 \hat{\tau}_3^z$ and $c_{1011} \hat{Z}_1^1 \hat{Z}_2^0 \hat{Z}_3^1 \hat{Z}_4^1 \equiv J_{134} \hat{\tau}_1^z \hat{\tau}_3^z \hat{\tau}_4^z$. Contributions comprising two (three, ...) \hat{Z} operators are called ZZ (ZZZ, ...) interactions. If all higher-order terms, ZZ, ZZZ, etc., vanish, the system is a perfect quantum memory, which is easily seen by moving to the interaction frame via the usual transformation $\hat{U} = \exp(it \sum_i h_i \hat{\tau}_i^z)$, where all quantum states remain stationary. However, the rapid drop in the IPR observed in the simulations suggests that the l -qubits described by $\hat{\tau}$ - or \hat{Z} -operators will differ significantly from the p -qubits formed by the ground and the first excited state of the individual transmons. As discussed in Sec. 2.3.2, this induces long-range ZZ, ZZZ, ... correlations between the l -qubits. Nonetheless, Eq. (4.15b) can describe a good quantum memory, provided that the weights of these terms are small. As of today, transmon research has focused solely on the two-body (ZZ/J_{ij}) terms [291, 336, 337] that cause dephasing of general qubit states and are the leading parasitic interactions that impede further improvement of two-qubit gates.⁶ Hence, great efforts have been made to mitigate this ‘crosstalk’ between neighboring qubits [336, 338]. In general, however, this involves a substantial amount of additional overhead, e.g., in the form of new coupling architectures [339], additional off-resonant driving [313], by combining transmon qubits with qubits that have opposite anharmonicity [337, 340], or by adding tunable couplers [341, 342]. A rough estimate for the level above which quantum computing becomes infeasible is $J_{ij} \sim 50\text{--}100$ kHz [337]. This ‘danger threshold’ is not to be understood as a fixed, broadly accepted upper limit but rather as a moving target that tends to shift toward lower values: earlier setups with flux-tunable transmons dealt with a residual ZZ interaction as large as 300 kHz [6], whereas in very recent work on a similar architecture, couplings lower than 8 kHz are still viewed with concern [95].

Here, we calculate the strength of all correlations $c_{\mathbf{b}}$ in Eq. (4.15b) for a chain of five transmons. Besides the fact that our results allow for a direct quantitative comparison to the above threshold, this analysis has the further advantage that it removes the basis dependence of the IPR: an l -qubit is a universal object that does not depend on a chosen representation, and the same applies to the strength of the correlations $|c_{\mathbf{b}}|$. Calculating the correlations is a two-step process. Before one can extract them from Eq. (4.15b), one has to begin with the nontrivial step of identifying the few qubit needles in a haystack of noncomputational states, as detailed in the next section.

4.8.1 Identifying qubit states

Embodied in the generic form of the Hamiltonian \hat{H}_{MBL} in Eq. (4.15b) is the idea of local *two-state* degrees of freedom. The actual bosonic Hilbert space of the full model (4.1), for which

⁶We already encountered one of its troublesome consequences in the context of the CR gate in 3.4. There, it was argued that due to the ZZ interaction, the driving frequency acquires a dependency of the target qubit state.

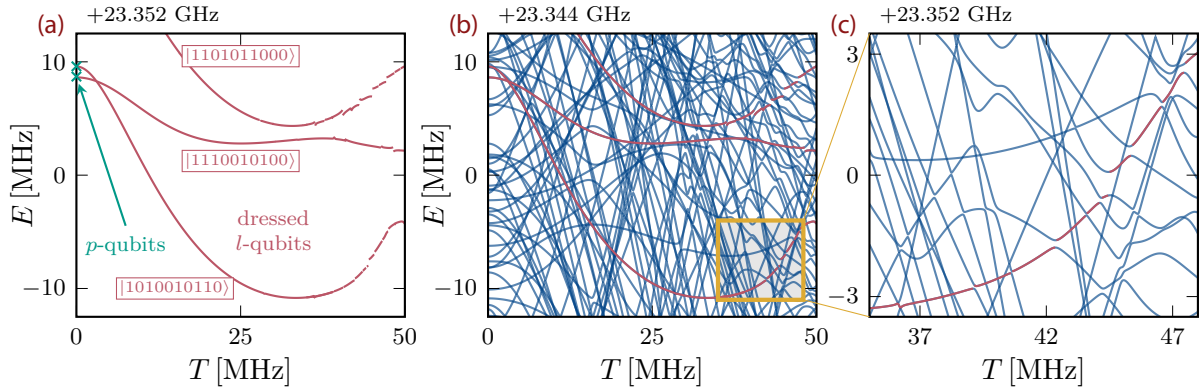


Figure 4.24 – Identifying qubit states. (a) Every quantum computing architecture operates under the assumption that L qubits and, thus, 2^L computational states are at hand. The two-level systems can be truly local p -qubits or l -qubits with contributions from neighboring sites if $T > 0$. However, this picture is a flagrant simplification: in real transmon systems, the qubit states are fully intermingled with (much more) states comprising local excitation numbers other than ‘0’ and ‘1’. This is demonstrated in (b) (the data are identical to Fig. 4.6). The first point to work through in any transmon quantum computing program is the transition from (b) to (a), i.e., the identification of a handful of computational states in a much larger surrounding Hilbert space. This can be accomplished by identifying computational states at $T = 0$ and tracking them through all the anticrossings visible in (b), a task that becomes increasingly difficult when the size of the anticrossing gaps increases for larger T . This is exemplified in (c), where a computational state is tracked through a series of anticrossings.

all preceding conclusions have been reached, is much larger because a transmon is a multi-level system. The compulsory first step towards quantum computing is to ignore all but the 2^L states identified as the computational states. This reduction is quite radical: For $L = 10$, the highest computational state $|111\dots\rangle$ has $N_{\text{ex}} = 10$. Constructing the basis from all product states obeying $N_{\text{ex}} \leq 10$, the $2^{10} = 1024$ computational states face 183,732 noncomputational ‘junk states’ living at similar energies⁷, i.e., only about 0.55% of the (already truncated) Hilbert space is relevant. The comparison of Fig. 4.24(a) and (b) illustrates this point: Panel (a) shows the situation one supposes for a quantum computer. Three multi-qubit energy levels of the Hamiltonian (4.15b) are shown as a function of T . However, the actual scenario in a real transmon processor is the one visualized in (b), where these computational states are fully intermingled with a much larger number of noncomputational states. Considering the extent of the simplification when moving from (b) to (a), the step may seem unnatural, but it is fundamental to any quantum computer.

Filtering out multi-qubit states is trivial for $T = 0$ because one can immediately map the 2^L bitstring labels to the p -qubits states with local excitations ‘0’ and ‘1’. To correctly assign the labels for $T > 0$, the idea is to follow the trace of the qubit levels, as shown in Fig. 4.24. As one might guess from Fig. 4.24(b), this is a delicate operation: one has to navigate through a dense bundle and decide at each (anti)crossing which path to follow further. Here, we find that at small T , anticrossings with small gaps arise, and the bitstring label follows the level running diabatically straight through the anticrossing. On the technical side, the *fidelity change* [343, 344] is exploited to detect and characterize the anticrossings in the spectrum. This procedure for the qubit label assignment works fine deep in the MBL phase, where the l -qubits retain large parts of the p -qubit identity, but becomes more ambiguous when the anticrossing gaps become

⁷This assumes that the excitation bundles are well-defined even for $N_{\text{ex}} = 10$, which is not necessarily the case. The situation is then even worse, with myriads of unbound states kicking in at relevant energies.

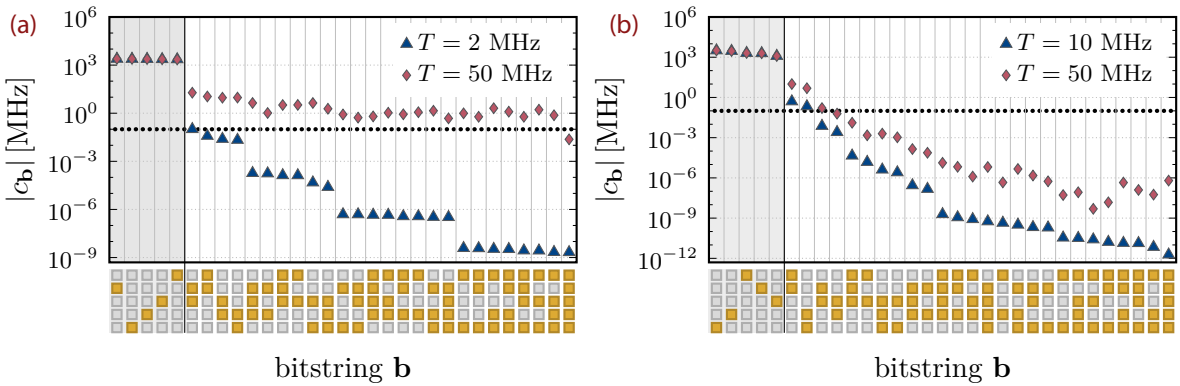


Figure 4.25 – Walsh coefficients⁸ $c_{\mathbf{b}}$ for two different values of the coupling strength T for (a) scheme-A and (b) scheme-B disorder. The x axis shows the 31 different bitstrings with at least one ‘1’. The bitstrings are represented as columns of five colored boxes where $\square = 0$ and $\blacksquare = 1$. For both disorder cases, one finds a hierarchy in the correlations according to their locality for small T . In the large- T data, the systematic is lost. This effect is stronger for lower disorder, as expected. In (a), nearly all correlations lie within the dangerous region estimated as $c_{\mathbf{b}} \gtrsim 100 \text{ kHz}$, marked by the dashed line. Again, this effect is less pronounced for scheme-B disorder, but some ZZ couplings exceed the threshold here as well. The large difference in the ZZ correlations for $T = 10 \text{ MHz}$ in (b) is a peculiarity of the specific disorder realization and not a generic feature.

gradually larger, as illustrated in Fig. 4.24(c). Finally, it is the defining property of the ETH phase that states cannot be distinguished from each other (by local operators). Consistently marking 2^L states as distinct qubits is, therefore, hopeless.

4.8.2 Extracting l -qubit correlations: Walsh transformation

Having performed the multi-qubit states identification, one is left with a subset of 2^L energies, each labeled with a bitstring tag \mathbf{b} . Restricted to the qubit subspace, the truncated diagonal Hamiltonian has the generic form

$$H_{\text{qubits}} = E_{00000}|00000\rangle\langle 00000| + E_{10000}|10000\rangle\langle 10000| + \dots + E_{11111}|11111\rangle\langle 11111|. \quad (4.16)$$

From this, the correlation coefficients $c_{\mathbf{b}}$ of the τ -Hamiltonian (4.15b) are directly inferred by a Walsh-Hadamard transformation [345]:

$$c_{\mathbf{b}} = \frac{1}{2^L} \sum_{\mathbf{b}'} (-1)^{b_1 b'_1} (-1)^{b_2 b'_2} \dots (-1)^{b_L b'_L} E_{b'_1 b'_2 \dots b'_L} = \frac{1}{2^L} \sum_{\mathbf{b}'} (-1)^{\mathbf{b} \cdot \mathbf{b}'} E_{\mathbf{b}'}. \quad (4.17)$$

The form of Eq. (4.17) suggests a certain similarity between the Walsh transform and the Fourier transform. In fact, for a bit length of 1 ($\mathbf{b} = 0, 1$), the connection between the ‘coefficients’ c_0, c_1 and E_0, E_1 reduces to a discrete Fourier transform where the length of the input sequence is two. For $L > 1$, Eq. (4.17) essentially describes an L -dimensional discrete Fourier transform of size 2 in every dimension [346]. It is a very instructive example to trace the transition from Eq. (3.52) to Eq. (3.53) in Sec. 3.4.2, explicitly using the tool of the Walsh transformation.

Fig. 4.25 introduces results for the coefficients $c_{\mathbf{b}}$ for $E_J = 12.5 \text{ GHz}$ and two fixed values of the coupling T . For the sake of clarity, we use a graphical depiction where each Walsh coefficient $c_{\mathbf{b}}$ is portrayed as five colored boxes representing the bitstring \mathbf{b} , e.g., the coefficient c_{11001} is visualized as $\blacksquare \blacksquare \square \blacksquare \blacksquare$. Fig. 4.25(a) displays the coefficients for scheme-A and (b) for scheme-B

⁸The data underlying Fig. 4.25 have been calculated by Evangelos Varvelis.

disorder. Shown are the 31 Walsh coefficients of a single disorder realization for a five-transmon chain⁹ with at least one nonzero bit in \mathbf{b} (c_{00000} is an irrelevant energy shift). In both panels, the $|c_{\mathbf{b}}|$ are sorted from largest to smallest for the small- T data (2 MHz for scheme A and 10 MHz for scheme B). For both disorder variants, we find the MBL expectation of a clear hierarchy in the coefficients according to their locality (i.e., the maximal distance between two ‘1’s in \mathbf{b}) confirmed if T is small: nearest-neighbor ZZ couplings are the largest, followed by bordering ZZZ and next-nearest-neighbour ZZ couplings, as predicted by Eq. (2.22). This can be seen particularly clearly in Fig. 4.25(a) for the $T = 2$ MHz data, where jumps in $|c_{\mathbf{b}}|$ by several orders of magnitude indicate that the maximal distance of two ‘1’s has increased by one. For stronger couplings ($T = 50$ MHz) and scheme-A disorder, the $|c_{\mathbf{b}}|$ no longer decrease continuously when following the bitstring axis from left to right, heralding the loss of the order by locality. For example, we find $|\text{██████}| > |\text{██████}|$. Of even greater importance is that all (but one) of the $c_{\mathbf{b}}$ have exceeded the danger threshold of 100 kHz indicated by the dotted line, in some cases by several orders of magnitude. For scheme-B disorder, these effects are less pronounced, as can be inferred from the large- T data in Fig. 4.25(b). A residual order by locality is recognizable, even if some $c_{\mathbf{b}}$ (those with a maximal distance of four or five) intermingle. Most correlations lie below the danger threshold; however, there are still two ZZ couplings that, according to consensus, are already large enough to jeopardize the functioning of the transmon array as a quantum computer. It is noteworthy that this result holds for parameters we would have prescribed—even with the sensitive IPR analysis—as deep in the MBL phase. The scheme-A results, where danger looms from all correlations, are obtained for parameters taken from the gray area between deep MBL and full delocalization, where at least the level statistics suggest equal proximity to integrability and hard chaos.

To further elaborate on this point, we show the evolution of the Walsh coefficients with increasing coupling strength T in Fig. 4.26 for (a) scheme-A and (b) scheme-B disorder. For clarity of visualization, this figure does not display all 31 correlations but only mean values, averaged as illustrated in Fig. 4.27. As we have verified, a conclusive picture is obtained by averaging not only the Walsh coefficients with the same pattern of ‘1’s (as in the second row of Fig. 4.27) but all coefficients with the same locality, i.e., the same maximum spacing between two ‘1’s, see the last row of Fig. 4.27. For scheme-A disorder, the averaged ZZ couplings approach the 100 kHz barrier already at a very low value of about 3 MHz. The contiguous ZZZ and next-nearest-neighbor ZZ terms follow shortly after at approximately 10 MHz, indicating that the integrity of the qubits is already compromised at coupling strengths associated with an IPR of around 0.8. For scheme-B disorder, the situation is somewhat more mellow, but strong ZZ couplings kicking in at around 10 MHz (again, a coupling strength that appears to be deeply MBL according to our previous diagnostics) show that even in flux-tunable transmons, the situation is far from being hazard-free. In particular, when comparing the critical T values extracted here to the coupling strength currently favored experimentally in the two different design strategies, one finds that they are comparable in size for both disorder classes. Hence, our results do not imply that recent scheme-B setups are less affected or even not affected at all. Furthermore, the fact that higher-order terms such as ZZZ , which have not yet been studied, let alone attempted to be ameliorated, are treading the ZZ coupling’s heels suggests that some of the aforementioned ingenious workarounds aiming to break the linkage between large T and strong ZZ couplings are ultimately insufficient.

⁹Note that in contrast to the preceding sections, the focus is not on a specific excitation bundle, but on all computational states. The Hamiltonian needs to be constructed with all basis states, ranging from $N_{\text{ex}} = 0$ to (at least) $N_{\text{ex}} = L$.

Figure 4.26 –

Averaged Walsh coefficients as a function of the coupling strength¹⁰ for a single disorder realization and (a) scheme-A disorder and (b) scheme-B disorder. Shown are the absolute values, averaged over all coefficients with the same maximal distance of two ‘1’s, as detailed in Fig. 4.27. The dashed line and the gray-shaded area mark the danger zone where $|c_b| \gtrsim 100$ kHz. For scheme-A disorder, ZZ correlations enter this region for couplings as small as 3 MHz, closely followed by next-nearest-neighbor ZZ and contiguous ZZZ couplings. For scheme-B disorder, the critical T value is about three times larger. Panel (a) also shows the specific coefficient c_{01101} . Jumps occurring here for $T \gtrsim 20$ MHz are a result of switching the labeling at avoided crossings with increasingly large gaps.

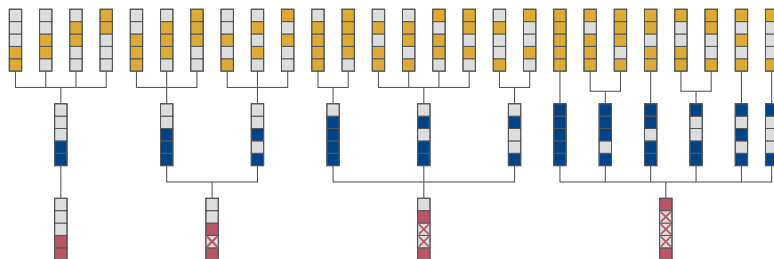
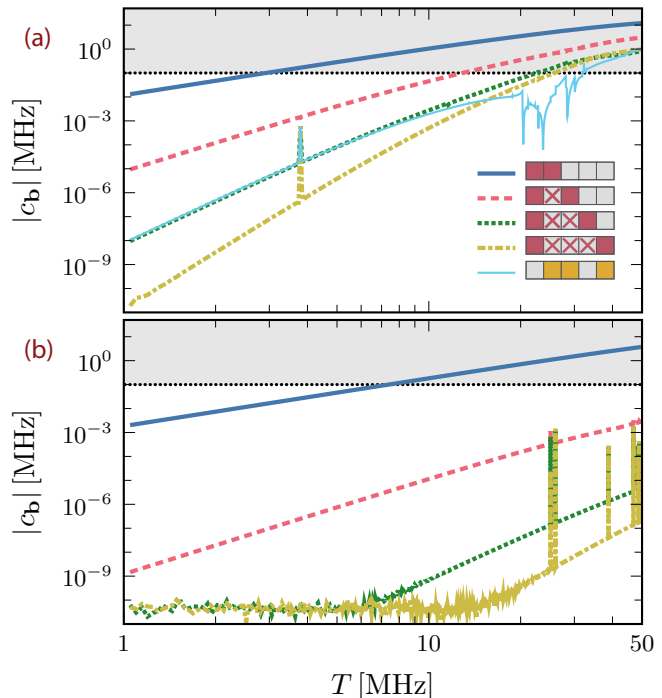


Figure 4.27 – Averaging correlations. The figure shows different ways to average the correlations, or Walsh coefficient, c_b to make the visualization in Fig. 4.26 more accessible. The first average is over equivalent correlations, i.e., bitstrings where the positions of the ‘1’s differ only by a translation or mirror symmetry. Our analysis reveals (in accordance with the MBL expectations) that no crucial information is lost when averaging over all bitstrings with the same maximal distance of two ‘1’s, as is done in the third row, leaving us with only four different classes of correlations that behave qualitatively different.

Briefly summarized, the Walsh-Hadamard transformation reveals that the twilight zone, identified as the region of hybrid or nearly Poisson statistics and with dressed wave functions, is compromised to a great extent. Even with an IPR of 0.8, i.e., almost perfectly localized wave functions, the l -qubit correlations become dangerously large. The comfort zone for quantum computing is considerably diminished to the small margin of T , where the IPR is close to one.

4.9 Dynamics

The information on whether locally encoded information is preserved at infinite times or quickly scrambled during thermalization is contained in the *static* wave functions of the Hamiltonian in Eq. (4.1) alone. Hence, we can conclude the suitability of a specific processor realization as a

¹⁰The data underlying Fig. 4.26 have been calculated by Evangelos Varvelis.

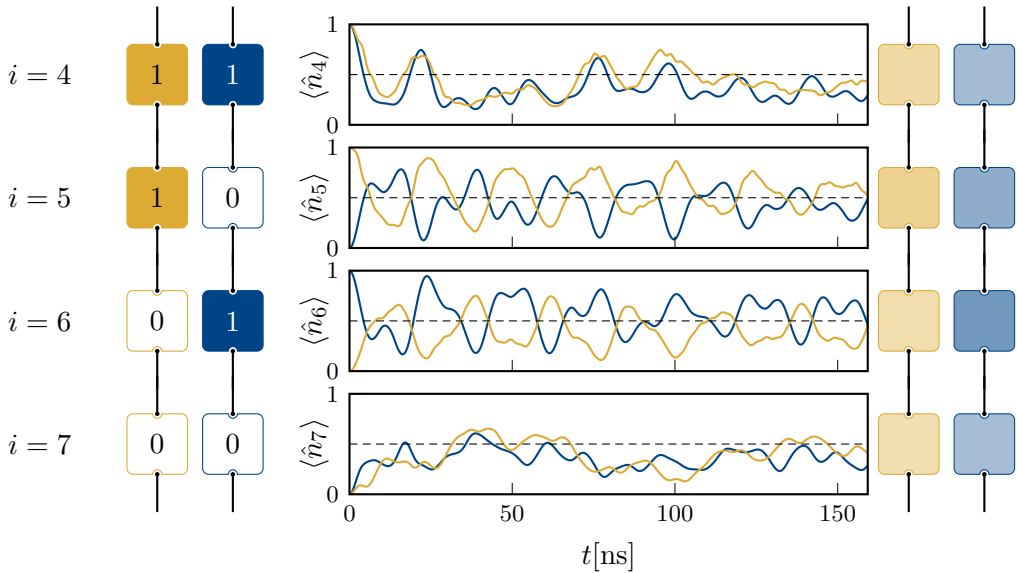


Figure 4.28 – Time evolution of local densities for a single disorder realization in a ten-transmon chain with $E_J = 12.5$ GHz and $T = 20$ MHz. Contrasted are the time-evolved densities $\langle \hat{n}_i \rangle$ for the transmon sites $i = 4-7$ for two different initial conditions, one with an alternating 0–1 pattern (blue) and one that has $\langle \hat{n}_5 \rangle = 1$ and $\langle \hat{n}_6 \rangle = 0$ but is otherwise identical (yellow). These initial states are visualized with the color coding of the transmon qubits sketched left (white = 0, deep yellow/blue = 1). For both initial conditions, all $\langle \hat{n}_i \rangle$ quickly approach 1/2. The distinct patterns are lost, and both initial configurations converge toward an approximately uniform density. This can be seen on the right, where the background opacity of the sketched transmons encodes the local densities averaged over 400 ns.

quantum memory without any dynamical considerations. For quantum computing applications, it is nevertheless interesting to relate the timescales on which the effects of chaos occur to typical qubit lifetimes. Thus, we close the circle and simulate quench experiments, the initial means to illustrate the danger inherent to chaotic fluctuations. We consider an $L = 10$ chain geometry subject to scheme-A disorder and set $E_J = 12.5$ GHz. An initial product state with nonuniform excitation density, like $|0101\dots\rangle$, is time evolved under the full Hamiltonian in Eq. (4.1). To monitor the loss of information, we examine, e.g., the weight $|\langle \psi_0 | \psi(t) \rangle|^2$ of the initial state $|\psi(0)\rangle$ in the time-evolved wave function $|\psi(t)\rangle$, or the IPR of $|\psi(t)\rangle$. For states like $|0101\dots\rangle$, the time evolution of the staggered density,

$$n_{\text{stagg}} = \frac{1}{L} \sum_{i=1}^L (-1)^i \left(\langle \hat{n}_i \rangle - \frac{1}{2} \right), \quad (4.18)$$

is also a useful indicator for the remanent information content [347]. This quantity has been used as a yardstick for many-body localization in ultracold atom experiments [208, 348]. As before, \hat{n}_i in Eq. (4.18) returns the level number l when acting on the single transmon eigenfunction belonging to the l th level and is equal to the occupation number in the Bose-Hubbard limit. The term 1/2 guarantees that $|0101\dots\rangle$ has $n_{\text{stagg}} = 1/2$, making Eq. (4.18) similar to the definition of the staggered magnetization in spin systems [188]. It should be noted that n_{stagg} is not bounded by 1/2 in the bosonic transmon system.

To begin with, we consider the two initial computational states $|\psi_0^A\rangle = |0101010101\rangle$ and $|\psi_0^B\rangle = |0101100101\rangle$. $|\psi_0^A\rangle$ has a strictly alternating 0–1 pattern. For $|\psi_0^B\rangle$, the excitation numbers at transmon sites 5 and 6 are swapped. This is illustrated in the two transmon chain excerpts shown left in Fig. 4.28, where the opacity of the background color encodes the local

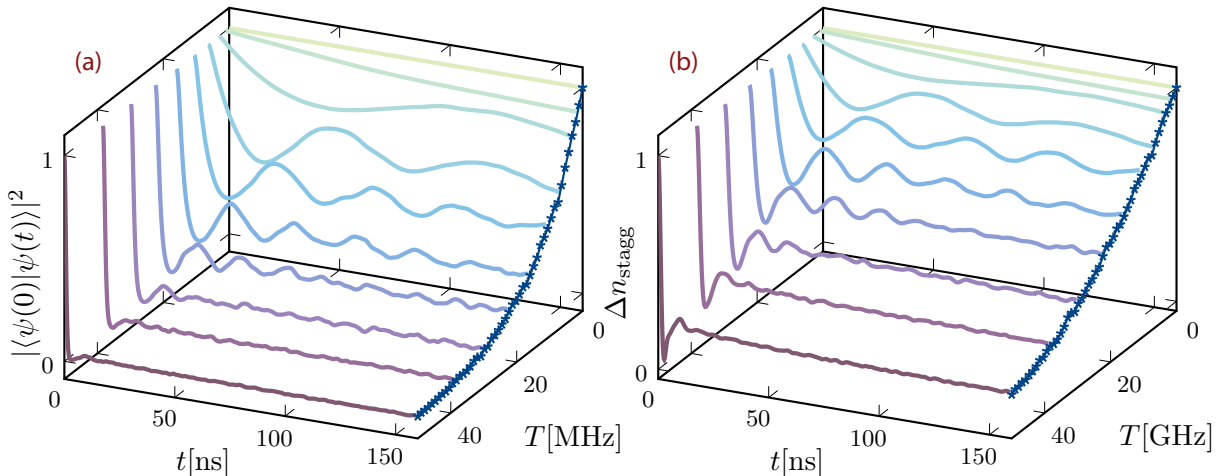


Figure 4.29 – Information loss and relaxation. (a) Overlap of the time-evolved wave function $|\psi(t)\rangle$ with the initial state $|\psi(0)\rangle = |0101\dots\rangle$. (b) Difference in the staggered excitation density for the two maximally dissimilar initial states $|\psi_A(0)\rangle = |0101\dots\rangle$ and $|\psi_B(0)\rangle = |1010\dots\rangle$. Both panels demonstrate that relaxation happens on timescales shorter than transmon qubit lifetimes. The long-term averages shown in blue on the right in both panels indicate that information is preserved in the MBL regime (small T) but quickly decreases upon increasing T . The simulations are performed for scheme-A disorder and $E_J = 12.5$ GHz. All results are averaged over at least 800 disorder realizations.

excitation number $\langle \hat{n}_i \rangle$. The four panels in the center of Fig. 4.28 show the time-evolved $\langle \hat{n}_i(t) \rangle$ for a single, randomly chosen disorder realization. The evolution of $\langle \hat{n}_4 \rangle$ and $\langle \hat{n}_7 \rangle$ is similar for $|\psi_0^A\rangle$ and $|\psi_0^B\rangle$. The expectation values do not stick close to their initial values but fluctuate, frequently crossing the line where $\langle \hat{n}_i \rangle = 1/2$, which makes inferences about the initial value unfeasible. In addition, $\langle \hat{n}_5 \rangle$ and $\langle \hat{n}_6 \rangle$, the two values in which $|\psi_0^A\rangle$ and $|\psi_0^B\rangle$ initially differ, approach each other and fluctuate with decreasing amplitude around the value 1/2. Hence, the difference between the initial states is quickly blurred out. The data presented span a time range of 150 ns, the lower end of gate times in fixed-frequency architectures and much shorter than transmon qubit lifetimes. The colored backgrounds in the transmon cartoons shown right encode the time-averaged local densities, where the average is over 400 ns, showing that the initial density wave turns into an approximately uniform, and thus information-free, distribution¹¹.

Next, we consider disorder averages and vary the strength of the capacitive coupling. Fig. 4.29(a) shows $|\langle \psi_0 | \psi(t) \rangle|^2$ for $0 \leq t \leq 150$ ns and values of T between 0 MHz and 50 MHz. One observes a similar behavior for all couplings: an initially rapid drop is followed by a spell of small fluctuations around a saturation value that is smaller for larger T . The IPR of $|\psi(t)\rangle$ (not shown) exhibits the same behavior, indicating that initial information is quickly erased. The blue curve, drawn right in Fig. 4.29(a), is an estimate for the long-term remanent information. Shown is the time-averaged weight $|\langle \psi_0 | \psi(t) \rangle|^2$ where the average is over $150 \mu\text{s}$, i.e., typical decoherence times of fixed-frequency transmons and three orders of magnitude larger than the time range shown. For small couplings, the remanent information is close to one, as expected for parameters taken from deep in the MBL region. It quickly decreases as the MBL regime is left behind upon increasing T . For all coupling strengths, the long-term average is approached within the first 150 ns, for larger couplings $T > 20$ MHz even much earlier, see the purplish lines. Once the proximity of the long-term average is reached, $|\langle \psi_0 | \psi(t) \rangle|^2$ always stays close to it.

¹¹We verified that all $\langle \hat{n}_i \rangle$ fluctuate only weakly around the long-term averages.

Fig. 4.29(b) visualizes the difference in the time-dependent staggered density, $\Delta n_{\text{stagg}} = n_{\text{stagg}}^A - n_{\text{stagg}}^B$, where $|\psi_A(0)\rangle = |0101\dots\rangle$ as above and $|\psi_B(0)\rangle = |1010\dots\rangle$. These two states have the maximal possible Hamming distance [349] and differ in every single qubit value. As before, the time-averaged Δn_{stagg} is shown in blue on the right side. Δn_{stagg} behaves similarly to $|\langle\psi_0|\psi(t)\rangle|^2$. The fraction surviving for long times is close to one for small couplings, indicating that $|\psi_A\rangle$ and $|\psi_B\rangle$ are distinguishable over an entire qubit lifetime. Upon raising the coupling strengths, the remaining staggered density difference quickly decreases, and the information about the respective excitation pattern is lost. One again observes that equilibration happens on timescales of only a few nanoseconds.

We repeated the above analysis for $E_J = 44$ GHz and $E_J = 100$ GHz. The result is not surprising: thermalization happens in even shorter times, and the long-term averages of $|\langle\psi_0|\psi(t)\rangle|^2$, the IPR, and Δn_{stagg} are smaller than for $E_J = 12.5$ GHz.

What are the conclusions from this section? In a nutshell, it reinforces, but does not exacerbate, our findings from Sec. 4.5. If the static properties of the Hamiltonian indicate potential threats for quantum computing, then this danger sets in on relevant timescales. The long-term averages shown in Fig. 4.29 can be compared to the IPR. One then finds that a small IPR is associated with a significant and almost immediate information loss. For large IPRs, the information loss is only small.

4.10 Summary

All transmon-based quantum technology must find a way to navigate the narrow path between the Scylla of inefficiency (slow gates due to small T or large detunings) and the Charybdis of quantum chaos (large T , small disorder). Within this field of tension, there are different ways to lead the construction of localization-protected processor architectures to success. Two main strategies are to employ weak coupling at weak detuning, called scheme A here, or to intentionally introduce strong disorder (scheme B). What are entirely different engineering philosophies with different hardware setups reduces—from the MBL perspective—to different ways of blocking the tendency of quantum states to spread due to inter-transmon coupling by a sufficient amount of frequency detuning. The subject of this chapter has been the utilization of numerical simulations to study the robustness of these distinct design blueprints against the destabilizing impacts of quantum chaos. Using methodology of many-body localization theory—level ratio statistics, many-body wave function statistics, and quantification of l -qubit correlations via a Walsh-Hadamard transformation—we could map out the proximity of realistic present-day small-scale transmon processors to the ubiquitous sector of chaotic fluctuations.

As a first important result, our studies show that transmon arrays are suitable models to observe the transition from an MBL regime to a phase of chaotic fluctuations. The latter arises for strong capacitive coupling or small disorder in the Josephson energies, or, in MBL terminology, when the hopping amplitude between many-body wave functions is comparable to the on-site energy difference in the high-dimensional configuration space lattice.

A second major lesson is that the chaotic phase casts shadows that are much longer than one might have hoped: For scheme-A parameters, broad areas of experimentally relevant parameter ranges are affected by early indicators of quantum chaos, which limits the allowed range of coupling strengths to a few MHz, ultimately preventing faster gates in these architectures. In particular, computational states react very sensitively to the slightest deviations from the limit of extreme localization and become partially compromised, with the boundary to hard chaos still being far off. This entails the existence of a gray area in the parameter landscape: for couplings

where the system is still integrable according to the level ratio statistics, quantum information processing is nevertheless challenged by—not to say impossible because of—the strong dressing of wave functions and significant l -qubit correlations. One may be tempted to argue here that the existence of such a twilight zone is merely an artifact of the smallness of the systems studied, comprising only $\mathcal{O}(10)$ transmons. However, as current and medium-term future NISQ devices operate only with $\mathcal{O}(10)$ to $\mathcal{O}(100)$ qubits, finite-size effects are expected to play an essential role on technologically relevant scales. Furthermore, recent developments in localization theory emphasize that the actual MBL *phase* arising in the thermodynamic limit occupies far less parameter space than previously thought. To push it to the extreme: if the pessimists, who classify the localization phenomenon as a whole as a finite-size effect, are right, then the finite-size MBL *regime* is the best one can hope for. This applies all the more in higher-dimensional geometries, for which the prevailing view in the MBL community is that localization cannot be maintained in the thermodynamic limit.

For scheme-B parameters, representing the class of flux-tunable transmon architectures, the chaotic regime, just like the early indicators of compromised computational states, is pushed back to much larger coupling strengths. This buys the possibility of larger couplings and faster gates. However, the danger is not completely averted, as our Walsh transformation analysis has revealed.

Concerning the hierarchy in the sensitivity with which our diagnostic tools respond to the initial effects of chaotic fluctuations, we discussed the need to carefully balance the pristine MBL perspective and the more applied quantum computing perspective. Ultimately, it is this difference that establishes the existence of the gray area. From the applied perspective, the level statistics is a coarse tool that suggests safety in regions where the IPR already indicates a tendency of strong wave function spreading, although only over a small fraction of the available states. As alluded to, it is far from obvious that quantum computing should not be affected by initial signatures of delocalization (that are known to occur even in the MBL *phase* [191]) and only becomes impossible when states are completely delocalized. The Walsh analysis, focusing exclusively on the computational states and applied in the MBL context for the first time in our studies, confirms that the pessimism is justified. It confirms the threat to information processing applications indicated by the IPR drop in a basis-independent manner. By providing *absolute* bounds underpinned by experiments, we can connect it to the IPR and derive a danger threshold below which quantum computing becomes tarnished. This is beneficial because the IPR is considerably simpler to calculate. Our analysis suggests that ZZ correlations dangerously compromise the computational states when the IPR is still at around 0.8—hence, at the beginning of the gray area, which the MBL perspective would have declared as almost chaos-free. Even higher correlations are already waiting in the wings.

In summary, our study shows that traces of chaos are more prominent in the scheme-A design format. We expect that attempts to expand these architectures to larger or higher-dimensional geometries, which already is a tantalizing challenge for the reasons discussed in Sec. 1.5, gain additional complexity due to the MBL-related obstacles. But even flux-tunable transmon architectures are vulnerable. For a reliable cross-design scheme comparison of real devices, one should consider the coupling strength values to which the respective communities have converged in their experimental efforts over the years and consider the dimensionless parameter $\delta E_{i,j}/t_{i,j}$. In this respect, IBM devices and typical flux-tunable architectures do not differ much¹², and representative example processors are in the MBL phase. However, the scheme-A architectures are bound

¹²As discussed in Sec. 4.5.3, $\delta E_{i,j}$ contains contributions from the frequency disorder and the anharmonicity. Neglecting the latter, typical values of the ratio $\delta\nu/t_{i,j}$ are around 30 for both processor variants.

to the very small values of T ; otherwise, the early symptoms of delocalization become apparent. Since increasing the disorder is also not possible due to the specific needs of the CR gate, there is no room to shorten the gate time.¹³ Flux-tunable architectures can operate at much larger couplings while remaining in the MBL regime. This enables much shorter gate times, both absolute and compared to the respective qubit lifetimes.

Adapting to a more philosophical definition of the design approaches not by specific values of $\delta\nu$ but rather by their general handling of randomness, the tunable-coupler architectures bear some similarity to the scheme-B design: Both embrace disorder as a resource to protect information. However, the dimensionless parameter $\delta\nu/t$ is orders of magnitude larger when tunable couplers are exploited because the denominator can be tuned to zero (in a perturbative sense). Tunable couplers might thus offer a fundamental improvement from the MBL perspective, but they are not a panacea due to their huge hardware overhead.

With the drawbacks of fixed-frequency designs in mind, we devote the next chapter to the question of whether implementing frequency patterns can contribute to improving these processors.

¹³For completeness, we mention again that meticulously designed control pulses could reduce the gate time [300]. This has not been implemented experimentally.

Quantum chaos and frequency engineering

In its pursuit of better gate fidelities, IBM has proposed to implement frequency patterns where neighboring qubits are detuned by an amount that ideally circumvents the most urgent frequency collisions in the operation of the CR gate [306]. At the same time, in an engineering tour de force, they provided the LASIQ technique as a tool that might accomplish the realization of high-precision patterns in the future [294]. As of today, the annealing technique has been exploited to tweak the as-fabricated frequencies to eliminate some of the most pressing nearest-neighbor (NN) collisions, but no regular frequency ‘unit cell’ was implemented in any of the cloud devices. In this chapter, we risk looking into the (eventual) future and study systems with regular frequency arrangements to investigate these precision-engineering maneuvers—intended to increase two-qubit gate fidelities—from the many-qubits perspective.

This chapter is partly based on the publication [P1] by the author of this thesis.

5.1 Frequency pattern

IBM’s heavy-hexagon lattice favors an *ACBC* arrangement with three different mean frequencies, as shown in Fig. 3.16. Most conclusions in this chapter rely on simulations conducted for the simpler *ABAB* sublattice structure superimposed on a 3×3 transmon geometry as sketched in Fig. 5.1(a). The two sublattices are populated with Josephson energies drawn from normal distributions centered around $E_{J,A}$ and $E_{J,B}$, see Fig. 5.1(b) for a visualization. The width of the distributions, to which we refer as the residual disorder strength, is determined by the LASIQ precision. We expect the principal many-body properties to be the same in this layout and IBM’s more ambitious approach. Sec. 5.4 gives a brief MBL-inspired glance at the ideal of an IBM processor. The choice of parameters used in this chapter is closely guided by the recent reports on LASIQ-tuned transmon processors [294, 308]. To be specific, we take $E_{J,A} = 12.57$ GHz and $E_{J,B} = 13.79$ GHz [294] and set the anharmonicity to $E_C = 330$ MHz, the prototypical value of IBM’s cloud devices [59]. The current precision with which a desired target Josephson energy can be achieved is about 60 MHz [294], which is an order of magnitude better than what is found in pre-LASIQ transmons. The distributions for E_J before and after LASIQ-tuning are contrasted in Fig. 5.1(b).

Here, we aim to examine how further progress in the LASIQ precision affects the localization properties of the transmon array by simulating disorder strengths down to the asymptotic case of the clean $\delta E_J = 0$ device. This is a topical and relevant issue because significant improvements in tuning precision are needed to scale beyond 100 to 200 qubits [294], a frontier that has already been exceeded as of today (and even with a fixed-frequency transmon architecture).

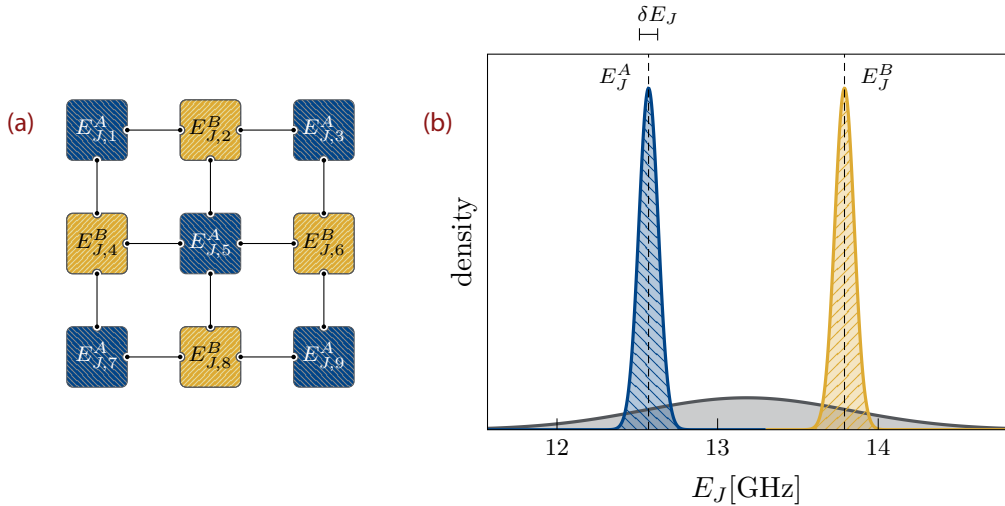


Figure 5.1 – Frequency alternation pattern. (a) ABAB frequency pattern on a 3×3 geometry. The A and B sublattice positions are populated with Josephson energies drawn from two different normal distributions as sketched in (b). Despite the precision tuning, the E_J s are subject to some residual random variations with frequency spread δE_J that, thanks to the LASIQ technique, is about an order of magnitude smaller than the natural disorder. For comparison, the gray Gaussian represents the scheme-A distribution with mean $(E_J^A + E_J^B)/2$, which was exploited in earlier chapters as an estimate for the as-fabricated disorder.

5.2 Overview: Bloch states, global MBL and permutation multiplets

A first impression of the system’s behavior under the influence of a disorder strength that varies over several orders of magnitude can be gained from Fig. 5.2. The upper panel shows the IPR and a newly introduced quantity, w_{pm} , that is discussed below. Panel (b) shows the evolution of the levels of the $N_{\text{ex}} = 5$ manifold for a single disorder realization¹ as a function of the LASIQ precision δE_J . Combining the information contained in the IPR and the energy spectrum, we conclude that four qualitatively different disorder regimes should be distinguished:

- (I) For strong disorder, $\delta E_J > 0.1$ GHz, the IPR is close to one, and the spectrum consists of a dense tangle of levels without any further substructures.
- (II) For δE_J between 0.1 GHz and 0.01 GHz, the IPR stays near one, but the spectrum now resolves a finer substructuring of the levels in *permutation multiplets*, see the discussion below.

With the energy resolution in Fig. 5.2(b), no further evolution can be extracted from the spectrum that appears utterly flat as the disorder is further reduced. The IPR, however, reveals the existence of two other parameter ranges:

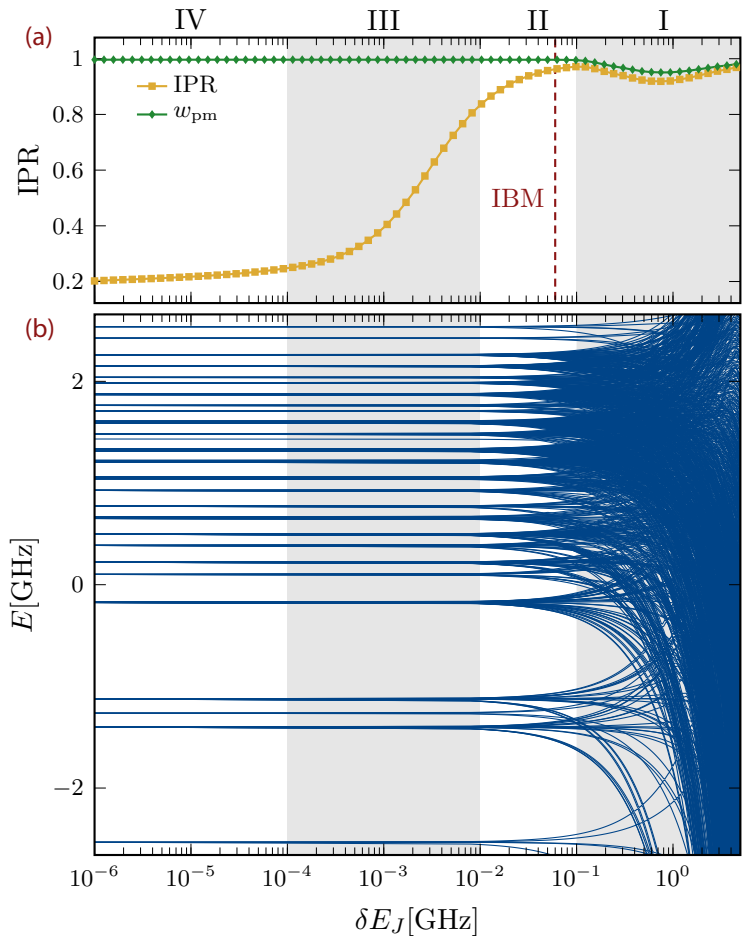
- (III) For δE_J between 10^{-4} GHz and 10^{-2} GHz, the IPR strongly decreases, and, finally,
- (IV) the IPR saturates at a low value for $\delta E_J < 10^{-4}$ GHz.

We start the journey through the four regions by discussing the asymptotic cases of very high (I) and very low (IV) disorder.

¹Depicting the spectrum of a single disorder realization as a function of the disorder δE_J may sound contradictory at first. What is meant by this is the following: We draw nine i.i.d variables x_i from the normal distribution with $\sigma = 1$. The Josephson energy of transmon i is then obtained as $E_{J,i} = E_{J,A} + x_i \delta E_J$ if i is on the A sublattice and similar for the B transmons.

Figure 5.2 –

Restructuring of the Hilbert space and evolution of the IPR as δE_J decreases. (a) IPR and multiplet weight w_{pm} , averaged over all 1,287 states of the $N_{\text{ex}} = 5$ bundle of a 3×3 transmon array. (b) Spectrum of a single disorder realization as a function of δE_J . According to the IPR and the spectrum, one can divide the disorder range δE_J into four sectors: an MBL phase, indicated by an IPR that is very close to one for disorder strengths $\delta E_J > 100$ MHz (I), the δE_J range between 10 MHz and 100 MHz with an IPR likewise close to one, but where, as shown in (b), the Hilbert space resolves itself in smaller bundles (II), a region where the IPR strongly decreases (III) and the domain $\delta E_J \lesssim 10^{-4}$ GHz, where the IPR saturates at a low value (IV). With the energy resolution in (b), the two latter cannot be distinguished in the spectrum. All calculations are performed for $T = 3$ MHz. The results in (a) are averaged over at least 8,000 disorder realizations.



5.2.1 The two limiting cases: strongly disordered and clean devices

The limiting case of very low disorder is readily understood: an ever further reduction of randomness culminates in a clean device with a perfect AB frequency arrangement. This evades all NN resonances and is desirable for optimizing the CR gate but has the unwelcome collateral effect of resonances between next-nearest neighbors (NNN). Weak effective coupling between degenerate NNN leads to hybridization of the wave function over the A or B sublattice. More formally, the case $\delta E_J \rightarrow 0$ restores the symmetries of the transmon array, e.g., translational symmetry for periodic boundary conditions or the symmetries of the 3×3 ‘crystal’ in our specific case study. The low value of the IPR in region IV indicates that wave functions respecting these symmetries, e.g., Bloch band eigenstates, are generically not localized on a specific lattice site. This embodiment of delocalization is not due to quantum chaos. Nevertheless, the wave functions are unsuitable for quantum computing applications.

In the second extreme case of massive disorder (I), the system is found in the regular (for later distinction called *global*) MBL phase. Here, the Josephson energy spread around the mean values $E_{J,A}$ and $E_{J,B}$ is much larger than the spacing between them, such that the underlying AB pattern is not resolved. For the small coupling of $T = 3$ MHz considered in Fig. 5.2, the system is therefore localized. The dense tangle of states seen at the right edge of Fig. 5.2(b) is the usual $N_{\text{ex}} = 5$ bundle familiar from the discussion in Chapter 4. If the disorder strength

is slightly reduced to ≈ 1 GHz but still large enough to conserve the single-bundle structure in the spectrum, the wave functions weakly hybridize, and the IPR shows a minor decrease, as expected.

5.2.2 Permutation multiplets

When starting in the global MBL phase and pushing the fluctuations in E_J to smaller values, the effect of the AB frequency ‘unit cell’ to the many-body energies starts to exceed the disorder contribution: Shifting an excitation from an A to a B site changes the energy by an amount that is larger than the typical energy variation due to the randomness in E_J . The same holds for the anharmonicity shift occurring when multiple excitations occupy the same transmon. Thus, as shown in Fig. 5.2(b), for $\delta E_J \lesssim 0.1$ GHz (region II) and the small T values that are relevant in fixed-frequency architectures, a further splintering of the Hilbert space in excitation structures or *permutation multiplets* occurs. Such a multiplet is defined by all permutations of a specific distribution of excitations to the transmons. This next smaller hierarchy level has already been discussed in Sec. 4.2.1. Compared to Fig. 4.3, where all excitation structures were characterized solely by their total anharmonicity, the situation is more involved here. The higher number of multiplets reflects the complexity of the AB pattern. Adapting the notation introduced earlier, we denote, for example, the permutation multiplet formed by the states with one A transmon in $|2\rangle$, one in $|1\rangle$, two B transmons in $|1\rangle$, and the remaining transmons in the ground state as $\{A21B11\}$. For the 3×3 model at hand, the 1,287 states of the $N_{\text{ex}} = 5$ bundle are split into 35 permutation multiplets containing between one and 120 states. The lowest multiplet is $\{A5\}$ (five states), followed by $\{A41\}$ (20 states) and so on, up to the highest multiplet $\{A1B1111\}$ (five states). For a detailed overview, see Appendix C.4.

States from the same permutation multiplet cannot be nearest neighbors in configuration space: due to the bipartiteness of the lattice, a single hopping process necessarily changes the number of excitations on the A and B sublattices and thereby modifies the excitation structure. An important implication is that hybridization gets efficiently suppressed when the multiplets initially take shape because energetically close states are far away in configuration space. In consequence, the IPR increases again to almost 1 at the upper edge of region II. We refer to this phenomenon as localization within multiplets or *intra-multiplet localization*. As marked by the dashed red line in Fig. 5.2(a), IBM’s current LASIQ precision lies precisely in this regime, near the maximum of the IPR. This spot manages the difficult balancing act between too little disorder (unfavorable from the MBL perspective because the IPR decreases, see the later discussion) and too strong disorder (unfavorable for the gate fidelity because frequency collisions are not avoided) quite well.

Strictly speaking, the partitioning of wave functions in permutation multiplets is only exactly defined for $T = 0$, but not for the many-body eigenstates of the interacting system. However, as T is small compared to a typical inter-multiplet distance of ~ 100 MHz, it is to be expected that the mixing of multiplets is negligible. Indeed, assigning many-body wave functions to a specific multiplet is possible throughout the entire disorder regime. For large and intermediate disorder, the IPR close to one indicates that a single basis state dominates in the many-body wave function. Therefore, we can tag the many-body wave function with the multiplet label associated with this state. For low disorder, it is easily verified that many-body wave functions taken from a particular, energetically well-resolved multiplet have only support from the basis vectors that define this multiplet in the $T \rightarrow 0$ limit. This observation is quantified with the total spectral weight of the many-body wave function $|\psi_i\rangle$ that is carried by its dominant multiplet

$c(|\psi_i\rangle)$, defined as

$$w_{\text{pm}}(|\psi_i\rangle) = \sum_{|\phi\rangle \in c(|\psi_i\rangle)} |\langle \phi | \psi_i \rangle|^2. \quad (5.1)$$

As the green curve in Fig. 5.2(a) illustrates, the averaged permutation multiplet weight w_{pm} stays close to one over the entire disorder range. Particularly illuminating is the comparison of w_{pm} and the IPR. While no changes occur in w_{pm} for $\delta E_J \rightarrow 0$, the IPR shows the sequence of transitions through the regions II to IV. The combination $w_{\text{pm}} \approx 1$ and $\text{IPR} \ll 1$ indicates that all many-body wave functions are distributed over many configuration states, but all contributing states belong to the same multiplet. By analogy with the above, we term this effect *intra-multiplet delocalization* or delocalization within multiplets.

In summary, we interpret the four disorder regions as global MBL (I), localization within multiplets (II), delocalization within multiplets (III), and formation of a symmetry-dominated regime (IV) where the wave functions approximately obey the symmetries of the transmon geometry. In the next sections, we examine in more detail the system's viability as a quantum computer, with a particular focus on region III. Specifically, we aim to apply the level statistic analysis to investigate whether one really encounters a quantum chaotic region with level ratios that follow the Wigner-Dyson distribution. However, this requires some prior issues to be clarified first.

5.3 Quantum chaos in engineered frequency patterns

Several pitfalls must be circumvented to make reliable statements about the presence of quantum chaos in region III. A first important insight is that the *quantitative* study of weakly disordered (transmon) systems—and, in particular, evaluating them for their suitability as quantum computers—must begin with the identification of the relevant subspaces. Whenever the Hilbert space disintegrates into smaller substructures (here the permutation multiplets), each of them should be taken as a separate entity and analyzed individually. Otherwise the extent of chaos in the computationally relevant states is underestimated. The level ratio analysis requires particular attention. For an illustration of these points, it is sufficient to restrict to the simpler example of the $L = 5$ chain, discussed in the next section, where the bundle $N_{\text{ex}} = 3$ consists of a manageable number of 35 states. Further details can be found in Appendix C.

5.3.1 A simple example: the $L = 5$ chain

Provided that δE_J is chosen small enough, the 35-dimensional Hilbert space of the $L = 5$ chain with *ABABA* frequency arrangement splits into nine different permutation multiplets, three of which, $\{A111\}$, $\{A21\}$, and $\{A11B1\}$, are considered in more detail here (for an overview of the remaining multiplets, see Appendix C.1). As shown in Fig. 5.3(a), the disorder-averaged IPR shows a distinct δE_J -dependence for all three cases: For $\{A111\}$, the IPR stays close to one throughout the entire disorder range. This multiplet consists of the single state $|10101\rangle$, which is energetically isolated for small disorders and therefore does not hybridize. In particular, $|10101\rangle$ is an exact $\delta E_J = 0$ eigenstate that adheres to the symmetries of the clean transmon chain. The structure $\{A11B1\}$, comprising six computational states, shows a single sharp drop in the IPR. For $\{A21\}$, a first decrease in the IPR at a similar disorder strength is followed by a plateau and a second drop appearing at a δE_J that is about three orders of magnitude smaller. This behavior can be understood by recourse to the effective model in (4.2). All states of the multiplet $\{A111\}$ are interconnected to second order in the hopping matrix element J , whereas $\{A21\}$ further separates into two subsets that are cross-connected only to fourth order in J . This distinction

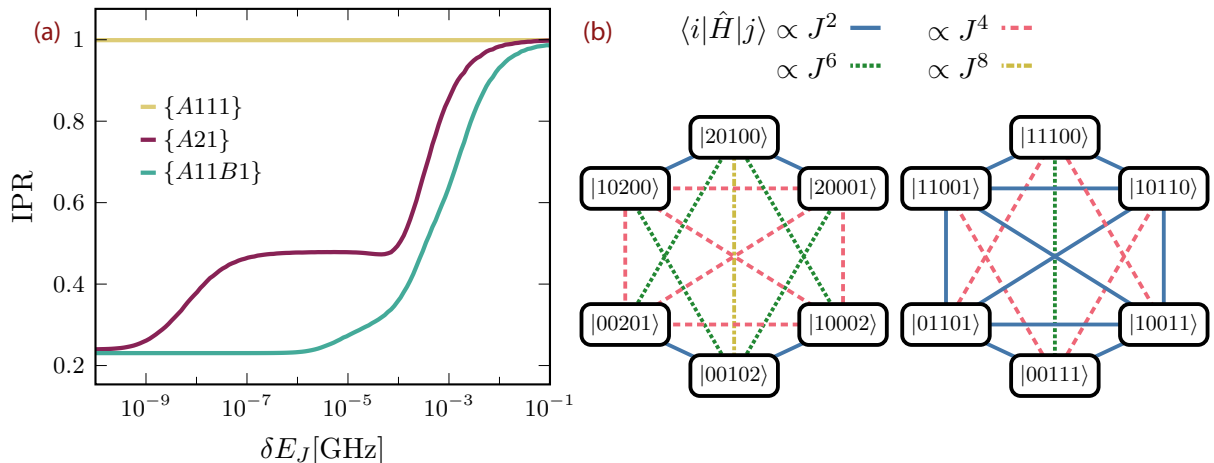


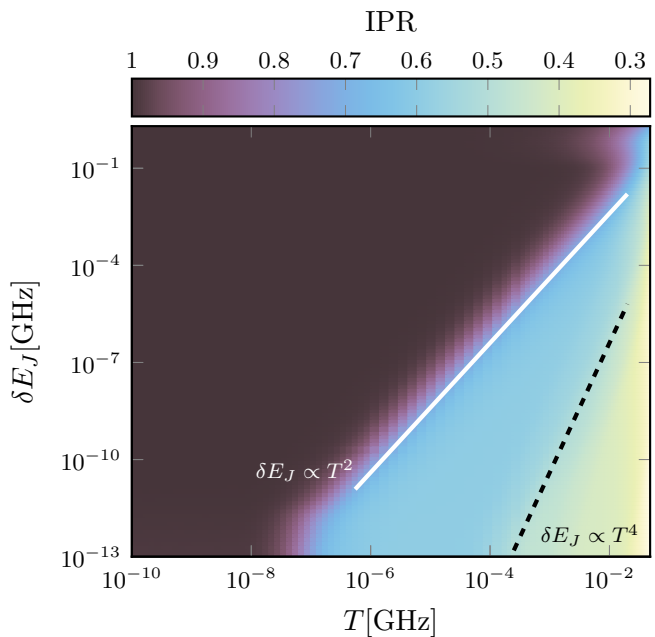
Figure 5.3 – Multiplet resolved IPR for the $L=5$ chain and visualization of the connectivity of the states forming the multiplets $\{A21\}$ and $\{A11B1\}$. (a) The IPRs for the three multiplets $\{A21\}$, $\{A11\}$, and $\{A11B1\}$ behave qualitatively differently. The difference in $\{A11B1\}$ (single drop in the IPR) and $\{A21\}$ (additional second drop at much smaller δE_J) can be understood with an eye to the connectivity graph, shown in (b), that visualizes to which order in J the states of each bundle are mutually coupled. $\{A21\}$ separates into two subsets that couple only to fourth order in J . In (a), the coupling is fixed to $T = 3$ MHz, and the IPR is averaged over 10,000 disorder realizations.

is illustrated by the connectivity graphs in Fig. 5.3(b). Decreasing the disorder strength creates resonances between second-nearest-neighbor transmons. Thinking of the transmon array as a hopping problem on a highly connected configuration space lattice, these translate to resonances between lattice sites whose distance is determined by the order in J to which the corresponding configuration states are coupled. With the expectation that delocalization occurs when the effective coupling exceeds the many-body level spacing, formulated in Eq. (2.27), it is reasonable to assume that the first drop in the IPR relates to the hybridization of wave functions over second-nearest neighbors in configuration space. The second decline, occurring only for $\{A21\}$, then indicates a strong mixing of the two subsets with a minimal distance of four. A closer investigation of the many-body wave functions supports this interpretation. Wave functions taken from the $\{A11B1\}$ bundle at disorders $\delta E_J < 10^{-5}$ GHz are linear combinations of the six states contained in the bundle. They are close to the exact $\delta E_J \rightarrow 0$ eigenstates and approximately respect the symmetries of the transmon chain. For the same δE_J , wave functions from $\{A21\}$ dominantly belong to one of the distinct subsets. Only after the second drop in the IPR one regains the chain symmetry in the eigenfunctions. For an explicit example, see Appendix C.3.

Fig. 5.4 shows the two-dimensional representation of the IPR for varying values of the coupling strength T and the residual randomness δE_J . Most strikingly, there are two clearly identifiable regions where the IPR declines. The δE_J values where the delocalization sets in depend on T as T^2 and T^4 , as indicated in Fig. 5.4. Akin to the discussion in Sec. 4.5.3, the quantity driving the onset of delocalization is $|t_{i,j}|/\delta E_{i,j}$, where $t_{i,j}$ is the *effective* hopping and $\delta E_{i,j}$ the energy difference between two configuration space lattice sites i, j . For second-nearest neighbors, using Eq. (4.2), the effective hopping $t_{i,j}$ has the form $J^2/\Delta E$ where the denominator is the energy difference to some virtually occupied intermediate lattice site, i.e., the energy difference between two multiplets. Most importantly, ΔE is approximately constant in the relevant part of the $T-\delta E_J$ plane because the contributions from the anharmonicity and the AB staggering dominate

Figure 5.4 –

Wave function statistics in the T - δE_J plane. Shown is the color-coded IPR, averaged over the 35 states from the $N_{\text{ex}} = 3$ bundle of the $L = 5$ transmon chain with an AB frequency pattern. As expected, the tendency of wave functions to delocalize grows if T increases or δE_J decreases. Two features are particularly striking: The value of δE_J showing the first inset of hybridization depends on T as T^2 . A second descent of the IPR occurs along the line where $\delta E_J \propto T^4$. As discussed in the main text, these two successive transitions can be understood as hybridization over second-nearest and fourth-nearest neighbors in configuration space. All results are averaged over at least 5,000 disorder realizations.



over the disorder. On the other side, for fixed $E_{J,A}$ and $E_{J,B}$ and lattice sites i and j from the same multiplet, the only contribution to $\delta E_{i,j}$ is due to the frequency disorder $\delta\nu \propto \delta E_J$. In total, this yields

$$\frac{t_{i,j}}{\delta E_{i,j}} \propto \frac{J^2}{\delta E_J} \propto \frac{T^2}{\delta E_J}, \quad (5.2)$$

for the relevant scaling variable, in accordance with the observations in Fig. 5.4. A similar argument holds for the forth-nearest neighbors in configuration space. We show in Appendix C.1 that an appropriate rescaling of the T axis yields a good data collapse in the respective parameter ranges.

The main takeaway from the example of the $L = 5$ chain is that different multiplets should be explored separately. When all the states of an entire excitation bundle are analyzed simultaneously, different effects, each of which appears only in a small subset of multiplets, superpose, as in Fig. 5.4. Besides, in more complicated geometries, additional effects like hybridization between $|300\dots\rangle$ and $|003\dots\rangle$ (a second-order process but with a small hopping amplitude that is not captured by the effective Hamiltonian \hat{H}_{eff}) kick in and blur the second transition $\delta E_J \propto T^4$.

Regarding level statistics, there are two more subtleties to consider: First, when calculating level ratios for all states of an excitation bundle, whenever E_i and E_{i+1} belong to different multiplets, the corresponding R_n ratio contributes to the histogram bin at $R_n = 0$. As detailed in Appendix C.3, this significantly distorts the KL divergences for the small system sizes under consideration. Second, considering again $\{A21\}$ for disorders around the first decline of the IPR, we can think of the two subsets visualized in Fig. 5.3(b) as two independent, weakly cross-correlated submanifolds that are chaotically correlated among themselves and overlap in energy. Accordingly, the level structure will show avoided crossings within states from the same manifold and crossings (more precisely, anticrossings that are orders of magnitude smaller) between states from different manifolds. This shifts the overall level statistics for the entire permutation multiplet towards a Poisson distribution even though, strictly speaking, one deals with two independent chaotic substructures. Appendix C.3 gives a visualization of this situation.

5.3.2 Unveiling quantum chaos: chaotic multiplets

With the insight gained in the previous section, it is now a straightforward task to scan the multiplets of the more complex 3×3 geometry for signatures of quantum chaos. We focus on a one-dimensional cut through the $T\text{-}\delta E_J$ plane and fix $T = 3$ MHz as in Fig. 5.2. A two-dimensional representation for the IPR akin to Fig. 5.4 for the 3×3 array (and larger chains) is provided in Appendix C.2.

Our main findings, which we exemplify with the multiplets $\{A111B11\}$ and $\{A21B11\}$, are summarized in Fig. 5.5. $\{A111B11\}$ is the largest computational multiplet containing 60 of the 126 computational states. With a total of 120 states contained, $\{A21B11\}$ is the largest multiplet overall. We focus on a disorder range centered around regime III, which is shaded in gray. To start the discussion, we inspect the two spectra in the bottom row. Shown is an enlarged view of the levels belonging to the multiplets (d) $\{A111B11\}$ and (e) $\{A21B11\}$ for the exact same disorder realization exploited in the compilation of Fig. 5.2. On the blown-up energy scale, one notices that the levels that previously appeared flat are still strongly dispersing for $\delta E_J > 10^{-4}$ GHz. In particular, region III is characterized by strong level repulsion in both multiplets, indicating that a region of fully evolved quantum chaos is entered if the residual disorder falls below 10^{-2} GHz. The KL divergences calculated only for the levels from the respective bundles, shown in (b) and (c), quantitatively confirm this observation. In both cases, in the foothills of the regime of intra-multiplet localization (II), one finds $D(P||P_{\text{Poisson}}) \approx 0$ and $D(P||P_{\text{Wigner}}) \approx 1$. Upon lowering the disorder, the situation reverses: along with the IPR, whose calculation is likewise restricted to the respective bundles, $D(P||P_{\text{Wigner}})$ decreases and approaches the proximity of zero, evidencing that region III is a no-go area for quantum computing. For selected values of δE_J , the disorder-averaged R_n histograms underlying the calculation of the KL divergences are shown in (a). As expected, for values of randomness taken from regions II and III, the histograms show a good (yet not perfect) match with what is predicted for integrable systems and GOE matrices, respectively.

Regarding the computational multiplet, the wave function spreading implied by the decreasing IPR is potentially even more harmful than in the situation discussed in Chapter 4. There is some hope that a transmon array with dressed l -qubit wave functions can serve as a viable quantum computer, provided that one can unambiguously assign bitstring tags to a set of energies and that the qubit-qubit correlations, divulged via the Walsh-Hadamard transformation, fall below a certain threshold. For simple Gaussian disorder, where all excitation structures are thoroughly intermingled, wave functions can simultaneously have a small IPR and a single dominating computational state, such that at least the qubit state identification is feasible. Here, in contrast, this first preparatory step of the Walsh analysis already fails: all states delocalize within the computational multiplet. A small IPR implies that wave functions are superpositions of many *computational* states, so reliable labeling with bitstrings is impracticable.

Further reduction of the disorder drives the system closer to region IV. Near the transition between III and IV, the IPR saturates, but the level ratio distribution moves closer to the Poisson prediction, as can be inferred from the decay of the corresponding KL divergence. However, waterproof signs of a regime of uncorrelated levels never fully develop because the symmetry-induced correlations gain importance. In region IV, both KL divergences exhibit a sharp increase to high values, and neither the Poisson nor the Wigner distribution resembles the numerically obtained probabilities. This behavior is a symptom of the level clustering into finer bundles for $\delta E_J < 10^{-4}$ GHz. These structures are the ‘molecular multiplets’ of the 3×3 array. The point group symmetry determines the remaining degeneracies. Accordingly, the R_n histogram, shown on the very left in (a), does not reflect universal fluctuation properties but the specific, unique

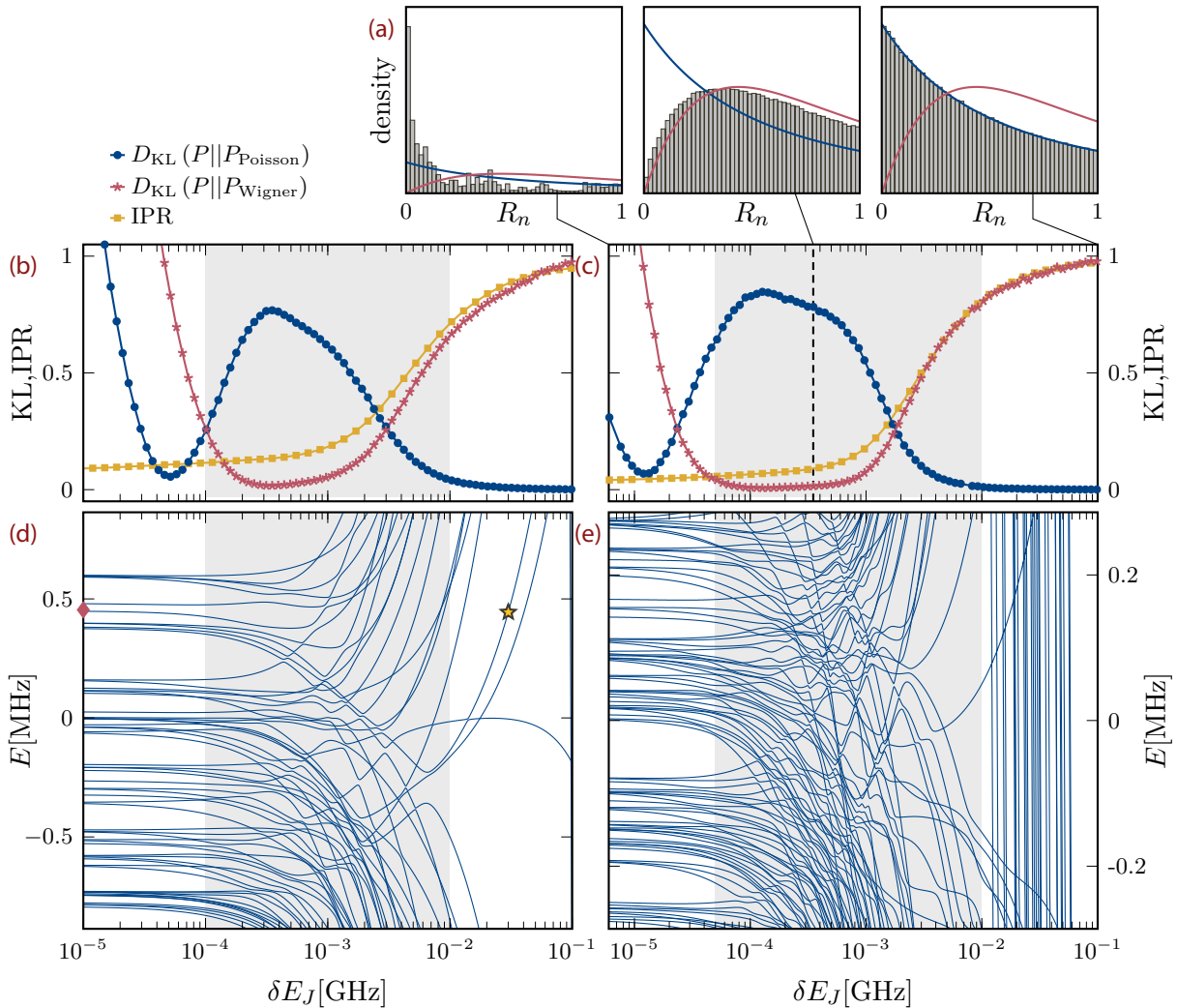
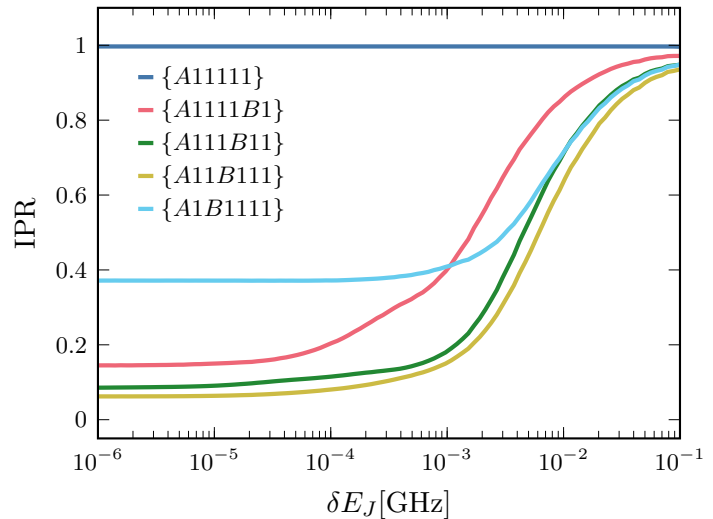


Figure 5.5 – Quantum chaos in precision-engineered transmon arrays. Shown are the wave function statistics (IPR), level statistics (KL divergences), and the spectrum as a function of the residual disorder δE_J for the multiplets $\{A111B11\}$ (left) and $\{A21B11\}$ (right). The spectra presented in the lower row show enlarged views of the levels displayed in Fig. 5.2(b). In region II, the levels are still strongly dispersing. The disorder region III, distinguished by the fast-decreasing IPR in Fig. 5.2(a), exhibits strong level repulsion and many avoided crossings. Finally, for disorder strength $\delta E_J \lesssim 10^{-4}$, the permutation multiplets disintegrate into even smaller bundles that are the molecular multiplets of the 3×3 geometry. These findings are substantiated by the KL divergences (calculated for the R_n ratios from the respective permutation multiplets) and by the R_n histograms shown for three selected values of δE_J for $\{A21B11\}$. For $\delta E_J > 10^{-2}$ GHz, $D(P||P_{\text{Poisson}}) \approx 0$, and wave functions are localized. For $\delta E_J < 10^{-2}$ GHz, $D(P||P_{\text{Wigner}})$ decreases and reaches a small value indicating proximity (yet not a perfect agreement, see the histogram) to the predictions of Wigner-Dyson statistics—an unmistakable sign that quantum chaos is lurking if the LASIQ precision becomes *too* good. If the residual disorder is pushed below 10^{-4} GHz, the R_n histogram exhibits neither good agreement with Poisson nor with Wigner-Dyson statistics. It has no system-independent, universal form but characterizes the energy levels of the clean system. Those depend on the point group symmetries of the array geometry. Accordingly, the KL divergences are of no use here. All results in (b) and (c) are averaged over at least 8,000 disorder realizations. The markers in (d) designate the energies whose wave functions are discussed in the main text.

Figure 5.6 –

Delocalization of computational states. Shown is the IPR for the five computational multiplets of the $N_{\text{ex}} = 5$ bundle, containing a total of 126 computational states. For three of the multiplets, the IPR decreases below 0.2. These three multiplets already contain 120 states. Only for $\{A11111\}$ —a multiplet containing only a single state—the IPR stays close to one. Results are averaged over at least 8,000 disorder realizations.



level structure of the clean device. For the 3×3 geometry, the point group is C_{4v} (or D_4 , as these two are equivalent for a planar arrangement). The irreducible representations of this group are one- and two-dimensional. Hence, some levels are two-fold degenerate (as can already be guessed from the spectra shown in (d) and (e)), resulting in the clear peak at very small R_n values (see also the discussion in Appendix C.3).

5.3.3 Wave functions

For completeness, we provide explicit examples for wave functions taken from the computational multiplet $\{A111B11\}$ in regimes II and IV. To visualize the contributing basis states, we use the same representation of ‘0’s and ‘1’s as in Sec. 4.8, adapted to the 3×3 geometry. For example, the basis state where the transmons 1,2,7 are in the first excited state and the remaining transmons in the ground state is depicted as

Now, the wave function belonging to the level marked by the yellow star in Fig. 5.5(d) is approximately given by $|\psi_{\star}\rangle \approx \frac{1}{\sqrt{5}} \left(\begin{array}{c} \text{yellow} \\ \text{gray} \\ \text{gray} \\ \text{gray} \\ \text{gray} \end{array} \right)$, i.e., as expected from the IPR, wave functions are dominated by a single basis vector. As δE_J decreases, one penetrates into the chaotic sea, and the eigenstate rapidly and constantly changes its composition. Finally, in region IV, the symmetries come to light. For example, the wave function belonging to the level marked by the red diamond on the left in Fig. 5.5(d) is approximately given by

$$|\psi_{\diamond}\rangle \approx a \left(\begin{array}{c} \text{yellow} \\ \text{yellow} \\ \text{yellow} \\ \text{gray} \\ \text{gray} \end{array} \right) + b \left(\begin{array}{c} \text{yellow} \\ \text{gray} \\ \text{yellow} \\ \text{gray} \\ \text{gray} \end{array} \right) + c \left(\begin{array}{c} \text{yellow} \\ \text{gray} \\ \text{yellow} \\ \text{yellow} \\ \text{gray} \end{array} \right) + \dots, \quad (5.3)$$

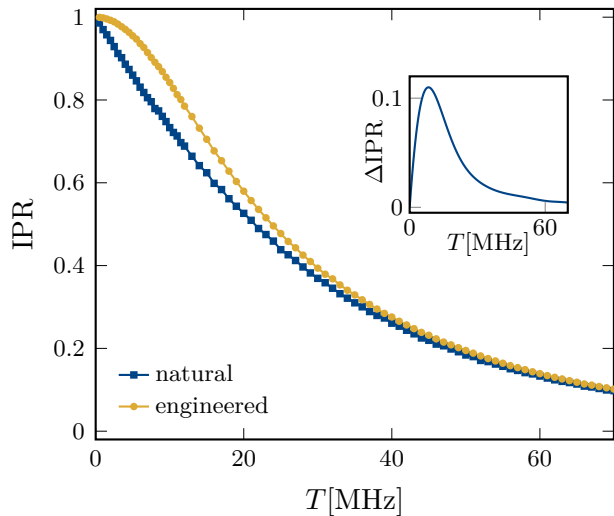
with some coefficients a, b, c . It is easy to see that this particular linear combination is indeed invariant under the point group symmetries of the 3×3 array.

5.3.4 Delocalization of computational states

Fig. 5.6 displays the IPR for all computational multiplets of the 3×3 geometries. Specifically, besides the already discussed manifold $\{A111B11\}$, these are $\{A11111\}$ (one state), $\{A1111B1\}$ (20), $\{A11B111\}$ (40), and $\{A1B1111\}$ (5). Except for $\{A11111\}$, which does not hybridize because it consists of a single, energetically isolated state, all multiplets show a single sharp

Figure 5.7 –

Comparison of IPR before and after LASIQ tuning as a function of T . The blue line shows the IPR for the natural disorder reported in Ref. [294] for various values of the coupling. The yellow line shows the IPR for the post-LASIQ parameters, likewise given in Ref. [294]. LASIQ not only reduces the number of frequency collisions but also enhances the localization, especially for small T . The inset shows the difference in the IPR after and before the laser annealing. All results are averaged over at least 1,100 disorder realizations.



decrease in the IPR, guiding us to conclude that the entire computational subspace (except for gets compromised if the LASIQ precision significantly improves. In particular, comparison with the full bundle in Fig. 5.2 reveals that most of the computational states delocalize above average.

5.4 Effect of LASIQ on IBM's recent chips

Having established the general delocalization mechanism in precision-tuned transmon arrays, we finish this chapter with two remarks on (i) the effect of LASIQ tuning with state-of-the-art precision and (ii) the emergence of quantum chaos in IBM's more elaborated heavy-hexagon geometry.

5.4.1 IPR before and after annealing

To gauge whether the currently realizable patterns have positive or detrimental effects on the many-body properties, we calculate the T -dependent IPR for the parameters of the as-fabricated Josephson junctions and the LASIQ-tuned bimodal frequency distribution that are both reported in Ref. [294]. The latter is very similar to the previous parameter choice, with the only difference being a minor deviation in the two frequency spreads ($\delta E_{J,A} = 61$ MHz and $\delta E_{J,B} = 64$ MHz). The parameters for the untuned processor are $E_J = 13.78$ GHz and $\delta E_J = 611$ MHz. The results for the IPR before and after annealing are contrasted in Fig. 5.7. For all values of T , the ‘LASIQ-tuned IPR’ lies indeed above the one for the array built with as-fabricated transmons. As displayed in the small inset, showing $\Delta\text{IPR} = \text{IPR}_{\text{after}} - \text{IPR}_{\text{before}}$, the amelioration of the IPR is particularly noticeable in the small T range favored in fixed-frequency architectures. The evolution of the LASIQ-tuned IPR starts with an eye-catching plateau-like stagnation. Wave function hybridization is initially suppressed and only sets in when T acquires a value high enough to circumvent the inter-multiplet energy barrier between nearest neighbors or to enable hopping between nearly degenerate NNN. Hence, LASIQ tuning with contemporary precision not only diminishes the number of frequency collisions but also decreases the tendency of wave functions to spread out, particularly for the experimentally relevant small-coupling range.

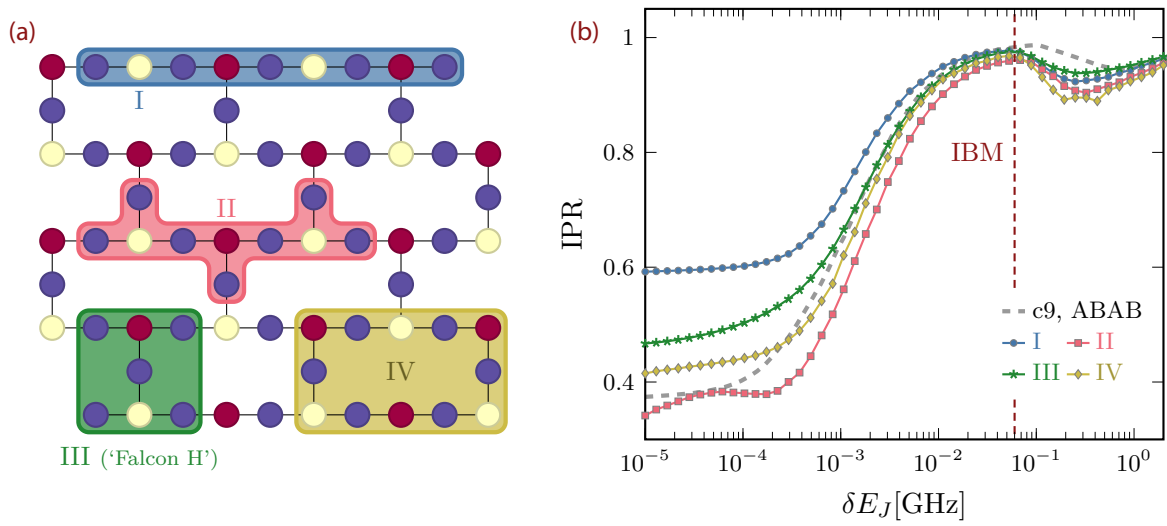


Figure 5.8 – Quantum chaos in cross-resonance architectures on the heavy-hexagon lattice. Panel (a) shows the ‘Hummingbird’ chip with an *ACBC* frequency pattern. The colored backgrounds highlight the different parts we investigate in more detail in (b). Using the IPR as a quality indicator, one observes that the utopia of a collision-free chip, arising for $\delta E_J \rightarrow 0$, is unattainable. The more complex design shows the same sequence of transitions that the *AB* arrangement exhibited, including a quantum chaotic region for too low disorder. Parameters are taken from Ref. [294], that—based on Monte Carlo simulations—proposes the frequency mean values $\nu_1 = 5$ GHz (yellow), $\nu_2 = 5.07$ GHz (red), and $\nu_3 = 5.14$ GHz (purple) for the (negative) anharmonicity $E_C = 330$ MHz. For comparison, we show results for the $L = 9$ chain with the simpler *AB* pattern. The number of disorder realizations varies from 400 for geometry IV to more than 22,000 for geometry III. We choose $T = 3$ MHz for the coupling strength.

5.4.2 Chaos on the heavy-hexagon lattice

The *AB* sublattice pattern considered so far is a helpful simplification for highlighting some generic properties that emerge in transmon arrays with ‘too good’ frequency precision. IBM designed the more complex heavy-hexagon geometry and proposed to implement an *ACBC* frequency pattern on it to avoid the seven most likely types of frequency collisions during the CR gate operation [294, 306]. This particular pattern is again shown in Fig. 5.8(a). Here, we argue that the insights gained for the simpler model—in particular, the existence of a quantum chaotic region for too low disorder—retain their validity for more elaborate frequency arrangements and geometries.

To accomplish this, we calculate the IPR as a function of the residual disorder strength δE_J for the different sections of the heavy-hexagon lattice that are highlighted by the colored background in Fig. 5.8(a). As depicted in Fig. 5.8(b), all four lattice excerpts show very similar behavior, which exhibits no qualitative difference from the simpler *AB* unit cell. One observes the same sequence of disorder regimes, starting with delocalized states in the clean device at very low disorder, proceeding to intra-multiplet delocalization, intra-multiplet localization, and inter-multiplet hybridization before reaching the global MBL phase at large disorder. The similarity, despite the more complicated pattern, is hardly surprising. As for the *AB* pattern, there are degenerate NNN qubits—the control qubits in CR gate language—or, in other words, degeneracies between second-nearest-neighbor lattice sites in configuration space. Hence, the hybridization mechanisms discussed in the previous sections remain valid. The magnitude of the decrease in the IPR at low disorder depends on the number of degenerate NNN transmons contained in the specific geometries. The dashed gray line shows the IPR for the $L = 9$ chain with an *AB*

pattern to facilitate comparison with the previous results. The data shown in Fig. 5.8(b) are averaged over all permutation multiplets belonging to a fixed excitation manifold. We choose $N_{\text{ex}} = 5$ for all geometries except for geometry IV, where $N_{\text{ex}} = 6$. We checked that the IPR decreases stronger if the averaging is restricted to the computational multiplets alone, confirming the previous observation that computational states are (on average) particularly vulnerable. On very close examination, one can see that the minimum at large δE_J , signaling the inset of trans-multiplet coupling, occurs at slightly smaller disorder strengths for the *ACBC* pattern. This is due to the lower average inter-multiplet separation arising from the particular parameter choices and the more complex multiplet structure. To be specific, for the *ACBC* pattern, we use $\nu_A = 5$ GHz, $\nu_B = 5.07$ GHz for the target qubits, and $\nu_C = 5.14$ GHz for the control qubits, which is predicted to optimize CR gate performance [294]. In contrast, the $L = 9$ chain result uses the experimental laser-tuning parameters $\nu_A = 5.43$ GHz and $\nu_B = 5.70$ GHz [294] with a larger energy separation.

In conclusion, the chaotic phase resists both the progression to a lower connectivity lattice and the implementation of a more complex frequency pattern, and even emerges at similar values of the residual disorder.

5.5 Summary

In this chapter, we discussed the role of localization physics in transmon processors with high-precision-tuned frequency patterns. Our principal finding is that quantum chaos survives the engineering maneuvers, and disorder remains an essential resource for qubit protection. More precisely, we find that one can distinguish between four different disorder regions, each of which is characterized by the relation between the amount of randomness and the system's other energy scales: If the disorder outscores all other relevant energies, we find the global many-body localized phase, where the staggering of frequencies is insignificant. When the pattern and the anharmonicity contribution to the energy dominate over the disorder, the global MBL phase is succeeded by a regime where new substructures, the permutation multiplets, emerge. The residual disorder then determines whether states are efficiently localized in these substructures (when the disorder exceeds the *effective* coupling t_{eff}), whether one enters the realm of chaos and states delocalize within the multiplets (when t_{eff} and disorder are comparable), or whether molecular multiplets emerge and the symmetries of the transmon array gain importance (when t_{eff} dominates over the disorder). To build a functioning computing device, one must carefully target the ideal spot between the extremes of delocalized chaotic or symmetric wave functions for too little disorder at one end and systematically failing gates due to frequency collisions for too large disorder at the other end. From an MBL perspective, we can identify the maximum of the IPR as the optimal δE_J , where the multiplets have formed, and nearest neighbors are detuned by an amount that enhances the CR gate fidelity but where the residual disorder prevents the inset of intra-multiplet delocalization.

How do our results relate to contemporary experiments? The currently achievable LASIQ precision of $\delta\nu \approx 14$ MHz is sufficient to see the formation of multiplets, yet too high to create the dangerous NNN resonances. The recent engineering attempts have, therefore, successfully hit the optimum of intra-multiplet localization, see the vertical lines in Figs. 5.2 and 5.8. The current precision is yet not sufficient to reliably produce collision-free chips when scaling up to more than ~ 100 qubits. For example, the ‘Eagle’ generation (127 qubits) has a probability of only 8% of being collision-free when populated with an *ACBC* pattern subject to a residual disorder that is given by the current LASIQ accuracy. Scaling up to 1,000 qubits requires an

estimated precision improvement by a factor of two [294]. With the IPR already being near its maximum with the current fidelity, further reduction of δE_J quickly increases the tendency towards delocalization (although the IPR can still be acceptable with half as much disorder). In particular, as the promised land of never-failing gates and collision-free devices is found at $\delta E_J = 0$, quantum chaos is an inevitable obstacle for building ever larger pattern-engineered chips.

Stepping aside from the comparison with experimental values, which are subject to rapid and constant change, our investigations also bring to light two more universal findings: First, our results are a clear-cut demonstration that conclusions drawn from considerations of small-sized clusters of two to a few qubits have limited significance for the many-body problem that a quantum computer poses. The identification of the frequency collisions and the proposal of the *ACBC* frequency pattern to avoid them emanate from an effective model of the CR gate [291, 306] consisting of a minimal setup of a control, a target, and a spectator qubit. As shown, when transferred to larger geometries, the suggested *local* redesign of the transmon processor has consequences on *long-range* scales beyond the reach of the minimal model. Thus, incorporating many-body physics into the design of transmon quantum computers is much needed, as it reveals aspects for which the established few-qubit picture is blind.

Second, we found that reliable predictions on the localization properties of the weakly disordered transmon array can only be made if the application of the diagnostic tools is preceded by the extra step of identifying the relevant subspaces. In its most general form, our observation is that whenever the Hilbert space splinters into ‘sectors’ that are at most weakly cross-correlated, one has to consider all of them separately to fully uncover the amount of chaoticity. The exact form of the sector depends on the specific scenario. We encountered several instances of this mechanism. One example is that the level statistics restricted to the computational bundle $\{A111B11\}$ is much closer to the Wigner distribution than the statistics for the complete bundle (see the discussion in Appendix C.3). Particular care must be taken when the sectors overlap in energy. The absence of inter-subspace correlations fools one into seeing Poisson statistics, where in fact, when the subspaces are correctly decomposed, each of them exhibits strong level repulsion. An example along this line is the $\{A21\}$ bundle of the $L = 5$ chain, where the multiplet *itself* is separated into two subsets. It is easy to imagine that with more complicated patterns, one can generate a spectrum where *different* weakly cross-correlated multiplets with chaotic intra-multiplet correlations can show Poisson statistics because they overlap in energy. This mechanism is quite generic and comes in different manifestations—not only in transmon physics. For example, our observation was echoed in Ref. [350], where the spectrum of the one-dimensional ionic Hubbard model was shown to separate into overlapping symmetry sectors, each of which is well described by GOE matrices. However, neglecting the separation in independent blocks yields a nearly perfect agreement with Poissonian level statistics.

To finish, we note that a curious side effect of our results is that the computational states whose multiplet consists of a single state (e.g., the multiplet $\{A11111\}$ of the 3×3 array) are resistant to delocalization down to $\delta E_J = 0$. This opens the perspective to experimentally test the predictions of this chapter (once the LASIQ precision has matured or by mimicking patterns with flux-tunable transmons). Bitstring information should be preserved much longer in these states than in strongly hybridizing multiplets.

Classical transmon dynamics

The simulations of transmon-based quantum computers on classical computers are limited to small system sizes because the Hilbert space dimension quickly surpasses the limit of what is numerically feasible. Even with sophisticated methods like shift-invert exact diagonalization [351], one is restricted to less than 20 coupled transmons. On the other hand, *classical* equations of motion (EOM) are easily solved for much larger systems sizes. Considering the Cooper pair number operator \hat{n} and the superconducting phase $\hat{\varphi}$ as a pair of classical conjugate variables (and ignoring that they have no exact classical equivalent) opens the door to handling many more qubits. Studying large classical systems is pointless if it is done only as an end in itself. However, the BGS conjecture [141], discussed in Chapter 2, gives us hope that analyzing the classical dynamics can provide us with information about the quantum properties. In this chapter, we aim to test the validity of the BGS hypothesis for our model for small system sizes. We investigate whether signatures of classical chaos appear in parameter regions that showed strong level repulsion and wave function delocalization in the quantum case. Ideally, an unequivocal connection between the quantum system and its $\hbar \rightarrow 0$ -version would allow one to draw conclusions about the viability of numerically inaccessible transmon arrays as quantum computers from the behavior of their classical counterparts alone.

The study of classical chaos in arrays of superconducting qubits was initialized by Börner [352] and later extended to frequency-engineered transmon arrays by Böninghaus [353]. Here, we extend the work presented in these references, which partly exploits parameters outside the experimental core region and focuses on single disorder realizations. Furthermore, we consider a few examples demonstrating that one can consider system sizes where the quantum case is (and will remain) unreachable in numerical simulations on classical computers. The results presented in this chapter are reported in Ref. [P2].

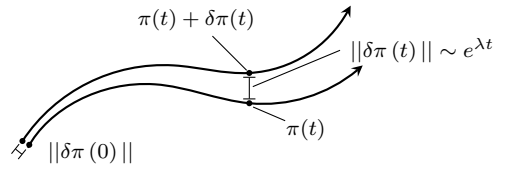
6.1 Equations of motion

To obtain the classical equations of motion describing arrays of capacitively coupled transmons, we revert the circuit quantization discussed in Sec. 3.1.3 and denote the operators $\hat{\varphi}_i, \hat{n}_i$ to classical variables φ_i, n_i . From the (symbolic) commutation relation $[\hat{\varphi}_i, \hat{n}_j] = i\delta_{i,j}$, see Eq. (3.7), it follows that φ_i and n_j satisfy the Poisson bracket

$$\{\hbar\varphi_i, n_j\} = \delta_{i,j}. \quad (6.1)$$

Figure 6.1 –

Lyapunov exponents determine the rate with which two trajectories $\pi(t)$ and $\pi(t) + \delta\pi(t)$, initially separated by a distance $\|\delta\pi(0)\|$, diverge in phase space. The distance grows as $\|\delta\pi(t)\| \sim \exp(\lambda t)$, where λ is the maximal Lyapunov exponent.



Hamilton's canonical equations of motion then read

$$\hbar\dot{\varphi}_i = \{\hbar\varphi_i, H\} = \frac{\partial H}{\partial n_i} = 8E_C n_i + T \sum_{j=\text{NN}(i)} n_j, \quad (6.2)$$

$$\dot{n}_i = \{n_i, H\} = -\frac{\partial H}{\partial \hbar\varphi_i} = -\frac{E_{J,i}}{\hbar} \sin \varphi_i, \quad (6.3)$$

where H is the classical Hamilton function obtained by replacing $\hat{\varphi}$ and \hat{n} with their classical counterparts in the Hamiltonian \hat{H} in Eq. (4.1). The sum in Eq. (6.2) is over the nearest-neighbor transmons j coupled to the transmon at site i . As pointed to in Sec. 3.2.1, the transmon can be interpreted as a rigid quantum rotor in a gravitational field, where $\hat{L}_z = \hbar\hat{n}$. In this view, the classical Hamilton function describes a system of mathematical pendulums whose moment of inertia is $I = ml^2 = \hbar^2/8E_C$ and—setting the length of the pendulum stiff $l = 1$ —with gravitational acceleration $g = 8E_C E_J/\hbar^2$. The coupling leads to a somewhat peculiar interaction between the angular momenta of neighboring pendulums.

For the implementation, we divide Eq. (6.2) by $\hbar \cdot 10^9$ and Eq. (6.3) by $2\pi \cdot 10^9$, which yields the familiar $\frac{\text{GHz}}{\hbar}$ units on the right-hand side. All factors appearing on the left-hand side are absorbed by rescaling the time t as $t \rightarrow t' = \frac{t}{2\pi} \cdot 10^{-9}$ such that a time step $\Delta t' = 1$ in the simulation corresponds to an actual time of about $\Delta t = 0.159$ ns.

6.1.1 Mimicking qubit states

As before, we are primarily interested in energies relevant to quantum computing applications, i.e., the energies of computational states with local occupation numbers ‘0’ and ‘1’. To mimic the qubit states $|0\rangle$ and $|1\rangle$ of a single transmon classically, we adopt the following convention: The kinetic energy of the rotor is set to zero, i.e., $n = 0$. We calculate the lowest energies of the quantum model E_i , $i = 0, 1$ and deflect the pendulum by an angle φ_i such that the potential energy $-E_J \cos \varphi_i$ is equal to the energy E_i of the quantum system, i.e.,

$$\varphi_i = \arccos\left(-\frac{E_i}{E_J}\right). \quad (6.4)$$

A classical transmon pendulum with energy E_0 (E_1) initialized in this way is said to be in the state $|0\rangle$ ($|1\rangle$). For multi-transmon arrays, the Josephson energy E_J in Eq. (6.4) varies from site to site. It is then straightforward to initialize the pendulum system in any classical computational state (and the generalization to higher occupation numbers is also evident).

6.2 Lyapunov exponents and methods

In Chapter 2, we emphasized that the exponentially fast divergence of initially nearby trajectories is a characteristic, even defining property of classical chaos. To capture the rate of separation

quantitatively, one considers the difference vector $\delta\pi = \pi - \pi'$ of two trajectories $\pi = (\mathbf{q}, \mathbf{p})$ and $\pi' = (\mathbf{q}', \mathbf{p}')$ in the $2S$ -dimensional phase space and linearizes the equations of motion for small $\delta\pi$, yielding

$$\delta\dot{\pi} = \mathbf{M}\delta\pi. \quad (6.5)$$

The matrix \mathbf{M} contains the second derivatives of the Hamilton function with respect to \mathbf{q} and \mathbf{p} . With the ansatz $\delta\pi(t) = \pi_0 \exp(\lambda t)$, one arrives at the eigenvalue equation for the matrix \mathbf{M} ,

$$\mathbf{M}\pi_0 = \lambda\pi_0. \quad (6.6)$$

The eigenvalues λ are referred to as *Lyapunov exponents*. If $\lambda > 0$, the solutions for the separation vectors diverge, i.e., trajectories that are initially close repel. The existence of a positive Lyapunov exponent is usually taken as an indicator of classical chaos (this also implies that the linearized EOMs are not a reasonable basis for reliable predictions about the evolution of $\delta\pi$). The number of Lyapunov exponents is equal to the phase space dimension $2S$. The different λ describe the distinct separation velocities for different orientations of the initial separation vector $\delta\pi$ in phase space. Of particular importance is the largest Lyapunov exponent λ_{\max} . In general, an arbitrary initial separation will have a component in the direction of the phase space vector associated with λ_{\max} . The exponentially growing contribution of λ_{\max} to $\|\delta\pi(t)\|$ will expunge the effect of the remaining λ , such that λ_{\max} alone can monitor the degree of chaoticity. For a visualization, see Fig. 6.1. For more details on Lyapunov exponents, see, e.g., Refs. [116, 123].

In the following, we calculate λ_{\max} to quantify the degree of chaos in the dynamical system defined by the $2S$ differential equations (6.2) and (6.3). Two different methods are employed to calculate the largest Lyapunov exponent: The results presented below rely on a method proposed by Benettin [354], where two nearby trajectories evolve in time, with their distance vector being repeatedly rescaled while preserving its direction. The Lyapunov exponent is extracted from the averaged time, after which a certain phase space distance threshold $\|\delta\pi\|$ is exceeded, see the original paper [354] or Ref. [355] for details. To cross-check the results, the complete Lyapunov spectrum is also calculated using the ‘H2’ method proposed in Refs. [356, 357]. For both methods, we use the implementation provided by the software library `DynamicalSystems.jl` [355] that, in turn, is based on `DifferentialEquations.jl` [358]. The equations of motion are solved using the implementation of Tsitouras 5/4 Runge-Kutta method [359]. We verified that the results for λ_{\max} are invariant if higher-order methods (Verner’s “Most Efficient” 7/6 Runge-Kutta method [360]), lower error thresholds, and longer evolution times (the exact λ_{\max} is obtained as a $t \rightarrow \infty$ limit) are used. The units of the Lyapunov exponent are inverse to the time unit. In our case, this implies that $\lambda_{\max}/2\pi$ is measured in GHz. In what follows, we suppress the factor $\text{GHz}/2\pi$ and directly visualize the numerically obtained values.

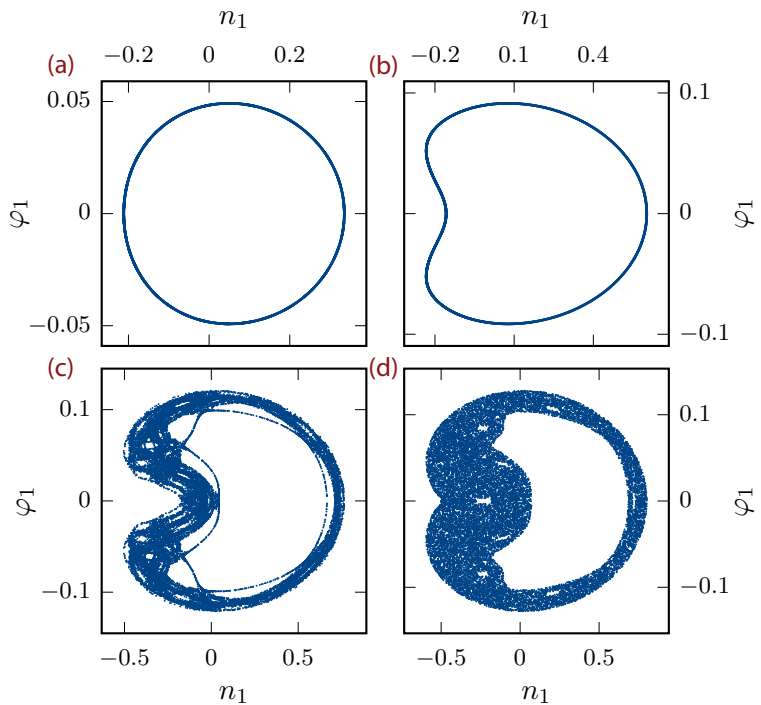
6.3 Results

6.3.1 Two coupled transmons

A striking results of Ref. [352] was the observation that chaos already emerges in the classical two-transmon Hamiltonian, provided that the system is excited to sufficiently high energies. For such low-dimensional phase spaces, a handy tool for analyzing the dynamics are Poincaré sections. The idea is to capture a stroboscopic impression of the motion in phase space by marking the system every time it crosses a directional hyperplane. To be specific, we record all pairs (φ_1, n_1) with $\varphi_2 = 0$ and $n_2 > 0$, i.e., the Poincaré section is the projection of the intersection of the phase space trajectory with the $\varphi_2 = 0$ plane to the φ_1 - n_1 plane, where the requirement $n_2 > 0$ fixes a

Figure 6.2 –

Poincaré sections for two coupled transmons. The four panels show Poincaré sections in the φ_1 - n_1 plane with $\varphi_2 = 0$ and $n_2 > 0$. The initial conditions are $\varphi_1^{\text{init}} = n_2^{\text{init}} = 0$, $n_1^{\text{init}} = 0.01$, and $\varphi_2^{\text{init}} = \pi - x$. Specifically, we choose (a) $x = 0.1$ (b) $x = 0.05$, (c) $x = 0.02$ (d) $x = 0.0005$. The projected trajectory changes from a curve to an area as φ_2^{init} approaches π , indicating the onset of classical chaos. We set $E_{J,1} = 98.8$ GHz, $E_{J,2} = 101.2$ GHz, $T = 40$ MHz, and $E_C = 250$ MHz. Inspired by Ref. [352].



crossing direction. For integrable systems, the existence of two conserved quantities restricts the phase space trajectories to two-dimensional tori such that the intersection with the plane $\varphi_2 = 0$ results in a curve in the (φ_1, n_1, n_2) space. The projection to the φ_1 - n_1 plane is also a curve. On the other side, if only the Hamilton function is conserved, the phase space trajectory lies on a three-dimensional submanifold, and the intersection with the plane $\varphi_2 = 0$ is a two-dimensional object in the (φ_1, n_1, n_2) space. Projecting to the φ_1 - n_1 plane yields an area covering a finite fraction of the plane that becomes densely filled as $t \rightarrow \infty$. Studying Poincaré sections thus allows one to distinguish between chaotic and integrable dynamics.

To monitor the onset of irregular dynamics, we vary the initial angle φ_2^{init} while keeping $\varphi_1^{\text{init}} = n_2^{\text{init}} = 0$ and $n_1^{\text{init}} = 0.01$ fixed. Fig. 6.2 shows four different Poincaré sections for initial angles φ_2^{init} , which—from (a) to (d)—get progressively closer to π . While the closed curves for (a) and (b) indicate that the motion is (quasi)periodic and thus integrable, one observes a qualitative change upon further increasing φ_2^{init} . The Poincaré section then extends over a finite fraction of the φ_1 - n_1 plane, as is expected for chaotic systems where only energy is conserved.¹

In Fig. 6.3, we show the chaotic trace of Fig. 6.2(c) together with additional Poincaré sections belonging to trajectories with different initial conditions but identical energy. What stands out is the coexistence of irregular orbits and simple, regular trajectories, forming integrable islands in the surrounding chaos. This is a typical trait of weakly nonintegrable systems [116] and is usually discussed in the context of the Kolmogorov-Arnold-Moser (KAM) theorem [361] that considers the stability of tori of an integrable system when adding small perturbations. Here, however, we do not add an integrability-breaking term to the Hamiltonian but control the strength of the

¹The largest Lyapunov exponent further corroborates these findings. We observe that λ_{\max} remains close to zero for $\varphi_2^{\text{init}} \lesssim \pi - 0.03$ but acquires a nonzero value if the initial angle further increases. However, the Lyapunov analysis for the specific initial conditions with $\varphi_2^{\text{init}} \approx \pi$ has the inconvenience that the precise number depends strongly on the parameters of the algorithms. In particular, it never truly converges in the evolution times considered. This pathology is only observed for this specific initial condition and is why we refrain from providing specific numbers. Note, however, that one always finds a nonzero Lyapunov exponent for the same initial condition, regardless of the convergence issues in the $\lambda_{\max} \neq 0$ regime.

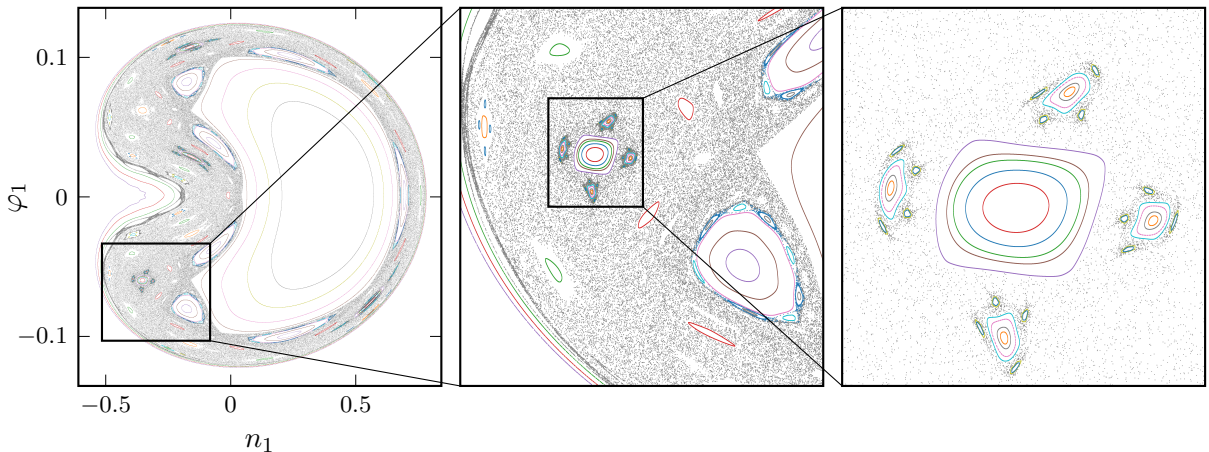


Figure 6.3 – Coexistence of chaotic and regular orbits in a system of two coupled transmons. The chaotic orbit, shown in gray, has the same initial conditions as in Fig. 6.2(c). All trajectories belong to the same energy. Upon magnification of the excerpts, one notices a recurring pattern of regular orbits surrounded by smaller integrable islands. This self-similarity is a textbook example of the Poincaré-Birkhoff theorem.

nonintegrability via the energy (the famous Hénon-Heiles model [362] is similar in that regard). Nevertheless, one observes other KAM characteristics as well, for example, the emergence of self-similarity on all scales as a consequence of the splitting of all rational tori into chains of elliptic and hyperbolic fixpoints (Poincaré-Birkhoff theorem, see, e.g., Ref. [132]). This is illustrated by the enlarged views in Fig. 6.3, where the magnification reveals a recurring pattern of regular islands.

These considerations establish that systems of only two transmons can show chaotic dynamics, but it should be noted that chaos is generated very artificially:

- The chosen Josephson energies E_J lie above the experimental core region.
- The coupling T is near the upper limit of current experiments.
- The excitation energies surpass the relevant range for information processing.

For initial conditions mimicking the computational states $|00\rangle, |10\rangle, |11\rangle$, the signatures of chaos disappear. Furthermore, the traits of chaos are a peculiarity of how the energy is initially divided between the two transmons. For example, the Lyapunov exponents strictly vanish for initial conditions where an energy similar to the one in Fig. 6.2(d) is distributed equally to both transmons. As is to be discussed next, chaos loses its synthetic form once the number of transmons increases. It then affects the dynamics of systems with energies and parameters relevant to quantum computing applications.

6.3.2 Ten coupled transmons

We now turn to our paradigmatic example of the $L = 10$ chain and focus on energies pertinent to quantum information processing. More precisely, the system is prepared in the $|1010\dots\rangle$ state, i.e., the angles φ_i on the even (odd) sites are chosen such that the initial single transmon energies correspond to the quantum mechanical energies E_0 (E_1). Fig. 6.4(a) shows the results for the disorder-averaged maximal Lyapunov exponent for scheme-A disorder and the same values of the Josephson energy E_J and the coupling T used for the quantum model in Sec. 4.5. Notably, λ_{\max} is nonzero almost everywhere in the $T-E_J$ plane, indicating that the ten-transmon chain shows

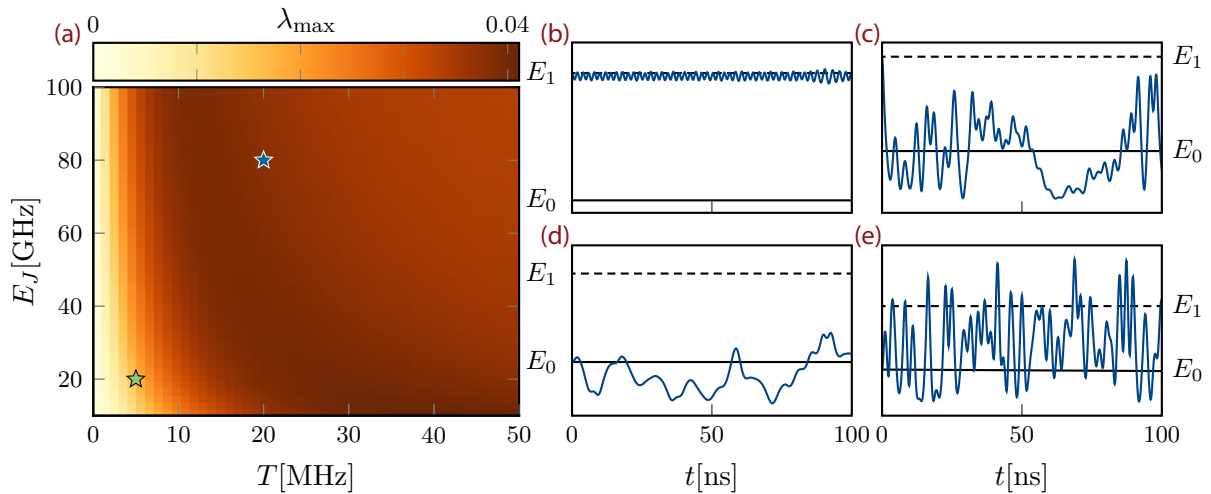


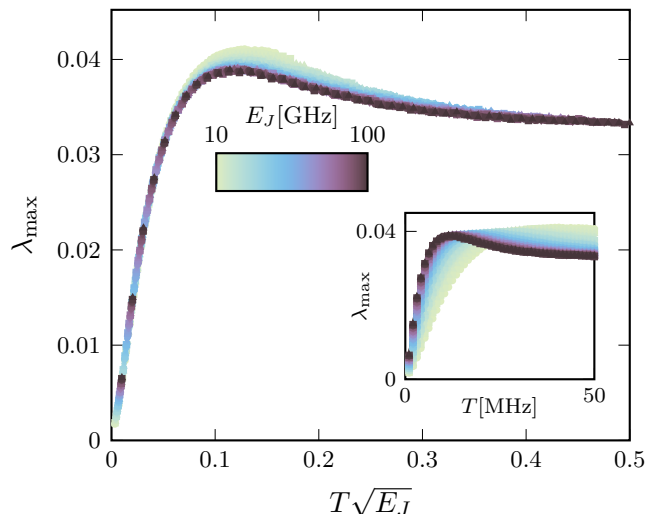
Figure 6.4 – Classical chaos in a chain of ten coupled transmons. (a) Disorder averaged maximal Lyapunov exponent for scheme-A disorder and the same T and E_J values as in Fig. 4.13. The transmon is initialized in the $|1010\dots\rangle$ state. For each parameter point, λ_{\max} is averaged over at least 8,000 disorder realizations. Panels (b)–(e) show the time-dependent single transmon Hamilton functions for the sites 5 (upper row) and 6 (lower row) for two disorder realizations. The left (right) column corresponds to a disorder realization with parameters marked by the green (blue) star in (a). In all panels, the quantum mechanical energies E_0 and E_1 are indicated by the solid and dashed vertical lines. Whereas the transmon energies remain near their initial values in (b) and (d), they fluctuate heavily on timescales much shorter than typical decoherence times in (c) and (e). Only in the first case can one draw credible conclusions about the initial bitstring ‘1010…’ from the energies at $t > 0$. This consideration shows that the magnitude of λ_{\max} , which is small for (b) and (d), but large for (c) and (e), can serve as a quality indicator of the classical transmon ‘storage device’.

traits of classical chaos in a significant part of the relevant parameter ranges and for energies at which quantum computers operate. A λ_{\max} near zero is only found in a narrow region around $T = 0$. On closer inspection, one recognizes that the Lyapunov exponent is not monotonically increasing. Following one of the horizontal lines with a fixed E_J , it becomes apparent that a maximum and a minor drop follow the initial sharp increase. Finally, λ_{\max} settles at a value slightly below its maximum amplitude as T increases further.

Using the timescale on which the local excitation numbers $\langle \hat{n}_i \rangle$ fluctuate as a barometer, we discussed in Sec. 4.9 that the compromising effects of quantum chaos occur fast compared to typical decoherence or gate times, which renders information storage impossible. Classically, one may attempt to encode local information in the energies of the individual transmons. As an example, consider the Hamilton function for the transmon at lattice site 5, i.e., $H_5(t) = 4E_C n_5(t) - E_{J,5} \cos \varphi_5(t)$. If $H_5(t)$ takes the value of the ground state energy E_0 , this encodes the bit value ‘0’, and similar for E_1 and ‘1’. For proper information storage, once initialized in, say, ‘1’, transmon 5 should stay close to E_1 , or at least not cross E_0 in an uncontrolled way. We analyzed the temporal fluctuations in the ‘on-site’ energies for transmon arrays initialized in the $|1010\dots\rangle$ state and the parameter points marked by the stars in Fig. 6.4(a). The results are shown in Fig. 6.4(b)–(e). For clarity, the visualization focuses on the lattice sites 5 (upper row) and 6 (lower row). The left column ((b) and (d)) show $H_5(t)$ and $H_6(t)$ for the parameters marked by the green star in panel (a). This point has a nonzero yet very small Lyapunov exponent. The local transmon energies fluctuate around their initial values (E_1 (E_0) for transmon 5 (6)) but remain close such that $H_5(t) \approx E_1$ and $H_6(t) \approx E_0$ for all t . The information is therefore maintained over the considered timescale. The situation is quite different for the blue star in (a).

Figure 6.5 –

Data collapse for the maximal Lyapunov exponent. As for the KL divergences and the IPR, the individual horizontal lines of fixed E_J forming the 2D representation of λ_{\max} in Fig. 6.4(a) (and also shown in the inset) can be collapsed onto each other by rescaling the coupling with the respective value of the Josephson energy as $T \rightarrow T\sqrt{E_J}$. Especially for small $T\sqrt{E_J}$, i.e., in the region where λ_{\max} rapidly increases, all data collapses almost perfectly on a single line, indicating that $T\sqrt{E_J}$ is the crucial quantity controlling the onset of classical chaos.



With the Lyapunov exponent close to its maximal value, the local transmon energies fluctuate rapidly with an amplitude that exceeds the energy spacing between E_0 and E_1 . For example, as shown in (c), the local energy of transmon 5 drops from E_1 to E_0 after only a few nanoseconds and never fully recovers. Information about the initial ‘1010...’ bitstring is rapidly washed out. The two disorder realizations for which the results in Fig. 6.4(b)–(d) were obtained are ‘typical representatives’ of their parameter points in the sense that the individual Lyapunov exponent are close to the disorder-averaged values. This analysis thus suggests a valid correspondence between the suitability of the system as a classical memory and the magnitude of the Lyapunov exponent.

Another striking feature in Fig. 6.4(a) is that the lines of constant λ_{\max} are similar to the contour lines of the IPR and the KL divergences in the quantum model. In fact, rescaling the T axis as $T \rightarrow T\sqrt{E_J}$ reconciles the individual traces of the Lyapunov exponent underlying Fig. 6.4(a). As shown in Fig. 6.5, all $\lambda_{\max}(T)$ obtained for different Josephson energies (shown in the inset) are collapsed onto each other. The data collapse works particularly well in the small- T region. Thus, the classical systems show an intriguingly close relationship to the quantum system, for which we identified the parameter $T\sqrt{E_J}$ as the transition-driving quantity. In Sec. 4.5.3, a good data collapse was obtained by rescaling T as $TE_J^{0.54}$.

6.3.3 Towards larger system sizes

The above discussion shows that the predictions of the BGS conjecture are accurately met for arrays of capacitively coupled transmons, paving the way to apply classical simulations to larger systems for predicting the danger posed by *quantum* chaos. Fig. 6.6(a) depicts the disorder-averaged maximal Lyapunov exponent for chain geometries containing between two and 40 transmons. Chains with $L > 20$ elude quantum mechanical simulation. As before, the arrays are initialized in the classical analog of the $|1010\dots\rangle$ state. We set $E_J = 10$ GHz and exploit scheme-A disorder. Besides demonstrating that classical simulations can easily handle larger systems, Fig. 6.6(a) also shows a slight tendency toward more chaos as the system size increases. In particular, already the four-transmon chain becomes chaotic when initialized in a typical computational state.

Fig. 6.6(b) depicts results for the 65-qubit ‘Hummingbird’ processor, scheme-A disorder, and three different values of the Josephson energy E_J . For the heavy-hexagon geometry, one has

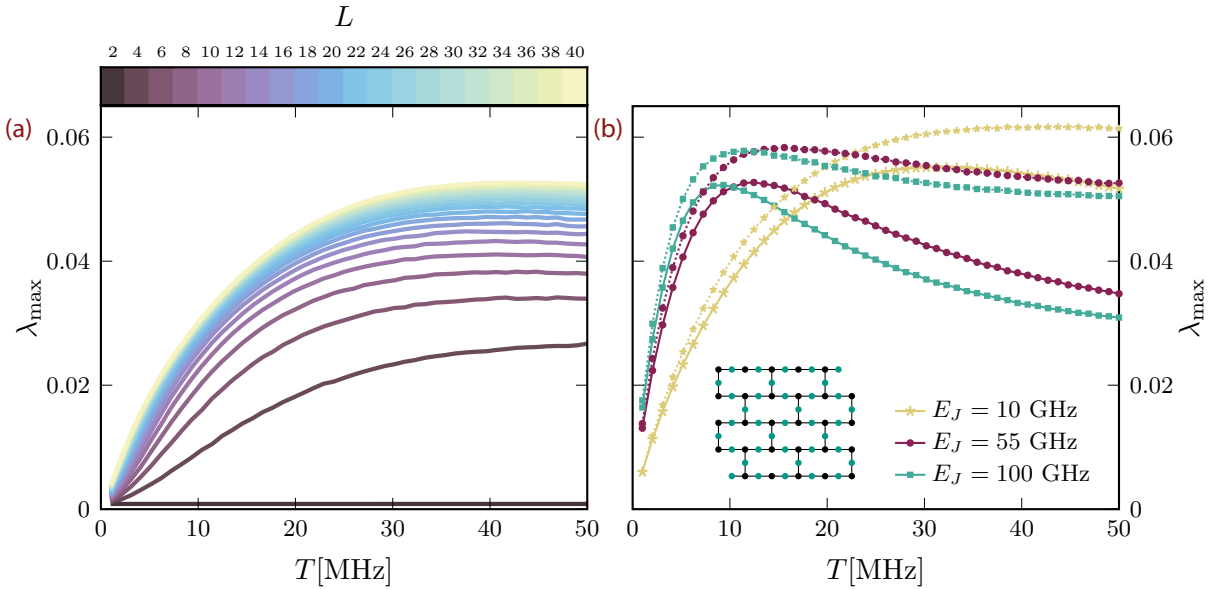


Figure 6.6 – Classical chaos in large systems, beyond the limit of what can be simulated quantum mechanically. (a) Maximal Lyapunov exponent for transmon chains of varying length L , initialized in the $|1010\dots\rangle$ state. All results are averaged over at least 18,000 disorder realizations. Quantum mechanical simulations are restricted to $L < 20$. (b) Results for the ‘Hummingbird’ layout. In the inset, green (black) lattice sites denote control (target) qubits. The solid (dotted) lines correspond to an initial states where all target (control) qubits are initialized in the state $|1\rangle$ and the remaining transmons in the ground state. Results are averaged over at least 5,000 disorder realizations.

to distinguish between two initial conditions with an alternating 1–0 pattern: The dotted lines show the results when all target qubits (shown in black in the small inset) are initialized in $|0\rangle$ and the control qubits (green) in $|1\rangle$. For the solid lines, the situation is reversed. As the number of control qubits exceeds the target qubits, the energy density is higher if the control qubits are initialized in $|1\rangle$. For this configuration, the Lyapunov exponent is found to be larger, signaling a stronger propensity to chaos. The nonmonotonicity in λ_{\max} is more pronounced in this two-dimensional geometry, a trend that continues on the square lattice with even higher connectivity (results are not shown).

For a single disorder realization, it takes $\mathcal{O}(10)$ seconds² to calculate the Lyapunov exponents for the 130-dimensional phase space of a ‘Hummingbird’ processor on a single core of an ordinary desktop computer. For the same system, when initializing, e.g., all control (target) qubits in the state $|1\rangle$ ($|0\rangle$), the corresponding excitation bundle (that, strictly speaking, is no longer well-defined at such high energies) alone contains more than 10^{27} states.

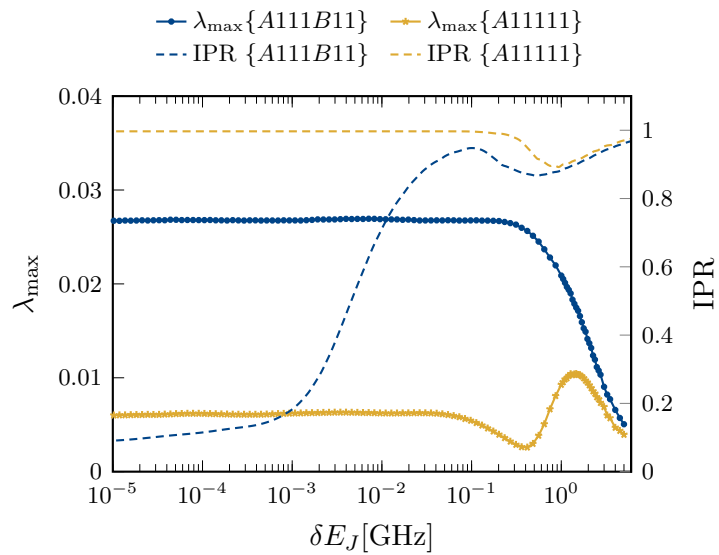
6.3.4 Classical chaos in frequency-engineered transmon arrays

Finally, we show that the classical analysis is also sensitive to the more subtle forms of delocalization we encountered in the precision-engineered transmon arrays in Chapter 5. We exemplify this with the familiar 3×3 geometry with a superimposed AB frequency pattern. This problem was first addressed in Ref. [353]. We discuss two different initial conditions: First, three of the five A transmons and two of the B transmons are initialized in the $|1\rangle$ state. The remaining

²This estimate holds for the default settings of the software library [355], with which the results of Fig. 6.6 were obtained. For example, neighboring trajectories evolve for a total of 10,000 time units. See Ref. [355] for more details.

Figure 6.7 –

Classical chaos in precision-engineered transmon arrays. Shown is the disorder-averaged λ_{\max} calculated for initial conditions mimicking states from the two multiplets $\{A111B11\}$ and $\{A11111\}$. For comparison with the quantum model, the IPR of the respective bundles is depicted as well (dashed lines). The classical results reflect several properties of the quantum system, e.g., the inset of early chaos indicators at similar disorder strengths or the more pronounced susceptibility of the $\{A111B11\}$ bundle. All results are averaged over at least 30,000 disorder realizations.



transmons start in $|0\rangle$. Second, all excitations are put on the A sublattice. In the parlance of Chapter 5, this corresponds to initial configurations from the permutation multiplets $\{A111B11\}$ and $\{A11111\}$. All systems parameters are chosen as in Fig. 5.5. Fig. 6.7 shows the results for the disorder-averaged, maximal Lyapunov exponent as a function of the residual disorder, i.e., the frequency spread δE_J around the two mean values $E_{J,A}$ and $E_{J,B}$. Recourse to the quantum mechanical model (partially) explains the observed behavior. Thus, to facilitate the discussion, the bundle-specific IPR is also displayed in Fig. 6.7.

When the pattern structure is negligible for large disorder, the Lyapunov exponent is close to zero for both multiplets. Quantum mechanically, this regime corresponds to the global MBL phase with an IPR close to one. For the multiplet $\{A111B11\}$, both the classical and the quantum model exhibit signatures of chaos as the disorder lessens. The IPR displays the characteristic succession of disorder regimes discussed in Chapter 5: a slight decrease before the multiplets form, followed first by a plateau where states are localized within multiplets, then by the quantum chaotic phase for even smaller δE_J and, finally, the symmetry-dominated regime. Not all these successive transitions are resolved in the Lyapunov exponent. λ_{\max} increases for the same disorder strength where the first drop in the IPR occurs but quickly saturates at a disorder strength of about $\delta E_J = 300$ MHz without resolving the regime of intra-multiplet localization. Further reducing the frequency spread does not increase the chaoticity.

The multiplet $\{A11111\}$ contains only a single state. Therefore, the IPR remains close to one for all values of δE_J , except for the small disorder range ($\delta E_J \sim 1$ GHz) between global MBL and multiplet formation. This behavior is fairly accurately reflected by λ_{\max} , which exhibits a maximum at a similar disorder strength. However, after further lowering the disorder, λ_{\max} saturates at a small nonzero value, about four times smaller than for $\{A111B11\}$.

In summary, the Lyapunov exponent shares many, though not all, characteristics of the feature-rich IPR. For example, classical chaos and delocalization of quantum mechanical wave functions set in at similar disorder strength. The two multiplets show different behavior in both, their low- δE_J Lyapunov exponents and IPRs, suggesting that the classical analysis can resolve the difference in the susceptibility of multiplets to quantum chaos. On the other side, the classical system tends to be somewhat more prone to the onset of chaos, an observation that has also been made in other systems [363]. For example, there is no further minimum of λ_{\max} mirroring the regime of intra-multiplet delocalization.

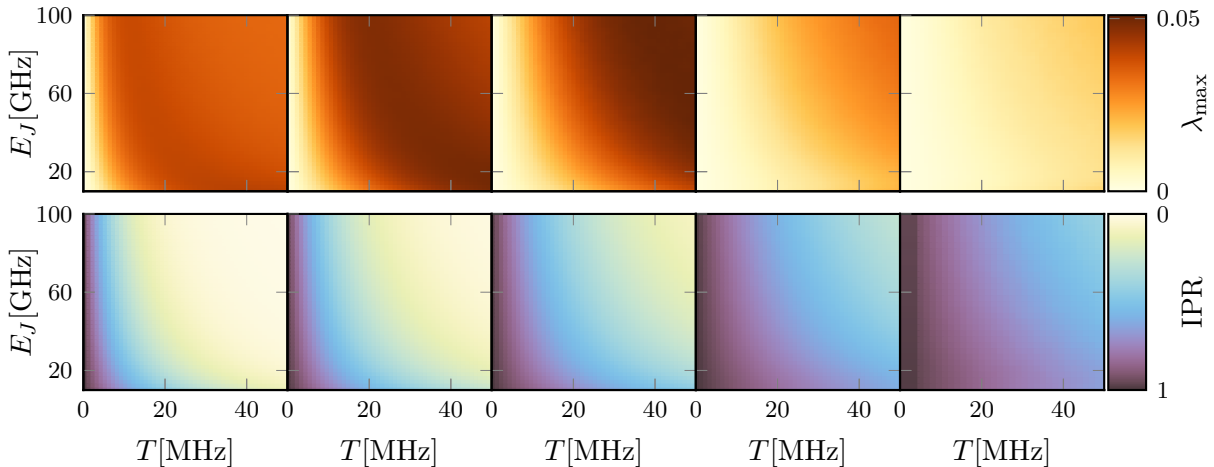


Figure 6.8 – Comparison of classical and quantum chaos for various disorder regimes ranging from scheme A (left) to scheme B (right). There is a striking similarity, especially for small $T\sqrt{E_J}$, between the evolution of the maximum Lyapunov exponent (top row) and the IPR (bottom row). In both the classical and the quantum model, the important parameter interpolating between regular and chaotic behavior is $T\sqrt{E_J}$ (for a disorder that scales as $\delta E_J \propto \sqrt{E_J}$). Increasing the disorder pushes the chaotic region to the upper right corner in the T - E_J phase diagrams. To be specific, the disorder is defined as $\delta\nu = c \cdot E_C$ or equivalently $\delta E_J = \frac{c}{4}\sqrt{2E_J}$, where, from left to right, $c = 1/2$ (scheme A), $c = 1$, $c = 2$, $c = 4$, $c = 6$ (scheme B).

6.4 Summary

In this chapter, we considered the transmon quantum computer as a classical system of coupled nonlinear pendulums and used the Lyapunov exponent to quantify the degree of classical chaos. Signatures of irregular dynamics already emerge in systems of only two transmons, albeit at very high energies. For the ten-transmon chain, chaos emerges at energies, system parameters, and timescales relevant to quantum computing applications.

In particular, this analysis demonstrates an intimate connection between the properties of the classical and quantum model. This is summarized in Fig. 6.8, which shows λ_{\max} (upper row) and the IPR (lower row) for various regimes between scheme-A and scheme-B disorder. In many facets, their behavior is similar: increasing the disorder pushes the realm of chaos to the upper right corner of the T - E_J phase diagram and enlarges the chaos-free comfort zone. We note, however, that despite the intriguing similarity, some features of the classical model are unique. For example, the ‘twilight zone’ of hybrid level statistics has a slightly larger Lyapunov exponent than the region of hard quantum chaos.

In proof-of-principle calculations, we demonstrated that the classical simulation can tackle much larger systems. Statements about the scaling of the complexity of solving the transmon EOMs with increasing system size are difficult to make. The calculation time varies enormously when changing the integration methods or the desired accuracy. What can be said, however, is that the complexity increases slower than for quantum mechanical calculations. For example, using an explicit ODE solver, the effort for a single time step grows as $\mathcal{O}((m+1)L)$, where L is the number of transmons and m is the coordination number. This gives hope that classical simulations can keep up with the processor sizes expected in the upcoming years (e.g., IBM’s 4,158-qubit ‘Kookaburra’ processor announced for 2025).³

³In passing, we note that some tentative results for a 1,121-qubit system (inspired by IBM’s largest monolithic ‘Condor’ processor) fit neatly into the presented results.

What is the predictive power of classical simulations? Our analysis shows an unequivocal, qualitative connection between the classical and the quantum mechanical system at the level of disorder averages. The missing pieces to make the classical analysis a potent tool for identifying optimal system parameters are

- to establish a quantitative relationship, e.g., a mapping between specific values of the Lyapunov exponent and the IPR.
- a demonstration that the correspondence between λ_{\max} and the IPR also holds on the level of individual disorder realizations.

Let us elaborate on the second point: For fixed E_J and T , the values for both IPR and λ_{\max} scatter around a mean value, which so far has been the focus of our considerations. What is to be shown is that individual disorder realizations, which show unusually little signatures of classical chaos (lower λ_{\max} than the mean), also have an exceptionally high IPR. For small systems, like the $L = 10$ chain, this is straightforward (yet left for further research) to check. If the assumption is confirmed, *classical* simulations could identify the configurations in the Josephson energy landscape that are most appropriate for *quantum* computing, even for system sizes beyond the reach of a quantum mechanical simulation.

Of course, we have opened the richly filled toolbox of classical chaos theory only for a crack. It would also be interesting to apply other methods which have recently gained popularity for the quantification of classical chaos, like the generalized alignment index method [364] or the 0-1 test [365], to our system to investigate whether these can contribute in formulating sharper quantitative connection between the classical and the quantum system.

Concluding remarks

All quantum computing efforts operate in a tension field between efficient qubit operation and qubit protection. The paradigmatic example for this *protecting-operating dilemma* is the irreconcilability of perfect shielding from the environment to prevent rapid decoherence with the need to couple qubits to the environment for enabling manipulation and readout. The work conducted within the framework of this thesis introduced a novel incarnation of the protecting-operating dilemma. By bringing the concepts of many-body localization to the transmon architectures for quantum computing, we showed that qubits must not only be protected from decoherence but also from the intrinsic, destabilizing effects of *quantum chaos* and eigenstate thermalization. Chaotic fluctuations emerge regardless of the properties of the individual qubits, i.e., even for hypothetical qubits with infinite decoherence times. A central role is played by disorder that arises either due to imperfections in the fabrication process or as artificially introduced site-to-site variations in the Josephson energies. Disorder has a Janus-faced character: Too much disorder prevents the onset of chaotic fluctuations but sacrifices operational efficiency because entangling gate operations are slowed down. For too little disorder, any locally encoded information is quickly lost during the unitary time evolution of the thermalizing system. The most important finding established in this thesis is that this hazard is not a hypothetical one. We demonstrated that the abysses of chaos reach close to the parameter regions in which some of the contemporary transmon platforms operate. Quantum chaos affects the processing of information on timescales much shorter than typical decoherence times.

Transmon engineering research is characterized by a certain ephemerality: it constantly breeds new proposals for qubit variants [312], coupling schemes [366], or gate techniques [367], see the references for proposals that appeared in 2022. Predicting whether an idea will prevail is difficult. What starts promisingly often has to be abandoned, modified, or further extended because the initial approach is not scalable. An example is the LASIQ technology: Since it was first unveiled in the fall of 2020, it has served as an indispensable tool to lift IBM's quantum computers to the current level of maturity, signaled by a constant increase in the quantum volume [311]. At the same time, however, it has become abundantly clear that LASIQ alone is insufficient to keep pace with the company's own roadmap [297]. The development of modular quantum computer designs, which is being driven forward in parallel with the construction of the monolithic processors (that ends with the 'Condor' chip in 2023), will, for example, be accompanied by a major turnaround in the coupling hardware and exploit a tunable coupler architecture [368]. For these reasons, the ultimate aspiration of an MBL perspective to the transmon quantum computer should not exclusively be to capture the current state of the technology or to follow the innovations of transmon engineers¹ at every turn. Equally important are the timeless find-

¹As an example of the transitory nature of the 'state of the art', we note that days before this work was completed, IBM made its 'Prague' processor [369] publicly available. It realizes a strongly detuned *AB* frequency pattern ($\nu_A - \nu_B$ is around three times larger than expected for fixed-frequency architectures). This processor exploits

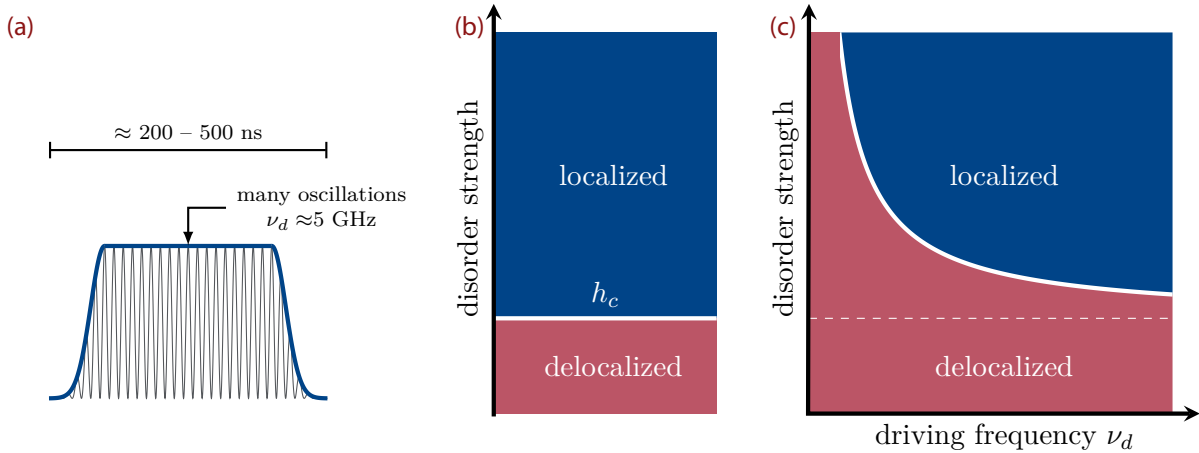


Figure 7.1 – Fate of the MBL phase under a periodic drive. (a) The cartoonish sketch of a CR drive tone shows that the envelope contains many oscillations, such that one can consider the transmon array as a Floquet system. (b)–(c) An MBL phase that exists above a critical disorder strength h_c can survive a periodic drive with frequency ν_d , provided that the driving frequency is high enough. Figure inspired by Ref. [218].

ings that remain valid independent of new ingenious workarounds to mellow, e.g., the frequency crowding problem. From this bird’s eye perspective, the most important insight of this study is that the MBL perspective offers a fresh perspective on transmon-based quantum computers. It reveals new insights that are overlooked in the ‘traditional’ two- or few-qubit picture. The MBL toolbox should therefore complement the existing quality indicators. As an example, reconsider the results of the Walsh analysis in Chapter 4. So far, the superconducting qubit community has only tried to free qubits from the nearest-neighbor ZZ couplings, which are indeed the most dangerous ones. However, our analysis indicates that more remote couplings crucially affect the identity of the l -qubits. Pondering the influence of more distant correlations—exponentially smaller but also exponentially more numerous—on the structure of many-body eigenstates has always been an integral part of MBL theory. Along similar lines, this also applies to the results presented in Chapter 5. The idea of implementing a ‘frequency unit cell’, i.e., a pattern that continues disorder-free in the processor geometry, is motivated by the examination of NN frequency collisions in minimal setups of two to three qubits. However, regular patterns are a fundamental obstacle in realizing a functioning computing device. Wave functions delocalize due to principles that lie outside the well-studied ZZ paradigm. Therefore, insights from MBL physics are relevant for transmon processors, including from an engineering perspective.

Looking forward, there are many possible extensions of our work. Most trivially, the model considered here can be used to work through the unique dynamical properties that characterize the MBL phase, like the logarithmically slow entanglement spreading or the recently discussed memory hierarchy for many-body localization [370]. Just as the static diagnostic monitors a varying extent of delocalization in the MBL *regime*, it is interesting to investigate the behavior of the different dynamical quantities for experimentally relevant parameters in small transmon arrays. Conceptually, no radically new insights are to be expected there because, for example, the entanglement growth is a symptom of the nonlocal nature of the wave functions condensed in the Walsh coefficients and the IPR. A more progressive step is to revert the approximations made in Chapter 1 that yielded the minimal ‘quantum memory’ model and to study whether dynamical instabilities during gate operations might be a further stumbling block in realizing a

a new hardware approach [369], even though no further details are known yet.

high-quality transmon quantum computer. A pilot project [P3] investigated a minimal system consisting of two transmons coupled to a common oscillator that is driven with a fine-tuned control pulse to implement an entangling BGATE [371]. It was shown that signatures of irregular dynamics emerge in the eigenphase distribution of the time evolution operator, which is described by the circular unitary ensemble [372] if the dynamics are chaotic. Such small systems, e.g., the $L = 3$ transmons chain, showed little evidence of delocalization in the static case, indicating that the implementation of gates meets new, chaos-related challenges. Beyond this rather meticulously designed and artificial gate approach, all-microwave gates in fixed-frequency architectures, in general, deserve special attention from an MBL perspective. These gates are activated by periodically driving a transmon or, as above, a common oscillator. As schematically shown in Fig. 7.1(a) for the CR gate, the gate duration is long compared to the drive frequency. One can therefore consider the transmons as a periodically driven Floquet system. Pioneering work by Abanin *et al.* [219] and Lazarides *et al.* [218] demonstrated that a periodic drive bears the capability of fundamentally altering the MBL-ETH phase diagram shown in Fig. 7.1(b). The localized phase that exists for a disorder exceeding some critical value h_c gets diminished once a periodic drive sets in, provided that the driving frequency is slow enough, as can be seen in Fig. 7.1(c). Quantitatively, one can capture the reshaping of the phase boundary by estimating the probabilities of adiabatic Landau-Zener transitions occurring in the time-evolved spectrum [219]. In general, a *local* drive is expected not to alter the stability of the MBL phase. The above picture holds for a global drive on all system constituents. For the transmon array, this raises the question of whether it is possible to run multiple gates simultaneously or whether the already small margin for a good balance between disorder and coupling strength is further diminished. A first attempt to bring the ‘curvature measures’ for capturing the Landau-Zener probabilities introduced in Ref. [373] to small instances of cross-resonance architectures has been made in Ref. [374].

Concerning an experimental validation of our predictions, one should note that in a real quantum computer, many harmful influences play in concert to prevent the device from working error-free, such that it might be a nontrivial task to isolate the effect of delocalization. However, recent developments allow one to directly probe the many-body spectrum and scan it for signatures of level repulsion [211]. Flux-tunable architectures deserve special attention: Even though they typically operate with a larger frequency spread, they can mimic the smaller scheme-A disorder of fixed-frequency architectures. They could also be exploited to implement frequency patterns, a task for which it remains doubtful whether it can be carried out with the current state of the LASIQ technology. Similarly, tunable couplers allow one to probe the entire coupling range T considered here [39].

While this thesis investigated the implications of many-body physics for the construction of transmon quantum computers, one can also turn the table and exploit transmon arrays as *simulators* of interacting many-body systems. This opposite perspective has gained considerable attention in the last few years, from theory [183] and experiments [211, 335, 375]. Superconducting qubits have established themselves as one of the leading platforms for investigating the intricacies of localization physics. In particular, the hope is that transmon experiments could be used to shed more light on the renewed discussion on finite size effects in MBL systems [204, 376]. Recently, signatures of the MBL phase were probed in a processor of 19 transmons [377], a system size at the very top edge of what classical computers can simulate.

As a final closing remark, it should be said that—despite the observation made here that some transmon platforms are close to the edge of chaos with all its devastating consequences—we take this work to be a constructive contribution: Ideally, it is a first step towards establishing the many-body perspective as an integral part of future processor design efforts. The sharp tools

presented here can help to identify optimized device configurations that precisely hit the difficult compromise in the ‘low vs. high disorder’ or ‘slow gates vs. quantum chaos’ manifestation of the protecting-operating dilemma. This holds in particular for the Walsh analysis that reacts very sensitively to early indicators of delocalization. Initial efforts in this direction have been made in Ref. [378], that employs the Walsh diagnostic to design a quasi-periodic frequency patterning that effectively localizes the system. Moreover, we established a close analogy between the occurrence of chaos in classical systems of coupled mathematical pendulums and the appearance of quantum chaos. This suggests that classical chaos theory can serve as a useful benchmarking tool for system sizes beyond the reach of a quantum mechanical simulation and specifically for the processor geometries that are expected to be launched in the upcoming years. First follow-up work [376, 379] shows that the symbiosis of the very theoretical branches of many-body localization theory and classical chaos theory with the more applied field of superconducting qubit engineering is considered very fruitful and beneficial.

Appendix for Chapter 3

A

A.1 Examples of LASIQ tuned chips

In Sec. 3.5.1, we claimed that the frequency distribution in fixed-frequency processor architectures is usually well described by a single Gaussian. For the IBM cloud devices, the width of this normal distribution is around 100 MHz. This holds even for chips where the frequencies are modulated post-fabrication to reduce the number of NN frequency collisions. Here, we substantiate this statement with further examples of processors from the IBM cloud [59]. We consider one chip of each of the three generations in use in mid-2022, the ‘Falcon’, ‘Hummingbird’, and ‘Eagle’

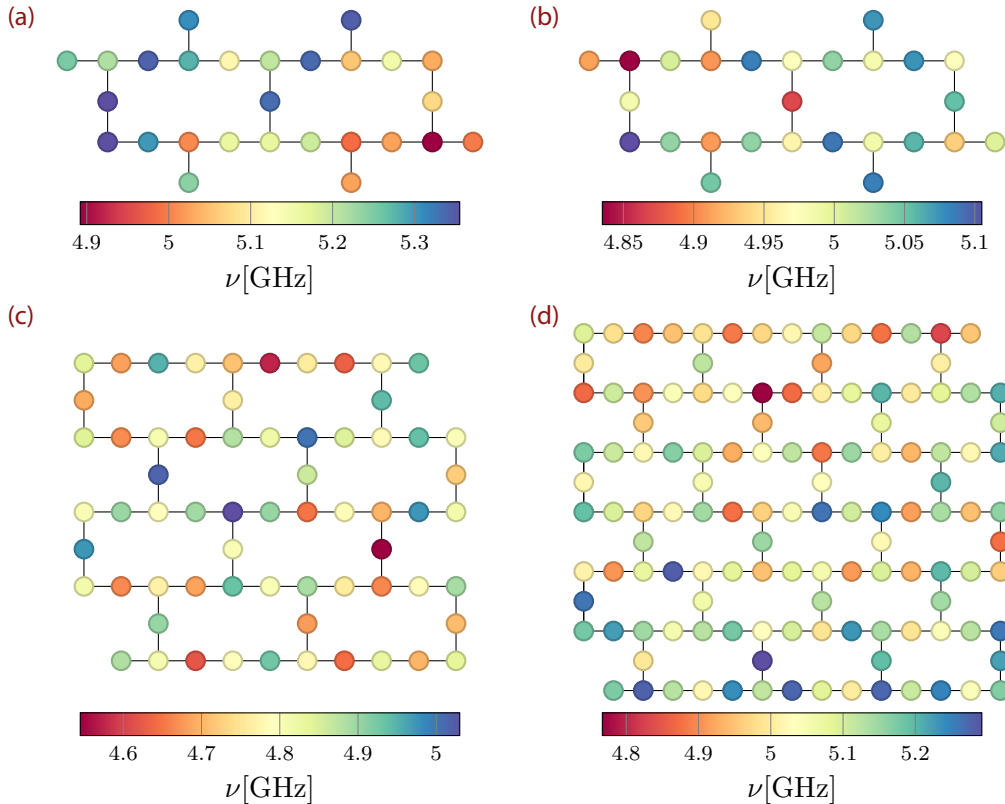


Figure A.1 – Processor geometries and spatial distribution of frequencies for (a) an untuned ‘Falcon’ chip and (b)–(d) LASIQ-tuned IBM cloud devices. Panel (b) shows the ‘Montreal’ (‘Falcon’), (c) the ‘Manhattan’ (‘Hummingbird’), and (d) the ‘Washington’ (‘Eagle’) processor. For all four presented chips, whether LASIQ tuned or not, there are no apparent spatial correlations between nearby frequencies.

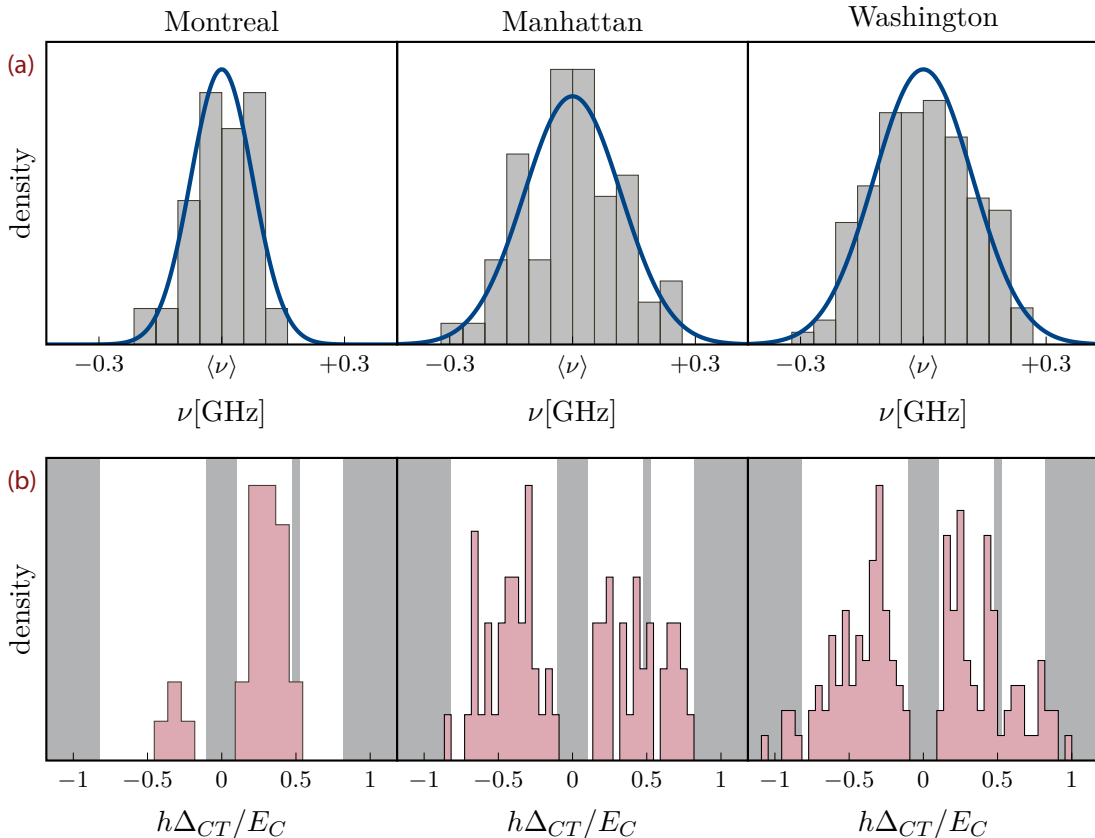


Figure A.2 – Frequency probabilities and distribution of NN frequency differences akin to Fig. 3.17 for the ‘Montreal’, ‘Manhattan’, and ‘Washington’ chip. Panel (a) shows that all distributions are consistent with a single Gaussian, even though the distributions of the NN frequency differences shown in (b) reveal clear LASIQ-induced anti-correlations between neighboring frequencies. This should be contrasted with Fig. 3.17(c), which shows that the frequency collisions occur much more frequently in untuned devices.

processors (the most recent ‘Osprey’ is yet to be available online). Fig. A.1 shows the processor layouts and the color-coded qubit frequencies. Panels (b), (c), and (d) illustrate the ‘Montreal’ (‘Falcon’), ‘Manhattan’ (‘Hummingbird’), and ‘Washington’ (‘Eagle’) chips. As expected, there is no regular frequency structure. For comparison, Fig. A.1(a) shows the untuned ‘Falcon’ processor discussed in Ref. [308], whose frequency distribution is qualitatively similar.

Fig. A.2 illustrates the distribution of the frequencies ν and the NN frequency differences $\nu_C - \nu_T$ for the three example processors, akin to Fig. 3.17 in Chapter 3. As shown in Fig. A.2(a), for all chips, we find our expectation of an approximately Gaussian distribution of the frequencies confirmed. At the same time, the distribution of the detunings between control and target qubits, visualized in Fig. A.2(b), reveals clear signs of the LASIQ procedure. The forbidden regions where NN frequency collisions occur are shaded in gray. These regions are (at least partially) successfully avoided.

Fig. A.3 further shows that not only is the form of the disorder similar for the currently available LASIQ tuned chips and the scheme-A ‘natural’ disorder but that the disorder strength is also comparable in both cases. Shown is the average Josephson energy $\langle E_J \rangle$ obtained for all chips from the publicly documented data¹ for ν and E_C [59] and the disorder strength, defined as

¹All calibration data was downloaded on 11/23/2021, except for the data for ‘Washington’ (12/15/2021), ‘Manhattan’ (11/16/2021), and ‘Dublin’ (11/08/2021).

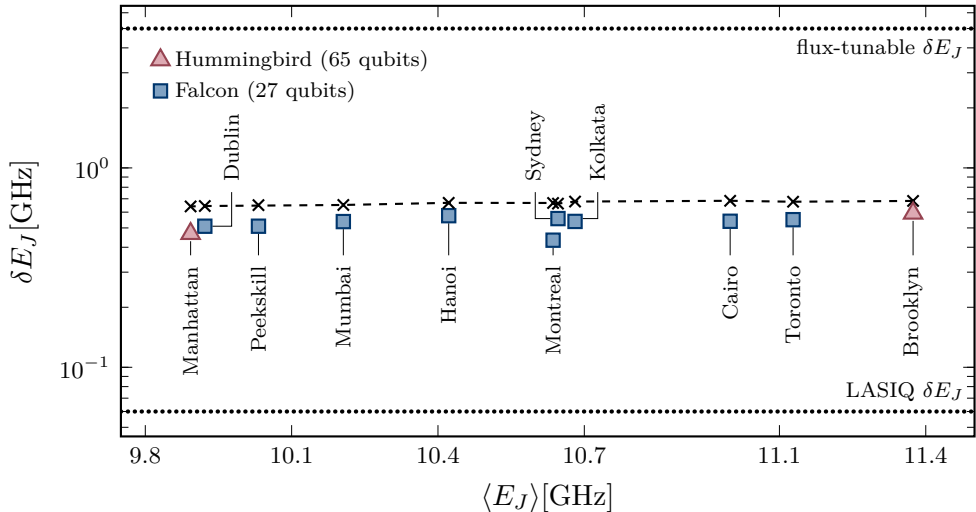


Figure A.3 – Experimental parameters of IBM cloud devices. Variance δE_J and mean value $\langle E_J \rangle$ of the Josephson energies for nine realizations of the 27-qubit ‘Falcon’ design and two realizations of the 65-qubit ‘Hummingbird’ design. The cross-shaped markers denote the scheme-A disorder calculated for each processor’s averaged value of E_J and E_C . In all chips, the Josephson energy spread is close to (although slightly smaller than) the definition of scheme-A disorder. For comparison, the dashed lines indicate the much higher variance used in flux-tunable architectures and the residual disorder after LASIQ tuning. The latter is understood as the LASIQ precision, i.e., the width of the hypothetical Gaussian obtained if LASIQ were used to align all frequencies.

the standard deviation of the normal distributions fitted to the E_J histograms with a maximum likelihood estimation. In our simulations, scheme-A disorder is defined as $\delta\nu = E_C/2$, which translates to $\delta E_J = \sqrt{E_C E_J / 8}$. To compare the disorder found in the IBM devices to the scheme-A definition, we can calculate the scheme-A disorder equivalent for each cloud processor by evaluating the expression for δE_J with the mean values for E_C and E_J that characterize each IBM chip. The result is shown as a dashed line with cross-shaped markers in Fig. A.3. The actual disorder is slightly smaller than the scheme-A estimate, but both are in reasonable proximity.

The essence is that our analysis in Chapter 4 with Gaussian scheme-A disorder applies to current IBM devices, including the recent Eagle generation, despite the LASIQ progress in fabrication precision. In configuration space, the controlled detuning of neighboring transmons translates to the detuning between a lattice point and *one* of its neighbors. Thus, in the high-coordination lattice, only a tiny fraction of the hopping processes becomes off-resonant such that the overall localization picture is expected to be affected at most slightly.

Appendix

Appendix for Chapter 4

B

This appendix supplements Chapter 4 with a more in-depth discussion of the technical details of the implementation (B.1–B.3) and with further results not included in the main body.

B.1 Truncation of the Hilbert space

This section builds on Sec. 4.3.2 and further comments on the several ways to truncate the Hilbert space, which is necessary to facilitate numerical diagonalization. Consider the basis formed by the states $|l_1 \dots l_L\rangle$, where $\{l_i\}$ is a set of local transmon excitation numbers. The first possibility is to restrict the Hilbert space of each transmon to the lowest k levels, i.e., $l_i < k$, yielding $\dim \mathcal{H} = k^L$. This approach suffers from several major drawbacks. For concreteness, let us assume that we are interested in the properties of typical computational states with five ‘1’s in an $L = 10$ chain. For an accurate description, all the energetically close states from the $N_{\text{ex}} = 5$ bundle should be considered. Following the above truncation scheme, one approximates each transmon by a six-level system (ground state and five excited states). The dimension of the truncated Hilbert space is $\dim \mathcal{H} = 6^{10}$, shifting the problem over the edge of what MBL studies with Krylov subspace methods usually encounter [351, 380]. At the same time, we expect states from the fifth excitation bundle or bundles in the vicinity to have the most significant impact. In our example, states up to $N_{\text{ex}} = 50$ are included in the Hamiltonian. In fact, the vast majority of states are energetically so far away from the target window that their impact is expected to be negligible. On the other hand, all bundles with $N_{\text{ex}} > 5$ are incomplete, e.g., states with the excitation structure $\{7\}, \{61\}$ are missing in the manifold with $N_{\text{ex}} = 7$. A priori, one cannot exclude that these states influence the target bundle with $N_{\text{ex}} = 5$.

The better alternative when constructing a set of basis vectors is to pick out those Fock states $|l_1 \dots l_L\rangle$ whose energies are close to a specified target energy for $T = 0$. Thus, if we want to study the energy range occupied by the states with $N_{\text{ex}} = 5$, one chooses an energy window around this bundle and constructs the Hamiltonian matrix restricted to states within that window. The remaining question to be answered is how large this range must be selected to obtain meaningful results. To exemplify the influence of the Hilbert space dimension on the levels of the interacting system, we consider Fig. B.1, where the spectrum of the $N_{\text{ex}} = 3$ bundle of a chain of length $L = 6$ are shown as a function of the coupling strength T . Shown in blue are the energies calculated by diagonalizing the Hamiltonian restricted to that bundle, i.e., a 56×56 matrix. For the spectrum in red, all states with $N_{\text{ex}} \leq 6$ are used to construct the Hamiltonian, increasing the Hilbert space dimension to $\dim \mathcal{H} = 924$. The difference in the energies is hardly noticeable on the scale set by the width of the bundle, see (a). Zooming in reveals that the major effect of the enlarged Hilbert space is that all levels are slightly pushed down. Most importantly, this shift is nearly identical for all states and does not lead to qualitatively different features. For example, one still observes the same avoided crossings.

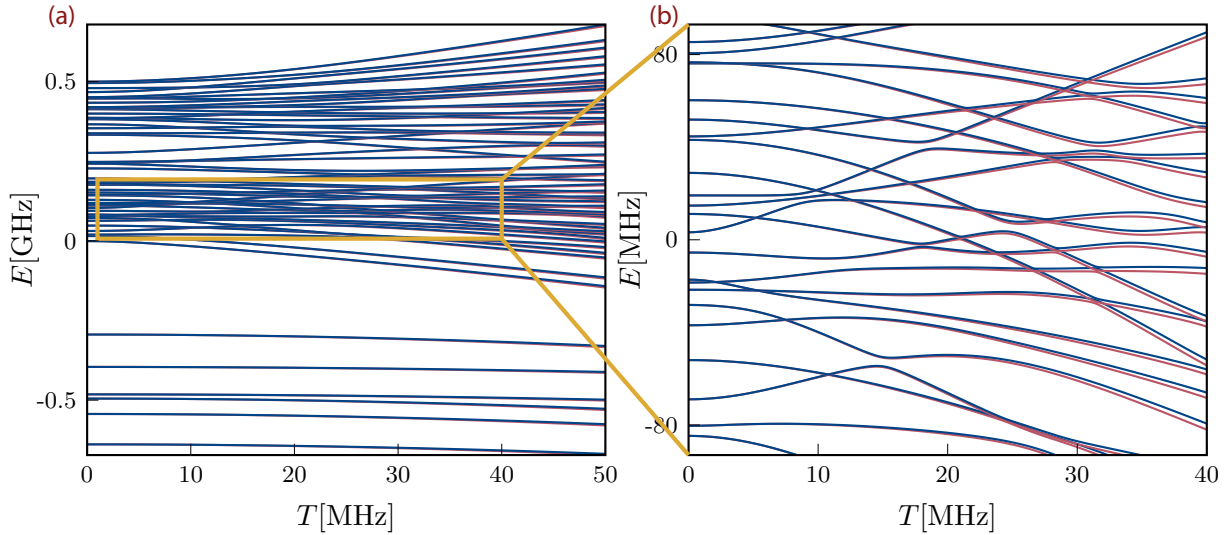


Figure B.1 – Influence of the Hilbert space dimension on the energy levels. (a) Shown are the 56 levels from the $N_{\text{ex}} = 3$ bundle for an $L = 6$ chain, calculated for a 56- (blue) and 924-dimensional (red) Hilbert space. As revealed in (b), the primary influence of the additional states is a slight shift downwards in energy for all levels, which does not influence the quantitative analysis of the chaotic traits of the bundle.

In particular, the effect of the inflated the Hilbert space on the default diagnostics, IPR and Kullback-Leibler divergence, is minuscule. This is illustrated for $L = 10$ and $N_{\text{ex}} = 5$ in Fig. B.2. The KL divergence, calculated with respect to the Poisson distribution, is independent of whether the underlying energies are obtained by diagonalization of a $2,002 \times 2,002$ matrix, i.e., a Hilbert space restricted to states of the specific $N_{\text{ex}} = 5$ excitation sector, as in (b), or whether these energies are just a small fraction of a much larger spectrum belonging to a Hilbert space whose basis includes states of different N_{ex} . Specifically, for (a), the Hamilton matrix has a dimension of around $25,000 \times 25,000$, i.e., the 25,000 Fock states lowest in energy were chosen as the basis. This includes states with occupation numbers up to $N_{\text{ex}} = 8$. For isolated points in the two-dimensional phase diagram and very few disorder realization, using the software library ARPACK [381], we convinced ourselves that further increasing the number of basis states up to around 150,000 does not alter the results for the KL divergence of the $N_{\text{ex}} = 5$ bundle. This guides us to conclude that restricting the Hilbert space to a sector of fixed N_{ex} yields reliable results for the respective energy window. Specifically for $L = 10$ and $N_{\text{ex}} = 5$, 2,002 basis states suffice for accurate results. In a way, this is not entirely surprising: A moderate disorder conserves the energetically separated manifolds of fixed N_{ex} for $T > 0$. In addition, the interaction does not couple multiplets to adjacent bundles $N_{\text{ex}} \pm k$ where k is odd. Our truncation scheme reflects some of the approximations behind the effective model (4.2), see the discussion in the next section.

In summary, these considerations show that a restriction of the Hilbert space to a fixed N_{ex} manifold whose dimension for arbitrary L and N_{ex} is given by Eq. (4.3) vastly reduces the computational effort compared to $\dim \mathcal{H} = (1 + N_{\text{ex}})^L$ for the naive truncation scheme while giving an accurate description of the system properties as long as the notion of an excitation bundle is well-defined.

For larger disorder, the concept of clearly resolved bundles of fixed N_{ex} is lost, and the above truncation scheme is not a priori justified. Therefore, we repeatedly conducted our analysis and

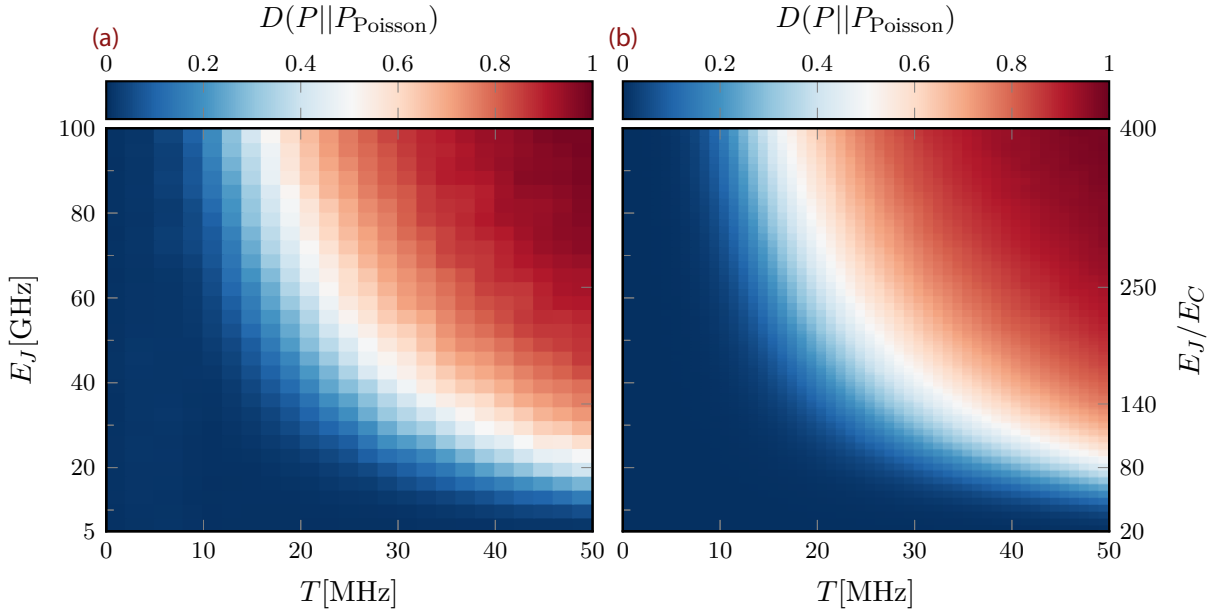


Figure B.2 – Influence of the Hilbert space dimension on the Kullback-Leibler divergence, calculated with respect to the Poisson distribution for the $N_{\text{ex}} = 5$ sector of a chain with $L = 10$. For (a), the Hilbert space includes approximately 25,000 basis states comprising contributions from the manifolds $N_{\text{ex}} = 0, \dots, 8$. For (b), the Hamiltonian is constructed within the sector of $N_{\text{ex}} = 5$ and $\dim \mathcal{H} = 2,002$. Apart from the coarser T - E_J grid in (a), the results are identical. Note that the data shown in (b) are not identical to Fig. 4.13. Here, δE_J is fixed to 625 MHz and does not scale as $\sqrt{E_J}$.

followed one of the following recipes for constructing the Hamiltonian and applying the diagnostic tools (described here for a ten-transmon chain):

- (i) The basis is constructed from the $T = 0$ product states, starting with the ground state and including all states up to an energy threshold. Choose the eigenstates $|i\rangle$ and energies E_i with $i = 1,002, \dots, 3,003$ to calculate the KL divergences and the IPR. These become the 2,002 states that span the $N_{\text{ex}} = 5$ sector for smaller disorders.
- (ii) Use the same basis and choose roughly 2,002 states centered around the mean energy of the $N_{\text{ex}} = 5$ basis states at $T = 0$ for applying the diagnostic tools.

In both cases, the selection of eigenstates for the diagnostics is dominated by—but does not consist exclusively of—states with $N_{\text{ex}} = 5$. States from higher and (fewer) states from lower bundles are also included.

- (iii) Restrict the Hamiltonian to the $N_{\text{ex}} = 5$ subspace, even if this neglects states from other bundles which are thoroughly intermingled with $N_{\text{ex}} = 5$ states.

All three approaches give nearly identical results in the T - E_J parameter regions under consideration. In particular, the Kullback-Leibler divergence does not change when switching between recipes (i) to (iii). It always indicates nearly perfect agreement with Poissonian level statistics. The IPR shows a minor tendency towards delocalization for (iii) compared to (i) and (ii). For example, the contour line where $\text{IPR}=1/2$ moves downwards to the left, barely recognizable in Fig. 4.15. Note that for the scheme-B disorder regime, the system is in the MBL phase for all T and E_J values under consideration. Thus, in the context of our analysis, it cannot be excluded that the approaches (i) to (iii) diverge when the system approaches the quantum chaotic region.

Table B.1 – Overview of coupling matrix elements contained in the full, truncated, and effective model.

The table lists all configuration states coupled to the state $|\psi\rangle = |0130\rangle$ in a chain geometry consisting of four transmons. The colored rows indicate couplings to states with the same N_{ex} as $|\psi\rangle$. Only the couplings highlighted in blue survive the RWA and enter the effective model. The coupling matrix elements in the last row are obtained for a single disorder realization with $E_J = 12.5$ GHz and $E_C = 250$ MHz.

l_1	l_2	l_3	l_4	ΔN_{ex}	$ \langle \psi \hat{H}_{\text{int}} l_1 l_2 l_3 l_4 \rangle / T$	l_1	l_2	l_3	l_4	ΔN_{ex}	$ \langle \psi \hat{H}_{\text{int}} l_1 l_2 l_3 l_4 \rangle / T$
0	1	3	0	0	—	0	2	0	0	-2	0.06
0	0	0	0	-4	0.04	0	2	2	0	0	2.57
0	0	2	0	-2	1.88	0	2	4	0	2	2.82
0	0	4	0	0	2.06	0	2	6	0	4	0.44
0	0	6	0	2	0.32	0	4	0	0	0	0.003
0	0	8	0	4	0.09	0	4	2	0	2	0.15
0	1	0	1	-2	0.04	0	4	4	0	4	0.17
0	1	0	3	0	0.002	0	6	0	0	2	0.0005
0	1	0	5	2	0.0001	0	6	2	0	4	0.02
0	1	0	7	4	0.00002	0	8	0	0	4	0.0001
0	1	2	1	0	1.89	1	0	3	0	0	1.17
0	1	2	3	2	0.07	1	2	3	0	2	1.6
0	1	2	5	4	0.006	1	4	3	0	4	0.1
0	1	4	1	2	2.07	3	0	3	0	2	0.04
0	1	4	3	4	0.08	3	2	3	0	4	0.06
0	1	6	1	4	0.32	5	0	3	0	4	0.004

B.1.1 Comparison of the full, the truncated, and the effective model

In this section, we extend the discussion from Sec. 4.3.1 and examine the difference in the effective model (4.2) and the full model (4.1) for different truncation schemes in more detail¹, explicitly considering one ‘row’ of the Hamiltonian matrix.

Concretely, we consider the configuration state $|\psi\rangle = |0130\rangle$ of an $L = 4$ transmon chain, and investigate to which states it is coupled through the capacitive coupling $T(\hat{n}_1\hat{n}_2 + \hat{n}_2\hat{n}_3 + \hat{n}_3\hat{n}_4)$. We restrict the discussion to states that obey $N_{\text{ex}} \leq 8$. The result is summarized in Table B.1. $|\psi\rangle$ is marked in red. In total, there is a nonzero interaction matrix element between $|\psi\rangle$ and 31 other states, specified by the local occupation numbers $|l_1 l_2 l_3 l_4\rangle$ that are provided in columns 1–4. The fifth column shows the difference in the total excitation number N_{ex} between the respective states and $|\psi\rangle$. The approximate absolute value of the coupling matrix element is given in the last column. Among the 31 states, only six, color-coded by the blue and yellow background, have the same total excitation number. When the Hilbert space is restricted to contain only states with the same N_{ex} as $|\psi\rangle$, these are the states that enter the construction of the Hamiltonian. There is a further difference between the states highlighted in blue and yellow. The matrix elements for the latter ones are orders of magnitude smaller because they contain the small off-diagonal charge operator contributions $\langle 0|\hat{n}|3\rangle$ and $\langle 1|\hat{n}|4\rangle$. The matrix elements for these processes are small and not included in the effective model (4.2) that couples $|\psi\rangle$ only

¹We are focusing solely on the difference in the interacting part of the Hamiltonian. Note, however, that this is not the only difference between the two models, as we take, for example, the cosine nonlinearity fully into account.

to the four states highlighted in blue (in Bose-Hubbard parlance, these are hopping processes where the three bosons inserted at site 3 simultaneously change their position to site 2 or 4). Numerically, we do not incorporate the hierarchy in the coupling entries: the only approximation is the truncation. We consider all states from the same bundle and, depending on the chosen energy window around the target energy, more states, starting with those where $\Delta N_{\text{ex}} = \pm 2$. The last column accurately reflects the properties of the charge operator discussed in Sec. 4.3. Matrix elements are large if all involved off-diagonal entries of the charge operator $\langle k|\hat{n}|k+m\rangle$ have $|m|=1$ and decrease if $|m|$ increases. Furthermore, the off-diagonals of \hat{n} increase as k increases (asymptotically as $\sqrt{k+1}$), reproducing the hierarchy within the blue rows. Finally, there is no coupling between bundles differing by an odd number of excitations (all entries in column 4 are even).

Summarizing the information contained in Table B.1, the truncated model neglects couplings between highly detuned states that can be both strongly (e.g., row 3, where two excitations on neighboring transmon sites are added), or—the majority—weakly coupled. The effective model further discards the coupling to states that are close in energy but only weakly coupled (yellow rows).

B.2 Details on the implementation

In this section, we substantiate the aspects of the implementation that were mentioned in the context of the Hilbert space truncation and the discussion in Sec. 3.2.4 with more technical details.

B.2.1 The single transmon Hamiltonian in the charge basis

For numerical diagonalization, the Hamiltonian of a single transmon is most conveniently formulated in the basis of the eigenstates of the charge operator \hat{n} . As discussed in Sec. 3.2.4, the Hilbert space spanned by the eigenvectors $|m\rangle$ must be truncated at some largest $|m|=m_{\max}$. The restricted charge operator in its eigenbasis can then be written as a diagonal matrix with entries ranging from $-m_{\max}$ to m_{\max} . The $\cos\phi$ contribution is tridiagonal as discussed in Eq. (3.43). The matrix representation H_T of the transmon Hamiltonian in Eq. (3.9) in the charge eigenbasis takes the form

$$H_T = 4E_C \begin{pmatrix} (-m_{\max})^2 & 0 & \dots & \dots & 0 \\ 0 & (-m_{\max} + 1)^2 & \ddots & & \vdots \\ \vdots & \ddots & \ddots & \ddots & \vdots \\ \vdots & & \ddots & (m_{\max} - 1)^2 & 0 \\ 0 & \dots & \dots & 0 & m_{\max}^2 \end{pmatrix} - \frac{E_J}{2} \begin{pmatrix} 0 & 1 & 0 & \dots & 0 \\ 1 & \ddots & \ddots & \ddots & \vdots \\ 0 & \ddots & \ddots & \ddots & 0 \\ \vdots & \ddots & \ddots & \ddots & 1 \\ 0 & \dots & 0 & 1 & 0 \end{pmatrix}. \quad (\text{B.1})$$

Eq. (B.1) is the starting point used to calculate all single transmon properties, like the energies or the off-diagonal entries of the charge operator, $\langle i|\hat{n}|j\rangle$, between the energy eigenstates $|i\rangle$ and

$|j\rangle$. In all calculations, m_{\max} is fixed to 50, which ensures that all eigenvalues and eigenvectors of interest are obtained with standard double machine precision, see Fig. 3.9.

B.2.2 Matrix representation of the interacting Hamiltonian

Conceptually the matrix implementation consists of two distinct steps: First, collect all basis vectors that should be included in the calculation. For example, the list of basis vectors may incorporate all Fock states with a fixed total excitation number N_{ex} , as is often the case in our simulations. Alternatively, one can define a target energy and an energy window and select all $T = 0$ eigenstates whose energies lie within this window to construct the Hamiltonian. When the first step is completed, calculate the matrix elements between all basis vectors. The noninteracting part of the Hamiltonian is trivially diagonal in the chosen basis, and each entry is a specific sum of single transmon energies. For example, the basis vector $|102\rangle$ of an array consisting of three transmons is associated with the diagonal entry

$$\langle 102 | \hat{H} | 102 \rangle = E_{1,1} + E_{2,0} + E_{3,2}, \quad (\text{B.2})$$

where $E_{i,\alpha}$ corresponds to the level α of transmon i .

The capacitive coupling determines the off-diagonal entries of the Hamiltonian matrix. Their explicit form is provided in Eq. (4.4).

B.2.3 Verifying the implementation

There are several options to check that the implementation of the Hamiltonian was carried out flawlessly. Most importantly, one can compare the spectra of the Hamilton or the matrices themselves, calculated using independent implementations in the various possible bases.

Comparison with φ basis. Although not very convenient for larger systems or to perform disorder averages, the entries of the Hamilton matrix can be calculated using the φ representation of the transmon eigenstates. For example, the matrix entry of $\hat{n}_1 \hat{n}_2$ between the two distinct states $|ijkl\rangle$ and $|i'j'k'l'\rangle$ of an $L = 4$ transmon chain reads

$$\begin{aligned} \langle i j k l | \hat{n}_1 \hat{n}_2 | i' j' k' l' \rangle &= \int_{-\pi}^{\pi} d\varphi_1 \cdots \int_{-\pi}^{\pi} d\varphi_4 \psi_i^*(\varphi_1) \dots \psi_l^*(\varphi_4) \left[i \frac{\partial}{\partial \varphi_1} i \frac{\partial}{\partial \varphi_2} \right] \psi_{i'}(\varphi_1) \dots \psi_{l'}(\varphi_4) \\ &= M_1^{ii'} M_2^{jj'} \delta_{kk'} \delta_{ll'}, \end{aligned} \quad (\text{B.3})$$

where $M_\alpha^{ii'}$ —the off-diagonal element of \hat{n} in the φ representation—was defined as

$$M_\alpha^{ii'} = i \int_{-\pi}^{\pi} d\varphi_\alpha \psi_i^*(\varphi_\alpha) \frac{\partial}{\partial \varphi_\alpha} \psi_{i'}(\varphi_\alpha). \quad (\text{B.4})$$

Here, $\psi_i(\varphi)$ is the eigenfunction of the Hamiltonian \hat{H}_T in the φ representation as provided in Eq. (3.42). The implementation of the Mathieu functions in the software library Mathematica [263] and Eqs. (B.3) and (B.4) were exploited as an alternative and independent way to calculate the Hamiltonian for small system sizes.

Comparison with charge basis. Implementing the interacting Hamiltonian in the charge basis is straightforward. For an example system consisting of three coupled transmons, the matrix is given by

$$H = H_{T,1} \otimes \mathbb{1} \otimes \mathbb{1} + \mathbb{1} \otimes H_{T,2} \otimes \mathbb{1} + \mathbb{1} \otimes \mathbb{1} \otimes H_{T,3} + T(n_1 \otimes n_2 \otimes \mathbb{1} + \mathbb{1} \otimes n_2 \otimes n_3), \quad (\text{B.5})$$

where $\mathbb{1}$ is the $2m_{\max} + 1$ -dimensional identity matrix, $H_{T,i}$ is given by Eq. (B.1) (the additional index i accounts for the site dependence of the Josephson energy), and n_i is diagonal with entries ranging from $-m_{\max}$ to m_{\max} . As an additional reassurance that the actual implementation is error-free, the Hamiltonian is constructed in the charge representation for a small L and a moderate m_{\max} . This reduces each transmon to a $(2m_{\max} + 1)$ -level system (but one should keep in mind that only the lowest eigenvalues accurately describe true transmon eigenenergies due to the truncation of the Hilbert space). The eigenvalues are then compared to those from the actual implementation of the Hamiltonian, where the list of basis vectors is obtained by truncating the local Hilbert space of each transmon to the lowest $(2m_{\max} + 1)$ levels and forming all $(2m_{\max} + 1)^L$ possible product states. The two variants are identical up to a unitary transformation if the same m_{\max} is used to obtain the single transmon energies and the off-diagonal elements of \hat{n} .

Alternatively, one can consider different matrix dimensions in the two representations. As an example, take the charge representation of the matrix describing the $L = 4$ transmon chain with $m_{\max} = 8$. The dimension of the Hilbert space truncated in this way is $\dim \mathcal{H} = (2 \cdot 8 + 1)^4 = 83,521$. The lowest eigenvalues are efficiently calculated using Krylov subspace methods. They can be compared to the eigenvalues of a much smaller, say $\approx 1,500 \times 1,500$ -dimensional Hamiltonian constructed with the 1,500 product states that are lowest in energy but where the single transmon properties are calculated with a higher m_{\max} . One can confirm that the lowest eigenenergies are indeed identical. Higher states agree up to an order of magnitude that is set by the choice of m_{\max} in the charge representation.

The facilities for comparison described here have been exploited for small systems, both chain and two-dimensional geometries, to convince ourselves of the correctness of the implementation.

Comparison with Bose-Hubbard model. Finally, an additional possibility to verify the flawlessness of the implementation is the comparison of the matrix elements describing the full model in Eq. (4.1) to the asymptotic expressions in the effective model (4.2). There are three cases to distinguish here: the ‘on-site’ energies (in configuration space), the off-diagonals contained in Eq. (4.2), and the additional coupling terms that arise in the full model but are neglected in the rotating-wave approximation. For large E_J/E_C , one finds the correct asymptotic behavior, with the difference in the on-site energies vanishing fastest.

B.2.4 Calculation of the reduced density matrix

The wave function metrics in Fig. 4.10 are straightforward to calculate because they directly process the coefficients c_i of the eigenstates in the product basis as obtained in the diagonalization. The entanglement entropy S_{EE} is an exception. It requires the calculation of the reduced density matrix in the first step. A minor subtlety is that the Hamiltonian is generally restricted to the subspace of a fixed N_{ex} , but the basis of the subsystem contains all states with excitations from 0 to N_{ex} . For concreteness, we consider $L = 10$ and $N_{\text{ex}} = 5$ and divide the ten-transmon chain into two subsystems, A and B , comprising the first (sites 1–5) and second (sites 6–10) half of the chain. We are interested in the reduced density matrix $\hat{\rho}_A$ of subsystem A if the entire

system is in one of its eigenstates $|i\rangle$. We write $|i\rangle$ in the form $\hat{\rho} = |i\rangle\langle i| = \sum_{m,n} \rho_{m,n}|m\rangle\langle n|$, where $|m\rangle$ and $|n\rangle$ are the Fock states characterized by ten (L) excitation numbers. To proceed, we introduce the notation $|m\rangle = |a, \alpha\rangle$, where a and α are the five ($L/2$) quantum numbers referring to the transmons in subsystem A (Arabic letters) and B (Greek letters), respectively. The total excitation number in A ranges from 0 to 5, such that there are 252 different states $|a\rangle$, and similar for $|b\rangle$. For the density matrix, we obtain

$$\hat{\rho} = \sum_{\substack{a,b,\alpha,\beta \\ a+\alpha=5 \\ b+\beta=5}} \rho_{a\alpha,b\beta} |a, \alpha\rangle\langle b, \beta|. \quad (\text{B.6})$$

The restriction, symbolically written as $a + \alpha = 5$, ensures that for $|a\rangle$ fixed, the sum contains only those degrees of freedoms $|\alpha\rangle$ of B such that $|a, \alpha\rangle$ has the correct $N_{\text{ex}} = 5$, and similar for b and β . From the 252^2 possibilities $|a, \alpha\rangle$, this picks out the 2,002 correct combinations. With $\hat{\rho}$ written in the form (B.6), it is straightforward to trace out the degrees of freedom of B (we suppress the restriction, but it still holds):

$$\hat{\rho}_A = \sum_{\gamma} \langle \gamma | \left(\sum_{a,b,\alpha,\beta} \rho_{a\alpha,b\beta} |a\rangle |\alpha\rangle\langle b|\langle \beta| \right) | \gamma \rangle = \sum_{a,b} \rho_{a,b}^A |a\rangle\langle b|, \quad (\text{B.7})$$

where the matrix elements of the reduced density matrix are given by

$$\rho_{a,b}^A = \sum_{\alpha,\beta,\gamma} \rho_{a\alpha,b\beta} \langle \gamma | \alpha \rangle \langle \beta | \gamma \rangle = \sum_{\alpha} \rho_{a\alpha,b\alpha}. \quad (\text{B.8})$$

In summary, when numerically calculating $\hat{\rho}_A$, one has to take the restriction for the degrees of freedom α of B in the sum in Eq. (B.8) into account.

B.3 Influence of the disorder distribution

For the analysis presented in Chapter 4, we assumed Gaussian disorder for the distribution of the Josephson energies $E_{J,i}$, in accordance with the disorder found in recent transmon chips. MBL studies commonly assume a box disorder distribution that is uniform in the restricted interval $[-h, h]$, where h denotes the disorder strength. Here, we show that switching the specific disorder manifestation does not lead to a qualitative change in the results, provided that one carefully translates between the definitions of disorder for the respective distributions. The subtlety is that for a Gaussian distribution, the disorder is interpreted in a standard deviation sense, i.e., $\delta E_J \equiv \sigma_{\text{Gauss}}$. Results for a specific Gaussian disorder δE_J can be compared to the box distribution of equal standard deviation, that is $[-\sqrt{3}\delta E_J, \sqrt{3}\delta E_J]$. In other words, for comparison with Gaussian disorder, one should interpret $h/\sqrt{3}$ as the disorder strength associated with the box distribution $[-h, h]$.² This is illustrated in Fig. B.3. The results for the Kullback-Leibler divergences as a function of T line up almost perfectly. For reference, results

²Requiring the standard deviations to be equal is not the unique way to construct the box distribution equivalent to a Gaussian with a given σ . One can also adjust the width of the box distribution such that the expected distance between two independent draws from the two distributions is identical. For a Gaussian with σ , this is $\frac{2\sigma}{\sqrt{\pi}}$, and for the box distribution $\frac{x}{3}$, where x is the box length. Hence, an alternative definition of the box disorder is $\frac{\sqrt{\pi}}{3}h$. Ultimately, the two definitions are nearly identical ($\frac{\sqrt{\pi}}{3} \approx \frac{1}{\sqrt{3}}$), such that—based on the numerical results—one cannot judge whether one of them is more appropriate.

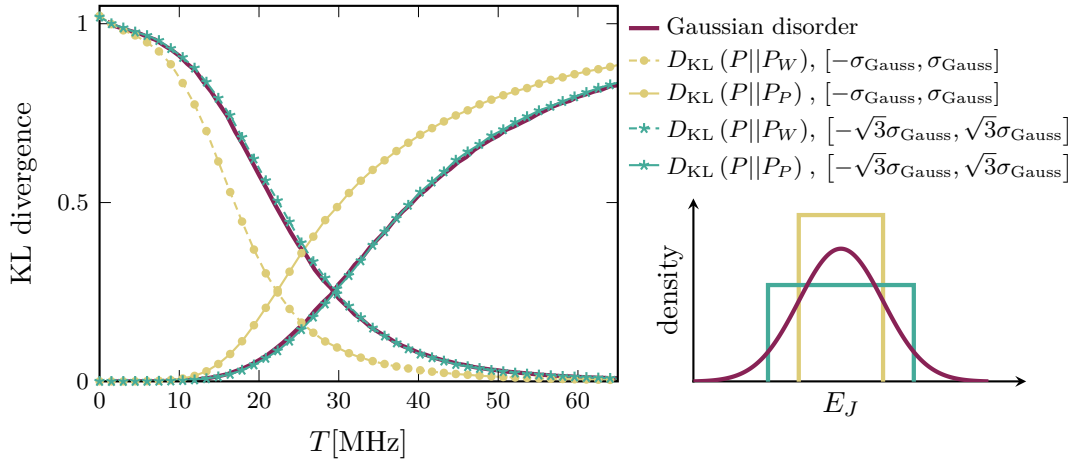


Figure B.3 – Kullback-Leibler divergences for uniform and Gaussian disorder for the ‘standard parameters’ from Sec. 4.4, i.e., $E_C = 250$ MHz, $E_J = 44$ GHz. The blue lines show results for Gaussian disorder with $\delta E_J \equiv \sigma_{Gauss} \approx 1.17$ GHz. The red line/star markers show results for the box distribution $[-\sqrt{3}\sigma_{Gauss}, \sqrt{3}\sigma_{Gauss}]$. The green line/point markers show results for the box distribution $[-\sigma_{Gauss}, \sigma_{Gauss}]$. The colored distributions in the lower right corner visualize the disorder choices underlying the equally colored lines.

for the box distribution $[-\sigma_{Gauss}, \sigma_{Gauss}]$ are also displayed. As expected, the system is more prone to chaos because the box distribution is narrower and describes a less disordered system. Given these findings, we expect no qualitative and only small quantitative changes for different forms of reasonable disorder distributions for the results discussed in Chapter 4.

B.4 Quantifying chaos near the maximal density of states

In this section, we revisit in more detail the changes in the quantitative measures of chaos when the underlying wave functions and levels are restricted to the small energy interval near the maximal density of states, as described in Sec. 4.6.1. To start, Fig. B.4(a) shows the individual traces underlying the two-dimensional representation of the KL divergence with respect to the Poisson distribution shown in Fig. 4.18, supplemented by the corresponding data for $D(P||P_{\text{Wigner}})$. The data collapse shown in Fig. B.4(b) is obtained by rescaling the T axis as $T \rightarrow TE_J^\mu$ with the same exponent μ found for the complete $N_{\text{ex}} = 5$ excitation bundle in Sec. 4.5.3. For comparison, the dotted line shows the trace of the collapsed data obtained for the full bundle. As discussed, the transition from MBL to chaos is much clearer, and $D(P||P_{\text{Wigner}})$ gets closer to zero (which is easier to see in $D(P||P_{\text{Poisson}})$ approaching 1) when neglecting the integrable edges of the spectrum. This also affects the wave function metrics discussed in Fig. 4.10, three of which are shown in Fig. B.5, now only for states from the vicinity of the maximal density of states. Specifically, we show (a) the participation entropy S_P , (b) the IPR, and (c) the eigenvector similarity (EVS) for $E_J = 12.5$ GHz and $E_J = 100$ GHz. The gray lines show the respective results for the full bundle. All quantities exhibit a sharper transition to the chaotic regime. Additionally, except for the IPR for $E_J = 12.5$ GHz, the metrics now tend to converge towards the values expected in the ergodic phase.

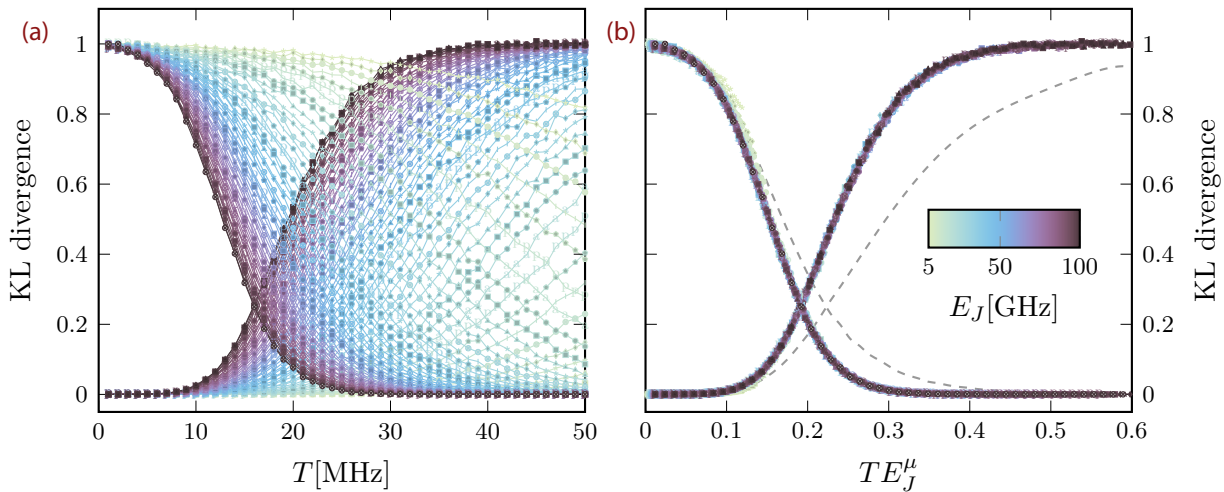


Figure B.4 – Data collapse for the KL divergences, calculated with level ratios taken from a small ϵ interval ($\Delta\epsilon = 0.05$) around the maximum DOS for scheme-A disorder. Panel (a) shows the original data and (b) the almost perfect collapse obtained by rescaling T as $T \rightarrow TE_J^{0.54}$.

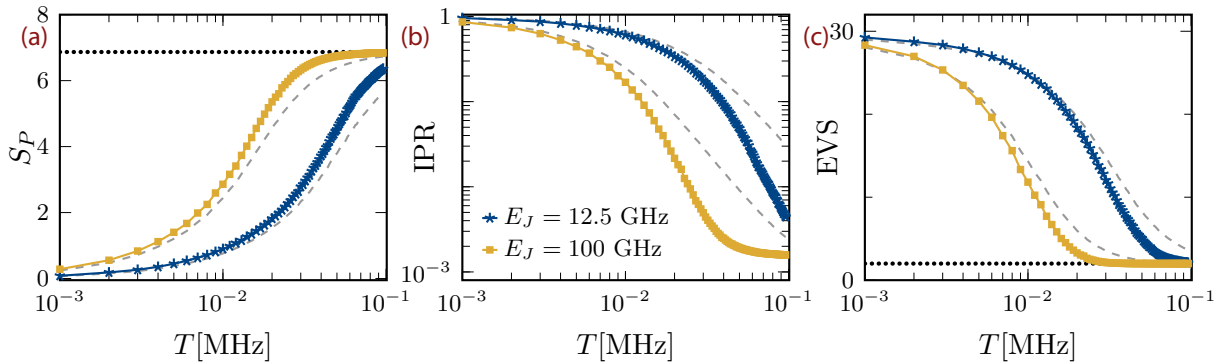


Figure B.5 – Delocalizing of wave functions near the maximal DOS. (a) Participation entropy S_P , (b) IPR, and (c) EVS for states taken from an interval around the maximal DOS for two values of E_J . The dashed (solid) gray lines show the results for the entire bundle for $E_J = 100$ GHz (12.5 GHz). All results are averaged over at least 1,800 disorder realizations.

B.5 Results for scheme-B parameters and two-dimensional geometries

Fig. B.6 shows the results for the level and wave function statistics for the two-dimensional 3×3 geometry subject to scheme-B disorder. Despite the higher connectivity, we observe no deviations from Poisson statistics in the parameter region under investigation. The dressing effect, mirrored in the decreasing IPR, is much weaker than for scheme-A processors, compare Fig. 4.23. The dressing is significant outside the experimental core region, as for the $L = 10$ chain geometry in Fig. 4.15, but now the IPR drops to values of approximately 0.7 for $E_J/E_C = 50$ and $T \approx 30$ MHz, a rather large coupling that is, however, feasible with tunable architectures. The curves shown in Fig. B.6(b) are the contour lines where the IPR is 0.5 for the 3×3 geometry (solid) and the surface-7 layout with scheme-B disorder (dash-dotted). For comparison, the contour lines for the one-dimensional arrangements consisting of the same number of transmons are also shown ($L = 7$

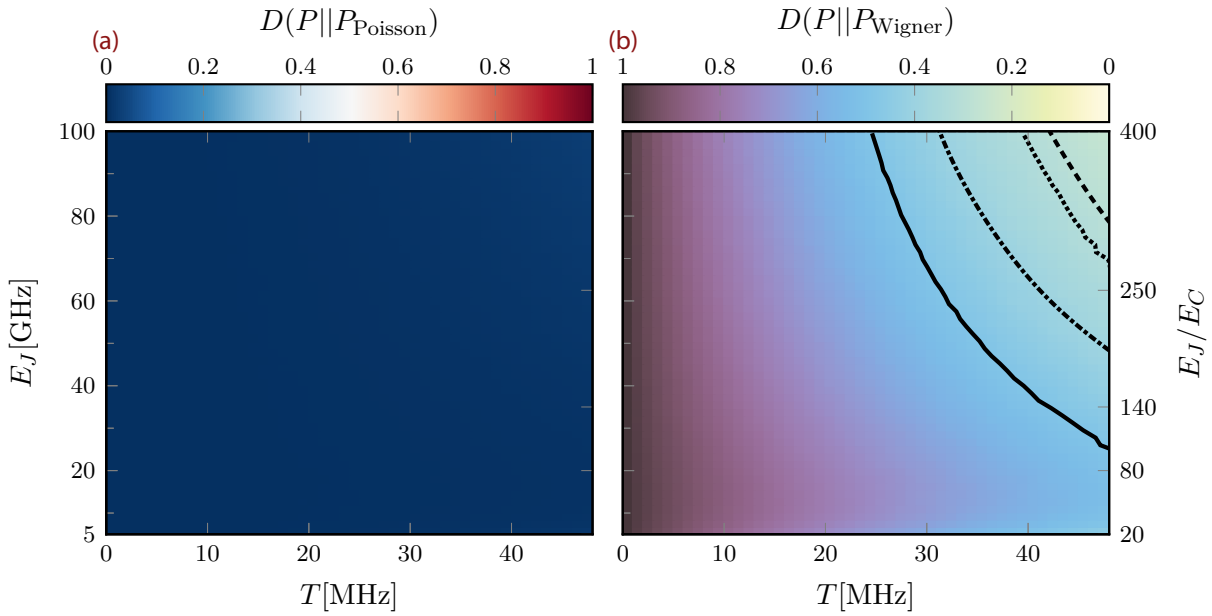


Figure B.6 – Level and wave function statistics for scheme-B parameters and two-dimensional transmon geometries. (a) KL divergence with respect to the Poisson distribution. (b) IPR. The black lines are the contour lines where IPR = 1/2 for the 3×3 array (solid), the surface-7 chip (dash-dotted), and the $L = 9$ (dotted) and $L = 7$ chains (dashed). All results are averaged over at least 2,400 disorder realizations and all states of the $N_{\text{ex}} = 5$ manifold.

dashed, $L = 9$ dotted). The succession of the four lines emphasizes our previous observation that the transition to higher dimensions increases the proneness to chaos and delocalization. The decrease of the IPR appearing for $E_J \approx 5$ GHz is again the effect of an artificial narrowing of the disorder distribution that arises when fixing $E_J = 5$ GHz as the smallest allowed Josephson energy. The results shown are obtained for the $N_{\text{ex}} = 5$ excitation bundles. The calculations were repeated for the $N_{\text{ex}} = 4$ manifold. The results show no qualitative and a minor quantitative change, with a tendency towards a smaller dressing effect.

Appendix for Chapter 5

C

This appendix enriches the discussion in Chapter 5 with further details. The first section provides additional information on the IPR results for the five-transmon chain, including a separate analysis of all permutation multiplets of the $N_{\text{ex}} = 3$ bundle. Thereafter, we discuss the two-dimensional representation of the IPR in the T - δE_J plane for larger geometries. The last two sections are rather technical: They start with a detailed discussion on the pitfalls lurking in applying level statistics to quantify quantum chaos when the Hilbert space under consideration splinters into sectors that all deserve a separate analysis. Finally, we close this appendix with an overview of the entire multiplet structure of the $N_{\text{ex}} = 5$ bundle of the 3×3 geometry.

C.1 Additional details on the $L=5$ chain

C.1.1 Data collapse for the T - δE_J phase diagrams

In this section, we further substantiate our findings of Sec. 5.3.1, where the quantities $T^2/\delta E_J$ and $T^4/\delta E_J$ were identified as the driving force controlling the delocalization of the wave functions over second- and forth-nearest neighbors in configuration space. The horizontal lines underlying the T - E_J IPR diagram shown in Fig. 5.4 are shown in Fig. C.1(a). Panels (b) and (c) show

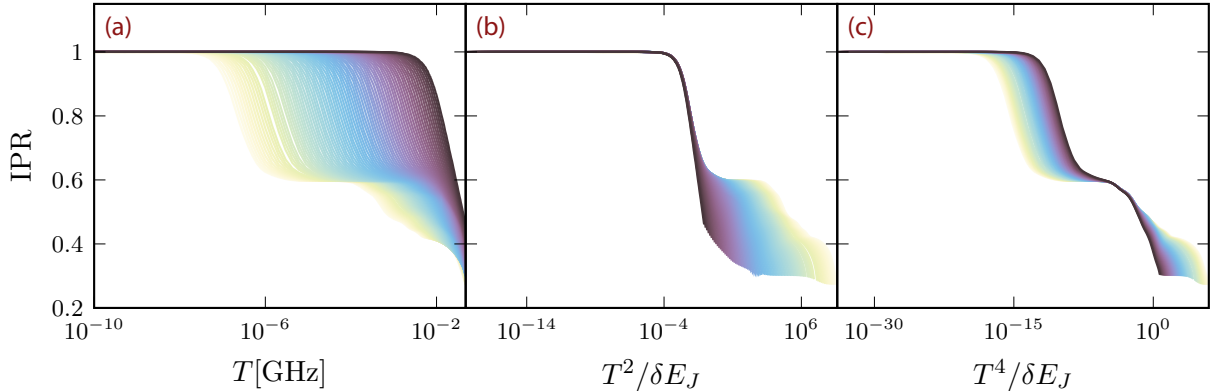


Figure C.1 – Data collapse in the T - δE_J phase diagram for the IPR calculated for all multiplets of the $N_{\text{ex}} = 3$ manifold of a five-transmon chain. Panel (a) shows the same data as in Fig. 5.4, with each curve corresponding to one of the horizontal lines of fixed disorder. Panels (b) and (c) show the same data with a rescaled T axis, such that the parameter ranges where the IPR decreases are collapsed onto each other, validating that the quantities $T^2/\delta E_J$ and $T^4/\delta E_J$ play a decisive role in controlling the inset of delocalization. The data in (c) are restricted to a disorder range $\delta E_J < 10^{-6}$ GHz.

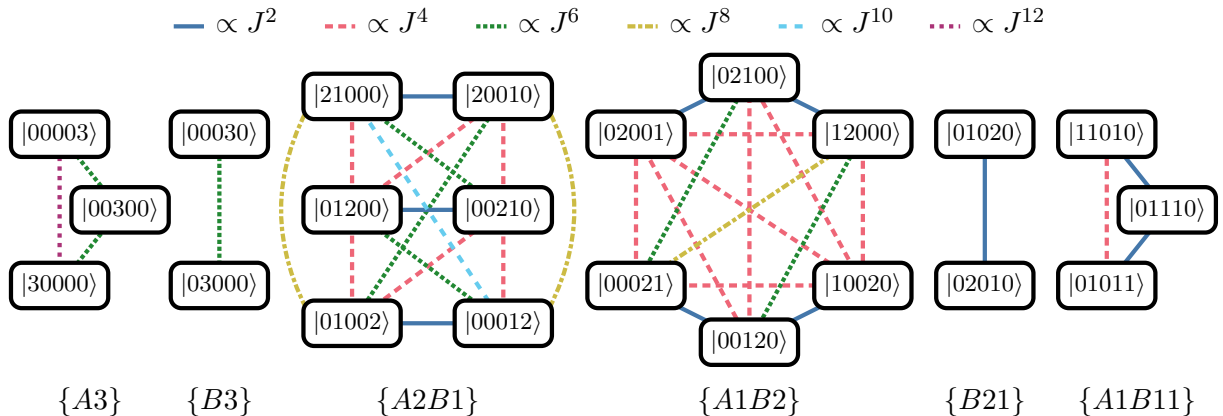


Figure C.2 – Connectivity graphs for the permutation multiplets of a five-transmon chain with AB frequency pattern. The color coding and line style of the links show to which order in J the states couple in Eq. (4.2). Three qualitatively different behaviors are distinguished, depending on how many of the states of each multiplet are connected via second-order hopping processes, see the main text for details.

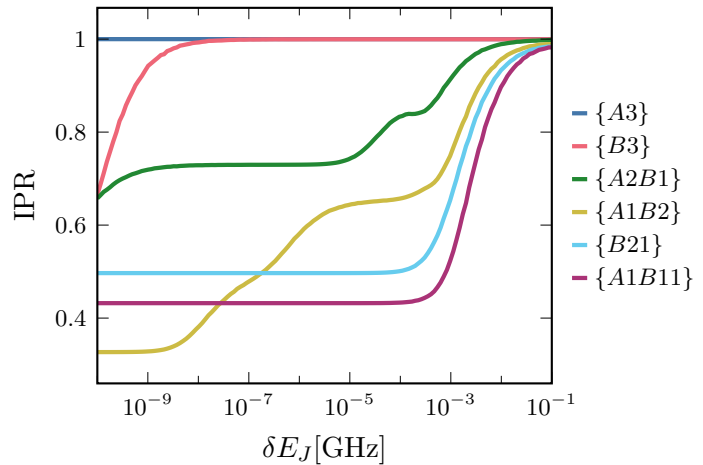
the same data, but with the T axis rescaled as $T \rightarrow T^2/\delta E_J$ and $T \rightarrow T^4/\delta E_J$. The individual traces, each belonging to a different, fixed δE_J value, collapse almost perfectly onto each other in (b) the region of the first decrease in the IPR and (c) the range where the second drop occurs. Panel (b) contains all data belonging to δE_J values between $5.5 \cdot 10^{-12}$ GHz (bright yellow) and 0.03 GHz (dark purple). In (c), we set an upper disorder threshold of $\delta E_J = 10^{-6}$ GHz. Only the data with a smaller disorder are included, the reason being that otherwise, the coupling T reaches a magnitude where other effects, e.g., inter-multiplet hybridization, darken the clean scaling behavior.

C.1.2 Detailed analysis of all multiplets of the $N_{\text{ex}} = 3$ bundle

The 35 states of the $N_{\text{ex}} = 3$ bundle separate into nine permutation multiplets. Sorted energetically from bottom to top, these are $\{A3\}$, $\{A21\}$, $\{B3\}$, $\{A2B1\}$, $\{A111\}$, $\{A1B2\}$, $\{A11B1\}$, $\{B21\}$ and $\{A1B11\}$. Here, we complement the analysis of the three multiplets $\{A11B1\}$, $\{A21\}$ and $\{A111\}$ presented in the main text. The different manifolds show a very multifaceted behavior, which can be deduced from the connectivity graphs in Fig. C.2. As before, this figure visualizes the effective model in Eq. (4.2). The six remaining multiplets belong to three different categories: For $\{B21\}$ and $\{A1B11\}$, all states are connected via two hopping processes, i.e., to second order in J , akin to the excitation structure $\{A11B1\}$. $\{A2B1\}$ and $\{A1B2\}$ behave similarly to $\{A21\}$ and further split into subsets of states that are mutually coupled to second order, but where the cross-connection involves more hopping processes. Finally, connecting states from $\{A3\}$ or $\{B3\}$ involves at least six single excitation hops. The behavior of the IPR accurately reflects these qualitative differences, as is shown in Fig. C.3. For $\{A1B11\}$ and $\{B21\}$, the IPR drops for $\delta E_J \approx 10^{-3}$ GHz and then remains constant over the entire low-disorder range. Inspection of the eigenfunctions shows that they possess the expected symmetry properties for $\delta E_J \lesssim 10^{-3}$ GHz. The excitation structures $\{A3\}$ and $\{B3\}$ are immune to delocalization over almost the entire surveyed disorder range. The hybridization between $|03000\rangle$ and $|00030\rangle$ occurs due to the second-order hopping process, where all three excitations move simultaneously. This process is neglected in the effective model but included in the simulations. Finally, $\{A2B1\}$ and $\{A1B2\}$ show a more feature-rich behavior with several parameter ranges where the IPR drops, interpen-

Figure C.3 –

Multiplet-resolved IPR for the $L=5$ chain. As expected from the findings in Fig. C.2, three different behaviors can be distinguished: a single drop in the IPR for $\{A1B11\}$ and $\{B21\}$, no hybridization (or only at very low disorder) for $\{A3\}$ and $\{B3\}$, and a more complicated trajectory involving several plateaus of constant and regions of decreasing IPR for $\{A2B1\}$ and $\{A1B2\}$, see the main text for details. All results are averaged over at least 10,000 disorder realizations.



etrated by plateaus of constant IPR, being evidence of the further substructures emerging in the corresponding connectivity graphs.

C.2 Two-dimensional representation of the IPR

Fig. C.4 shows the inverse participation ratios as a function of the residual disorder δE_J and the coupling T for (a) the $L = 10$ transmon chain and (b) the 3×3 geometry. The IPR is averaged over all states from the $N_{\text{ex}} = 5$ excitation bundle in both cases. The inset of delocalization is driven by the parameter $T^2/\delta E_J$, as indicated by the $\text{IPR} = 1/2$ contour lines. These are shown for the 3×3 geometry (dashed), the $L = 10$ chain (dotted), and the $L = 9$ chain (solid). In accordance with the findings for the simpler Gaussian disorder discussed in Chapter 4, the two-dimensional geometry is found to be more prone to the inset of chaos than the chains: for a fixed coupling T , the IPR declines below 1/2 for larger disorder. For δE_J between 100 MHz and 1 GHz, hybridization between different multiplets causes a minor drop in the IPR shortly before the global MBL phase is reached upon further increasing the disorder. A second decrease in the IPR that scales as $T^4/\delta E_J$ is not discernible because the disorder range does not extend to sufficiently small values.

C.3 Quantifying chaos with level statistics in a restructuring Hilbert space

As mentioned in Chapter 5 and detailed below, the level ratio analysis is particularly prone to mislead one to conclusions about the degree of chaos prevailing in a system. There are three spots where caution is advised.

First, when calculating $r_i = (E_{i+1} - E_i)/(E_i - E_{i-1})$, the level ratio will either be very large or very small when the involved energies belong to two different multiplets because the intermultiplet spacing is, in general, much larger than the spacing within multiplets, see Fig. 5.2. In consequence, the specific r_i value contributes to the lowest R_n bin, whose weight is, therefore, artificially increased. This effect is significant because the number of multiplets—determining how often ratios with one huge spacing occur—is not negligibly small compared to the total number of level ratios entering the histograms. For the example of $L = 6$ and $N_{\text{ex}} = 3$, 56 energies and thus 54 r_n values per disorder realization enter the histograms, 20 of which contain energies from different multiplets and thus contribute to the lowest bin. For illustration, consider

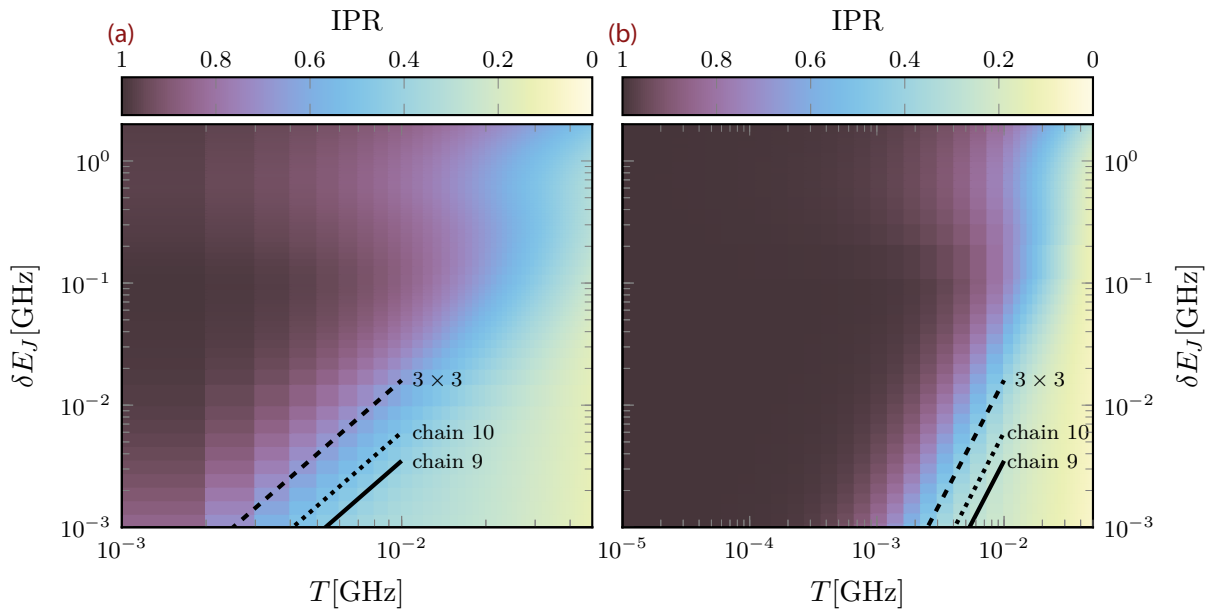


Figure C.4 – IPR for the $L=10$ chain and the 3×3 geometry in the T - δE_J plane. (a) Data for the ten-transmon chain. (b) Data for the 3×3 geometry. The black curves, where $\delta E_J \propto T^2$, mark the line where the IPR falls below $1/2$ for the 3×3 geometry and chains of $L = 9$ and $L = 10$. All results are averaged over all states of the $N_{\text{ex}} = 5$ excitation bundle and at least 3,500 (3×3) and 2,500 ($L = 10$) disorder realizations.

Fig. C.5(a). The histogram displays the level ratio distribution for $L = 6$, $N_{\text{ex}} = 3$, $T = 0$ GHz, and $\delta E_J = 10^{-6}$ GHz. It exhibits a strong peak at $R_n = 0$ (and a second, much smaller peak at $R_n \approx 0.6$ originating from a multiplet that contains a single state). Removing these spurious contributions from the histogram yields an almost perfect agreement with the Poisson distribution. However, calculating the KL divergence from the histogram as shown would signal a substantial discrepancy from integrability, even though the system consists of several independent integrable subsystems—the permutation multiplets. This effect persists for stronger disorders up to values where the multiplets initially start to form. The softening of the multiplet structures then ensures that other bins also benefit from the falsely included small R_n values, as is shown in Fig. C.5(b) for $\delta E_J = 100$ MHz. The impact of the fallacious R_n ratios becomes less pressing for larger system sizes. For example, if $L = 12$ and $N_{\text{ex}} = 6$, there are 130 ‘wrong’ R_n compared to a total of 12,374 level ratios per disorder realization. For the 3×3 and $L = 10$ geometries that we mainly consider, however, the consequences are still measurable.

Second, distinct multiplets show different levels of sensitivity to the emergence of level repulsion. In particular, not all multiplets show footprints of delocalization or Wigner-Dyson statistics within the disorder ranges that our simulations focus on.

Fig. C.5(c) illustrates the combined effect of these two points for the example of the $N_{\text{ex}} = 5$ bundle of the 3×3 geometry. The KL divergences calculated for all levels are shown in blue. They display no clear tendency towards the formation of a Wigner-Dyson distribution. On the contrary: around $\delta E_J = 10^{-2}$ GHz, $D(P||P_{\text{Wigner}})$ even increases, an effect of the development of the peak at small R_n . When excluding these fraudulent values from the statistics, the effect disappears, and $D(P||P_{\text{Wigner}})$ clearly declines in the quantum chaotic region, but without ever reaching proximity to zero. $D(P||P_{\text{Poisson}})$ increases only mildly in this region, indicating that the level statistic now obeys a mixture of the Wigner-Dyson and Poisson predictions, as expected

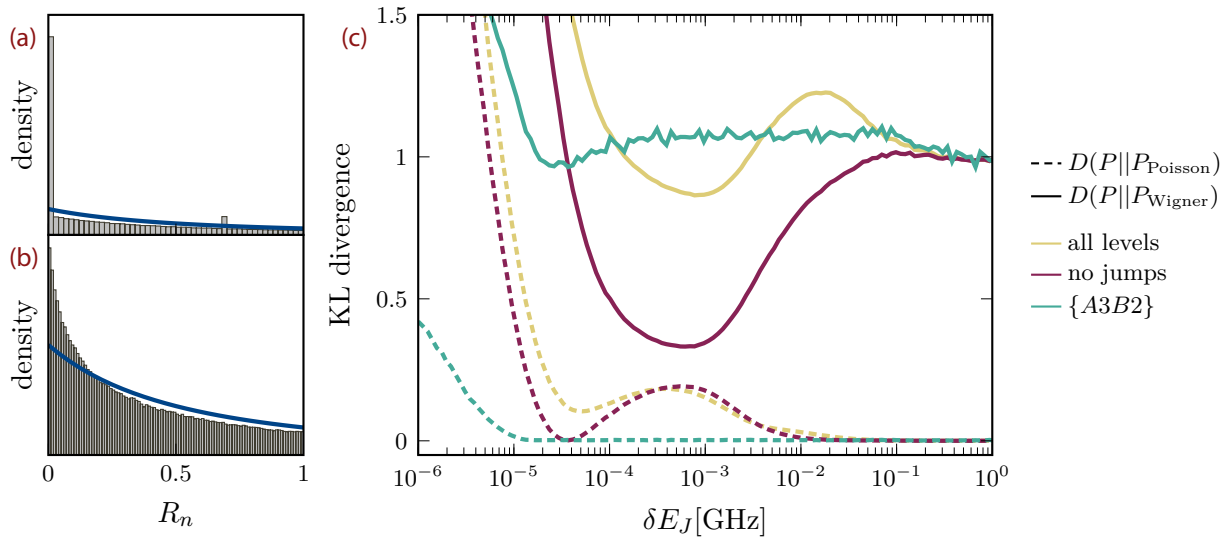


Figure C.5 – Fallacies of level statistics in predicting quantum chaos. (a) Histogram for the R_n ratios of the $N_{\text{ex}} = 3$ bundle of an $L = 6$ chain, calculated for $\delta E_J = 10^{-6}$ GHz and $T = 0$ GHz. The dominant peak at $R_n = 0$ arises from level ratios, whose calculation involves energies from different multiplets. (b) Histogram for larger $\delta E_J = 0.1$ GHz, i.e., the disorder strength where the Hilbert space starts to restructure into the multiplets. Calculating KL divergences for the displayed histograms predicts no agreement with either of the two main statistics, although all individual multiplets show good agreement with the Poisson distribution. Panel (c) shows how this impedes an accurate estimation of the chaoticity. $D(P||P_{\text{Wigner}})$ only approaches zero if the ‘wrong’ R_n values are excluded from the statistics. Even then, the degree of chaos in the relevant states is strongly underestimated because the existence of integrable bundles, e.g., the $\{A3B2\}$ whose KL divergences are shown in green, shifts the histograms towards the Poisson distribution. Results in (a) and (b) are averaged over 20,000 disorder realizations, in (c) over at least 8,000 disorder realizations.

for statistics where both integrable and chaotic multiplets enter. As an example, we show the KL divergences for the multiplet $\{A3B2\}$, which obeys good agreement with Poisson statistics throughout the relevant disorder region. Only when the statistics are restricted to, e.g., the computational bundle $\{A111B11\}$ as in Fig. 5.5, does the KL divergence reveal the full extent of chaos and the lack of suitability of the system as a quantum computer.

The first two points have shown that meaningful predictions are only possible if the relevant subspaces to which the MBL toolbox is applied are carefully identified. To finish, we sharpen this observation for the case when sectors of the Hilbert space that should be treated independently overlap in energy. As one instance of the phenomenon, we consider the $L = 5$ chain and focus on the multiplet $\{A1B2\}$. For one randomly chosen disorder realization, the six levels of this sector are shown in Fig. C.6(a). At $\delta E_J = 0.01$ GHz, all eigenstates are dominated by a single Fock states, namely—from lowest to highest in energy— $|00021\rangle$, $|00120\rangle$, $|10020\rangle$, $|02001\rangle$, $|02100\rangle$, $|12000\rangle$. The multiplet can be separated into two sets, each consisting of the three states that are connected via second-order hopping processes, see Fig. C.2. In the disorder range surveyed in Fig. C.6(a), states from different subsets do not hybridize. Each eigenstate can, therefore, safely be assigned to one of the subsets, as symbolized by the two different colors. Levels belonging to the same subset repel each other but straightly cross¹ through levels of a different color. For a disorder strength $\delta E_J < 10^{-4}$ GHz, levels of different subsets form pairs. The two eigenfunctions that are lowest in energy are given by $|\psi_1\rangle = 0.98|10020\rangle + 0.1|00120\rangle + \dots$

¹In fact, very tiny avoided crossings appear between differently colored levels. These are only resolved upon blowing up the energy scale by several orders of magnitude.

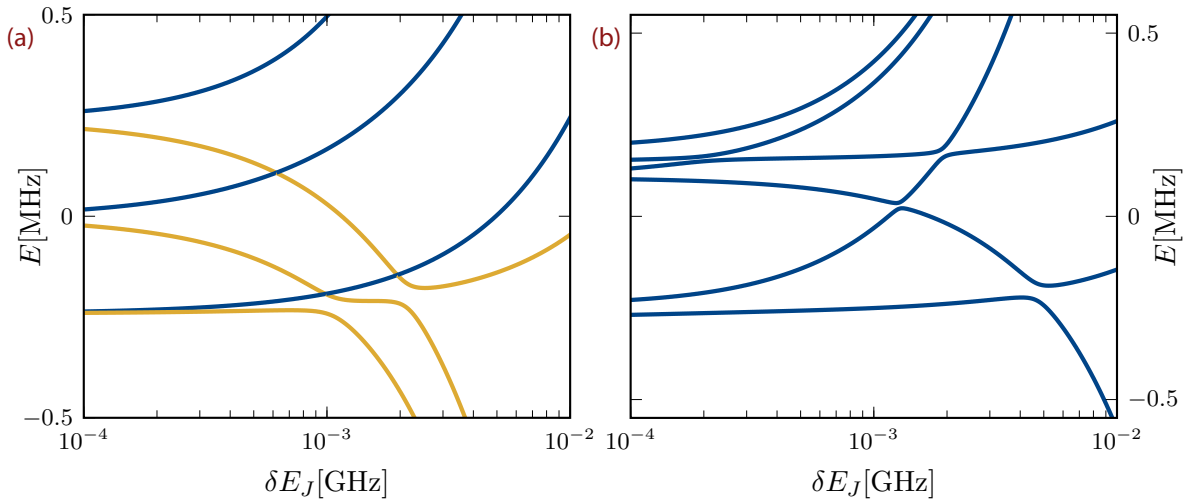


Figure C.6 – Comparison of the spectra for the multiplets $\{A1B2\}$ and $\{A11B1\}$ as a function of δE_J for a single disorder realization. (a) The six levels can be divided into two sets containing three levels each and shown in different colors, where states from the same subset repel and states from different subsets cross. In contrast, no further splitting into finer hierarchy levels occurs for $\{A11B1\}$ and (for this particular disorder realization) all repel each other.

and $|\psi_2 = 0.98|02001\rangle + 0.1|02100\rangle + \dots$, i.e., they are related by the mirror symmetry of the chain. Only for a much smaller disorder, they further hybridize to form (anti-)symmetric combinations of $|\psi_1\rangle$ and $|\psi_2\rangle$. The same holds for the other two pairs. In summary, for the disorder regime monitored in Fig. C.6, the multiplet $\{A2B1\}$ consists of two very weakly correlated subsets of strongly correlated states. An overall level statistics analysis cannot resolve this further splintering and tends to show an agreement with Poisson statistics. For comparison, the spectrum restricted to the $\{A11B1\}$ multiplet is shown in Fig. C.6(b). For this particular disorder realization, all levels repel each other. The wave functions for $\delta E_J = 10^{-6}$ GHz nearly possess the symmetries. For example, the lowest wave function is approximately given by $0.5(|10011\rangle + |11001\rangle) + 0.49(|10110\rangle + |01101\rangle) + \dots$.

The above exemplifies how a permutation multiplet can further splinter into smaller subsets. One can also envision a situation where, for example, due to a more complicated frequency unit cell, different multiplets that are far apart in configuration space overlap in energy and—despite being individually well described by GOE matrices—falsely mimic the level statistics of an integrable system. Stepping aside from the transmon array Hamiltonian, we already mentioned in Chapter 5 that Ref. [350] recently discussed this phenomenon in a different context, where the overlapping sectors correspond to different symmetry blocks.

C.4 Permutation multiplets for the 3×3 geometry with AB frequency pattern

For completeness, we provide an overview of all permutation multiplets that arise for small δE_J in the 3×3 geometry with an AB frequency pattern superimposed on it, as shown in Fig. 5.2. The 1,287 states of the $N_{\text{ex}} = 5$ bundle split into 35 multiplets, five of which are computational multiplets with excitation numbers 0 and 1. All multiplets are listed in Table C.1, sorted from lowest to highest in energy as obtained for our choices of the mean Josephson energies. The blue cells mark computational multiplets.

Table C.1 – Permutation multiplets for the $N_{\text{ex}}=5$ bundle of a 3×3 geometry with an AB frequency arrangement. The A column gives the local excitation structure on the A sublattice, i.e., an entry 32 means that one of each of the five A transmons is in $|2\rangle$ and $|3\rangle$, respectively. The other three A transmons are in the ground state $|0\rangle$. The same holds for column B . The column labeled N_{states} gives the number of states in the multiplet. In total, there are 35 multiplets with 1,287 states. Five of them are computational multiplets, highlighted in blue, containing a total of 126 computational states.

	A	B	N_{states}		A	B	N_{states}		A	B	N_{states}		
1.	5	–	5		13.	3	11	30		25.	–	311	12
2.	41	–	20		14.	22	1	40		26.	1111	1	20
3.	–	5	4		15.	2111	–	20		27.	1	22	30
4.	4	1	20		16.	11	3	40		28.	2	111	20
5.	1	4	20		17.	21	2	80		29.	11	21	120
6.	32	–	20		18.	–	32	12		30.	111	11	60
7.	–	41	12		19.	211	1	120		31.	–	221	12
8.	311	–	30		20.	1	31	60		32.	1	211	60
9.	3	2	20		21.	11111	–	1		33.	11	111	40
10.	31	1	80		22.	2	21	60		34.	–	2111	4
11.	221	–	30		23.	21	11	120		35.	1	1111	5
12.	2	3	20		24.	111	2	40					

Appendix

Field-driven effects in Kitaev spin liquids

D

While all chapters contained in this thesis address the many-body perspective on the transmon quantum computer, a second, orthogonal line of research was devoted to the investigation of the fate of the Kitaev model [382]—the drosophila of *spin liquid theory* [383, 384]—when exposed to magnetic fields. The results have been incorporated into the publications [P4–P6]. These are characterized by a considerable devotion to technical details and do not require a supplementing in-depth explanation. Hence, we restrict here to a brief overview and contextualization and refer to the respective publications for further details.

Quantum spin liquids (QSL) are states of matter with an anomalously high degree of long-range entanglement [383]. Among their salient features are the lack of symmetry-breaking magnetic order at the lowest temperatures, despite the strong interactions between the constituent spins, and the emergence of nonlocal excitations with nontrivial exchange statistics. The Kitaev model [382], consisting of spin-1/2 degrees of freedom at the vertices of a honeycomb lattice that interact via bond-directional nearest-neighbor Ising exchange, is a paradigmatic example for a model hosting a QSL. Its unique combination of conceptual simplicity, exact solvability, and experimental relevance [385, 386] has led to an explosion of interest that has continued unabated since its introduction in 2006 [387]. The crucial ingredient is the directional dependence of the Ising easy-axis: labeling the three inequivalent bond directions in the honeycomb lattice as shown in Fig. D.1(a), only the \hat{S}^x components interact along the x bonds and similar for the y and z links. Because of this peculiar interaction, a spin can minimize its energy with only one of its neighbors; a phenomenon called exchange frustration. A powerful framework to describe QSL is to decompose the constituent spins into partons, either bosons or fermions, and emergent gauge fields in a deconfined phase [384, 388]. Recasting the spins in this new form is usually only a better starting point for (often uncontrolled) approximations. However, the Kitaev model, expressed in terms of *Majorana fermions* and a static \mathbb{Z}_2 gauge field, reduces to a simple quadratic Hamiltonian for every gauge field configuration, describing itinerant fermions on the honeycomb lattice. Remarkably, the ground state of the gauge field is exactly known [382, 389]. Excitations in the gauge sector are massive. Around the point of isotropic couplings, the Majorana fermions form a gapless band structure with a Dirac cone.

Exposing the Kitaev model to a magnetic field disrupts the exact solvability. A field in the perturbative regime that couples to all spin components gaps out the band structure. The Kitaev model transitions into an exotic phase with non-Abelian topological order [382]. Despite its intriguing characteristics, few efforts have been made in the years following its introduction to gain insights into the physics of the in-field Kitaev model beyond the perturbative regime. Since 2015, however, field-induced effects have been brought into focus by experimental results on the material $\alpha\text{-RuCl}_3$, which is believed to realize Kitaev-type interactions between spin-orbit

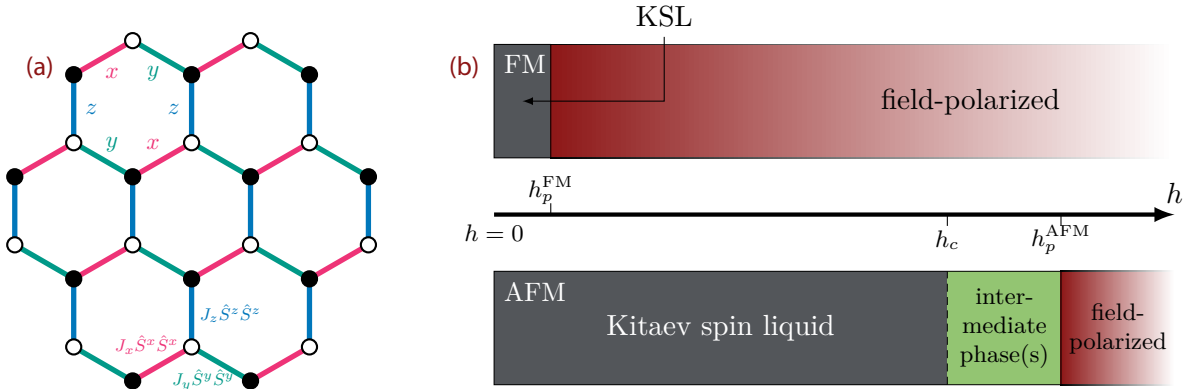


Figure D.1 – The Kitaev model. (a) Visualization of the Kitaev model and its bond-dependent interactions. (b) Generic in-field phase diagram for antiferromagnetic and ferromagnetic exchange interactions. While for FM interactions one observes a single phase transition at small fields (more than an order of magnitude smaller than the coupling strength J), the AFM model shows a richer behavior. The KSL phase is much more stable and, in addition, the polarized phase is preceded by an intermediate phase.

entangled, effective $j = 1/2$ moments located on ruthenium honeycomb layers [390]. $\alpha\text{-RuCl}_3$ orders magnetically for temperatures below 7 Kelvin [391], indicating the presence of order-stabilizing residual couplings beyond the pure Kitaev terms. However, a magnetic field destroys the ordering tendency [392, 393]. Whether the system undergoes a transition to a field-induced spin liquid phase or enters the trivially polarized phase is intensely debated [385]; in any case, these findings have rekindled the efforts to understand the Kitaev model for larger field strengths. The problem was thereupon tackled with the whole methodological richness of condensed matter physics [394–398]. All studies are consistent regarding the general phase diagram shown in Fig. D.1(b). Notably, the Kitaev models with ferromagnetic (FM) and antiferromagnetic (AFM) exchange interactions behave remarkably differently. The FM model exhibits a single phase transition from the non-Abelian QSL to a partially polarized phase. For AFM couplings, on the other side, the Kitaev spin liquid (KSL) phase sustains field strengths that are an order of magnitude larger. It experiences an *intermediate phase* before it transitions to the partially polarized phase. The precise nature of the intermediate phase has not yet been conclusively clarified. Initialized in Ref. [394], a series of studies provided strong evidence for the emergence of a $U(1)$ spin liquid¹ [395, 400].

Our studies add to the efforts of obtaining a more consistent picture of spin liquid physics in the presence of magnetic fields. Generalizations of the Kitaev model to other lattice geometries² or higher spins serve as the central ingredients for our investigations. Specifically, we conducted

- a systematic analysis of the Kitaev model on the lattices shown in Fig. D.2 in the presence of a field pointing in [001] direction [P4]. To address this problem, we employed a Majorana mean-field theory [406] based on the exact solution of the Kitaev model in terms of Jordan-Wigner fermions [407–409]. Without a magnetic field, the lattices at hand show a

¹In this context, it is worth mentioning that besides Kitaev's original Majorana decomposition, there are other insightful fractionalization schemes. The $U(1)$ spin liquid is most easily understood when expressing the Hamiltonian in terms of complex fermions [399]. The non-Abelian small-field phase then appears as a topological parton superconductor. The magnetic field destroys the superconducting order, accompanied by a Higgs transition in the gauge sector, which changes the gauge field from \mathbb{Z}_2 to $U(1)$. The intermediate phase is a parton metal with a Fermi surface. The excitations in the gauge sector are likewise gapless.

²The Kitaev model is exactly solvable on any tricoordinated lattice, independent of the dimension. However, one often has to rely on numerics to obtain the gauge field configuration with minimal energy.

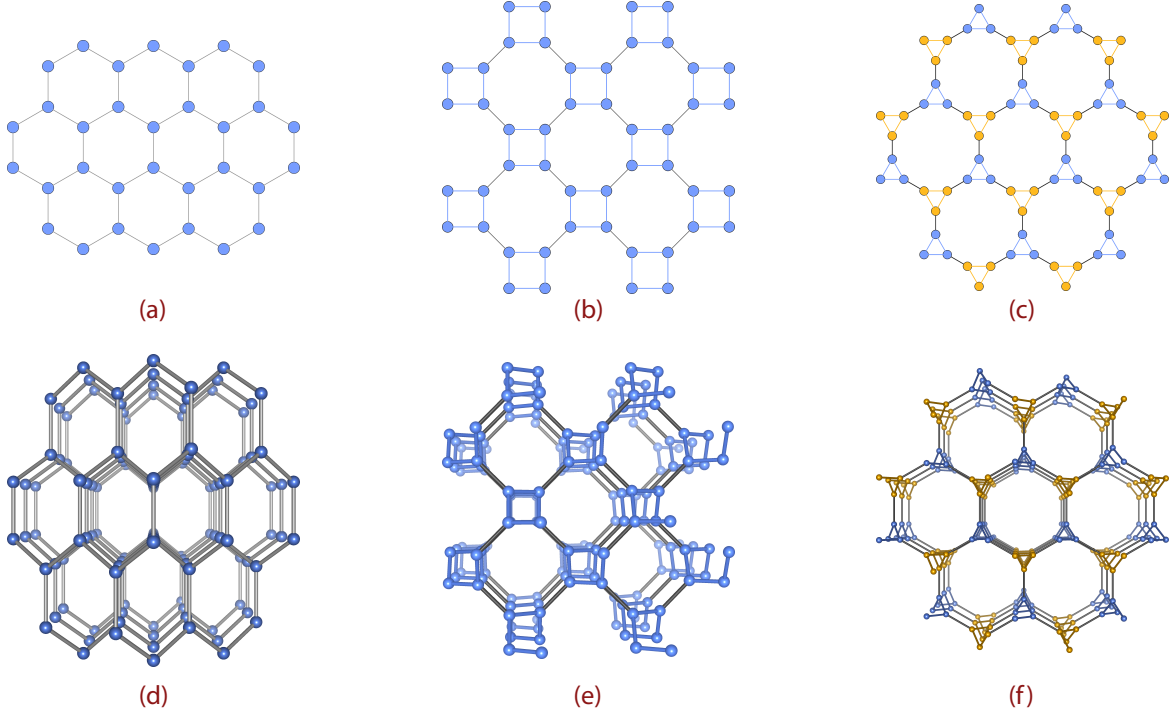


Figure D.2 – Tricoordinated lattices in two and three dimensions. Specifically, the figure shows the (a) honeycomb, (b) square-octagon [401] and (c) decorated honeycomb lattice [402] and the three-dimensional counterparts, the (d) (10,3)b or hyperhoneycomb [403], (e) (10,3)a or hyperoctagon [404] and (f) (10,3)c [405] lattice.

cornucopia of different spin liquid ground states: the KSL can be gapped with Dirac cones, Weyl points, nodal lines, or Fermi surfaces [405], gapped with Abelian topological order [401] or gapless and *chiral* [402]. Across all lattices, we find the generic phase diagrams shown in Fig. D.1(b), regardless of the precise nature of the zero-field KSL. For AFM couplings, the transition from the KSL to the intermediate phase at h_c is accompanied by a change in the topology of the Majorana band structure. In particular, we find an intimate link between the transition into and nature of the intermediate phase and the zero-field Kitaev model with fixed AFM J_x , J_y , and variable J_z . For example, the two cases $J_z = 0$ and $h = h_c$ yield the same Majorana zero modes. Our study highlights the richness of AFM Kitaev models from the perspective of the itinerant Majorana fermions. It comes with the limitation that transitions in the gauge sector, like the $\mathbb{Z}_2 \leftrightarrow U(1)$ transition predicted to occur in a [111] field [394], are not covered therein. For further details, Ref. [P4] should be consulted.

- a symmetry analysis of the Kitaev models on the geometries in Fig. D.2 to establish the symmetry-allowed canting patterns for magnetic fields pointing along high-symmetry directions [P5]. This is motivated by the conjecture, based on exact diagonalization and DMRG studies of the square-octagon and the decorated honeycomb lattices [P5], that AFM Kitaev models generically exhibit a field-induced intermediate regime, characterized by significant spin canting and separated from the polarized regime by a crossover. The symmetry analysis does correctly predict the observed canting patterns. Furthermore, it explains why the Kitaev model on the decorated (Fig. D.2(c)) and the original honeycomb model, despite the intriguing similarities at low fields (same symmetries and same non-Abelian topological order), behave remarkably differently at intermediate fields. For the honeycomb lattice, a

symmetry obstruction forbids the spins to cant away from the [111] field without prompting a transition to a symmetry-broken phase. Instead, it harbors a $U(1)$ QSL phase. In addition, the symmetry analysis can identify high-symmetry field directions on other lattices, which obstruct spin canting, and are, therefore, promising candidates for further testing. Such field directions exist, for example, for the three-dimensional hyperhoneycomb lattice shown in Fig. D.2(d). More details are provided in Ref. [P5].

- a complex fermion mean-field analysis [399, 410] for the spin-1 [P6] and the spin-1/2 Kitaev model on the honeycomb lattice. For the latter, the theory correctly predicts some properties in the perturbative regime (magnetization grows faster for FM than for AFM couplings, expected scaling of the band structure gap with the field strength). However, it struggles to detect reasonable results for intermediate field strengths because the calculations tend to converge toward the (unphysical) fully-polarized solution. This technical severity was already observed in the Heisenberg-Kitaev model [410].

Bibliography

- [P1] **C. Berke**, E. Varvelis, S. Trebst, A. Altland, and D. P. DiVincenzo, Transmon platform for quantum computing challenged by chaotic fluctuations, *Nature Communications* **13** (1), 2495 (2022).
- [P2] S.-D. Börner, **C. Berke**, D. P. DiVincenzo, S. Trebst, and A. Altland, Classical chaos in quantum computers, *Phys. Rev. Res.* **6** (3), 033128 (2024).
- [P3] D. Basilewitsch, S.-D. Börner, **C. Berke**, A. Altland, S. Trebst, and C. P. Koch, Chaotic fluctuations in a universal set of transmon qubit gates, arXiv:2311.14592 (2023).
- [P4] **C. Berke**, S. Trebst, and C. Hickey, Field stability of Majorana spin liquids in antiferromagnetic Kitaev models, *Physical Review B* **101** (21), 214442 (2020).
- [P5] C. Hickey, M. Gohlke, **C. Berke**, and S. Trebst, Generic field-driven phenomena in Kitaev spin liquids: Canted magnetism and proximate spin liquid physics, *Physical Review B* **103** (6), 064417 (2021).
- [P6] C. Hickey, **C. Berke**, P. P. Stavropoulos, H.-Y. Kee, and S. Trebst, Field-driven gapless spin liquid in the spin-1 Kitaev honeycomb model, *Phys. Rev. Research* **2** (2), 023361 (2020).
- [1] R. de Wolf, The potential impact of quantum computers on society, *Ethics and Information Technology* **19** (4), 271–276 (2017).
- [2] J. Preskill, Quantum computing and the entanglement frontier, arXiv:1203.5813 (2012).
- [3] M. Dyakonov, *The Case Against Quantum Computing*, IEEE Spectrum, (2018) <https://spectrum.ieee.org/the-case-against-quantum-computing> (visited on 06/03/2022).
- [4] M. Dyakonov, When will we have a quantum computer?, *Solid-State Electronics* **155**, 4–6 (2019).
- [5] S. Sheldon, E. Magesan, J. M. Chow, and J. M. Gambetta, Procedure for systematically tuning up cross-talk in the cross-resonance gate, *Physical Review A* **93** (6), 060302 (2016).
- [6] R. Barends et al., Superconducting quantum circuits at the surface code threshold for fault tolerance, *Nature* **508** (7497), 500–503 (2014).
- [7] J. Kelly et al., State preservation by repetitive error detection in a superconducting quantum circuit, *Nature* **519** (7541), 66–69 (2015).
- [8] A. D. Córcoles, E. Magesan, S. J. Srinivasan, A. W. Cross, M. Steffen, J. M. Gambetta, and J. M. Chow, Demonstration of a quantum error detection code using a square lattice of four superconducting qubits, *Nature Communications* **6** (1), 6979 (2015).

- [9] A. Hagar and M. Cuffaro, Quantum Computing, in *The Stanford encyclopedia of philosophy*, edited by E. N. Zalta, Winter 2019 (Metaphysics Research Lab, Stanford University, 2019).
- [10] J. Preskill, Quantum Computing in the NISQ era and beyond, *Quantum* **2**, 79 (2018).
- [11] D. P. DiVincenzo, The Physical Implementation of Quantum Computation, *Fortschritte der Physik* **48** (9-11), 771–783 (2000).
- [12] Y. I. Manin, *Computable and Non-Computable* (Sovetskoe Radio, 1980).
- [13] R. P. Feynman, Simulating physics with computers, *International Journal of Theoretical Physics* **21** (6), 467–488 (1982).
- [14] D. E. Deutsch, Quantum theory, the Church–Turing principle and the universal quantum computer, *Proceedings of the Royal Society of London. A. Mathematical and Physical Sciences* **400** (1818), 97–117 (1985).
- [15] D. E. Deutsch, Quantum computational networks, *Proceedings of the Royal Society of London. A. Mathematical and Physical Sciences* **425** (1868), 73–90 (1989).
- [16] D. Deutsch and R. Jozsa, Rapid solution of problems by quantum computation, *Proceedings of the Royal Society of London. Series A: Mathematical and Physical Sciences* **439** (1907), 553–558 (1992).
- [17] D. R. Simon, “On the power of quantum computation”, in *Proceedings of the 35th Annual Symposium on Foundations of Computer Science* (1994), pp. 116–123.
- [18] P. W. Shor, Polynomial-Time Algorithms for Prime Factorization and Discrete Logarithms on a Quantum Computer, *SIAM Journal on Computing* **26** (5), 1484–1509 (1997).
- [19] P. Shor, “Algorithms for quantum computation: discrete logarithms and factoring”, in *Proceedings 35th annual symposium on foundations of computer science* (1994), pp. 124–134.
- [20] R. L. Rivest, A. Shamir, and L. Adleman, A method for obtaining digital signatures and public-key cryptosystems, *Communications of the ACM* **21** (2), 120–126 (1978).
- [21] L. K. Grover, “A fast quantum mechanical algorithm for database search”, in *Proceedings of the twenty-eighth annual ACM symposium on Theory of Computing* (1996), pp. 212–219.
- [22] L. K. Grover, Quantum Mechanics Helps in Searching for a Needle in a Haystack, *Physical Review Letters* **79** (2), 325–328 (1997).
- [23] Y. Ozhigov, “Quantum computer can not speed up iterated applications of a black box”, in *Quantum computing and quantum communications*, edited by C. P. Williams (1999), pp. 152–159.
- [24] M. Amico, Z. H. Saleem, and M. Kumph, An Experimental Study of Shor’s Factoring Algorithm on IBM Q, *Physical Review A* **100** (1), 012305 (2019).
- [25] H. D. Zeh, On the interpretation of measurement in quantum theory, *Foundations of Physics* **1** (1), 69–76 (1970).
- [26] P. Krantz, M. Kjaergaard, F. Yan, T. P. Orlando, S. Gustavsson, and W. D. Oliver, A quantum engineer’s guide to superconducting qubits, *Applied Physics Reviews* **6** (2), 021318 (2019).

- [27] R. J. Schoelkopf, A. A. Clerk, S. M. Girvin, K. W. Lehnert, and M. H. Devoret, “Qubits as spectrometers of quantum noise”, in *Quantum noise in mesoscopic physics*, edited by Y. V. Nazarov (Springer Netherlands, 2003), pp. 175–203.
- [28] M. A. Nielsen and I. L. Chuang, *Quantum Computation and Quantum Information: 10th Anniversary Edition* (Cambridge University Press, 2010).
- [29] D. P. DiVincenzo, Two-bit gates are universal for quantum computation, *Physical Review A* **51** (2), 1015–1022 (1995).
- [30] A. Barenco, C. H. Bennett, R. Cleve, D. P. DiVincenzo, N. Margolus, P. Shor, T. Sleator, J. A. Smolin, and H. Weinfurter, Elementary gates for quantum computation, *Physical Review A* **52** (5), 3457–3467 (1995).
- [31] S. Lloyd, Almost Any Quantum Logic Gate is Universal, *Physical Review Letters* **75** (2), 346–349 (1995).
- [32] J. L. Dodd, M. A. Nielsen, M. J. Bremner, and R. T. Thew, Universal quantum computation and simulation using any entangling Hamiltonian and local unitaries, *Physical Review A* **65** (4), 040301 (2002).
- [33] M. J. Bremner, C. M. Dawson, J. L. Dodd, A. Gilchrist, A. W. Harrow, D. Mortimer, M. A. Nielsen, and T. J. Osborne, Practical Scheme for Quantum Computation with Any Two-Qubit Entangling Gate, *Physical Review Letters* **89** (24), 247902 (2002).
- [34] Y. R. Sanders, J. J. Wallman, and B. C. Sanders, Bounding quantum gate error rate based on reported average fidelity, *New Journal of Physics* **18** (1), 012002 (2015).
- [35] J. F. Poyatos, J. I. Cirac, and P. Zoller, Complete Characterization of a Quantum Process: The Two-Bit Quantum Gate, *Physical Review Letters* **78** (2), 390–393 (1997).
- [36] A. D. Córcoles, J. M. Gambetta, J. M. Chow, J. A. Smolin, M. Ware, J. Strand, B. L. T. Plourde, and M. Steffen, Process verification of two-qubit quantum gates by randomized benchmarking, *Physical Review A* **87** (3), 030301 (2013).
- [37] E. Magesan et al., Efficient Measurement of Quantum Gate Error by Interleaved Randomized Benchmarking, *Physical Review Letters* **109** (8), 080505 (2012).
- [38] E. Magesan, J. M. Gambetta, and J. Emerson, Scalable and Robust Randomized Benchmarking of Quantum Processes, *Physical Review Letters* **106** (18), 180504 (2011).
- [39] F. Arute et al., Quantum supremacy using a programmable superconducting processor, *Nature* **574** (7779), 505–510 (2019).
- [40] D. Cory et al., NMR Based Quantum Information Processing: Achievements and Prospects, *Fortschritte der Physik* **48** (9-11), 875–907 (2000).
- [41] P. Kok, W. J. Munro, K. Nemoto, T. C. Ralph, J. P. Dowling, and G. J. Milburn, Linear optical quantum computing with photonic qubits, *Reviews of Modern Physics* **79** (1), 135–174 (2007).
- [42] X. Wu, X. Liang, Y. Tian, F. Yang, C. Chen, Y.-C. Liu, M. K. Tey, and L. You, A concise review of Rydberg atom based quantum computation and quantum simulation, *Chinese Physics B* **30** (2), 020305 (2021).
- [43] M. Saffman, Quantum computing with atomic qubits and Rydberg interactions: progress and challenges, *Journal of Physics B: Atomic, Molecular and Optical Physics* **49** (20), 202001 (2016).

- [44] R. C. C. Leon et al., Coherent spin control of s-, p-, d- and f-electrons in a silicon quantum dot, *Nature Communications* **11** (1), 797 (2020).
- [45] J. I. Cirac and P. Zoller, Quantum Computations with Cold Trapped Ions, *Physical Review Letters* **74** (20), 4091–4094 (1995).
- [46] H. Häffner, C. F. Roos, and R. Blatt, Quantum computing with trapped ions, *Physics Reports* **469** (4), 155–203 (2008).
- [47] Devoret, Michel H., “Quantum Fluctuations in Electrical Circuits”, in *Quantum fluctuations: les houches, session lxiii*, edited by S. Reynaud, E. Giacobino, and J. Zinn-Justin (Elsevier, 1997), pp. 351–386.
- [48] A. J. Leggett, Macroscopic Quantum Systems and the Quantum Theory of Measurement, *Progress of Theoretical Physics Supplement* **69**, 80–100 (1980).
- [49] A. J. Leggett, Macroscopic Quantum Tunnelling and all that, in *Essays in Theoretical Physics*, edited by W. E. Parry (Pergamon, 1984), pp. 95–127.
- [50] M. H. Devoret, J. M. Martinis, and J. Clarke, Measurements of Macroscopic Quantum Tunneling out of the Zero-Voltage State of a Current-Biased Josephson Junction, *Physical Review Letters* **55** (18), 1908–1911 (1985).
- [51] J. M. Martinis, M. H. Devoret, and J. Clarke, Energy-Level Quantization in the Zero-Voltage State of a Current-Biased Josephson Junction, *Physical Review Letters* **55** (15), 1543–1546 (1985).
- [52] J. Clarke, A. N. Cleland, M. H. Devoret, D. Esteve, and J. M. Martinis, Quantum Mechanics of a Macroscopic Variable: The Phase Difference of a Josephson Junction, *Science* **239** (4843), 992–997 (1988).
- [53] Y. Nakamura, Y. A. Pashkin, and J. S. Tsai, Coherent control of macroscopic quantum states in a single-Cooper-pair box, *Nature* **398** (6730), 786–788 (1999).
- [54] B. D. Josephson, Possible new effects in superconductive tunnelling, *Physics Letters* **1** (7), 251–253 (1962).
- [55] M. H. Devoret, A. Wallraff, and J. M. Martinis, Superconducting Qubits: A Short Review, arXiv:cond-mat/0411174 (2004).
- [56] J. Clarke and F. K. Wilhelm, Superconducting quantum bits, *Nature* **453** (7198), 1031–1042 (2008).
- [57] J. M. Martinis and K. Osborne, Superconducting Qubits and the Physics of Josephson Junctions, arXiv:cond-mat/0402415 (2004).
- [58] J. Koch, T. M. Yu, J. Gambetta, A. A. Houck, D. I. Schuster, J. Majer, A. Blais, M. H. Devoret, S. M. Girvin, and R. J. Schoelkopf, Charge-insensitive qubit design derived from the Cooper pair box, *Physical Review A* **76** (4), 042319 (2007).
- [59] <https://www.ibm.com/quantum-computing/>.
- [60] D. Ristè, J. G. van Leeuwen, H.-S. Ku, K. W. Lehnert, and L. DiCarlo, Initialization by Measurement of a Superconducting Quantum Bit Circuit, *Physical Review Letters* **109** (5), 050507 (2012).
- [61] B. M. Terhal, Quantum error correction for quantum memories, *Reviews of Modern Physics* **87** (2), 307–346 (2015).

- [62] P. Shor, “Fault-tolerant quantum computation”, in Proceedings of 37th Conference on Foundations of Computer Science (1996), pp. 56–65.
- [63] D. P. DiVincenzo and P. W. Shor, Fault-Tolerant Error Correction with Efficient Quantum Codes, *Physical Review Letters* **77** (15), 3260–3263 (1996).
- [64] S. Beauregard, Circuit for Shor’s algorithm using $2n+3$ qubits, *Quantum Information & Computation* **3** (2), 175–185 (2003).
- [65] C. Gidney and M. Ekerå, How to factor 2048 bit RSA integers in 8 hours using 20 million noisy qubits, *Quantum* **5**, 433 (2021).
- [66] A. Y. Kitaev, Fault-tolerant quantum computation by anyons, *Annals of Physics* **303** (1), 2–30 (2003).
- [67] C. Nayak, S. H. Simon, A. Stern, M. Freedman, and S. Das Sarma, Non-Abelian anyons and topological quantum computation, *Reviews of Modern Physics* **80** (3), 1083–1159 (2008).
- [68] F. Hassler, “Majorana Qubits”, in *Quantum information processing: lecture notes of the 44th IFF Spring School 2013*, edited by D. DiVincenzo, Bd. 52 (Forschungszentrum Jülich, 2013), B2.1–B2.21.
- [69] H. Zhang et al., Retraction Note: Quantized Majorana conductance, *Nature* **591** (7851), E30 (2021).
- [70] M. Kjaergaard, M. E. Schwartz, J. Braumüller, P. Krantz, J. I.-J. Wang, S. Gustavsson, and W. D. Oliver, Superconducting Qubits: Current State of Play, *Annual Review of Condensed Matter Physics* **11** (1), 369–395 (2020).
- [71] S. Bravyi, D. Gosset, R. König, and M. Tomamichel, Quantum advantage with noisy shallow circuits, *Nature Physics* **16** (10), 1040–1045 (2020).
- [72] S. Boixo, S. V. Isakov, V. N. Smelyanskiy, R. Babbush, N. Ding, Z. Jiang, M. J. Bremner, J. M. Martinis, and H. Neven, Characterizing quantum supremacy in near-term devices, *Nature Physics* **14** (6), 595–600 (2018).
- [73] A. P. Lund, M. J. Bremner, and T. C. Ralph, Quantum sampling problems, *Boson Sampling and quantum supremacy*, *npj Quantum Information* **3** (1), 1–8 (2017).
- [74] A. D. Córcoles, A. Kandala, A. Javadi-Abhari, D. T. McClure, A. W. Cross, K. Temme, P. D. Nation, M. Steffen, and J. M. Gambetta, Challenges and Opportunities of Near-Term Quantum Computing Systems, *Proceedings of the IEEE* **108** (8), 1338–1352 (2020).
- [75] I. Durham, D. Garisto, and K. Wiesner, *Physicists Need to Be More Careful with How They Name Things*, *Scientific American*, (2021) <https://www.scientificamerican.com/article/physicists-need-to-be-more-careful-with-how-they-name-things/> (visited on 02/02/2022).
- [76] K. Wiesner, The careless use of language in quantum information, arXiv:1705.06768 (2017).
- [77] J. Preskill, *Why I Called It ‘Quantum Supremacy’*, *Quanta Magazine*, (2019) <https://www.quantamagazine.org/john-preskill-explains-quantum-supremacy-20191002/> (visited on 02/02/2022).
- [78] E. Pednault, J. Gunnels, D. Maslov, and J. Gambetta, *On “Quantum Supremacy”*, IBM Research Blog, (2019) <https://www.ibm.com/blogs/research/2019/10/on-quantum-supremacy/> (visited on 02/02/2022).

- [79] C. Neill et al., A blueprint for demonstrating quantum supremacy with superconducting qubits, *Science* **360** (6385), 195–199 (2018).
- [80] E. Pednault, J. A. Gunnels, G. Nannicini, L. Horesh, and R. Wisnieff, Leveraging Secondary Storage to Simulate Deep 54-qubit Sycamore Circuits, arXiv:1910.09534 (2019).
- [81] F. Pan, K. Chen, and P. Zhang, Solving the Sampling Problem of the Sycamore Quantum Circuits, *Physical Review Letters* **129** (9), 090502 (2022).
- [82] S. Aaronson, *Why Google’s Quantum Supremacy Milestone Matters*, (2019) <https://www.nytimes.com/2019/10/30/opinion/google-quantum-computer-sycamore.html> (visited on 06/08/2022).
- [83] W. D. Oliver, Quantum computing takes flight, *Nature* **574** (7779), 487–488 (2019).
- [84] G. Kalai, “The argument against quantum computers”, in *Quantum, probability, logic: the work and influence of itamar pitowsky*, edited by M. Hemmo and O. Shenker (Springer International Publishing, 2020), pp. 399–422.
- [85] Y. Wu et al., Strong Quantum Computational Advantage Using a Superconducting Quantum Processor, *Physical Review Letters* **127** (18), 180501 (2021).
- [86] B. C. Sanders, Quantum Leap for Quantum Primacy, *Physics* **14**, 147 (2021).
- [87] H.-S. Zhong et al., Phase-Programmable Gaussian Boson Sampling Using Stimulated Squeezed Light, *Physical Review Letters* **127** (18), 180502 (2021).
- [88] L. S. Madsen et al., Quantum computational advantage with a programmable photonic processor, *Nature* **606** (7912), 75–81 (2022).
- [89] K. J. Satzinger et al., Realizing topologically ordered states on a quantum processor, *Science* **374** (6572), 1237–1241 (2021).
- [90] X. Mi et al., Time-crystalline eigenstate order on a quantum processor, *Nature* **601** (7894), 531–536 (2022).
- [91] P. Frey and S. Rachel, Realization of a discrete time crystal on 57 qubits of a quantum computer, *Science Advances* **8** (9), eabm7652 (2022).
- [92] D. Jafferis, A. Zlokapa, J. D. Lykken, D. K. Kolchmeyer, S. I. Davis, N. Lauk, H. Neven, and M. Spiropulu, Traversable wormhole dynamics on a quantum processor, *Nature* **612** (7938), 51–55 (2022).
- [93] A. G. Fowler, M. Mariantoni, J. M. Martinis, and A. N. Cleland, Surface codes: Towards practical large-scale quantum computation, *Physical Review A* **86** (3), 032324 (2012).
- [94] J. F. Marques et al., Logical-qubit operations in an error-detecting surface code, *Nature Physics* **18** (1), 80–86 (2022).
- [95] S. Krinner et al., Realizing repeated quantum error correction in a distance-three surface code, *Nature* **605** (7911), 669–674 (2022).
- [96] S. Lloyd, Rolf Landauer (1927-99), *Nature* **400** (6746), 720–720 (1999).
- [97] W. D. Oliver and P. B. Welander, Materials in superconducting quantum bits, *MRS Bulletin* **38** (10), 816–825 (2013).
- [98] E. Magesan, J. M. Gambetta, and J. Emerson, Scalable and Robust Randomized Benchmarking of Quantum Processes, *Physical Review Letters* **106** (18), 180504 (2011).

- [99] S. Krinner, S. Storz, P. Kurpiers, P. Magnard, J. Heinsoo, R. Keller, J. Lütolf, C. Eichler, and A. Wallraff, Engineering cryogenic setups for 100-qubit scale superconducting circuit systems, EPJ Quantum Technology **6** (1), 1–29 (2019).
- [100] R. N. Das, J. Yoder, D. Rosenberg, D. Kim, D. Yost, J. Mallek, D. Hover, V. Bolkhovsky, A. Kerman, and W. Oliver, “Cryogenic Qubit Integration for Quantum Computing”, in 2018 IEEE 68th Electronic Components and Technology Conference (ECTC) (2018), pp. 504–514.
- [101] D. Rosenberg et al., 3D integrated superconducting qubits, npj Quantum Information **3** (1), 1–5 (2017).
- [102] B. Foxen et al., Qubit compatible superconducting interconnects, Quantum Science and Technology **3** (1), 014005 (2017).
- [103] A. Blais, S. M. Girvin, and W. D. Oliver, Quantum information processing and quantum optics with circuit quantum electrodynamics, Nature Physics **16** (3), 247–256 (2020).
- [104] A. Vepsäläinen et al., Impact of Ionizing Radiation on Superconducting Qubit Coherence, Nature **584** (7822), 551–556 (2020).
- [105] O. E. Dial, *Eagle’s quantum performance progress*, IBM Research Blog, (2021) <https://research.ibm.com/blog/eagle-quantum-processor-performance> (visited on 06/09/2022).
- [106] F. Leymann and J. Barzen, The bitter truth about gate-based quantum algorithms in the NISQ era, Quantum Science and Technology **5** (4), 044007 (2020).
- [107] M. H. Devoret and R. J. Schoelkopf, Superconducting Circuits for Quantum Information: An Outlook, Science **339** (6124), 1169–1174 (2013).
- [108] C. K. Andersen, A. Remm, S. Lazar, S. Krinner, N. Lacroix, G. J. Norris, M. Gabureac, C. Eichler, and A. Wallraff, Repeated quantum error detection in a surface code, Nature Physics **16** (8), 875–880 (2020).
- [109] M. Srednicki, Chaos and quantum thermalization, Physical Review E **50** (2), 888–901 (1994).
- [110] J. M. Deutsch, Quantum statistical mechanics in a closed system, Physical Review A **43** (4), 2046–2049 (1991).
- [111] D. A. Abanin and Z. Papić, Recent progress in many-body localization, Annalen der Physik **529** (7), 1700169 (2017).
- [112] I. V. Gornyi, A. D. Mirlin, and D. G. Polyakov, Interacting Electrons in Disordered Wires: Anderson Localization and Low- T Transport, Physical Review Letters **95** (20), 206603 (2005).
- [113] D. M. Basko, I. L. Aleiner, and B. L. Altshuler, Metal–insulator transition in a weakly interacting many-electron system with localized single-particle states, Annals of Physics **321** (5), 1126–1205 (2006).
- [114] D. A. Abanin, E. Altman, I. Bloch, and M. Serbyn, Colloquium: Many-body localization, thermalization, and entanglement, Reviews of Modern Physics **91** (2), 021001 (2019).
- [115] E. N. Lorenz, *The Essence of Chaos* (University of Washington Press, 1993).
- [116] C. Timm, *Theoretische Mechanik*, (2022) https://tu-dresden.de/mn/physik/itp/cmt/ressourcen/dateien/skripte/Skript_TM.pdf?lang=de (visited on 06/28/2022).

- [117] L. D’Alessio, Y. Kafri, A. Polkovnikov, and M. Rigol, From quantum chaos and eigenstate thermalization to statistical mechanics and thermodynamics, *Advances in Physics* **65** (3), 239–362 (2016).
- [118] T. Guhr, A. Müller-Groeling, and H. A. Weidenmüller, Random-matrix theories in quantum physics: common concepts, *Physics Reports* **299** (4), 189–425 (1998).
- [119] R. Nandkishore and D. A. Huse, Many body localization and thermalization in quantum statistical mechanics, *Annual Review of Condensed Matter Physics* **6** (1), 15–38 (2015).
- [120] F. Alet and N. Laflorencie, Many-body localization: An introduction and selected topics, *Comptes Rendus Physique* **19** (6), 498–525 (2018).
- [121] Y. G. Sinai, On the foundations of the ergodic hypothesis for a dynamical system of statistical mechanics, *Dokl. Akad. Nauk. SSSR* **153** (6), 1261–1264 (1963).
- [122] J. Liouville, Note sur l’intégration des équations différentielles de la Dynamique, présentée au Bureau des Longitudes le 29 juin 1853. *Journal de Mathématiques Pures et Appliquées*, 137–138 (1855).
- [123] J. Emerson, Quantum Chaos and Quantum-Classical Correspondence, arXiv:quant-ph/0211035 (2002).
- [124] E. P. Wigner, Characteristic Vectors of Bordered Matrices With Infinite Dimensions, *Annals of Mathematics* **62** (3), 548–564 (1955).
- [125] E. P. Wigner, Characteristics Vectors of Bordered Matrices with Infinite Dimensions II, *Annals of Mathematics* **65** (2), 203–207 (1957).
- [126] E. P. Wigner, On the Distribution of the Roots of Certain Symmetric Matrices, *Annals of Mathematics* **67** (2), 325–327 (1958).
- [127] E. P. Wigner, On the statistical distribution of the widths and spacings of nuclear resonance levels, *Mathematical Proceedings of the Cambridge Philosophical Society* **47** (4), 790–798 (1951).
- [128] F. J. Dyson, The Threelfold Way. Algebraic Structure of Symmetry Groups and Ensembles in Quantum Mechanics, *Journal of Mathematical Physics* **3** (6), 1199–1215 (1962).
- [129] A. Altland and M. R. Zirnbauer, Random Matrix Theory of a Chaotic Andreev Quantum Dot, *Physical Review Letters* **76** (18), 3420–3423 (1996).
- [130] A. Altland and M. R. Zirnbauer, Nonstandard symmetry classes in mesoscopic normal-superconducting hybrid structures, *Physical Review B* **55** (2), 1142–1161 (1997).
- [131] N. Rosenzweig and C. E. Porter, “Repulsion of Energy Levels” in Complex Atomic Spectra, *Physical Review* **120** (5), 1698–1714 (1960).
- [132] R. Ketzmerick, *Chaos and Quantum Chaos*, (2021) <https://tu-dresden.de/mn/physik/itp/cp/studium/lehrveranstaltungen/chaos-and-quantum-chaos-2021> (visited on 06/26/2022).
- [133] M. L. Mehta, *Random Matrices* (Elsevier, 2004).
- [134] F. Haake, *Quantum Signatures of Chaos*, 3. (Springer Berlin, Heidelberg, 2010).
- [135] A. A. Abul-Magd and A. Y. Abul-Magd, Unfolding of the Spectrum for Chaotic and Mixed Systems, *Physica A: Statistical Mechanics and its Applications* **396**, 185–194 (2014).
- [136] V. Oganesyan and D. A. Huse, Localization of interacting fermions at high temperature, *Physical Review B* **75** (15), 155111 (2007).

- [137] T. A. Brody, J. Flores, J. B. French, P. A. Mello, A. Pandey, and S. S. M. Wong, Random-matrix physics: spectrum and strength fluctuations, *Reviews of Modern Physics* **53** (3), 385–479 (1981).
- [138] J. B. French, P. A. Mello, and A. Pandey, Ergodic behavior in the statistical theory of nuclear reactions, *Physics Letters B* **80** (1), 17–19 (1978).
- [139] A. Pandey, Statistical properties of many-particle spectra: III. Ergodic behavior in random-matrix ensembles, *Annals of Physics* **119** (1), 170–191 (1979).
- [140] R. U. Haq, A. Pandey, and O. Bohigas, Fluctuation Properties of Nuclear Energy Levels: Do Theory and Experiment Agree?, *Physical Review Letters* **48** (16), 1086–1089 (1982).
- [141] O. Bohigas, M. J. Giannoni, and C. Schmit, Characterization of Chaotic Quantum Spectra and Universality of Level Fluctuation Laws, *Physical Review Letters* **52** (1), 1–4 (1984).
- [142] D. Wintgen and H. Friedrich, Classical and quantum-mechanical transition between regularity and irregularity in a Hamiltonian system, *Physical Review A* **35** (3), 1464–1466 (1987).
- [143] L. F. Santos and M. Rigol, Onset of quantum chaos in one-dimensional bosonic and fermionic systems and its relation to thermalization, *Physical Review E* **81** (3), 036206 (2010).
- [144] M. Krbálek and P. Seba, The statistical properties of the city transport in Cuernavaca (Mexico) and random matrix ensembles, *Journal of Physics A: Mathematical and General* **33** (26), L229 (2000).
- [145] M. V. Berry, Semiclassical theory of spectral rigidity, *Proceedings of the Royal Society of London. A. Mathematical and Physical Sciences* **400** (1819), 229–251 (1985).
- [146] E. B. Bogomolny, B. Georgeot, M.-J. Giannoni, and C. Schmit, Chaotic billiards generated by arithmetic groups, *Physical Review Letters* **69** (10), 1477–1480 (1992).
- [147] M. V. Berry and M. Tabor, Level clustering in the regular spectrum, *Proceedings of the Royal Society of London. A. Mathematical and Physical Sciences* **356** (1686), 375–394 (1977).
- [148] A. Pandey and R. Ramaswamy, Level spacings for harmonic-oscillator systems, *Physical Review A* **43** (8), 4237–4243 (1991).
- [149] Y. Alhassid, The statistical theory of quantum dots, *Reviews of Modern Physics* **72** (4), 895–968 (2000).
- [150] C. Neill et al., Ergodic dynamics and thermalization in an isolated quantum system, *Nature Physics* **12** (11), 1037–1041 (2016).
- [151] J. R. Garrison and T. Grover, Does a Single Eigenstate Encode the Full Hamiltonian?, *Physical Review X* **8** (2), 021026 (2018).
- [152] M. Srednicki, The approach to thermal equilibrium in quantized chaotic systems, *Journal of Physics A: Mathematical and General* **32** (7), 1163–1175 (1999).
- [153] M. Rigol, Breakdown of Thermalization in Finite One-Dimensional Systems, *Physical Review Letters* **103** (10), 100403 (2009).
- [154] M. Rigol, V. Dunjko, and M. Olshanii, Thermalization and its mechanism for generic isolated quantum systems, *Nature* **452** (7189), 854–858 (2008).

- [155] L. C. Venuti and L. Liu, Ergodicity, eigenstate thermalization, and the foundations of statistical mechanics in quantum and classical systems, arXiv:1904.02336 (2019).
- [156] M. V. Berry, Regular and irregular semiclassical wavefunctions, *Journal of Physics A: Mathematical and General* **10** (12), 2083–2091 (1977).
- [157] J. T. Edwards and D. J. Thouless, Numerical studies of localization in disordered systems, *Journal of Physics C: Solid State Physics* **5** (8), 807–820 (1972).
- [158] P. W. Anderson, Absence of Diffusion in Certain Random Lattices, *Physical Review* **109** (5), 1492–1505 (1958).
- [159] L. Fleishman and P. W. Anderson, Interactions and the Anderson transition, *Physical Review B* **21** (6), 2366–2377 (1980).
- [160] P. Jordan and E. Wigner, Über das Paulische Äquivalenzverbot, *Zeitschrift für Physik* **47** (9), 631–651 (1928).
- [161] Y. Bar Lev, D. R. Reichman, and Y. Sagi, Many-body localization in system with a completely delocalized single-particle spectrum, *Physical Review B* **94** (20), 201116 (2016).
- [162] A. Pal and D. A. Huse, Many-body localization phase transition, *Physical Review B* **82** (17), 174411 (2010).
- [163] M. Žnidarič, T. Prosen, and P. Prelovšek, Many-body localization in the Heisenberg XXZ magnet in a random field, *Physical Review B* **77** (6), 064426 (2008).
- [164] D. J. Luitz, N. Laflorencie, and F. Alet, Many-body localization edge in the random-field Heisenberg chain, *Physical Review B* **91** (8), 081103 (2015).
- [165] M. Serbyn, Z. Papić, and D. A. Abanin, Local Conservation Laws and the Structure of the Many-Body Localized States, *Physical Review Letters* **111** (12), 127201 (2013).
- [166] D. A. Huse, R. Nandkishore, and V. Oganesyan, Phenomenology of fully many-body-localized systems, *Physical Review B* **90** (17), 174202 (2014).
- [167] M. Serbyn, Z. Papić, and D. A. Abanin, Universal Slow Growth of Entanglement in Interacting Strongly Disordered Systems, *Physical Review Letters* **110** (26), 260601 (2013).
- [168] L. Rademaker, M. Ortuño, and A. M. Somoza, Many-body localization from the perspective of Integrals of Motion, *Annalen der Physik* **529** (7), 1600322 (2017).
- [169] J. Z. Imbrie, On Many-Body Localization for Quantum Spin Chains, *Journal of Statistical Physics* **163** (5), 998–1048 (2016).
- [170] J. Z. Imbrie, Diagonalization and Many-Body Localization for a Disordered Quantum Spin Chain, *Physical Review Letters* **117** (2), 027201 (2016).
- [171] J. Z. Imbrie, V. Ros, and A. Scardicchio, Local integrals of motion in many-body localized systems, *Annalen der Physik* **529** (7), 1600278 (2017).
- [172] L. D. Faddeev, “How algebraic Bethe ansatz works for integrable model”, in *Les Houches School of Physics: Astrophysical Sources of Gravitational Radiation* (1996), pp. 149–219.
- [173] B. Sutherland, *Beautiful Models* (World Scientific, Singapore, 2007).
- [174] J. Šuntajs, J. Bonča, T. Prosen, and L. Vidmar, Quantum chaos challenges many-body localization, *Physical Review E* **102** (6), 062144 (2020).
- [175] V. Ros, M. Müller, and A. Scardicchio, Integrals of motion in the many-body localized phase, *Nuclear Physics B* **891**, 420–465 (2015).

- [176] X. Zotos, F. Naef, and P. Prelovsek, Transport and conservation laws, *Physical Review B* **55** (17), 11029–11032 (1997).
- [177] M. Žnidarič, A. Scardicchio, and V. K. Varma, Diffusive and Subdiffusive Spin Transport in the Ergodic Phase of a Many-Body Localizable System, *Physical Review Letters* **117** (4), 040601 (2016).
- [178] B. Bauer and C. Nayak, Area laws in a many-body localized state and its implications for topological order, *Journal of Statistical Mechanics: Theory and Experiment* **2013** (09), P09005 (2013).
- [179] J. A. Kjäll, J. H. Bardarson, and F. Pollmann, Many-Body Localization in a Disordered Quantum Ising Chain, *Physical Review Letters* **113** (10), 107204 (2014).
- [180] M. Serbyn, A. A. Michailidis, D. A. Abanin, and Z. Papić, Power-Law Entanglement Spectrum in Many-Body Localized Phases, *Physical Review Letters* **117** (16), 160601 (2016).
- [181] R. Singh, J. H. Bardarson, and F. Pollmann, Signatures of the many-body localization transition in the dynamics of entanglement and bipartite fluctuations, *New Journal of Physics* **18** (2), 023046 (2016).
- [182] H. F. Song, S. Rachel, C. Flindt, I. Klich, N. Laflorencie, and K. Le Hur, Bipartite fluctuations as a probe of many-body entanglement, *Physical Review B* **85** (3), 035409 (2012).
- [183] T. Orell, A. A. Michailidis, M. Serbyn, and M. Silveri, Probing many-body localization phase transition with superconducting circuits, *Physical Review B* **100** (13), 134504 (2019).
- [184] H. Kim and D. A. Huse, Ballistic Spreading of Entanglement in a Diffusive Nonintegrable System, *Physical Review Letters* **111** (12), 127205 (2013).
- [185] A. Nanduri, H. Kim, and D. A. Huse, Entanglement spreading in a many-body localized system, *Physical Review B* **90** (6), 064201 (2014).
- [186] M. Serbyn, Z. Papić, and D. A. Abanin, Quantum quenches in the many-body localized phase, *Physical Review B* **90** (17), 174302 (2014).
- [187] M. Serbyn, M. Knap, S. Gopalakrishnan, Z. Papić, N. Y. Yao, C. R. Laumann, D. A. Abanin, M. D. Lukin, and E. A. Demler, Interferometric Probes of Many-Body Localization, *Physical Review Letters* **113** (14), 147204 (2014).
- [188] V. Ros and M. Müller, Remanent Magnetization: Signature of Many-Body Localization in Quantum Antiferromagnets, *Physical Review Letters* **118** (23), 237202 (2017).
- [189] B. L. Altshuler, Y. Gefen, A. Kamenev, and L. S. Levitov, Quasiparticle Lifetime in a Finite System: A Nonperturbative Approach, *Physical Review Letters* **78** (14), 2803–2806 (1997).
- [190] A. D. Luca and A. Scardicchio, Ergodicity breaking in a model showing many-body localization, *EPL (Europhysics Letters)* **101** (3), 37003 (2013).
- [191] N. Macé, F. Alet, and N. Laflorencie, Multifractal Scalings Across the Many-Body Localization Transition, *Physical Review Letters* **123** (18), 180601 (2019).
- [192] M. Pino, L. B. Ioffe, and B. L. Altshuler, Nonergodic metallic and insulating phases of Josephson junction chains, *Proceedings of the National Academy of Sciences* **113** (3), 536–541 (2016).

- [193] M. Pino, V. E. Kravtsov, B. L. Altshuler, and L. B. Ioffe, Multifractal metal in a disordered Josephson junctions array, *Physical Review B* **96** (21), 214205 (2017).
- [194] M. Serbyn, Z. Papić, and D. A. Abanin, Thouless energy and multifractality across the many-body localization transition, *Physical Review B* **96** (10), 104201 (2017).
- [195] W. De Roeck and J. Z. Imbrie, Many-body localization: stability and instability, *Philosophical Transactions of the Royal Society A: Mathematical, Physical and Engineering Sciences* **375** (2108), 20160422 (2017).
- [196] W. De Roeck and F. Huveneers, Stability and instability towards delocalization in many-body localization systems, *Physical Review B* **95** (15), 155129 (2017).
- [197] A. Chandran, A. Pal, C. R. Laumann, and A. Scardicchio, Many-body localization beyond eigenstates in all dimensions, *Physical Review B* **94** (14), 144203 (2016).
- [198] W. De Roeck, F. Huveneers, M. Müller, and M. Schiulaz, Absence of many-body mobility edges, *Physical Review B* **93** (1), 014203 (2016).
- [199] M. Kiefer-Emmanouilidis, R. Unanyan, M. Fleischhauer, and J. Sirker, Slow delocalization of particles in many-body localized phases, *Physical Review B* **103** (2), 024203 (2021).
- [200] D. Sels and A. Polkovnikov, Dynamical obstruction to localization in a disordered spin chain, *Physical Review E* **104** (5), 054105 (2021).
- [201] D. A. Abanin, J. H. Bardarson, G. De Tomasi, S. Gopalakrishnan, V. Khemani, S. A. Parameswaran, F. Pollmann, A. C. Potter, M. Serbyn, and R. Vasseur, Distinguishing localization from chaos: Challenges in finite-size systems, *Annals of Physics* **427**, 168415 (2021).
- [202] R. K. Panda, A. Scardicchio, M. Schulz, S. R. Taylor, and M. Žnidarič, Can we study the many-body localisation transition?, *EPL (Europhysics Letters)* **128** (6), 67003 (2020).
- [203] P. Sierant and J. Zakrzewski, Challenges to observation of many-body localization, *Physical Review B* **105** (22), 224203 (2022).
- [204] A. Morningstar, L. Colmenarez, V. Khemani, D. J. Luitz, and D. A. Huse, Avalanches and many-body resonances in many-body localized systems, *Physical Review B* **105** (17), 174205 (2022).
- [205] D. Sels and A. Polkovnikov, Thermalization of dilute impurities in one-dimensional spin chains, *Phys. Rev. X* **13** (1), 011041 (2023).
- [206] I. Bloch, J. Dalibard, and W. Zwerger, Many-body physics with ultracold gases, *Reviews of Modern Physics* **80** (3), 885–964 (2008).
- [207] R. Blatt and C. F. Roos, Quantum simulations with trapped ions, *Nature Physics* **8** (4), 277–284 (2012).
- [208] M. Schreiber, S. S. Hodgman, P. Bordia, H. P. Lüschen, M. H. Fischer, R. Vosk, E. Altman, U. Schneider, and Immanuel Bloch, Observation of many-body localization of interacting fermions in a quasirandom optical lattice, *Science* **349** (6250), 842–845 (2015).
- [209] J. Smith, A. Lee, P. Richerme, B. Neyenhuis, P. W. Hess, P. Hauke, M. Heyl, D. A. Huse, and C. Monroe, Many-body localization in a quantum simulator with programmable random disorder, *Nature Physics* **12** (10), 907–911 (2016).
- [210] K. Xu et al., Emulating Many-Body Localization with a Superconducting Quantum Processor, *Physical Review Letters* **120** (5), 050507 (2018).

- [211] P. Roushan et al., Spectroscopic signatures of localization with interacting photons in superconducting qubits, *Science* **358** (6367), 1175–1179 (2017).
- [212] A. Lukin, M. Rispoli, R. Schittko, M. E. Tai, A. M. Kaufman, S. Choi, V. Khemani, J. Léonard, and M. Greiner, Probing entanglement in a many-body-localized system, *Science* **364** (6437), 256–260 (2019).
- [213] D. Roy, R. Singh, and R. Moessner, Probing many-body localization by spin noise spectroscopy, *Physical Review B* **92** (18), 180205 (2015).
- [214] G. De Tomasi, S. Bera, J. H. Bardarson, and F. Pollmann, Quantum Mutual Information as a Probe for Many-Body Localization, *Physical Review Letters* **118** (1), 016804 (2017).
- [215] S. A. Parameswaran, A. C. Potter, and R. Vasseur, Eigenstate phase transitions and the emergence of universal dynamics in highly excited states, *Annalen der Physik* **529** (7), 1600302 (2017).
- [216] D. A. Huse, R. Nandkishore, V. Oganesyan, A. Pal, and S. L. Sondhi, Localization-protected quantum order, *Physical Review B* **88** (1), 014206 (2013).
- [217] A. C. Potter and R. Vasseur, Symmetry constraints on many-body localization, *Physical Review B* **94** (22), 224206 (2016).
- [218] A. Lazarides, A. Das, and R. Moessner, Fate of Many-Body Localization Under Periodic Driving, *Physical Review Letters* **115** (3), 030402 (2015).
- [219] D. A. Abanin, W. De Roeck, and F. Huveneers, Theory of many-body localization in periodically driven systems, *Annals of Physics* **372**, 1–11 (2016).
- [220] R. Vosk and E. Altman, Many-Body Localization in One Dimension as a Dynamical Renormalization Group Fixed Point, *Physical Review Letters* **110** (6), 067204 (2013).
- [221] B. Swingle, Unscrambling the physics of out-of-time-order correlators, *Nature Physics* **14** (10), 988–990 (2018).
- [222] Y. Huang, Y.-L. Zhang, and X. Chen, Out-of-time-ordered correlators in many-body localized systems, *Annalen der Physik* **529** (7), 1600318 (2017).
- [223] A. Blais, A. L. Grimsmo, S. M. Girvin, and A. Wallraff, Circuit quantum electrodynamics, *Reviews of Modern Physics* **93** (2), 025005 (2021).
- [224] S. M. Girvin, “Circuit QED: superconducting qubits coupled to microwave photons”, in *Quantum machines: measurement and control of engineered quantum systems*, edited by M. H. Devoret, B. Huard, R. Schoelkopf, and L. F. Cugliandolo (Oxford University Press, 2014), pp. 113–255.
- [225] M. Tinkham, *Introduction to Superconductivity* (Dover Publications, 2004).
- [226] V. Ambegaokar and A. Baratoff, Tunneling Between Superconductors, *Physical Review Letters* **10** (11), 486–489 (1963).
- [227] D. Vion, A. Aassime, A. Cottet, P. Joyez, H. Pothier, C. Urbina, D. Esteve, and M. H. Devoret, Manipulating the Quantum State of an Electrical Circuit, *Science* **296** (5569), 886–889 (2002).
- [228] E. Collin, G. Ithier, A. Aassime, P. Joyez, D. Vion, and D. Esteve, NMR-like Control of a Quantum Bit Superconducting Circuit, *Physical Review Letters* **93** (15), 157005 (2004).
- [229] J. M. Chow et al., Universal Quantum Gate Set Approaching Fault-Tolerant Thresholds with Superconducting Qubits, *Physical Review Letters* **109** (6), 060501 (2012).

- [230] J. B. Chang et al., Improved superconducting qubit coherence using titanium nitride, *Applied Physics Letters* **103** (1), 012602 (2013).
- [231] R. Barends et al., Coherent Josephson Qubit Suitable for Scalable Quantum Integrated Circuits, *Physical Review Letters* **111** (8), 080502 (2013).
- [232] J. M. Martinis and A. Megrant, UCSB final report for the CSQ program: Review of decoherence and materials physics for superconducting qubits, arXiv:1410.5793 (2014).
- [233] R. Barends et al., Digitized adiabatic quantum computing with a superconducting circuit, *Nature* **534** (7606), 222–226 (2016).
- [234] H. Paik et al., Observation of High Coherence in Josephson Junction Qubits Measured in a Three-Dimensional Circuit QED Architecture, *Physical Review Letters* **107** (24), 240501 (2011).
- [235] C. Rigetti et al., Superconducting qubit in a waveguide cavity with a coherence time approaching 0.1 ms, *Physical Review B* **86** (10), 100506 (2012).
- [236] M. Steffen, Superconducting Qubits Are Getting Serious, *Physics* **4**, 103 (2011).
- [237] X. Y. Jin et al., Thermal and Residual Excited-State Population in a 3D Transmon Qubit, *Physical Review Letters* **114** (24), 240501 (2015).
- [238] A. Blais, R.-S. Huang, A. Wallraff, S. M. Girvin, and R. J. Schoelkopf, Cavity quantum electrodynamics for superconducting electrical circuits: An architecture for quantum computation, *Physical Review A* **69** (6), 062320 (2004).
- [239] A. Wallraff, D. I. Schuster, A. Blais, L. Frunzio, R.-S. Huang, J. Majer, S. Kumar, S. M. Girvin, and R. J. Schoelkopf, Strong coupling of a single photon to a superconducting qubit using circuit quantum electrodynamics, *Nature* **431** (7005), 162–167 (2004).
- [240] L. Casparis, T. W. Larsen, M. S. Olsen, F. Kuemmeth, P. Krogstrup, J. Nygård, K. D. Petersson, and C. M. Marcus, Gate-on Benchmarking and Two-Qubit Operations, *Physical Review Letters* **116** (15), 150505 (2016).
- [241] G. de Lange, B. van Heck, A. Bruno, D. J. van Woerkom, A. Geresdi, S. R. Plissard, E. P. A. M. Bakkers, A. R. Akhmerov, and L. DiCarlo, Realization of Microwave Quantum Circuits Using Hybrid Superconducting-Semiconducting Nanowire Josephson Elements, *Physical Review Letters* **115** (12), 127002 (2015).
- [242] J. M. Nichol, Wiring Up Superconducting Qubits, *Physics* **8**, 87 (2015).
- [243] T. W. Larsen, K. D. Petersson, F. Kuemmeth, T. S. Jespersen, P. Krogstrup, J. Nygård, and C. M. Marcus, Semiconductor-Nanowire-Based Superconducting Qubit, *Physical Review Letters* **115** (12), 127001 (2015).
- [244] G. Wendin, Quantum information processing with superconducting circuits: a review, *Reports on Progress in Physics* **80** (10), 106001 (2017).
- [245] U. Vool and M. H. Devoret, Introduction to Quantum Electromagnetic Circuits, *International Journal of Circuit Theory and Applications* **45** (7), 897–934 (2017).
- [246] X. Gu, A. F. Kockum, A. Miranowicz, Y.-X. Liu, and F. Nori, Microwave photonics with superconducting quantum circuits, *Physics Reports* **718–719**, 1–102 (2017).
- [247] B. Yurke and J. S. Denker, Quantum network theory, *Physical Review A* **29** (3), 1419–1437 (1984).

- [248] G. Burkard, R. H. Koch, and D. P. DiVincenzo, Multilevel quantum description of decoherence in superconducting qubits, *Physical Review B* **69** (6), 064503 (2004).
- [249] M. D. Hutchings, J. B. Hertzberg, Y. Liu, N. T. Bronn, G. A. Keefe, M. Brink, J. M. Chow, and B. L. T. Plourde, Tunable Superconducting Qubits with Flux-Independent Coherence, *Physical Review Applied* **8** (4), 044003 (2017).
- [250] M. A. Rol et al., Fast, High-Fidelity Conditional-Phase Gate Exploiting Leakage Interference in Weakly Anharmonic Superconducting Qubits, *Physical Review Letters* **123** (12), 120502 (2019).
- [251] M. A. Rol, L. Ciorciaro, F. K. Malinowski, B. M. Tarasinski, R. E. Sagastizabal, C. C. Bultink, Y. Salathe, N. Haandbaek, J. Sedivy, and L. DiCarlo, Time-domain characterization and correction of on-chip distortion of control pulses in a quantum processor, *Applied Physics Letters* **116** (5), 054001 (2020).
- [252] J. M. Gambetta, “Control of Superconducting Qubits”, in *Quantum information processing: lecture notes of the 44th IFF Spring School 2013*, edited by D. DiVincenzo, Bd. 52 (Forschungszentrum Jülich, 2013), B4.1–B4.50.
- [253] M. Metcalfe, E. Boaknin, V. Manucharyan, R. Vijay, I. Siddiqi, C. Rigetti, L. Frunzio, R. J. Schoelkopf, and M. H. Devoret, Measuring the decoherence of a quantronium qubit with the cavity bifurcation amplifier, *Physical Review B* **76** (17), 174516 (2007).
- [254] S. Goldstein, XVII.—On the Asymptotic Expansion of the Characteristic Numbers of the Mathieu Equation, *Proceedings of the Royal Society of Edinburgh* **49**, 210–223 (1930).
- [255] J. N. L. Connor, T. Uzer, R. A. Marcus, and A. D. Smith, Eigenvalues of the Schrödinger equation for a periodic potential with nonperiodic boundary conditions: A uniform semiclassical analysis, *The Journal of Chemical Physics* **80** (10), 5095–5106 (1984).
- [256] A. A. Houck, J. Koch, M. H. Devoret, S. M. Girvin, and R. J. Schoelkopf, Life after charge noise: recent results with transmon qubits, *Quantum Information Processing* **8** (2), 105–115 (2009).
- [257] F. W. J. Olver, A. B. Olde Daalhuis, D. W. Lozier, B. I. Schneider, R. F. Boisvert, C. W. Clark, B. R. Miller, B. V. S. H. S. Cohl, and M. A. McClain, eds., NIST Digital Library of Mathematical Functions, <http://dlmf.nist.gov/>, Release 1.1.2 of 2021-06-15.
- [258] É. Mathieu, Mémoire sur le mouvement vibratoire d'une membrane de forme elliptique. *Journal de Mathématiques Pures et Appliquées* **13**, 137–203 (1868).
- [259] N. W. McLachlan, Theory and application of Mathieu Functions, Publisher to the University Geoffrey Cumberlege, Oxford University Press (1951).
- [260] D. J. Daniel, Exact solutions of Mathieu's equation, *Progress of Theoretical and Experimental Physics* **2020** (4) (2020).
- [261] J. Meixner, F. W. Schäfke, and G. Wolf, *Mathieu Functions and Spheroidal Functions and their Mathematical Foundations: Further Studies* (Springer-Verlag, 1980).
- [262] Cottet, Audrey, *Implementation of a quantum bit in a superconducting qubit*, PhD Thesis (Université Paris VI, 2002).
- [263] W. R. Inc., Mathematica, Version 13.0.0, Champaign, IL, 2021.
- [264] L. Fousse, G. Hanrot, V. Lefèvre, P. Péllissier, and P. Zimmermann, MPFR: A multiple-precision binary floating-point library with correct rounding, *ACM Transactions on Mathematical Software* **33** (2), 13–es (2007).

- [265] D. T. Sank, *Fast, Accurate State Measurement in Superconducting Qubits*, PhD Thesis (University of California, Santa Barbara, 2014).
- [266] J. M. Chow, L. DiCarlo, J. M. Gambetta, F. Motzoi, L. Frunzio, S. M. Girvin, and R. J. Schoelkopf, Optimized driving of superconducting artificial atoms for improved single-qubit gates, *Physical Review A* **82** (4), 040305 (2010).
- [267] Z. Chen et al., Measuring and Suppressing Quantum State Leakage in a Superconducting Qubit, *Physical Review Letters* **116** (2), 020501 (2016).
- [268] H. Bernien et al., Probing many-body dynamics on a 51-atom quantum simulator, *Nature* **551** (7682), 579–584 (2017).
- [269] G. Wendin and V. S. Shumeiko, Quantum bits with Josephson junctions, *Low Temperature Physics* **33** (9), 724–744 (2007).
- [270] A. Blais, J. Gambetta, A. Wallraff, D. I. Schuster, S. M. Girvin, M. H. Devoret, and R. J. Schoelkopf, Quantum-information processing with circuit quantum electrodynamics, *Physical Review A* **75** (3), 032329 (2007).
- [271] J. Majer et al., Coupling superconducting qubits via a cavity bus, *Nature* **449** (7161), 443–447 (2007).
- [272] F. Yan, P. Krantz, Y. Sung, M. Kjaergaard, D. L. Campbell, T. P. Orlando, S. Gustavsson, and W. D. Oliver, Tunable Coupling Scheme for Implementing High-Fidelity Two-Qubit Gates, *Physical Review Applied* **10** (5), 054062 (2018).
- [273] A. Blais, A. M. van den Brink, and A. M. Zagoskin, Tunable Coupling of Superconducting Qubits, *Physical Review Letters* **90** (12), 127901 (2003).
- [274] T. Hime, P. A. Reichardt, B. L. T. Plourde, T. L. Robertson, C.-E. Wu, A. V. Ustinov, and J. Clarke, Solid-State Qubits with Current-Controlled Coupling, *Science* **314** (5804), 1427–1429 (2006).
- [275] R. C. Bialczak et al., Fast Tunable Coupler for Superconducting Qubits, *Physical Review Letters* **106** (6), 060501 (2011).
- [276] Y. Chen et al., Qubit Architecture with High Coherence and Fast Tunable Coupling, *Physical Review Letters* **113** (22), 220502 (2014).
- [277] S. Bravyi, D. DiVincenzo, and D. Loss, Schrieffer-Wolff transformation for quantum many-body systems, *Annals of Physics* **326** (10), 2793–2826 (2011).
- [278] Y. Xu et al., High-Fidelity, High-Scalability Two-Qubit Gate Scheme for Superconducting Qubits, *Physical Review Letters* **125** (24), 240503 (2020).
- [279] M. C. Collodo, J. Herrmann, N. Lacroix, C. K. Andersen, A. Remm, S. Lazar, J.-C. Besse, T. Walter, A. Wallraff, and C. Eichler, Implementation of Conditional Phase Gates Based on Tunable ZZ Interactions, *Physical Review Letters* **125** (24), 240502 (2020).
- [280] C. Leroux, A. Di Paolo, and A. Blais, Superconducting Coupler with Exponentially Large On:Off Ratio, *Physical Review Applied* **16** (6), 064062 (2021).
- [281] F. Beaudoin, M. P. da Silva, Z. Dutton, and A. Blais, First-order sidebands in circuit QED using qubit frequency modulation, *Physical Review A* **86** (2), 022305 (2012).
- [282] G. Burkard, D. Loss, D. P. DiVincenzo, and J. A. Smolin, Physical optimization of quantum error correction circuits, *Physical Review B* **60** (16), 11404–11416 (1999).

- [283] R. C. Bialczak et al., Quantum process tomography of a universal entangling gate implemented with Josephson phase qubits, *Nature Physics* **6** (6), 409–413 (2010).
- [284] L. DiCarlo et al., Demonstration of two-qubit algorithms with a superconducting quantum processor, *Nature* **460** (7252), 240–244 (2009).
- [285] G. S. Paraoanu, Microwave-induced coupling of superconducting qubits, *Physical Review B* **74** (14), 140504 (2006).
- [286] C. Rigetti and M. Devoret, Fully microwave-tunable universal gates in superconducting qubits with linear couplings and fixed transition frequencies, *Physical Review B* **81** (13), 134507 (2010).
- [287] J. C. Pommerening, *Multiqubit Coupling Dynamics and the Cross-Resonance Gate*, Master Thesis (RWTH Aachen, 2017).
- [288] J. M. Chow et al., Simple All-Microwave Entangling Gate for Fixed-Frequency Superconducting Qubits, *Physical Review Letters* **107** (8), 080502 (2011).
- [289] J. Zhang, J. Vala, S. Sastry, and K. B. Whaley, Geometric theory of nonlocal two-qubit operations, *Physical Review A* **67** (4), 042313 (2003).
- [290] M. Malekakhlagh, E. Magesan, and D. C. McKay, First-principles analysis of cross-resonance gate operation, *Physical Review A* **102** (4), 042605 (2020).
- [291] E. Magesan and J. M. Gambetta, Effective Hamiltonian models of the cross-resonance gate, *Physical Review A* **101** (5), 052308 (2020).
- [292] V. Tripathi, M. Khezri, and A. N. Korotkov, Operation and intrinsic error budget of a two-qubit cross-resonance gate, *Physical Review A* **100** (1), 012301 (2019).
- [293] M. Ware, B. R. Johnson, J. M. Gambetta, T. A. Ohki, J. M. Chow, and B. L. T. Plourde, Cross-resonance interactions between superconducting qubits with variable detuning, arXiv:1905.11480 (2019).
- [294] J. B. Hertzberg et al., Laser-annealing Josephson junctions for yielding scaled-up superconducting quantum processors, *npj Quantum Information* **7** (1), 1–8 (2021).
- [295] R. Versluis, S. Poletto, N. Khammassi, B. Tarasinski, N. Haider, D. J. Michalak, A. Bruno, K. Bertels, and L. DiCarlo, Scalable Quantum Circuit and Control for a Superconducting Surface Code, *Physical Review Applied* **8** (3), 034021 (2017).
- [296] J. Gambetta, *IBM’s roadmap for scaling quantum technology*, IBM Research Blog, (2021) <https://research.ibm.com/blog/ibm-quantum-roadmap> (visited on 05/20/2022).
- [297] J. Gambetta, *Expanding the IBM Quantum Roadmap to anticipate the future of quantum-centric supercomputing*, IBM Research Blog, (2022) <https://research.ibm.com/blog/ibm-quantum-roadmap-2025> (visited on 05/20/2022).
- [298] N. Sundaresan, I. Lauer, E. Pritchett, E. Magesan, P. Jurcevic, and J. M. Gambetta, Reducing Unitary and Spectator Errors in Cross Resonance with Optimized Rotary Echoes, *PRX Quantum* **1** (2), 020318 (2020).
- [299] M. Takita, A. D. Córcoles, E. Magesan, B. Abdo, M. Brink, A. Cross, J. M. Chow, and J. M. Gambetta, Demonstration of Weight-Four Parity Measurements in the Surface Code Architecture, *Physical Review Letters* **117** (21), 210505 (2016).
- [300] S. Kirchhoff, T. Keßler, P. J. Liebermann, E. Assémat, S. Machnes, F. Motzoi, and F. K. Wilhelm, Optimized cross-resonance gate for coupled transmon systems, *Physical Review A* **97** (4), 042348 (2018).

- [301] J. M. Gambetta, J. M. Chow, and M. Steffen, Building logical qubits in a superconducting quantum computing system, *npj Quantum Information* **3** (1), 1–7 (2017).
- [302] S. Rosenblatt et al., “Variability metrics in Josephson Junction fabrication for Quantum Computing circuits”, in Aps march meeting abstracts, Vol. 2017 (2017), Y46.002.
- [303] <https://github.com/qiskit/qiskit-terra>.
- [304] J. M. Kreikebaum, K. P. O’Brien, A. Morvan, and I. Siddiqi, Improving wafer-scale Josephson junction resistance variation in superconducting quantum coherent circuits, *Superconductor Science and Technology* **33** (6), 06LT02 (2020).
- [305] A. Smith, M. S. Kim, F. Pollmann, and J. Knolle, Simulating quantum many-body dynamics on a current digital quantum computer, *npj Quantum Information* **5** (1), 1–13 (2019).
- [306] C. Chamberland, G. Zhu, T. J. Yoder, J. B. Hertzberg, and A. W. Cross, Topological and Subsystem Codes on Low-Degree Graphs with Flag Qubits, *Physical Review X* **10** (1), 011022 (2020).
- [307] P. Nation, H. Paik, A. Cross, and Z. Nazario, *The IBM Quantum heavy hex lattice*, IBM Research Blog, (2021) <https://research.ibm.com/blog/heavy-hex-lattice> (visited on 05/20/2022).
- [308] E. J. Zhang et al., High-performance superconducting quantum processors via laser annealing of transmon qubits, *Science Advances* **8** (19), eabi6690 (2022).
- [309] A. Wack, H. Paik, A. Javadi-Abhari, P. Jurcevic, I. Faro, J. M. Gambetta, and B. R. Johnson, Quality, Speed, and Scale: three key attributes to measure the performance of near-term quantum computers, arXiv:2110.14108 (2021).
- [310] A. W. Cross, L. S. Bishop, S. Sheldon, P. D. Nation, and J. M. Gambetta, Validating quantum computers using randomized model circuits, *Physical Review A* **100** (3), 032328 (2019).
- [311] P. Jurcevic et al., Demonstration of quantum volume 64 on a superconducting quantum computing system, *Quantum Science and Technology* **6** (2), 025020 (2021).
- [312] J. M. Chávez-Garcia, F. Solgun, J. B. Hertzberg, O. Jinka, M. Brink, and B. Abdo, Weakly Flux-Tunable Superconducting Qubit, *Physical Review Applied* **18** (3), 034057 (2022).
- [313] K. X. Wei et al., Hamiltonian Engineering with Multicolor Drives for Fast Entangling Gates and Quantum Crosstalk Cancellation, *Physical Review Letters* **129** (6), 060501 (2022).
- [314] B. K. Mitchell, R. K. Naik, A. Morvan, A. Hashim, J. M. Kreikebaum, B. Marinelli, W. Lavrijsen, K. Nowrouzi, D. I. Santiago, and I. Siddiqi, Hardware-Efficient Microwave-Activated Tunable Coupling between Superconducting Qubits, *Physical Review Letters* **127** (20), 200502 (2021).
- [315] A. Morvan, L. Chen, J. M. Larson, D. I. Santiago, and I. Siddiqi, Optimizing frequency allocation for fixed-frequency superconducting quantum processors, *Physical Review Research* **4** (2), 023079 (2022).
- [316] M. Kjaergaard et al., Demonstration of density matrix exponentiation using a superconducting quantum processor, *Phys. Rev. X* **12** (1), 011005 (2022).

- [317] C. K. Andersen, A. Remm, S. Lazar, S. Krinner, J. Heinsoo, J.-C. Besse, M. Gabureac, A. Wallraff, and C. Eichler, Entanglement stabilization using ancilla-based parity detection and real-time feedback in superconducting circuits, *npj Quantum Information* **5** (1), 1–7 (2019).
- [318] V. Negîrneac et al., High-Fidelity Controlled- Z Gate with Maximal Intermediate Leakage Operating at the Speed Limit in a Superconducting Quantum Processor, *Physical Review Letters* **126** (22), 220502 (2021).
- [319] B. Foxen et al. (Google AI Quantum), Demonstrating a continuous set of two-qubit gates for near-term quantum algorithms, *Phys. Rev. Lett.* **125** (12), 120504 (2020).
- [320] C. J. Neill, *A path towards quantum supremacy with superconducting qubits*, PhD Thesis (University of California, Santa Barbara, 2017).
- [321] M. Serbyn and J. E. Moore, Spectral statistics across the many-body localization transition, *Physical Review B* **93** (4), 041424 (2016).
- [322] Y. Y. Atas, E. Bogomolny, O. Giraud, and G. Roux, Distribution of the Ratio of Consecutive Level Spacings in Random Matrix Ensembles, *Physical Review Letters* **110** (8), 084101 (2013).
- [323] E. Cuevas, M. Feigel'man, L. Ioffe, and M. Mezard, Level statistics of disordered spin-1/2 systems and materials with localized Cooper pairs, *Nature Communications* **3** (1), 1128 (2012).
- [324] C. R. Laumann, A. Pal, and A. Scardicchio, Many-Body Mobility Edge in a Mean-Field Quantum Spin Glass, *Physical Review Letters* **113** (20), 200405 (2014).
- [325] F. Monteiro, T. Micklitz, M. Tezuka, and A. Altland, Minimal model of many-body localization, *Physical Review Research* **3** (1), 013023 (2021).
- [326] S. Kullback and R. A. Leibler, On Information and Sufficiency, *The Annals of Mathematical Statistics* (1951).
- [327] J. M. Joyce, Kullback-Leibler Divergence, in *International Encyclopedia of Statistical Science*, edited by M. Lovric (Springer, 2011), pp. 720–722.
- [328] M. Mézard and A. Montanari, *Information, Physics, and Computation* (Oxford University Press, 2009).
- [329] J. Kelly, Z. Chen, B. Chiaro, B. Foxen, and J. M. Martinis, Operating and characterizing of a 72 superconducting qubit processor “Bristlecone”: part 1, *Bulletin of the American Physical Society* **64** (2) (2013).
- [330] K. Kudo and T. Deguchi, Finite-size scaling with respect to interaction and disorder strength at the many-body localization transition, *Physical Review B* **97** (22), 220201 (2018).
- [331] C. L. Bertrand and A. M. García-García, Anomalous Thouless energy and critical statistics on the metallic side of the many-body localization transition, *Physical Review B* **94** (14), 144201 (2016).
- [332] T. Devakul and R. R. P. Singh, Early Breakdown of Area-Law Entanglement at the Many-Body Delocalization Transition, *Physical Review Letters* **115** (18), 187201 (2015).
- [333] E. V. H. Doggen, I. V. Gornyi, A. D. Mirlin, and D. G. Polyakov, Many-body localization in large systems: Matrix-product-state approach, *Annals of Physics* **435**, 168437 (2021).

- [334] P. Sierant, D. Delande, and J. Zakrzewski, Thouless Time Analysis of Anderson and Many-Body Localization Transitions, *Physical Review Letters* **124** (18), 186601 (2020).
- [335] J. Braumüller et al., Probing quantum information propagation with out-of-time-ordered correlators, *Nature Physics* **18** (2), 172–178 (2022).
- [336] R. Winik et al., Cancellation of unwanted ZZ interactions for cross-resonance gates by superconducting qubit engineering, *2021*, P28.013 (2021).
- [337] J. Ku, X. Xu, M. Brink, D. C. McKay, J. B. Hertzberg, M. H. Ansari, and B. L. T. Plourde, Suppression of Unwanted ZZ Interactions in a Hybrid Two-Qubit System, *Physical Review Letters* **125** (20), 200504 (2020).
- [338] J. Long et al., A universal quantum gate set for transmon qubits with strong ZZ interactions, arXiv:2103.12305 (2021).
- [339] A. Kandala, K. X. Wei, S. Srinivasan, E. Magesan, S. Carnevale, G. A. Keefe, D. Klaus, O. Dial, and D. C. McKay, Demonstration of a High-Fidelity CNOT Gate for Fixed-Frequency Transmons with Engineered ZZ Suppression, *Physical Review Letters* **127** (13), 130501 (2021).
- [340] P. Zhao, P. Xu, D. Lan, J. Chu, X. Tan, H. Yu, and Y. Yu, High-Contrast ZZ Interaction Using Superconducting Qubits with Opposite-Sign Anharmonicity, *Physical Review Letters* **125** (20), 200503 (2020).
- [341] P. Mundada, G. Zhang, T. Hazard, and A. Houck, Suppression of Qubit Crosstalk in a Tunable Coupling Superconducting Circuit, *Physical Review Applied* **12** (5), 054023 (2019).
- [342] X. Li et al., Tunable Coupler for Realizing a Controlled-Phase Gate with Dynamically Decoupled Regime in a Superconducting Circuit, *Physical Review Applied* **14** (2), 024070 (2020).
- [343] M. Lubasch, *Quantum chaos and entanglement in the Bose-Hubbard model*, Diploma thesis (Rubrechts-Karls-Universität, Heidelberg, 2009).
- [344] P. Plötz, M. Lubasch, and S. Wimberger, Detection of avoided crossings by fidelity, *Physica A: Statistical Mechanics and its Applications* **390** (7), 1363–1369 (2011).
- [345] Y. A. Farkov, P. Manchanda, and S. A. H., *Construction of Wavelets Through Walsh Functions* (Springer, 2019).
- [346] H. Kunz, On the Equivalence Between One-Dimensional Discrete Walsh-Hadamard and Multidimensional Discrete Fourier Transforms, *IEEE Transactions on Computers* **C-28** (3), 267–268 (1979).
- [347] F. Andraschko, T. Enss, and J. Sirker, Purification and Many-Body Localization in Cold Atomic Gases, *Physical Review Letters* **113** (21), 217201 (2014).
- [348] P. Bordia, H. P. Lüschen, S. S. Hodgman, M. Schreiber, I. Bloch, and U. Schneider, Coupling Identical one-dimensional Many-Body Localized Systems, *Physical Review Letters* **116** (14), 140401 (2016).
- [349] R. W. Hamming, Error detecting and error correcting codes, *The Bell System Technical Journal* **29** (2), 147–160 (1950).
- [350] J. De Marco, L. Tolle, C.-M. Halati, A. Sheikhan, A. M. Läuchli, and C. Kollath, Level statistics of the one-dimensional ionic hubbard model, *Phys. Rev. Research* **4** (3), 033119 (2022).

- [351] F. Pietracaprina, N. Macé, D. J. Luitz, and F. Alet, Shift-invert diagonalization of large many-body localizing spin chains, *SciPost Physics* **5** (5), 045 (2018).
- [352] S.-D. Börner, *Classical Chaos in Transmon Qubit Arrays*, Bachelor Thesis (University of Cologne, 2020).
- [353] P. D. Bönninghaus, *Chaotic Instabilities in the Classical Limit of IBM Transmon Qubit Designs*, Bachelor Thesis (University of Cologne, 2021).
- [354] G. Benettin, L. Galgani, and J.-M. Strelcyn, Kolmogorov entropy and numerical experiments, *Physical Review A* **14** (6), 2338–2345 (1976).
- [355] G. Datseris, Dynamicalsystems.jl: a julia software library for chaos and nonlinear dynamics, *Journal of Open Source Software* **3** (23), 598 (2018).
- [356] G. Benettin, L. Galgani, A. Giorgilli, and J.-M. Strelcyn, Lyapunov Characteristic Exponents for smooth dynamical systems and for hamiltonian systems; a method for computing all of them. Part 1: Theory, *Meccanica* **15** (1), 9–20 (1980).
- [357] G. Benettin, L. Galgani, A. Giorgilli, and J.-M. Strelcyn, Lyapunov Characteristic Exponents for smooth dynamical systems and for hamiltonian systems; A method for computing all of them. Part 2: Numerical application, *Meccanica* **15** (1), 21–30 (1980).
- [358] C. Rackauckas and Q. Nie, Differentialequations.jl—a performant and feature-rich ecosystem for solving differential equations in julia, *Journal of Open Research Software* **5** (1) (2017).
- [359] C. Tsitouras, Runge–Kutta pairs of order 5(4) satisfying only the first column simplifying assumption, *Computers & Mathematics with Applications* **62** (2), 770–775 (2011).
- [360] J. H. Verner, Explicit Runge-Kutta Methods with Estimates of the Local Truncation Error, *SIAM Journal on Numerical Analysis* **15** (4), 772–790 (1978).
- [361] J. Pöschel, “A lecture on the classical KAM theorem”, in *Smooth ergodic theory and its applications*, Vol. 96, edited by A. Katok, R. de la Llave, and Y. Pesin, 21 (2001), pp. 707–732.
- [362] M. Henon and C. Heiles, The applicability of the third integral of motion: Some numerical experiments, *The Astronomical Journal* **69**, 73 (1964).
- [363] H. Kröger, J.-F. Laprise, G. Melkonyan, and R. Zomorrodi, “Quantum chaos versus classical chaos: why is quantum chaos weaker?”, in *The logistic map and the route to chaos: from the beginnings to modern applications*, edited by M. Ausloos and M. Dirickx (Springer Berlin Heidelberg, 2006), pp. 355–367.
- [364] C. Skokos, T. C. Bountis, and C. Antonopoulos, Geometrical properties of local dynamics in Hamiltonian systems: The Generalized Alignment Index (GALI) method, *Physica D: Nonlinear Phenomena* **231** (1), 30–54 (2007).
- [365] G. A. Gottwald and I. Melbourne, The 0-1 Test for Chaos: A Review, in *Chaos Detection and Predictability*, Vol. 915, edited by C. Skokos, G. A. Gottwald, and J. Laskar (Springer Berlin Heidelberg, 2016), pp. 221–247.
- [366] H. Goto, Double-Transmon Coupler: Fast Two-Qubit Gate with No Residual Coupling for Highly Detuned Superconducting Qubits, *Physical Review Applied* **18** (3), 034038 (2022).
- [367] W. Nuerbolati, Z. Han, J. Chu, Y. Zhou, X. Tan, Y. Yu, S. Liu, and F. Yan, Canceling microwave crosstalk with fixed-frequency qubits, *Applied Physics Letters* **120** (17), 174001 (2022).

- [368] J. Gambetta, *Quantum-centric supercomputing: The next wave of computing*, IBM Research Blog, (2022) <https://research.ibm.com/blog/next-wave-quantum-centric-supercomputing> (visited on 11/16/2022).
- [369] P. Jurcevic, D. Zajac, J. Stehlík, I. Lauer, and R. Mandelbaum, *IBM Quantum has achieved its highest Quantum Volume yet*, IBM Research Blog, (2022) <https://research.ibm.com/blog/quantum-volume-256> (visited on 11/16/2022).
- [370] A. Nico-Katz, A. Bayat, and S. Bose, Memory hierarchy for many-body localization: Emulating the thermodynamic limit, *Physical Review Research* **4** (3), 033070 (2022).
- [371] M. H. Goerz, F. Motzoi, K. B. Whaley, and C. P. Koch, Charting the circuit QED design landscape using optimal control theory, *npj Quantum Information* **3** (1), 1–10 (2017).
- [372] T. Timberlake, Random numbers and random matrices: Quantum chaos meets number theory, *American Journal of Physics* **74** (6), 547–553 (2006).
- [373] S. J. Garratt, S. Roy, and J. T. Chalker, Local resonances and parametric level dynamics in the many-body localized phase, *Physical Review B* **104** (18), 184203 (2021).
- [374] S.-D. Börner, *Dynamics of coupled transmon systems*, Master Thesis (University of Cologne, 2022).
- [375] M. Gong et al., Experimental characterization of the quantum many-body localization transition, *Physical Review Research* **3** (3), 033043 (2021).
- [376] M. Silveri and T. Orell, Many-qubit protection-operation dilemma from the perspective of many-body localization, *Nature Communications* **13** (1), 5825 (2022).
- [377] Q. Guo et al., Observation of energy-resolved many-body localization, *Nature Physics* **17** (2), 234–239 (2021).
- [378] E. Varvelis and D. P. DiVincenzo, Perturbative analysis of quasiperiodic patterning of transmon quantum computers: enhancement of many-body localization, *Phys. Rev. B* **109** (14), 144201 (2024).
- [379] J. Cohen, A. Petrescu, R. Shillito, and A. Blais, Reminiscence of classical chaos in driven transmons, *PRX Quantum* **4** (2), 020312 (2023).
- [380] D. J. Luitz and Y. B. Lev, The ergodic side of the many-body localization transition, *Annalen der Physik* **529** (7), 1600350 (2017).
- [381] R. B. Lehoucq, D. C. Sorensen, and C. Yang, Arpack users guide: solution of large scale eigenvalue problems by implicitly restarted arnoldi methods. 1997.
- [382] A. Kitaev, Anyons in an exactly solved model and beyond, *Annals of Physics* **321** (1), 2–111 (2006).
- [383] L. Savary and L. Balents, Quantum spin liquids: a review, *Reports on Progress in Physics* **80** (1), 016502 (2016).
- [384] Y. Zhou, K. Kanoda, and T.-K. Ng, Quantum spin liquid states, *Reviews of Modern Physics* **89** (2), 025003 (2017).
- [385] S. Trebst and C. Hickey, Kitaev materials, *Physics Reports* **950**, 1–37 (2022).
- [386] G. Jackeli and G. Khaliullin, Mott Insulators in the Strong Spin-Orbit Coupling Limit: From Heisenberg to a Quantum Compass and Kitaev Models, *Physical Review Letters* **102** (1), 017205 (2009).

- [387] M. Hermanns, I. Kimchi, and J. Knolle, Physics of the Kitaev Model: Fractionalization, Dynamic Correlations, and Material Connections, *Annual Review of Condensed Matter Physics* **9** (1), 17–33 (2018).
- [388] X.-G. Wen, *Quantum Field Theory of Many-Body Systems: From the Origin of Sound to an Origin of Light and Electrons* (Oxford University Press, 2007).
- [389] E. H. Lieb, Flux Phase of the Half-Filled Band, *Physical Review Letters* **73** (16), 2158–2161 (1994).
- [390] K. W. Plumb, J. P. Clancy, L. J. Sandilands, V. V. Shankar, Y. F. Hu, K. S. Burch, H.-Y. Kee, and Y.-J. Kim, α -RuCl₃: A spin-orbit assisted Mott insulator on a honeycomb lattice, *Physical Review B* **90** (4), 041112 (2014).
- [391] M. Majumder, M. Schmidt, H. Rosner, A. A. Tsirlin, H. Yasuoka, and M. Baenitz, Anisotropic Ru³⁺4d⁵ magnetism in the α -RuCl₃ honeycomb system: Susceptibility, specific heat, and zero-field NMR, *Physical Review B* **91** (18), 180401 (2015).
- [392] A. Banerjee et al., Proximate Kitaev quantum spin liquid behaviour in a honeycomb magnet, *Nature Materials* **15** (7), 733–740 (2016).
- [393] A. U. B. Wolter et al., Field-induced quantum criticality in the Kitaev system α -RuCl₃, *Physical Review B* **96** (4), 041405 (2017).
- [394] C. Hickey and S. Trebst, Emergence of a field-driven U(1) spin liquid in the Kitaev honeycomb model, *Nature Communications* **10** (1), 1–10 (2019).
- [395] H.-C. Jiang, C.-Y. Wang, B. Huang, and Y.-M. Lu, Field induced quantum spin liquid with spinon Fermi surfaces in the Kitaev model, arXiv:1809.08247 (2018).
- [396] M. Gohlke, R. Moessner, and F. Pollmann, Dynamical and topological properties of the Kitaev model in a [111] magnetic field, *Phys. Rev. B* **98** (1), 014418 (2018).
- [397] H.-Y. Lee, R. Kaneko, L. E. Chern, T. Okubo, Y. Yamaji, N. Kawashima, and Y. B. Kim, Magnetic field induced quantum phases in a tensor network study of Kitaev magnets, *Nature Communications* **11** (1), 1639 (2020).
- [398] Z. Zhu, I. Kimchi, D. N. Sheng, and L. Fu, Robust non-Abelian spin liquid and a possible intermediate phase in the antiferromagnetic Kitaev model with magnetic field, *Physical Review B* **97** (24), 241110 (2018).
- [399] F. J. Burnell and C. Nayak, SU(2) slave fermion solution of the Kitaev honeycomb lattice model, *Physical Review B* **84** (12), 125125 (2011).
- [400] L. Zou and Y.-C. He, Field-induced QCD₃-Chern-Simons quantum criticalities in Kitaev materials, *Physical Review Research* **2** (1), 013072 (2020).
- [401] S. Yang, D. L. Zhou, and C. P. Sun, Mosaic spin models with topological order, *Physical Review B* **76** (18), 180404 (2007).
- [402] H. Yao and S. A. Kivelson, Exact Chiral Spin Liquid with Non-Abelian Anyons, *Physical Review Letters* **99** (24), 247203 (2007).
- [403] S. Mandal and N. Surendran, Exactly solvable Kitaev model in three dimensions, *Physical Review B* **79** (2), 024426 (2009).
- [404] M. Hermanns and S. Trebst, Quantum spin liquid with a Majorana Fermi surface on the three-dimensional hyperoctagon lattice, *Physical Review B* **89** (23), 235102 (2014).

- [405] K. O'Brien, M. Hermanns, and S. Trebst, Classification of gapless \mathbb{Z}_2 spin liquids in three-dimensional Kitaev models, *Physical Review B* **93** (8), 085101 (2016).
- [406] J. Nasu, Y. Kato, Y. Kamiya, and Y. Motome, Successive Majorana topological transitions driven by a magnetic field in the Kitaev model, *Physical Review B* **98** (6), 060416 (2018).
- [407] H.-D. Chen and Z. Nussinov, Exact results of the Kitaev model on a hexagonal lattice: spin states, string and brane correlators, and anyonic excitations, *Journal of Physics A: Mathematical and Theoretical* **41** (7), 075001 (2008).
- [408] S. Mandal, R. Shankar, and G. Baskaran, RVB gauge theory and the topological degeneracy in the honeycomb Kitaev model, *Journal of Physics A: Mathematical and Theoretical* **45** (33), 335304 (2012).
- [409] X.-Y. Feng, G.-M. Zhang, and T. Xiang, Topological Characterization of Quantum Phase Transitions in a Spin-1/2 Model, *Physical Review Letters* **98** (8), 087204 (2007).
- [410] R. Schaffer, S. Bhattacharjee, and Y. B. Kim, Quantum phase transition in Heisenberg-Kitaev model, *Physical Review B* **86** (22), 224417 (2012).

Acknowledgements

First and foremost, I would like to express my sincere gratitude to Simon Trebst, my supervisor, for providing me with the opportunity to pursue exciting research projects and conducting me through this challenging and fulfilling time. I am grateful to him not only for his scientific guidance but also for the tremendous support he has given me in all the challenges that come with starting a family during the doctorate. I could not have wished for a more supportive work environment. I further thank Achim Rosch and Markus Braden for their kindness in acting as the second referee and chair of the thesis committee.

During my research, I enjoyed the privilege of working with many excellent scientists, each of whom contributed to the completion of this thesis. Above all, I would like to thank Ciarán Hickey, who mentored me during the first projects and with whom I had the pleasure of diving into the exciting world of spin liquids. In our five years together at the institute, he always had an open ear and a lot of patience with my questions. His influence on this work cannot be valued highly enough. Furthermore, I am greatly indebted to Alexander Altland and David DiVincenzo for their collaboration on the transmon project. Witnessing how their immense knowledge in very different fields led our joint project to success was very enlightening and great fun. In this context, I would also like to express my thanks to Evangelos Varvelis and Simon Börner for their good cooperation. I thank the German Research Foundation for funding my PhD position (CRC1238 and CRC183). The numerical simulations were performed on the JUWELS cluster at the Forschungszentrum Jülich and the CHEOPS cluster at RRZK Cologne.

I experienced a wonderful time at the University of Cologne, and I want to thank all members of our research group for contributing to making it so enjoyable. Many thanks for their valuable feedback go to all who proofread parts of this work: Kai, Vaishnavi, Martin, Ciarán, Florian, Marc, Guo-Yi and Carsten. I want to thank Carsten, Kai, Florian, and Tim, known as ‘Die festen Körper’, who did not let themselves be discouraged by the regular cancellations of the university run, and who were always ready to set new records for the glory of the institute. Of course, this acknowledgment would not be complete without a very special thank you to the members of the ‘Office of Excellence’, Vaishnavi, Carsten, and Kai, whose pleasant company I very much enjoyed.

A special thanks is also owed to Marc, with whom I climbed many steps of the academic ladder together and with whom I could always share the load in the more challenging times of the PhD.

Abschließend möchte ich mich bei meiner Familie für ihren Beitrag zum Gelingen dieser Arbeit bedanken: Bei meinen Eltern Beate und Andreas für die Ermutigung, die Herausforderung Promotion anzugehen, sowie die facettenreiche und fortwährende Unterstützung. Bei meinem Vater außerdem für das Korrekturlesen. Bei Gabi und Werner für ihre vielseitige Hilfe, vor allem in der Endphase der Arbeit. Bei Johanna, Magdalena und Linus für die Geduld und Rücksichtnahme, die aufmunternde Worte, die Ablenkung, die Abenteuer, die schöne Zeit.

Erklärung

Hiermit versichere ich an Eides statt, dass ich die vorliegende Dissertation selbstständig und ohne die Benutzung anderer als der angegebenen Hilfsmittel und Literatur angefertigt habe. Alle Stellen, die wörtlich oder sinngemäß aus veröffentlichten und nicht veröffentlichten Werken dem Wortlaut oder dem Sinn nach entnommen wurden, sind als solche kenntlich gemacht. Ich versichere an Eides statt, dass diese Dissertation noch keiner anderen Fakultät oder Universität zur Prüfung vorgelegen hat; dass sie – abgesehen von unten angegebenen Teilpublikationen und eingebundenen Artikeln und Manuskripten – noch nicht veröffentlicht worden ist sowie, dass ich eine Veröffentlichung der Dissertation vor Abschluss der Promotion nicht ohne Genehmigung des Promotionsausschusses vornehmen werde. Die Bestimmungen dieser Ordnung sind mir bekannt. Darüber hinaus erkläre ich hiermit, dass ich die Ordnung zur Sicherung guter wissenschaftlicher Praxis und zum Umgang mit wissenschaftlichem Fehlverhalten der Universität zu Köln gelesen und sie bei der Durchführung der Dissertation zugrundeliegenden Arbeiten und der schriftlich verfassten Dissertation beachtet habe und verpflichte mich hiermit, die dort genannten Vorgaben bei allen wissenschaftlichen Tätigkeiten zu beachten und umzusetzen. Ich versichere, dass die eingereichte elektronische Fassung der eingereichten Druckfassung vollständig entspricht.

Teilpublikationen: (bereits veröffentlicht)

- [P1] **C. Berke**, E. Varvelis, S. Trebst, A. Altland, and D. P. DiVincenzo, Transmon platform for quantum computing challenged by chaotic fluctuations, *Nature Communications* **13** (1), 2495 (2022).
- [P2] S.-D. Börner, **C. Berke**, D. P. DiVincenzo, S. Trebst, and A. Altland, Classical chaos in quantum computers, *Phys. Rev. Res.* **6** (3), 033128 (2024).
- [P3] D. Basilewitsch, S.-D. Börner, **C. Berke**, A. Altland, S. Trebst, and C. P. Koch, Chaotic fluctuations in a universal set of transmon qubit gates, *arXiv:2311.14592* (2023).
- [P4] **C. Berke**, S. Trebst, and C. Hickey, Field stability of Majorana spin liquids in antiferromagnetic Kitaev models, *Physical Review B* **101** (21), 214442 (2020).
- [P5] C. Hickey, M. Gohlke, **C. Berke**, and S. Trebst, Generic field-driven phenomena in Kitaev spin liquids: Canted magnetism and proximate spin liquid physics, *Physical Review B* **103** (6), 064417 (2021).
- [P6] C. Hickey, **C. Berke**, P. P. Stavropoulos, H.-Y. Kee, and S. Trebst, Field-driven gapless spin liquid in the spin-1 Kitaev honeycomb model, *Phys. Rev. Research* **2** (2), 023361 (2020).

Köln, den 22. Dezember 2023

(Christoph Berke)